Stochastic Modeling and Analysis of Power System with Renewable Generation

Chen, Peiyuan

Publication date:
2010

Document Version
Accepted author manuscript, peer reviewed version

Citation for published version (APA):
Chen, P. (2010). *Stochastic Modeling and Analysis of Power System with Renewable Generation*. Department of Energy Technology, Aalborg University.

STOCHASTIC MODELING AND ANALYSIS OF POWER SYSTEM WITH RENEWABLE GENERATION

by

Peiyuan Chen

Dissertation submitted to the Faculty of Engineering, Science & Medicine at Aalborg
University in partial fulfillment of the requirements for the degree of
Doctor of Philosophy in Electrical Engineering

Department of Energy Technology
Aalborg University, Denmark
January, 2010

Aalborg University
Department of Energy Technology
Pontoppidanstræde 101
DK-9220 Aalborg East

ISBN: 87-89179-89-6

Printed in Denmark by Aalborg University

Abstract

Unlike traditional fossil-fuel based power generation, renewable generation such as wind power relies on uncontrollable prime sources such as wind speed. Wind speed varies stochastically, which to a large extent determines the stochastic behavior of power generation from wind farms. With the increasing number of wind turbines (WTs) connected to distribution systems, network operators are concerned about how such a stochastic generation affects power losses of the network. Furthermore, the operators need to estimate how much and when the stochastic generation can reduce the loading of substation transformers and distribution feeders. Moreover, the network operators are interested in evaluating the maximum penetration level of wind power in their network before any technical requirements are violated.

The traditional approach to these studies is based on a deterministic analysis. For instance, the size of a substation transformer is determined by the sum of the maximum loading at individual radial feeders while assuming no generation output from local generators. However, such a deterministic analysis does not provide a realistic evaluation of system steady-state performance. A more realistic evaluation can be achieved through a probabilistic analysis that takes into account the stochastic behavior of wind power generation (WPG) and load demand. Such a probabilistic analysis may help network operators to cut down the cost associated with system planning. Thus, the objective of this thesis is to develop stochastic models of renewable generation and load demand for the optimal operation and planning of modern distribution systems through a probabilistic approach.

On the basis of statistical data, stochastic models of WPG, load and combined heat and power (CHP) generation are developed. The stochastic wind power model is constructed on the basis of an autoregressive integrated moving average (ARIMA) process. The model characterizes WPG by mean level, temporal correlation and driving noise. Such a model is valuable for researchers who do not have access to wind power measurements. The model can be used to evaluate year-to-year variation of wind power generation through a sensitivity analysis and to forecast very short-term wind power through a model-based prediction method. The stochastic load model is established on the basis of a seasonal autoregressive moving average (ARMA) process. It is demonstrated that such a stochastic model can be used to simulate the effect of load management on the load duration curve. As CHP units are turned on and off by regulating power, CHP generation has discrete output and thus can be modeled by a transition matrix based discrete Markov chain. As the CHP generation has a strong diurnal variation, reflecting the heat load and electricity price, it is proposed to use different transition matrices for different periods of a day. These three stochastic models are the main theoretical contributions of this thesis.

With these stochastic models, a realistic evaluation of the system steady-state performance can be carried out through a probabilistic load flow (PLF) analysis. Based on the PLF analysis, several studies are conducted and strategies are proposed to operate and plan a modern distribution system in an optimal way. In the first case study, a stochastic optimization algorithm is proposed that minimizes the expectation of power losses of a 69-bus distribution system by controlling the power factor of WTs. The optimization is subjected to the probabilistic constraints of bus voltage and line current. The algorithm combines a constrained nonlinear optimization algorithm and a Monte Carlo based PLF calculation. In the second case, it is demonstrated through a Danish distribution system (Støvring system) that the probability of transformer overloading and the time of the overloading can be identified through a probabilistic analysis. Based on the analysis, use of a gas turbine is determined as a cheaper solution than transformer expansion in order to solve the overloading problem. In the last case, an optimal constrained load flow algorithm is proposed to determine the maximum WT capacity in the modified Støvring system when allowing reactive power control and energy curtailment of WTs, subject to voltage and current constraints. These developed models and proposed algorithms serve as effective tools to assist network operators in decision-making during the operation and planning of power systems.

Acknowledgements

The financial support for the PhD project by the Danish Agency for Science Technology and Innovation under the project of 2104-05-0043 is gratefully acknowledged.

I would like to thank my supervisors Prof. Zhe Chen and Associate Prof. Birgitte Bak-Jensen for their kindness, support, and discussions throughout the whole PhD study. In addition, I would like to thank Prof. Zhe Chen for his generous help when I first moved to Aalborg.

I would like to thank the project steering committee members, including Stefan Sörensen, Niels Andersen and Anders Foosnæs, for their data supply, help and discussions during the project.

During my PhD study, a number of research works have been carried out in cooperation with several external researchers. Their contribution is highly appreciated. In particular, I would like to thank Dr. Troels Pedersen from the Department of Electronic Systems for his preciseness and intensive discussions on the stochastic wind power modeling; Associate Prof. Kasper K. Berthelsen from the Department of Mathematical Sciences for his interesting ideas and extensive discussions on discrete Markov model; Dr. Pierluigi Siano from University of Salerno for his kindness, generous help and discussions on optimization algorithms and all the work we have done together; Anestis Anastasiadis from the National Technical University of Athens for his help in probabilistic load flow and great hospitality during my study abroad in Athens; Dr. Roberto Villafáfila Robles from Universitat Politècnica de Catalunya for the project initialization and being a very good friend.

I would like to express my deepest gratitude to Prof. Torbjörn Thiringer from Chalmers University of Technology for his encouragement, inspiration and unconditional help during my Master and PhD study.

Of course, many thanks go to my friends and colleagues at the Institute of Energy Technology, especially Pukar, Jay, Erik and Torben, for making the working environment enjoyable.

In particular, I would like to thank my best friend Dmitrij Slepniov for his continuous support, encouragement and comments on my papers and thesis even though he is not a electric power engineer (probably becomes one after all the reading).

Finally, I would like to thank my family in China for their love and support.

Peiyuan Chen
January, 2010
Aalborg

Abbreviations

ACC	Autocorrelation Coefficient
AIC	Akaike Information Criterion
AR	Autoregressive
ARIMA	Autoregressive Integrated Moving Average
ARMA	Autoregressive Moving Average
BIC	Bayesian Information Criterion
CHP	Combined Heat and Power
DG	Distributed Generation
DLF	Deterministic Load Flow
LARIMA	Limited Autoregressive Integrated Moving Average
LARMA	Limited Autoregressive Moving Average
LMMSE	Linear Minimum Mean Square Error
MA	Moving Average
MSE	Mean Square Error
PACC	Partial Autocorrelation Coefficient
PLF	Probabilistic Load Flow
SRS	Simple Random Sampling
TSO	Transmission System Operator
WPG	Wind Power Generation
WT	Wind Turbine

Table of Contents

Chapter 1

Introduction

1.1 Background and motivation

The traditional power system, in which power is delivered to customers from central power plants through transmission and distribution networks, has been undergoing a significant change because of the deregulation of the power system and the integration of distributed generation (DG). In particular, the large-scale integration of DG into distribution systems may influence the operation and planning of the system to a great extent (Pecas Lopes 2002, Hatziargyriou, Sakis Meliopoulos 2002). Such influence involves network power losses, steady state voltage variation, short circuit level, voltage stability, distribution reliability issues, distribution system protection, distribution system planning, etc.

Furthermore, in contrast to conventional fossil fuel based power generation, renewable energy based DG such as wind power generation (WPG) and photovoltaic generation are not fully controllable due to the stochastic behavior of their prime sources such as wind speed and irradiance. These stochastic generations introduce additional uncertainties into the daily operation and long-term planning of a distribution system, which further complicates the understanding and analysis of the impact of DG on the system.

In Denmark, the two most common types of DG are wind power and combined heat and power (CHP) generation. By the end of 2008, the total installed wind turbine (WT) capacity was 3166 MW, which accounted for 24.1% of the total electricity generation capacity; the total installed small-scale CHP units was 1738 MW, which amounted to 13.2% of the total electricity capacity (Danish Energy Agency 2009). The integration of WPG and CHP generation to the medium voltage distribution systems provides a number of challenges to the network operators. One major challenge is on how to account for the stochastic behavior of WPG in an appropriate way. Furthermore, the traditional evaluation criterion is based on a deterministic approach, which may not provide a realistic assessment on the system performance as WPG, CHP generation and load demand fluctuate throughout a year. In order to address these issues, a probabilistic approach may be employed to take into account the stochastic behavior of system generation and load demand. Consequently, a realistic evaluation of the system performance may be achieved.

1.2 Overview of Previous Related Work

This section provides a general overview of the topics related to the thesis. A detailed literature review on specific topics can be found in the corresponding chapters.

1.2.1 Probabilistic analysis in power systems

Although the deterministic analysis is a common approach used in electric utilities, e.g. N-1 criterion and worst-case scenario, the probabilistic analysis in power systems also has a solid theoretical background (Anders 1990, Schilling et al. 1990, Billinton, Fotuhi-Firuzabad & Bertling 2001). The areas where probabilistic analysis is applied include reliability evaluation, probabilistic structural design of transmission systems, probabilistic load flow (PLF) and short circuit calculation, probabilistic system stability evaluation, etc (Anders 1990). The techniques used for these probabilistic analyses are usually based on fundamental probability theories of univariate random (stochastic) variables, multivariate random (stochastic) variables and random (stochastic) processes (Papoulis, Pillai 2002). The following summarizes a number of applications of probability analysis in power system studies.

In reliability evaluation, generator outage is simulated by a discrete random variable with binomial distribution (Billinton, Allan 1996). In PLF analysis, load demand at a single bus is commonly represented by a continuous random variable with normal distribution, while load demands at different buses are assumed independent of or linearly correlated with each other (Leite, Arienti & Allan 1984); wind power is modeled as a continuous random variable within different wind speed range (Hatziargyriou, Karakatsanis & Papadopoulos 1993). In short circuit analysis, each fault type is considered a discrete random variable (Anders 1990) and fault distance is characterized by a mean and standard value (Zhu, Lubkeman & Girgis 1997). These applications treat system components and phenomena as random variables. However, for wind power and load, the correlation in time plays an important role for the system evaluation over a certain period. In this case, it is no longer sufficient to model wind power and load by random variables. Instead, theories of random processes should be applied. For instance, wind speed time series is simulated by an autoregressive moving average model (Billinton, Chen & Ghajar 1996), and wind power time series is modeled by a transition matrix based Markov chain (Papaefthymiou, Klockl 2008). These models simulate the stochastic process of WPG and are mainly applied in reliability evaluations (Billinton, Wangdee 2007, Wangdee, Billinton 2006).

For evaluating system performance with these random variables and processes, two common approaches are applied: the analytical approach and the numerical approach. The analytical approach is based on a direct operation with random variables such as using the convolution method. The numerical approach refers to Monte Carlo simulation. A detailed discussion of these approaches is provided in Chapter 3.

1.2.2 Optimal operation and planning of distribution systems with DG

Traditional distribution systems are designed to deliver power from the transmission networks to local loads. This type of power supply is changed due to the integration of DG, which can supply the local loads directly and may reverse the power flow direction by injecting power to the transmission networks. Such a change may significantly influence the voltage profile, power losses, power quality, protection, reliability and planning of the distribution systems (Barker, De Mello 2000). The influence may be positive or negative, depending on the type, size and location of the DG and the characteristics of the distribution systems.

In order to ensure a secure, reliable and economic operation of the system, network operators intend to minimize the adverse impacts and to maximize the potential benefits brought by DG. This is normally achieved by optimizing the location and capacity of the DG in a distribution system.

To address such issues, the common practice is to formulate an optimization problem, which searches for the optimal location and capacity of the DG. The objective functions of the optimization problem may include minimizing the system power losses (Rau, Wan 1994, Nara et al. 2001, Kim et al. 2002, Celli et al. 2005), minimizing the investment and operating costs (El-Khattam et al. 2004), maximizing the net revenue received by distribution network operators (Harrison et al. 2007, Piccolo, Siano 2009), maximizing the capacity (Keane, O'Malley 2005, Harrison et al. 2008) or the produced energy from DG (Keane, O'Malley 2007), etc. The constraints of the optimization normally consist of bus voltage limits and line thermal limits. Some also take into account the short-circuit levels (Vovos et al. 2005) and reliability constraints (Greatbanks et al. 2003). As the DG location is a discrete variable, genetic algorithm can be used to find the optimal location (Kim et al. 2002, Celli et al. 2005). Other algorithms such as Tabu search (Nara et al. 2001) can also be used.

Nevertheless, one major limitation in these methods is that the stochastic behaviour of load and WPG is not fully or properly taken into account. In (Ochoa, Padilha-Feltrin & Harrison 2008), typical seasonal load profiles are used to represent the seasonal and diurnal variation of load. A one-week time series of WPG has been used to reflect its time-varying behavior. However, these are not sufficient to consider the stochastic behavior of load and WPG properly, as a typical daily or weekly curve cannot represent their stochastic behavior throughout a year. Therefore, more sophisticated stochastic models of load and WPG needs to be developed.

1.3 Problem formulation

Based on the foregoing literature review, the **objective** of this thesis is:

To develop stochastic models of renewable generation and load demand for the optimal operation and planning of modern distribution systems through a probabilistic approach.

In order to achieve the above objective, the problems to be tackled in this thesis are formulated as follows:

1) To develop stochastic models of WPG, CHP generation and load demand,
2) To evaluate system steady-state performance based on PLF techniques,
3) To investigate the impact of renewable energy based DG units on the steady-state performance of the distribution systems through a probabilistic approach with stochastic models,
4) To compare the deterministic approach and probabilistic approach for distribution system planning,
5) To design an optimal cable network for integrating wind energy to the grid,
6) To evaluate the maximum wind power penetration level of a distribution network integrated with renewable energy based DG,
7) To assess the impact of stochastic WPG on system frequency control.

1.4 Project limitation

The thesis has the following limitations:

1) Only steady-state analysis of power systems are carried out in the project. Power System stability and other transient analyses are not considered in this project,
2) The time scale of the analysis is at the step of 15 min or one hour over a period of one year or several years,
3) Other techniques for uncertainty analysis, such as interval analysis and fuzzy set method, are not considered,
4) The evaluation and verification is carried out on selected distribution networks.

1.5 Technical contribution of the thesis

The main technical contribution of the thesis is summarized as follows:

1) A parsimonious stochastic model is developed for simulating wind power time series. This model can be readily used for researchers who do not have a direct access to measurement data. The model can be used for reliability analysis and planning of power systems integrated with wind farms. The model can also be used for sensitivity analysis of wind level variation and the simulated wind power time series can be served as a database for testing wind power forecasting algorithms.
2) A new stochastic load model is developed for simulating the effect of load management.
3) A new optimization algorithm that combines the gradient-based optimization and Monte Carlo simulation of constrained load flow is proposed to evaluate the maximum WT capacity in a network while allowing reactive power control and energy curtailment.
4) Both the technical and economic evaluations are provided for demonstrating the advantage of using probabilistic approach as compared to the deterministic approach in distribution system planning.

1.6 Outline of the thesis

The thesis is composed of nine chapters:

In Chapter 1, the background and motivation of the thesis are described, together with an overview of the previous related work. Then, the objective, the problem formulation and the main contribution of the thesis are presented.

In Chapter 2, stochastic models of WPG, CHP generation and load demand are developed for Monte Carlo simulation.

In Chapter 3, the PLF techniques are presented, including both analytical approach and numerical approach.

In Chapter 4, a stochastic optimization algorithm is developed to minimize power losses of a distribution system by setting optimal WT power factor.

In Chapter 5, short-range distribution system planning through a probabilistic approach is performed.

In Chapter 6, optimal cable sizing for a medium voltage wind energy network is studied.

In Chapter 7, the maximum WT capacity of a distribution system is evaluated through an optimal constrained optimization algorithm.

In Chapter 8, the relation between wind power forecasting error and system steady-steady frequency deviation is investigated.

The summary and conclusions of the thesis are presented in Chapter 9. A number of topics for future work are also provided in the end.

1.7 List of publications

The following lists the scientific papers published during the PhD study. Paper [2] is included in section 2.1 and Chapter 4. Paper [4] is included in section 2.1. Paper [6] is included in section 2.2. Paper [7] is included in Chapter 5. The remaining publications are complementary to this thesis.

Book Chapter

[1] **P. Chen**, P. Siano, B. Bak-Jensen and Z. Chen, *Optimal Allocation of Power-Electronic Interfaced Wind Turbines Using a Genetic Algorithm-Monte Carlo Hybrid Optimization Method*, to be published by Springer-Verlag in the Book 'Wind Power Systems: Applications of Computational Intelligence', 2010.

Journal Papers

[2] **P. Chen**, P. Siano, B. Bak-Jensen and Z. Chen, 'Stochastic optimization of wind turbine power factor using stochastic model of wind power,' to be published on *IEEE Trans. Sustainable Energy*, vol. 1, no. 1, 2010.

[3] P. Siano, **P. Chen**, Z. Chen and A. Piccolo, 'Evaluating maximum wind energy exploitation in active distribution networks,' *IET Generation, Transmission & Distribution*, accepted for publication, Paper ID GTD-2009-0548, 2009.

[4] **P. Chen**, T. Pedersen, B. Bak-Jensen and Z. Chen, 'ARIMA-based time series model of stochastic wind power generation,' *IEEE Trans. Power Systems*, accepted for publication, 2009. Digital Object Identifier: 10.1109/TPWRS.2009.2033277.

Conference Papers

[5] **P. Chen**, K. K. Berthelsen, B. Bak-Jensen and Z. Chen, 'Markov model of wind power time series using Bayesian inference of transition matrix', *35th Annual Conference of the IEEE Industrial Electronics Society* (*IECON*), Porto, Nov. 2009

[6] **P. Chen**, B. Bak-Jensen and Z. Chen, 'Probabilistic load models for simulating the impact of load management', *IEEE Power & Energy Society General Meeting 2009*, Calgary, Canada, Jul. 2009

[7] **P. Chen**, B. Bak-Jensen, Z. Chen and S. Sörensen, 'Measurement based scenario analysis of short-range distribution system planning', *Asia-Pacific Power and Energy Engineering Conference*, Wuhan, China, Mar. 2009

[8] **P. Chen**, Z. Chen and B. Bak-Jensen, 'Comparison of steady-state SVC models in load flow calculations', *43rd International Universities Power Engineering Conference*, University of Padova, Italy, 2008.

[9] **P. Chen**, Z. Chen and B. Bak-Jensen, 'Probabilistic load flow: a review', *3rd International Conference on Electric Utility Deregulation and Restructuring and Power Technologies*, Nanjing, China, 2008

[10] **P. Chen**, Z. Chen, B. Bak-Jensen, R. Waagepetersen and S. Sörensen, 'Verification of a probabilistic model for a distribution system with integration of dispersed generation', *Proc. 16th Power Systems Computation Conference* (*PSCC*), Glasgow, University of Strathclyde, UK, 2008

[11] **P. Chen**, Z. Chen, B. Bak-Jensen, R. Robles Villafáfila and S. Sörensen, 'Study of power fluctuation from dispersed generations and loads and its impact on a distribution network through a probabilistic approach', *Proc. 9th International Conference on Electric Power Quality and Utilisation*, Barcelona, Spain, 2007

[12] R. Robles Villafáfila, R. Galceran, B. Bak-Jensen, **P. Chen**, Z. Chen and S. Sörensen, 'Probabilistic assessment of wind power production on voltage profile in distribution networks', *Proc. 9th International Conference on Electric Power Quality and Utilisation*, Barcelona, Spain, 2007

Chapter 2

Stochastic Models of Renewable Generation and Load Demand

This chapter develops stochastic models for WPG, load and CHP generation. Section 2.1 proposes an autoregressive integrated moving average (ARIMA) based time series model for stochastic WPG. The cross-correlation modeling of WPG from wind farms at adjacent locations is also demonstrated. Section 2.2 presents a seasonal autoregressive moving average (ARMA) model for load demand. The application of the stochastic load model for simulating the effect of load management is also illustrated. Section 2.3 introduces a discrete Markov chain model for CHP generation. Section 2.4 summarizes the above three developed models.

2.1 Stochastic wind power model

This section proposes a stochastic wind power model based on an ARIMA process. The model takes into account the nonstationarity and physical limits of stochastic WPG. The model is constructed based on wind power measurement of one year from the Nysted offshore wind farm in Denmark. The proposed limited-ARIMA (LARIMA) model introduces a limiter and characterizes the stochastic WPG by mean level, temporal correlation and driving noise. The model is validated against the measurement in terms of temporal correlation and probability distribution. The LARIMA model outperforms a first-order transition matrix based discrete Markov model in terms of temporal correlation, probability distribution and model parameter number. The proposed LARIMA model is further extended to include the monthly variation of the stochastic WPG.

2.1.1 Introduction

The high integration of wind power into electrical systems calls for new methods and simulation tools that can assist electric utilities in analyzing the impact of stochastic WPG on power system operation and planning (Willis, Scott 2000). Such analyses usually require a probabilistic approach, which commonly relies on sequential Monte Carlo simulations (Billinton, Wangdee 2007). The sequential Monte Carlo simulations consider both the probability distribution and the chronological characteristics of WPG, load profiles, and transition states of all the system components (Billinton, Wangdee 2007). Furthermore, sequential Monte Carlo simulations usually require a large number of simulation runs to obtain statistically reliable results, for instance to simulate rare events such as extreme wind situations. Thus, stochastic wind power models that are able to capture both the probability distribution and temporal correlation of the WPG are needed.

As depicted in Fig. 2.1, existing approaches for the stochastic modeling of the WPG fall into two categories: the wind speed approach (Billinton, Chen & Ghajar 1996, Brown, Katz & Murphy 1984, Shamshad et al. 2005, Castro Sayas, Allan 1996, Negra et al. 2008, Kitagawa, Nomura 2003) and the wind power approach (Papaefthymiou, Klockl 2008). Both approaches are based on wind speed measurements. The former approach requires a wind speed model. Available wind speed models include the autoregressive moving average (ARMA) model (Billinton, Chen & Ghajar 1996, Brown, Katz & Murphy 1984), the discrete Markov model (Shamshad et al. 2005, Castro Sayas, Allan 1996, Negra et al. 2008), and the wavelet-based model (Kitagawa, Nomura 2003). In contrast, the latter approach requires a wind power model. The available wind power model in (Papaefthymiou, Klockl 2008) uses a transition matrix based discrete Markov model.

The two approaches can be applied to the planning of future wind farms in the power system. However, both approaches entail wind speed measurements and an accurate wind farm model, which is usually unavailable. The accurate wind farm model is not needed in the case where wind power measurements are available. In fact, electric utilities measure and record wind power flowing into their networks. Thus, they have direct access to these wind power data. In this case, as shown in Fig. 2.1, wind power measurements can be directly used to build a wind power model, which may be used for system planning involving already operating wind farms. In addition, the need for wind speed measurements is alleviated.

In the case that only wind speed measurements are available, either the wind speed approach or the wind power approach may be applied. One disadvantage of the wind power approach is that WPG has both lower and upper limits and does not follow a standard probability distribution. This makes it more challenging to apply standard statistical models. On the other hand, one drawback of the wind speed approach is that an error, e.g. of 3%, in wind speed modeling may cause an error of around 9% in wind power. This is because wind power varies with the cube of wind speed when the speed is between cut in and rated value.

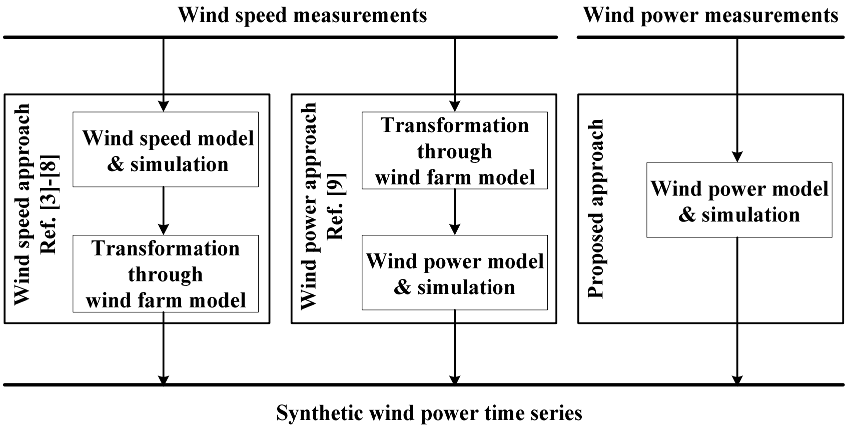

Fig. 2.1. Alternative approaches for modeling wind power time series.

In brief, the challenges of building a stochastic wind power model are that the WPG is a nonstationary and non-Gaussian random process, where a direct application of ARMA models is not feasible. As proposed in (Papaefthymiou, Klockl 2008), a discrete Markov model using transition matrix may be applied to modeling the WPG. This model is constructed based on a quantized wind power time series. The transition matrix defines the probabilities of moving from one state to any other states. However, the model presents several practical problems. Firstly, the model does not consider the nonstationary characteristic of the WPG. Secondly, the model requires a large number of parameters and thus calls for a large amount of training data. Finally, the model gives a poor fit with respect to the probability distribution. This lack-of-fit is due to the error induced when quantizing the wind power time series.

This section proposes a parsimonious stochastic wind power model based on an autoregressive integrated moving average (ARIMA) model. The proposed model takes into account the nonstationary characteristic of the WPG with only few model parameters. In addition, the proposed model does not rely on quantization and thus does not suffer from quantization errors.

The rest of the section is organized as follows. Subsection 2.1.2 introduces necessary notations and concepts. Subsection 2.1.3 performs a statistical analysis on a one-year wind power time series measured from the Nysted offshore wind farm in Denmark. A standard ARIMA model for the measurement data is then identified in subsection 2.1.4. Subsection 2.1.5 improves the identified ARIMA model by introducing a limiter to the feedback loop of the model. The proposed model, referred to as the limited-

ARIMA (LARIMA) model, is further extended to include the monthly variations of the WPG. Concluding remarks and future works are stated in subsection 2.1.7.

2.1.2 Methodology

This subsection presents the necessary notations and concepts of stationary and nonstationary random processes. Then, the ARIMA model for the nonstationary random process is introduced and the Box-Jenkins' procedures of model identification for a nonstationary time series is outlined. Interested readers are referred to (Box, Jenkins & Reinsel 1994) and (Wei 1990) for detailed information.

a. Wide-Sense Stationary and Nonstationary Random Process

Let *y*(1), …, *y*(N) denote an observed time series, which is modeled by a random process *Y*(*t*). The temporal correlation of the random process can be described by the autocorrelation coefficient (ACC) (Papoulis, Pillai 2002) and partial autocorrelation coefficient (PACC). The ACC expresses the linear correlation of data among adjacent observations of a random process. The theoretical ACC of a random process is usually not known, but can be estimated from the observed time series by the sample ACC as (Wei 1990)

$$\hat{\rho}_Y(k) = \frac{\frac{1}{\mathrm{N}-k}\sum_{i=1}^{\mathrm{N}-k}\left[y(i)y(i+k)\right] - \hat{m}_Y^2}{\hat{\sigma}_Y^2}, \text{for } k = 0,1,\ldots \mathrm{N}-1 \tag{2.1}$$

where $\hat{m}_Y$ and $\hat{\sigma}_Y^2$ are the sample mean and variance of the observed time series, respectively.

The PACC of *Y*(*t*) describes the correlation between *Y*(*t*) and *Y*(*t*+*k*) when the mutual linear dependency of *Y*(*t*+1), *Y*(*t*+2), …, *Y*(*t*+*k*-1) is removed. In other words, it is the correlation between *Y*(*t*) and *Y*(*t*+*k*) conditioned on *Y*(*t*+1), *Y*(*t*+2), …, *Y*(*t*+*k*-1). Given the sample ACC, the sample PACC $\hat{\gamma}_Y(k)$ can be calculated iteratively through (Wei 1990)

$$\hat{\gamma}_Y(k+1) = \frac{\hat{\rho}_Y(k+1) - \sum_{j=1}^{k}\hat{\gamma}_Y(k,j)\,\hat{\rho}_Y(k+1-j)}{1-\sum_{j=1}^{k}\hat{\gamma}_Y(k,j)\hat{\rho}_Y(j)}, \tag{2.2}$$

with $\hat{\gamma}_Y(0) = 1$, and

$$\hat{\gamma}_Y(k, j) = \hat{\gamma}_Y(k-1, j) - \hat{\gamma}_Y(k)\hat{\gamma}_Y(k-1, k-j) . \tag{2.3}$$

The standard error of the sample PACC is approximated by (Wei 1990)

$$S_{\text{PACC}} = \sqrt{1/\text{N}} . \tag{2.4}$$

Hence, ±2S_{PACC} can be used as critical limits on the sample PACC to test the hypothesis of a white noise process.

With respect to the WSS random process, a nonstationary random process $Y(t)$ distinguishes itself in a number of ways. It may have a time-varying mean $m_Y(t)$ and variance $\sigma_Y^2(t)$. Some transformations, such as differencing and variance-stabilizing (Wei 1990), are introduced to transform the nonstationary random process to an approximately stationary one.

For a process with a time-varying mean, a stochastic trend model can be applied (Wei 1990). The stochastic trend model is constructed by differencing the random process for d times, i.e.

$$Z(t) = (1-B)^d \, Y(t), \tag{2.5}$$

where B is the backshift operator such that $B^j Y(t) = Y(t-j)$.

For a process with a time-varying variance, the Box-Cox's power transformation is applied to stabilize the variance by (Wei 1990)

$$\text{T}(Y(t)) = \frac{Y^{\nu}(t)-1}{\nu\,\text{G}^{\nu-1}(Y)}, \tag{2.6}$$

where G(Y) is the geometric mean of Y(1), …, Y(N):

$$\mathrm{G}(Y)=\left(\prod_{i=1}^{\mathrm{N}} Y(i)\right)^{1/\mathrm{N}}, \tag{2.7}$$

and v is a parameter determining the transformation. The criterion for selecting v for variance stabilizing transformation is to minimize the residual sum of squares (Wei 1990)

$$SS(v)=\sum_{t=1}^{\mathrm{N}}\left(\mathrm{T}\big(y(t)\big)-\widehat{m}_Y\right)^2. \tag{2.8}$$

Some common transformations are listed in Table 2.1 together with the corresponding v. The values of ln($SS(v)$) are calculated from the wind power measurements presented in the following section and will be further discussed in section 2.1.4. The power transformation is usually applied before the differencing operation.

Table 2.1

Box-Cox Power Transformation (Wei 1990) and Logarithm of the Residual Sum of Squares of the Power-Transformed Wind Power Time Series

v	Transformation	ln($SS(v)$)
-1	$1/Y(t)$	38.5
-0.5	$1/\sqrt{Y(t)}$	26.1
0	$\ln Y(t)$	16.6
0.5	$\sqrt{Y(t)}$	15.5
1	$Y(t)$	17.1

b. The ARIMA-family model

An ARIMA(p, d, q) model of the nonstationary random process $Y(t)$ is expressed as (Box, Jenkins & Reinsel 1994)

$$\left(1-\sum_{i=1}^{p}\varphi_i B^i\right)(1-B)^d\, Y(t)=\theta_0+\left(1-\sum_{i=1}^{q}\theta_i B^i\right)a(t) \tag{2.9}$$

where $\{\varphi_i\}$ are the AR coefficients; $\{\theta_i\}$ are the moving average (MA) coefficients; $a(t)$ is a white Gaussian process with zero mean and variance σ_a^2; the parameter θ_0 is referred to as the deterministic trend term when $d > 0$. The deterministic trend term θ_0 can be omitted unless the sample mean $\widehat{m}_Z$ of the transformed time series $Z(t)$ as in (2.5) is significantly larger than its standard error $S\left(\widehat{m}_Z\right)$ (Wei 1990). The standard error can be approximated by

$$S\left(\widehat{m}_Z\right) = \sqrt{\sigma_Z^2\left(1+2\widehat{\rho}_Z(1)+2\widehat{\rho}_Z(2)+\cdots+2\widehat{\rho}_Z(k)\right)/\mathrm{N}}, \tag{2.10}$$

where σ_Z^2 is the sample variance of $Z(t)$ and $\widehat{\rho}_Z(1),\ldots,\ \widehat{\rho}_Z(k)$ are the first k significant sample ACCs of $Z(t)$.

In the case of $d = 0$, the ARIMA(p, d, q) model is reduced to an ARMA(p, q) model (Wei 1990). For an ARMA model, θ_0 is related to the sample mean $\widehat{m}_Y$ of the process as

$$\theta_0 = \widehat{m}_Y\left(1-\varphi_1-\cdots-\varphi_p\right). \tag{2.11}$$

The ARMA(p, q) model is reduced to an AR(p) model when $q = 0$, and an MA(q) model when $p = 0$. The coefficients of the ARMA model can be estimated by the Yule-Walker estimator, the least square estimator, the maximum likelihood estimator, etc (Wei 1990).

The Box-Jenkins's procedures of model identification for a nonstationary time series (Wei 1990) are summarized in four steps:

- Choose proper transformations of the observed time series. The most common transformations are variance-stabilizing transformation and differencing operation.
- Calculate the sample ACC and PACC of the observed time series to decide the necessity and degree of differencing.
- Calculate the sample ACC and PACC of the properly transformed time series to identify the orders of p and q of the ARIMA model.
- Test the deterministic trend term θ_0 if $d > 0$ to decide the necessity of including θ_0 in the model.

The Box-Jenkins' procedures of model identification will be followed in section 2.1.4, after the analysis of the measured wind power time series in section 2.1.3.

2.1.3 Statistical analysis of wind power time series

A statistical analysis is performed on a wind power time series measured at the Nysted offshore wind farm connected to the Lolland-Falster distribution system in Denmark. The wind farm's capacity is 165.6 MW. It consists of 72 fixed-speed wind turbines, each with capacity of 2.3 MW. The data are hourly measurements from Jan. 1 to Dec. 31, 2005.

The time-domain plots of the wind power time series for the whole year and first ten days in January are shown in Fig. 2.2. The WPG is on average higher in certain months (Nov. to Apr.) than in other months (May to Oct.). A strong temporal correlation is observed, e.g. a continuously high power generation between 48th h and 96th h. However, a dramatic change in power generation from almost maximum to zero is also observed between 168th h and 192nd h.

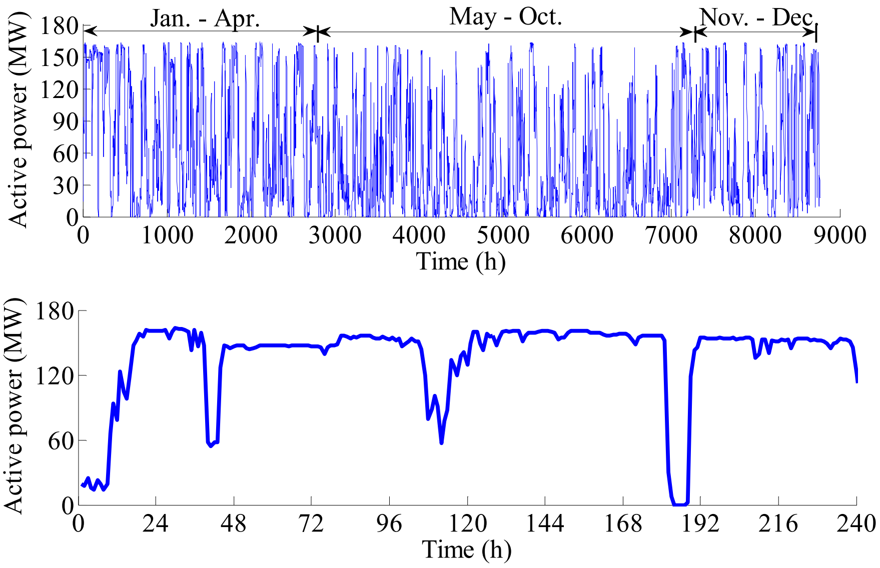

Fig. 2.2. Wind power time series from measurements: one-year time series (top), and first ten days in January (bottom)

The empirical probability density function of the measured time series is shown in Fig. 2.3. The probability mass concentrates around zero of the distribution, with a small rise around the rated power. This effect is expected from the actual operation of the wind farm due to power limitations at the cut-in and rated wind speed. As a result, the distribution is not a standard exponential or any other standard probability distribution.

The sample ACC and PACC of the measured time series are shown in Fig. 2.4. The sample ACC decays slowly. The sample PACC is significant for time lags up to 3. According to (Wei 1990), this indicates that the time series may be nonstationary. The implication of the sample ACC and PACC on the model identification is to be discussed in section 2.1.4.

The periodogram (Leon-Garcia 2009) of the time series is shown in Fig. 2.5. No particularly dominant frequency components are observed. The frequency component corresponding to 24 h is present, but very weak. Thus, it will not be considered in the sequel.

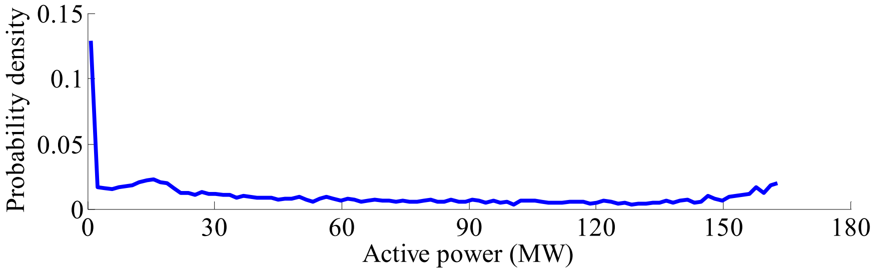

Fig. 2.3. Empirical probability density of the measured wind power time series.

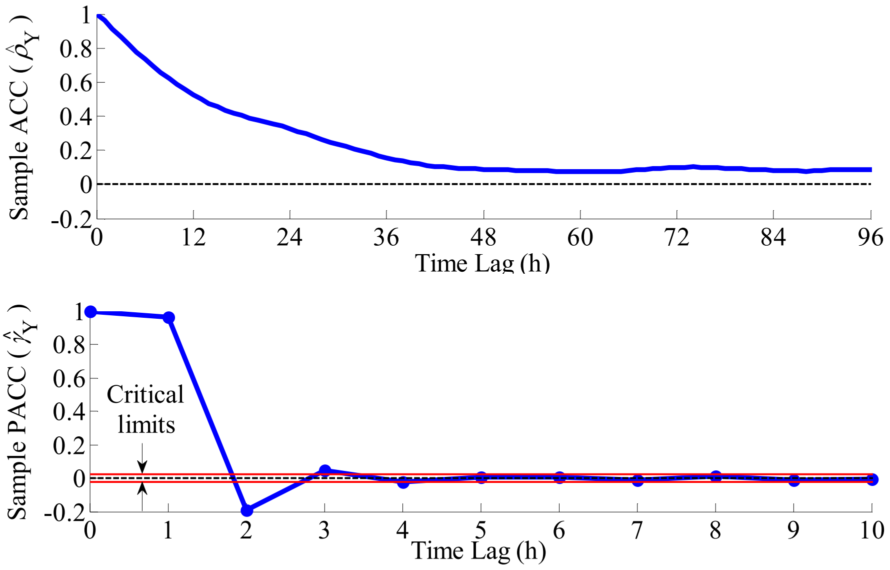

Fig. 2.4. Sample ACC (upper) and PACC (lower) of the measured wind power time series.

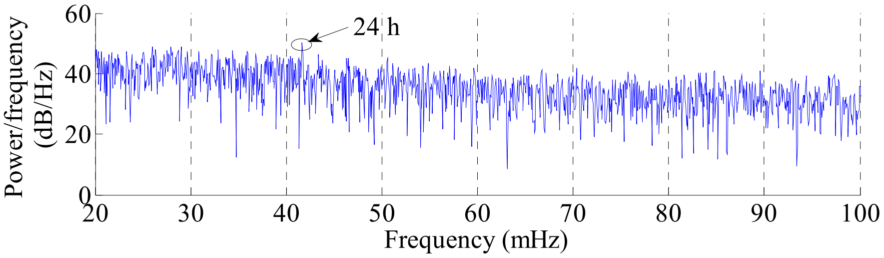

Fig. 2.5. Periodogram of the measured wind power time series.

2.1.4 ARIMA model of wind power time series

In this section, ARIMA models are identified for the wind power data described in section III based on the Box-Jenkins' procedures. Then, the model diagnostic and selection on the identified models are carried out. Finally, the deficiency of the selected models is discussed.

a. Model Identification

The computed natural logarithm of the residual sum of squares of the wind power data according to (2.8) is summarized in Table 2.1 for different values of the transformation parameter ν. The results indicate that a square-root transformation ($v = 0.5$) has the smallest residual sum of squares, and should therefore be applied to the data.

As shown in Fig. 2.4, the sample ACC of the measured time series decays slowly, while the sample PACC damps off after lag 3. This indicates that the differencing is needed (Wei 1990). With one degree of differencing on the square root of the measured time series, the resulting transformed time series is shown in Fig. 2.6. The time series now appears to be approximately stationary.

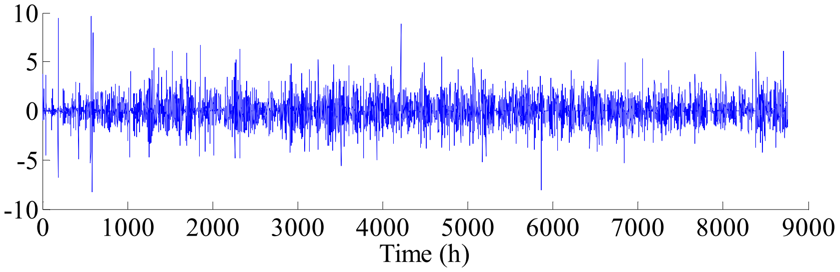

Fig. 2.6. Square root followed by one-order differencing of measured time series.

The sample ACC and PACC of the transformed time series are shown in Fig. 2.7. The sample ACC cuts off after time lag 1 and the sample PACC damps off after time lag 2. This matches with an MA(1) model with a negative θ_1 (Wei 1990). Fitting the MA(1) model directly on the transformed wind power time series gives $\theta_1 = -0.224$ and $\sigma_a^2 = 1.172$. The theoretical ACC of an MA(1) model is calculated by (Box, Jenkins & Reinsel 1994)

$$\rho(k) = \begin{cases} 1, & k=0 \\ -\theta_1 / \left(1+\theta_1^2\right), & k=1 \\ 0, & k \geq 2 \end{cases} . \tag{2.12}$$

The corresponding values of PACC can be obtained using (2.2). The theoretical ACC and PACC of the MA(1) model with $\theta_1 = -0.224$ are shown as the dashed lines in Fig. 2.7. The sample ACC and PACC of the transformed time series matches with the corresponding theoretical values of the MA(1) model.

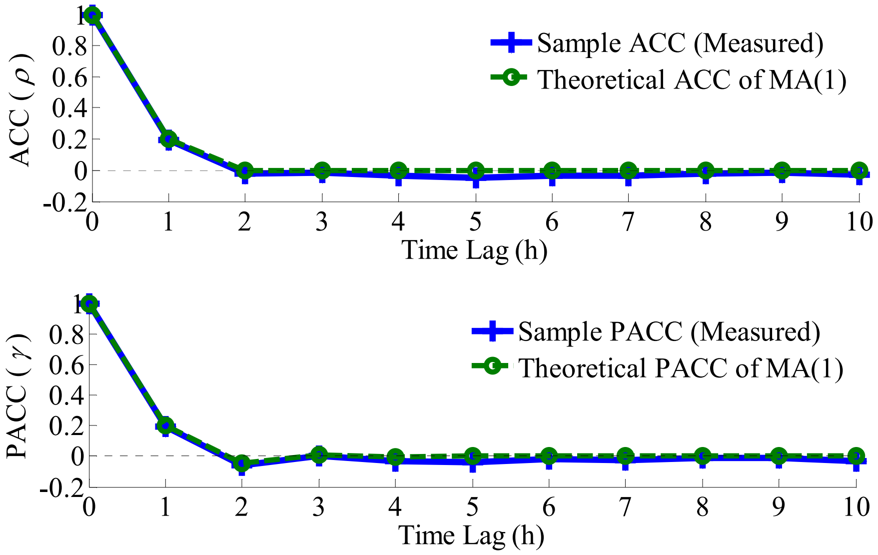

Fig. 2.7. ACC (upper) and PACC (lower): transformed wind power time series (solid) and MA(1) model with $\theta_1 = -0.2241$ (dashed).

Sample mean of the transformed time series (after square-root and differencing) is $\widehat{m}_Z = -2.0547\times10^{-5}$. According to (2.10), the standard error is $S\left(\widehat{m}_Z\right) = 0.0203$, which is much larger than the sample mean. Thus, the deterministic trend term θ_0 is insignificant and can be omitted from the model.

Consequently, the following ARIMA(0,1,1) model is entertained for the wind power time series. It is a first-order integrated MA model.

$$\begin{cases} (1-B)I_0(t)=(1-\theta_1 B)a(t) \\ Y(t)=I_0^2(t) \end{cases}, \qquad \text{for } t = 1,\ldots,\text{N}, \tag{2.13}$$

The block diagram of the model is shown in Fig. 2.8, where the back shifter *B* is the same as a unit delay. The estimated parameters, θ_1 and σ_a^2, are listed in Table 2.2.

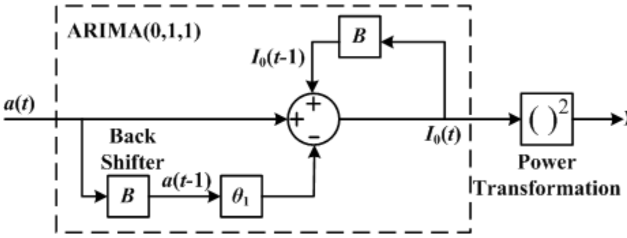

Fig. 2.8. Block diagram of ARIMA(0,1,1) model of wind power time series.

Table 2.2

Parameter Estimates for the ARIMA(0,1,1) and ARMA(1,1) Models

Model	φ_1	θ_0	θ_1	σ_a^2
ARIMA(0,1,1)	—	—	−0.224	1.172
ARMA(1,1)	0.971	0.197	−0.241	1.148

b. Model Diagnostic and Selection

The model diagnostic is required to assess the adequacy of the model by checking whether or not the model assumption is valid. The fundamental assumption is that the residual *a*(*t*) is white noise (Box, Jenkins & Reinsel 1994), i.e. an uncorrelated random process with zero mean and constant variance. The residual *a*(*t*) is obtained by

$$a(t) = (1-B)\sqrt{y(t)} + \theta_1 a(t-1) \tag{2.14}$$

The Box-Cox power transformation of the residual indicates that the residual sum of square is minimized when no transformation is applied. This indicates a constant variance of the residual (Wei 1990). The sample ACC and PACC of the residual are shown in Fig. 2.9. The values at lag 0 are equal to 1 and not shown. The sample ACC and PACC do not exhibit any obvious pattern and are generally within the critical limits. This indicates an uncorrelated random process. Therefore, the white noise assumption of the residual is found to be valid.

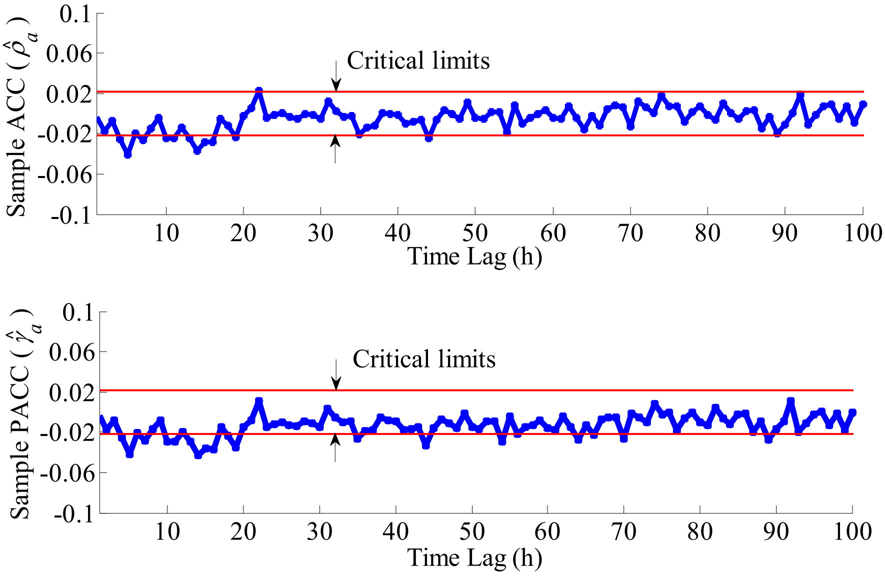

Fig. 2.9. Sample ACC and PACC of the residual of the ARIMA(0,1,1) model.

Although the ARIMA(0,1,1) model according to the preceding analysis is assessed to be an adequate model for the wind power time series, there may be several other adequate models as well. For example, higher-order ARIMA(p,1,q) models with $p > 0$ and $q > 1$. In addition, as shown in Fig. 2.8, the coefficient of the feedback of $I_0(t)$ is 1, corresponding to one degree of differencing. If the coefficient is varied within (0, 1), the model becomes an ARMA(1,1) model, which also shows a good modeling in ACC and PACC. The ARMA(1,1) model is expressed as

$$\begin{cases} (1-\varphi_1 B) I_0(t) = \theta_0 + (1-\theta_1 B) a(t) \\ Y(t) = I_0^2(t) \end{cases}, \qquad \text{for } t = 1, \ldots, \text{N}, \tag{2.15}$$

where the estimated parameters, φ_1, θ_0, θ_1 and σ_a^2, are listed in Table 2.2. Consequently, the problem in this case becomes selecting one model among the models of varying complexity.

Model selection criteria based on residuals are applied to choose the best model among the adequate ones. The common selection criteria are Akaike's information criterion (AIC) and Bayesian information criterion (BIC). The AIC of the ARIMA model is defined as (Wei 1990)

$$\text{AIC}(M) = \text{N} \ln \sigma_a^2 + 2M, \tag{2.16}$$

where M is the number of parameters in the model. The optimal order of the model is chosen by the value of M, so that AIC(M) is minimum. The parameters and AIC values of five adequate ARIMA models are summarized in Table 2.3.

Table 2.3

AIC Criteria of Different ARIMA Models

Model	Parameters	M	σ_a^2	AIC
ARMA(1,1)	φ_1, θ_0, θ_1, σ_a^2	4	1.1483	1219
ARIMA(0,1,1)	θ_1, σ_a^2	2	1.1717	1392
ARIMA(0,1,2)	θ_1, θ_2, σ_a^2	3	1.1721	1397
ARIMA(1,1,1)	φ_1, θ_1, σ_a^2	3	1.1721	1397
ARIMA(1,1,0)	φ_1, σ_a^2	2	1.1759	1423

The ARMA(1,1) model yields the smallest AIC value whereas the ARIMA(0,1,1) model gives the second smallest AIC value. It turns out that the AIC criterion favors the ARMA(1,1) model with 4 parameters instead of the ARIMA(0,1,1) model with 2 parameters. The BIC criterion leads to a similar conclusion. In fact, the ARMA(1,1) model resembles with the ARIMA(0,1,1) model as φ_1 is close to unity. This also implies that the time series may be nonstationary. In addition, the ARIMA(0,1,1) model requires less parameters. Hence, both the ARMA(1,1) and ARIMA(0,1,1) model are considered to be candidate models.

c. Model Deficiency

Due to the physical limitations of the wind farm, the WPG is bounded within [0, 165.6] MW. However, neither the ARMA nor the ARIMA model considers these limitations. The mean and variance of the ARMA(1,1) model are calculated by (Box, Jenkins & Reinsel 1994)

$$\begin{cases} m_{I_0} = \theta_0 / \left(1-\varphi_1\right) \approx 6.7 \\ \sigma_{I_0}^2 = \sigma_a^2 \left(1+\theta_1^2 - 2\varphi_1\theta_1\right) / \left(1-\varphi_1^2\right) \approx 30.0 \end{cases} . \tag{2.17}$$

However, the sample mean and variance of the square-root transformed wind power data are 6.7 and 16.5, respectively. Thus, the ARMA(1,1) model fits the measurement in terms of the mean but not the variance. The variance of the ARIMA(0,1,1) model does not converge and increases as time proceeds due to its nonstationarity property. The discrepancy in the variance indicates that the standard ARMA or ARIMA model cannot be directly applied to a bounded random process. The following proposes a new model for the bounded random process.

2.1.5 Proposed Model of wind power time series

This section first proposes four modified ARMA and ARIMA models for the bounded wind power time series: the ARMA model with limiter, ARIMA model with limiter, LARMA model, and LARIMA model. Then, the model that has the best fit in probability distribution is selected. Moreover, the selected model is compared with a transition matrix based discrete Markov model in terms of probability distribution and temporal correlation. Finally, the selected model is extended to include monthly variations of the WPG.

a. Modified ARMA and ARIMA Models

Since the wind power output is bounded, a limiting operation is introduced on $I_0(t)$ as

$$I(t) = \begin{cases} I_{\max}, & I_0(t) > I_{\max} \\ I_0(t), & I_{\min} \le I_0(t) \le I_{\max} \\ I_{\min}, & I_0(t) < I_{\min} \end{cases} . \tag{2.18}$$

where $I_{\max}$ and $I_{\min}$ denote the upper and lower bounds of the square root of the wind power output, respectively. For the considered wind farm, the wind power output is bounded within [0, 165.6] MW, yielding $I_{\max} = \sqrt{165.6} = 12.87$ and $I_{\min} = 0$. Consequently, the wind power time series can be simulated by

$$Y(t) = I^2(t), \qquad \text{for } t = 1, \ldots, \mathrm{N}. \tag{2.19}$$

The limiter may be included outside or inside the feedback loop of I_0(t) shown in Fig. 2.8. The model with the limiter outside the feedback loop is shown in Fig. 2.10 (a). The model is referred to as the ARMA model with limiter when $0 < \varphi_1 < 1$, and the ARIMA model with limiter when $\varphi_1 = 1$. The difference between these two models is that the ARMA model with limiter is a stationary model whereas the ARIMA model with limiter is a nonstationary model. The model with the limiter inside the feedback loop is shown in Fig. 2.10 (b). The model is referred to as the LARMA model when $0 < \varphi_1 < 1$, and the LARIMA model when $\varphi_1 = 1$, with 'L' indicating the introduction of the limiter. Similar to the other two models, the LARMA model is a stationary model whereas the LARIMA model is a nonstationary model.

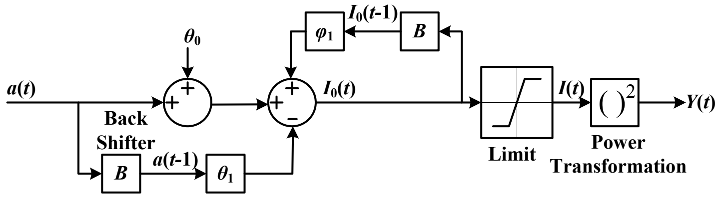

(a) ARMA(1,1) with limiter ($0 < \varphi_1 < 1$), ARIMA(0,1,1) with limiter ($\varphi_1 = 1$).

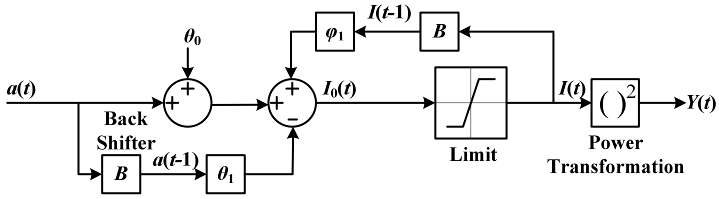

(b) LARMA(1,1) ($0 < \varphi_1 < 1$), LARIMA(0,1,1) ($\varphi_1 = 1$).

Fig. 2.10. Block diagrams of four ARIMA-type wind power time series models.

Due to the nonstationarity of an ARIMA model, its mean and variance diverge as time proceeds (Box, Jenkins & Reinsel 1994). With the inclusion of the limiter, however, the mean and variance of the

LARIMA model is bounded. Consider two extreme cases when σ_a^2 approaches zero and infinity while $\theta_0 = 0$. It is not difficult to derive that the mean and variance of $I(t)$ in the LARIMA model is bounded as:

$$\begin{cases} 0 \leq m_I \leq I_{\max}/2 \\ 0 \leq \sigma_I^2 \leq I_{\max}^2/4 \end{cases}. \tag{2.20}$$

Therefore, a modification is required to control the mean of the model. In other words, a deterministic trend term must be included. The value of θ_0 is adjusted until the sample mean of $Y(t)$ coincides with that of the measured time series $y(t)$. The variance is automatically adjusted as it is the autocorrelation at time lag zero minus the square of the mean. According to the simulation, $\theta_0 = 0.011$ for the LARIMA model.

b. Model Selection

The selection among the ARMA model with limiter, the ARIMA model with limiter, the LARMA model, and the LARIMA model depends on which one providing the best fit in terms of probability distribution. In order to compare the probability distribution of the four models, the quantile values of the time series simulated from the models are plotted against those from the original measurement data as shown in Fig. 2.11 (a)-(d). Each plot is computed from 100 independently generated time series of 8760 samples The quantile-quantile plot is a standard means of comparing probability distributions. Different quantiles correspond to values of a cumulative distribution function at different probabilities. If the simulated time series and the measured one are from the same probability distribution, then the quantile-quantile plot follows a straight line with a unit slope (the solid line in the figure).

It is observed from Fig. 2.11 (a) that the ARMA(1,1) model with limiter fits well for quantiles less than 120 MW, but fits poorly in the higher power region. The ARIMA(0,1,1) model with limiter shown in Fig. 2.11 (b) shows a poor fit in all quantiles. This observation indicates that the simulated values from the ARIMA(0,1,1) model with limiter hit the upper and lower limit most of the time. This effect is caused by the nonstationarity characteristic of the ARIMA model. The LARMA(1,1) model in Fig. 2.11 (c) also deviates evidently from the straight line and gives a poor fit in probability distribution. The LARIMA(0,1,1) model in Fig. 2.11 (d) gives the best fit among the four models. Due to the importance of the accuracy in probability distribution of WPG, the LARIMA(0,1,1) is favored among the four modified ARMA and ARIMA models. Thus, the LARIMA(0,1,1) model is finally selected as the best model for modeling the wind power time series. Fig. 2.11 (e) is to be discussed in the following subsection.

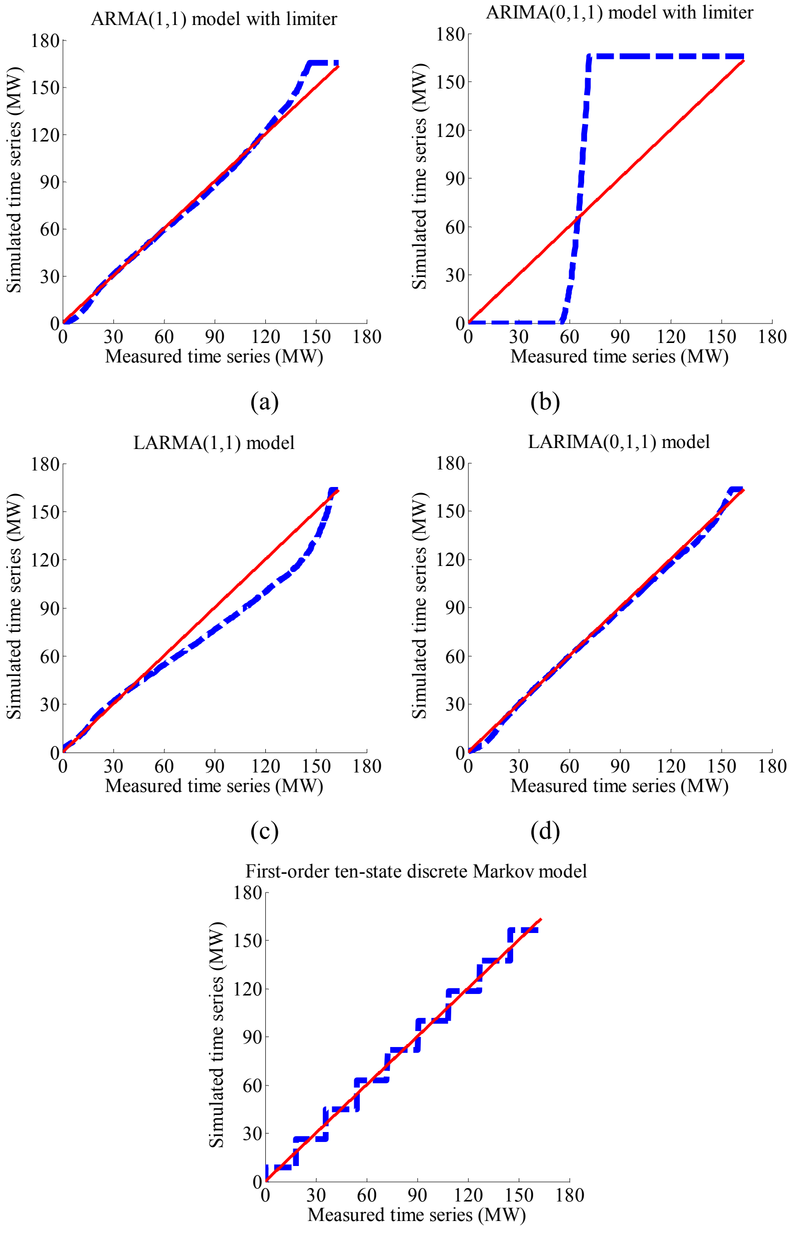
ARMA(1,1) model with limiter

ARIMA(0,1,1) model with limiter

LARMA(1,1) model

LARIMA(0,1,1) model

First-order ten-state discrete Markov model

(a)

(b)

(c)

(d)

(e)

Fig. 2.11. Quantile-quantile plots of simulated time series from six models against the measured time series (dashed line), and straight lines with unit slope (solid line).

c. LARIMA Model versus Discrete Markov Model

The LARIMA(0,1,1) model proposed in this paper is compared with the first-order transition matrix based discrete Markov model proposed in (Papaefthymiou, Klockl 2008). The first-order discrete Markov model is implemented as described in (Papaefthymiou, Klockl 2008) with a state number of ten. The comparisons are made in terms of probability distribution, ACC, PACC and model parameter number.

The quantile-quantile plot of the simulated time series using the first-order discrete Markov model is shown in Fig. 2.11 (e). Although the trend of the quantile-quantile plot follows the straight line, it exhibits a staircase-like behavior due to the use of quantization in the discrete Markov model. By comparing Fig. 2.11 (d) and (e), it is apparent that in terms of the fit of probability distribution, the proposed LARIMA(0,1,1) model outperforms the ten-state first-order discrete Markov model.

The sample ACC and PACC of the measured time series and the simulated time series using the LARIMA(0,1,1) and using the first-order discrete Markov model are shown in Fig. 2.12. The sample ACC of the LARIMA(0,1,1) model and the Markov model match with that of the measurement. However, the PACC exposes the difference between the LARIMA model and Markov model. The sample PACC of the measured time series approaches zero for time lags larger than three. The sample PACC of the LARIMA model matches that of the measured time series for time lags up to three and approaches zero for time lags larger than three. However, the PACC of the Markov model approaches zero for time lags larger than one.

Recall that PACC describes the correlation between $Y(t)$ and $Y(t+k)$ when the mutual linear dependency of $Y(t+1)$, $Y(t+2)$, …, $Y(t+k-1)$ is removed. For a first-order discrete Markov model, the next state depends only on the current state, not the other states visited before. Therefore, the PACC of the discrete Markov model approaches zero for time lags larger than 1. However, due to its feedback loop (see Fig. 2.10 (b)), the LARIMA(0,1,1) model gives good accuracy of the PACC at time lags larger than one. Therefore, the LARIMA(0,1,1) model gives a better fit in PACC than does the first-order discrete Markov model.

The fit of the first-order discrete Markov model to the measurement data can be improved by using higher order models, e.g. a second-order discrete Markov model. However, the number of parameters increases exponentially; the transition matrix of an n-state discrete Markov model of order r has $n^r(n-1)$ parameters. This leads to 90 parameters for a first-order ten-state model ($n = 10$, and $r = 1$), and 900 parameters for a second-order ten-state model ($n = 10$, and $r = 2$). In contrast, the proposed LARIMA(0,1,1) model is described by only three parameters. Generally, the accuracy of a fitted model depends essentially on the amount of data available relative to the number of parameters to be estimated (Linhart, Zucchini 1986). Thus, parsimonious models are preferred, and in some cases even required, when limited amount of data are available.

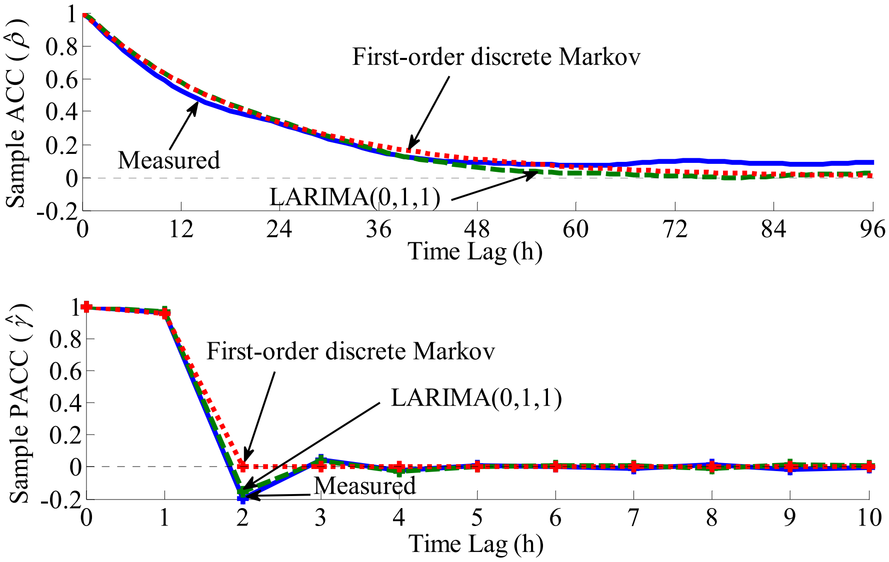

Fig. 2.12. Sample ACC (upper) and PACC (lower) of the measured time series, LARIMA(0,1,1) model, and first-order discrete Markov model.

In summary, the proposed LARIMA(0,1,1) model is superior to the first-order transition matrix based discrete Markov model in terms of the probability distribution, the PACC, and the model parameter number.

In addition, the time-domain plot and power spectral density of the simulated time series using the proposed LARIMA(0,1,1) model are shown in Fig. 2.13 and Fig. 2.14, respectively. As mentioned in section 2.1.3, the component corresponding to the diurnal period is not included in the present model. In the case of a strong diurnal period, the proposed model can be improved by applying a seasonal ARIMA model on the time series (Wei 1990).

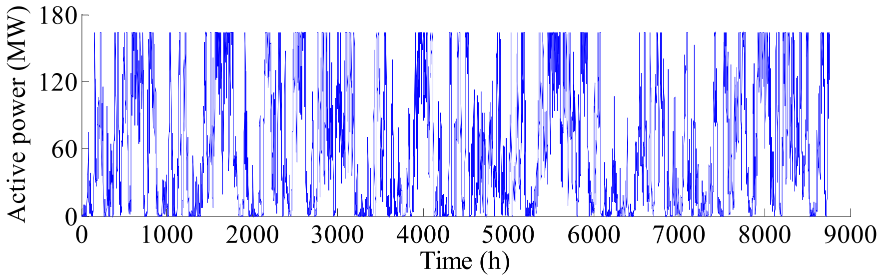

Fig. 2.13. Simulated wind power time series using the LARIMA(0,1,1) model.

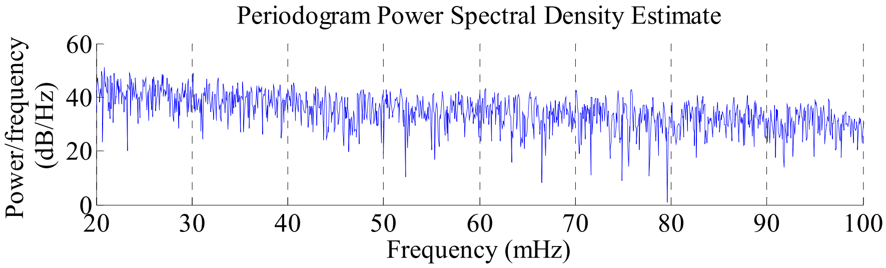

Fig. 2.14. Power spectral density of simulated wind power time series using the LARIMA (0,1,1) model.

d. Modeling of Seasonal Trend

So far a time series model that captures the averaged sample probability distribution, ACC, and PACC over a whole year has been developed. In order to take into account the seasonal trend, the same procedures can be applied to different parts of the time series representing different seasons or months. However, the length of each month (maximum 744 hours) of the time series is reduced approximately by a factor of 12 compared to that of a whole year (8760 hours). This shows the importance of a parsimonious model. A transition matrix based Markov model requires a large number of parameters. Thus, more data than a year are necessary to model the seasonal variability. In other words, the Markov model is not suitable when modeling seasonal trend with limited data. However, the proposed LARIMA(0,1,1) model relies on only three parameters, which is advantageous for modeling the seasonal trends.

Following the LARIMA(0,1,1) model in Fig. 2.10 (b), the estimated model parameters, θ_0, θ_1, and σ_a^2, for each month are shown in Fig. 2.15. It is noted that the values of the deterministic trend θ_0 are all negative in the summer months (May to October), and positive in the winter months (November to April). The phenomena reflect that the mean value of WPG is higher in winter months than in summer months. The monthly variation of θ_0 is large in the sense that its standard deviation is around 19 times of its mean. i.e. 0.0035. However, the monthly variation of θ_1 and σ_a^2 are quite small. The corresponding standard deviations are around 33% and 18% of the means, i.e. -0.225 and 1.165, respectively. This tends to indicate that the 12 monthly models can be connected by the same value of θ_1 and σ_a^2 but distinguished by θ_0. A longer time series measurement is required to further verify this conclusion. The monthly mean and variance of the simulated and measured time series are shown in Fig. 2.16. The results show that the model is able to capture the seasonal trend.

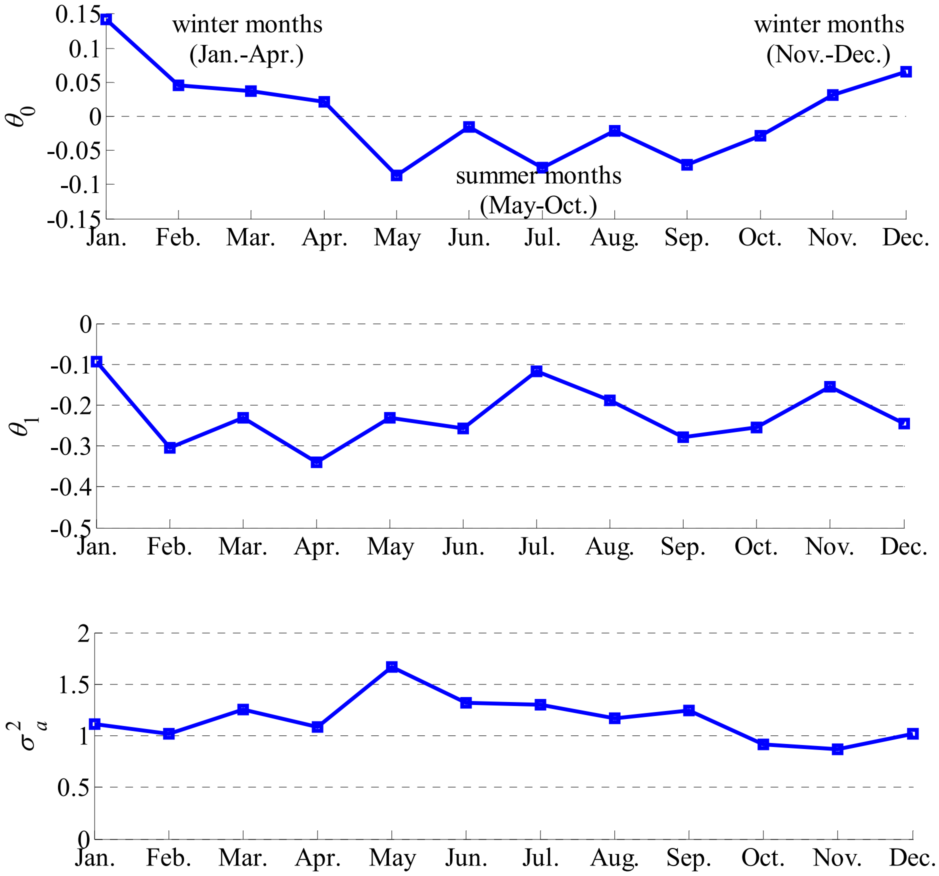

Fig. 2.15. ARIMA(0,1,1) based model parameters for each month: θ_0 (upper), θ_1 (middle), and σ_a^2 (lower).

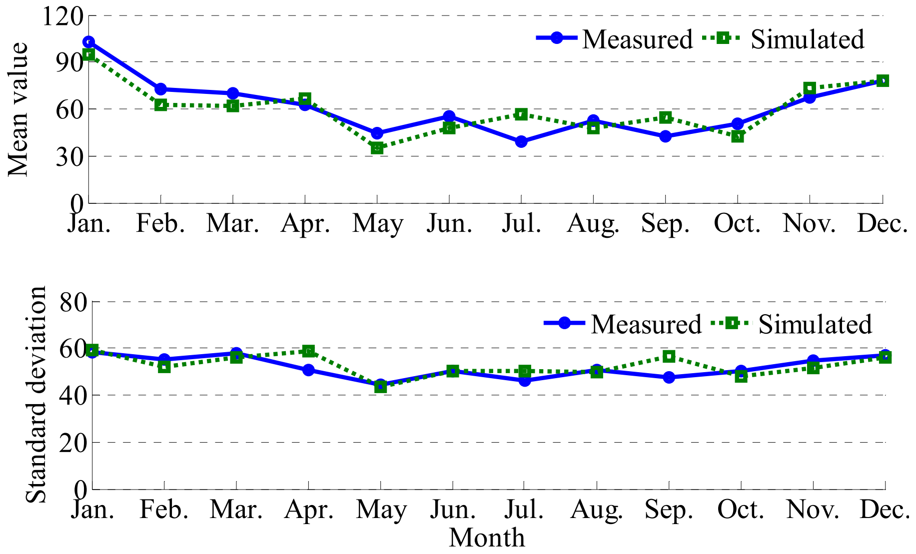

Fig. 2.16. Monthly mean (upper) and standard deviation (lower) of one-year measured (solid-circle) and simulated (dotted-square) time series considering seasonal trend in the model.

e. Further Discussions

The proposed LARIMA model captures the probability distribution, the ACC, the PACC and the seasonal trend adequately. However, as discussed in section 2.1.3, the 24 h period is ignored in the modeling of this wind power time series. The motivation for ignoring this effect is that the 24 h period is observed to be rather weak in the available data set shown in Fig. 2.5. Therefore, to adhere to the Principle of Parsimony, we leave out the explicit modeling of the diurnal period. In many cases, the diurnal period is also an important issue for modeling WPG. This is because of the strong diurnal period of electric loads that may be correlated (either positive or negative) with WPG. In the case of a time series that possesses a strong diurnal period or any other periods, the standard Box-Jenkins' seasonal ARIMA model can be applied (Box, Jenkins & Reinsel 1994, Wei 1990). Accordingly, the seasonal LARIMA model can also be developed.

It is worth pointing out that the wind power data used for developing the LARIMA model are from a wind farm with fixed speed wind turbines. For wind farms with variable speed wind turbines, both the probability distribution and the autocorrelation of the wind power may be different. The developed wind power model is only based on the data measured from the wind farm without the assumption of specific turbine types. Thus, the same modeling procedures can still be applied.

The proposed LARIMA model for WPG can be applied in the reliability assessment of power systems incorporating wind energy. For instance, the model can generate synthetic wind power time series, which are used in sequential Monte Carlo simulations to evaluate the adequacy of the system generation to meet future load demand. The proposed wind power model has a good fit in probability density function, especially on the tail regions. This fact, as well as the model's computational simplicity, makes the model especially suitable and reliable for Monte Carlo simulations.

2.1.6 Cross-correlation model of wind power time series

The correlation model of WPG consists of two parts: autocorrelation and cross-correlation. The autocorrelation of WPG is the correlation of wind power in time. On the other hand, the cross-correlation of WPG is the correlation of wind power between multiple wind farms (or WTs) in space. For modeling WPG from a single wind farm, only autocorrelation needs to be considered. For example, for modeling the WPG of the Nysted offshore wind farm (Denmark), the autocorrelation is captured by the LARIMA model adequately as shown in Fig. 2.12. However, in the case of multiple wind farms in a power system, both autocorrelation and cross-correlation should be taken into account.

In the literature, the cross-correlation model of multiple WPG is implemented through a trial-and-error approach (Billinton, Wangdee 2007, Wangdee, Billinton 2006), or a Gaussian copula (Papaefthymiou, Kurowicka 2009). Both approaches model the cross-correlation of wind speed at adjacent areas where wind farms are located. Then, the correlated wind speed is transformed through a wind farm power curve to obtain the correlated WPG.

The trial-and-error approach implemented in (Billinton, Wangdee 2007) and (Wangdee, Billinton 2006) considers only the correlation coefficient at time-lag zero. Correlation coefficients at higher time lags are neither addressed nor properly modeled. Furthermore, the approach makes the implementation of the model very difficult when three or more WPG are involved. On the other hand, the Gaussian copula approach proposed in (Papaefthymiou, Kurowicka 2009) is suitable for modeling the cross-correlation of multivariate stochastic variables. However, WPG is a stochastic process, of which the modeling of autocorrelation is very important. Therefore, the Gaussian copula approach is not appropriate as it is not able to model the autocorrelation of WPG.

This section proposes a multivariate-LARIMA model for simulating the cross-correlation of adjacent wind farms. As an example, the following illustrates a bivariate-LARIMA(0,1,1) model to simulate the cross-correlation of the WPG from two parts of the Nysted offshore wind farm.

In order to the model the cross-correlation of WPG from the two parts of the Nysted offshore wind farm, the LARIMA(0,1,1) model needs to be modified by including the cross-correlation structure. Such a modification leads to a bivariate-LARIMA(0,1,1) model as shown in Fig. 2.17. The bivariate-LARIMA model is composed of integration, limiters, power transformation, autocorrelation and cross-correlation. The cross-correlation structure consists of two parts: 1) a bivariate-Gaussian white noise with the covariance matrix $\mathbf{\Sigma}_a$, and 2) the cross-coupling of the white noise at time-lag one with weights of θ_{12} and θ_{21}. The mathematical formulation of the bivariate-LARIMA(0,1,1) model is summarized from (2.21)-(2.25). The corresponding model parameters are summarized in 0.

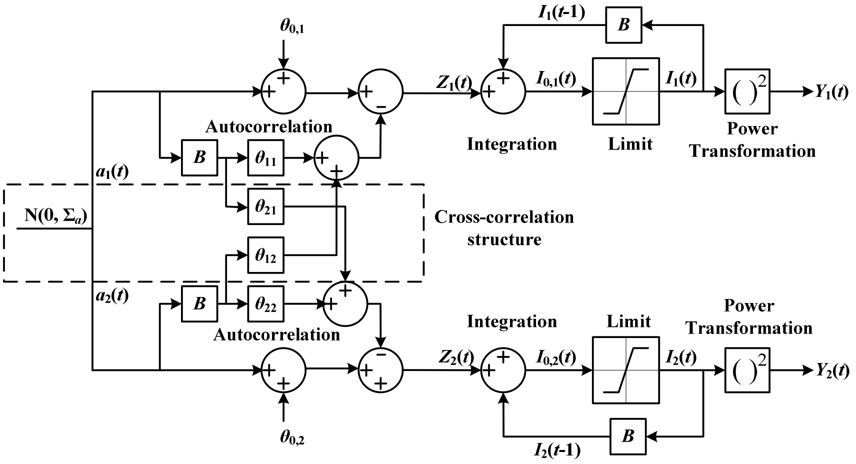

Fig. 2.17. Block diagram of the bivariate-LARIMA(0,1,1) model

$$\begin{bmatrix} Z_1(t) \\ Z_2(t) \end{bmatrix} = \begin{bmatrix} \theta_{0,1} \\ \theta_{0,2} \end{bmatrix} + \left\{ \begin{bmatrix} 1 & 0 \\ 0 & 1 \end{bmatrix} - \begin{bmatrix} \theta_{11} & \theta_{12} \\ \theta_{21} & \theta_{22} \end{bmatrix} B \right\} \begin{bmatrix} a_1(t) \\ a_2(t) \end{bmatrix}, \tag{2.21}$$

$$\begin{bmatrix} Z_1(t) \\ Z_2(t) \end{bmatrix} = \begin{bmatrix} I_{0,1}(t) - I_1(t-1) \\ I_{0,2}(t) - I_2(t-1) \end{bmatrix}, \tag{2.22}$$

$$I_1(t) = \begin{cases} I_{\max}, & I_{0,1}(t) > I_{\max} \\ I_{0,1}(t), & I_{\min} \le I_{0,1}(t) \le I_{\max} \\ I_{\min}, & I_{0,1}(t) < I_{\min} \end{cases}, \tag{2.23}$$

$$I_2(t)=\begin{cases} I_{\max}, & I_{0,2}(t)>I_{\max} \\ I_{0,2}(t), & I_{\min}\le I_{0,2}(t)\le I_{\max}, \\ I_{\min}, & I_{0,2}(t)<I_{\min} \end{cases} \tag{2.24}$$

$$\begin{bmatrix} Y_1(t) \\ Y_2(t) \end{bmatrix}=\begin{bmatrix} I_1^2(t) \\ I_2^2(t) \end{bmatrix}. \tag{2.25}$$

In order to validate the bivariate-LARIMA(0,1,1) model, two simulated time series ($Y_1(t)$ and $Y_2(t)$) of ten-year length (87600 data points) from the model are compared to the corresponding measurements ($y_1(t)$ and $y_2(t)$). These two sets of measurements are recorded separately from two parts of the wind farm, which have the same capacity (82.8 MW each part). The comparison is carried out in terms of sample ACC, PACC, cross-correlation coefficient, and probability distribution.

Fig. 2.18 (a) shows the sample ACC of the sum of the simulated time series ($Y_1(t) + Y_2(t)$), as well as the sum of the measured time series ($y_1(t) + y_2(t)$). Fig. 2.18 (b) shows the corresponding sample PACC. The results show a good fit in ACC and PACC between the bivariate-LARIMA model and the measurements. The sample PACC goes to zero for time lags larger than three. Fig. 2.18 (c) compares the sample cross-correlation coefficients of the simulated time series and the measured time series. It is worth pointing out that unlike autocorrelation, the values of cross-correlation are usually not symmetrical at the two sides of time-lag 0. Thus, both sides of the cross-correlation should be plotted. However, here the values of the cross-correlation at the two sides are very close, which is reasonable as it is between two parts of a wind farm. In this case, only one side of the cross-correlation is shown in Fig. 2.18 (c). The match in cross-correlation coefficients indicates that the proposed cross-correlation structure is sufficient to model the interdependence of the two parts of the wind farm. Furthermore, it is noted that the cross-correlation between the two parts of the wind farm is as high as their autocorrelation.

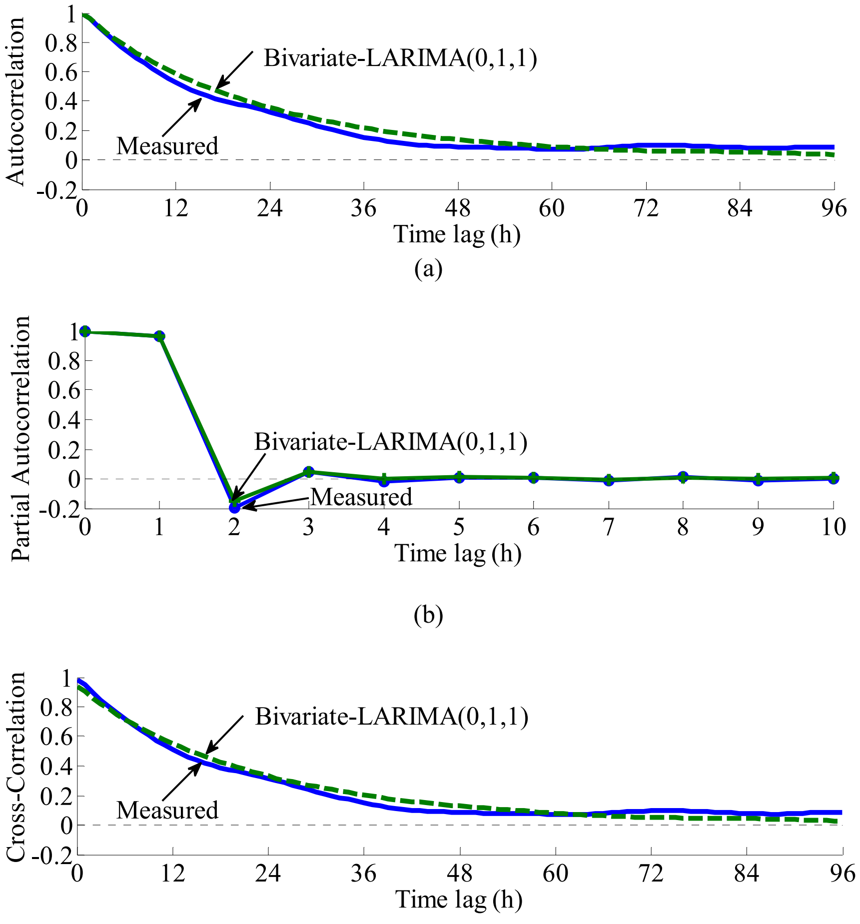

(a)

(b)

(c)

Fig. 2.18. Sample autocorrelation (a), partial-autocorrelation (b) and cross-correlation coefficients (c): Measured time series (solid) and the Bivariate-LARIMA(0,1,1) model (dashed).

Fig. 2.19 compares the probability distribution of the sum of the simulated time series ($Y_1(t) + Y_2(t)$) with the measurements by using a quantile-quantile plot. If the simulated time series and the measured time series have the same probability distribution, then their quantile-quantile plot follows a straight line with a unit slope. Fig. 2.19 shows that the probability distribution of the model fits that of the measurements adequately.

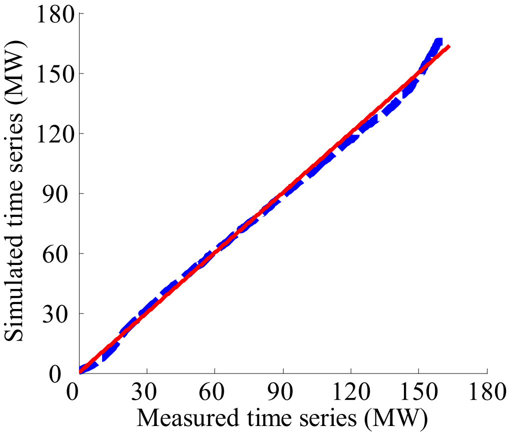

Fig. 2.19. Quantile-Quantile plot of the simulated time series from the bivariate-LARIMA(0,1,1) model against the measured time series (dashed), and straight lines with unit slope (solid).

In fact, the cross-correlation of multivariate time series has a significant impact on the probability distribution of the sum of the multivariate time series. In order to demonstrate this, Fig. 2.20 shows the histograms of the probability distribution of the sum of two time series. The two time series are: fully correlated, strongly correlated, weakly correlated and uncorrelated. The fully-correlated time series are identical to each other. The strongly correlated time series correspond to the simulated time series ($Y_1(t)$ and $Y_2(t)$) as for Fig. 2.18 and Fig. 2.19. The weakly correlated time series are also simulated from the bivariate-LARIMA(0,1,1) model. However, the cross-correlation values (off-diagonal elements) of the covariance matrix $\mathbf{\Sigma}_a$ of the white noise are one-tenth the values of the covariance matrix for the strongly correlated case (see (A.2) in 0). The uncorrelated time series are simulated using the LARIMA model without the cross-correlation structure. Fig. 2.20 shows a clear trend of the probability distribution when the cross-correlation between the two time series varies from full correlation to no correlation. The probability mass concentrates on the two ends of the distribution when the cross-correlation is strong. Whereas the probability mass moves to the center of the distribution when the cross-correlation is weak. In other words, a weak cross-correlation smoothens out the probability distribution of the total WPG. It is also worth pointing out that the mean values of the total WPG are identical for the four types of cross-correlation.

In summary, the bivariate-LARIMA(0,1,1) model captures the ACC, the PACC, the cross-correlation and the probability distribution of the two measured wind power time series adequately. It is also demonstrated that the modeling of the cross-correlation is of great importance as it strongly influences the probability distribution of the total WPG in a power system. Although the illustration is based on bivariate time series, the extension of the model to multivariate time series is mathematically straightforward. In the n-variate case, the cross-correlation structure shown in Fig. 2.17 is more complex, with an n×n covariance matrix of the white noise and an n×n matrix of the parameter $\boldsymbol{\theta}_1$.

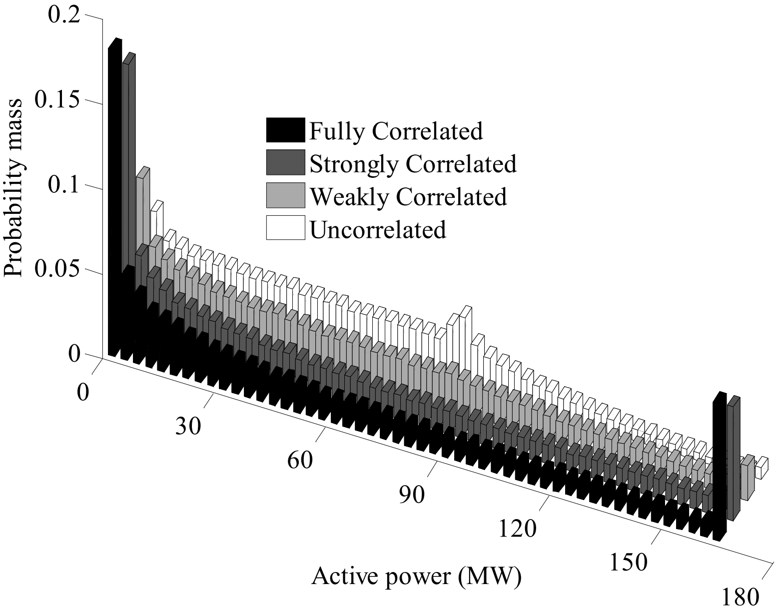

Fig. 2.20. Histogram of the probability mass of the sum of two time series when they are fully correlated, strongly correlated, weakly correlated and uncorrelated.

2.1.7 Conclusions of stochastic wind power model

This section contributes to the statistical analysis and the modeling of a nonstationary and bounded wind power time series. The analyses indicate that the examined wind power time series is a nonstationary random process with high fluctuation and temporal correlation. However, the time series has a rather weak 24 h period. It is found that its probability distribution does not resemble a standard distribution such as an exponential, or a Gaussian distribution.

A novel LARIMA model is proposed for the wind power time series. The LARIMA model is obtained by introducing a limiter into a standard ARIMA model to represent the upper and lower bounds of the WPG. The proposed model characterizes the WPG by three unknown parameters, representing the mean level (θ_0), temporal correlation (θ_1), and driving noise (σ_a^2) of the WPG, respectively. The proposed

LARIMA(0,1,1) model outperforms the ARMA(1,1) model with limiter and the LARMA(1,1) model when evaluating the probability distribution. The proposed LARIMA(0,1,1) model also outperforms the first-order transition matrix based discrete Markov model when evaluating the probability distribution, PACC and model parameter number. The monthly variation of the wind power time series is modeled by applying the LARIMA(0,1,1) model to the individual months of the time series. It is found that the monthly variation is mainly caused by different mean level (θ_0) of wind power in each month. The monthly variation in θ_1 and σ_a^2 is observed to be relatively small. Furthermore, a multivariate-LARIMA model is proposed to simulate the cross-correlation of WPG from two parts of a wind farm. The model captures the sample ACC, PACC, cross-correlation and probability distribution of the measured data adequately. A bivariate-LARIMA model is presented to demonstrate the model development and parameter estimation. As the number of time series increases, the order of the cross-correlation structure also increases. However, owing to the parsimony of the LARIMA model, the multivariate-LARIMA model is able to handle the cross-correlation of a significant number of time series.

The developed stochastic wind power model can facilitate the understanding and analysis of the impact of stochastic WPG on power system planning and reliability studies. The sensitivity analysis of the stochastic WPG with respect to the variation in mean level, temporal correlation and driving noise can be readily carried out using the proposed model. Future work on the proposed LARIMA model includes the derivation of analytical expressions for the probability density function as well as its moments. If wind power measurements of longer periods are available, the year-to-year variation can be modeled and used to improve the accuracy of the model for long-term planning applications.

2.2 Stochastic load model

2.2.1 Motivation

In a temporal simulation (Willis, Scott 2000) or a sequential Monte Carlo simulation (Billinton, Wangdee 2007), hourly load time series data are usually required. The data can be obtained from the measurements. Alternatively, the time series can be simulated from a stochastic load model. Such a stochastic load model is especially useful in the following two situations:

1) If measured load data are not available, an already-validated stochastic load model can be very helpful to generate a realistic load time series of arbitrary length.

2) If measured load data are available, a stochastic load model can be used to simulate a new load time series after some load management strategies are implemented.

The following example illustrates the second situation in more detail. A local network operator was concerned about a high system loading condition at 7 a. m. Thus, the network operator made an agreement with a local industrial park that if part of their load is shifted from 7 a.m. to 6 a.m., the companies in the industrial park will get a reduction in their electricity bill. The agreed amount of the load shifted has a mean value of 5 MW with ±10% error. This type of load specification can be represented by a Gaussian stochastic variable with the mean value of 5 MW and the standard deviation of 0.5 MW. To reflect such a load shift on the new load time series, the Gaussian stochastic variable can be subtracted from the original load time series at 7 a.m. every day and added to the original load time series at 6 p.m every day. In order to perform such mathematical operation with a Gaussian variable analytically, a stochastic load model expressed in terms of Gaussian variables needs to be developed. This example illustrates the purpose of and the requirement for developing a stochastic load model. In general, as shown in Fig. 2.21, there are six types of load shape to be achieved after different load management strategies (Gellings, Smith 1989). These six types are peak clipping, valley filling, load shifting, strategic conservation, strategic load growth and flexible load shape. Similar to the load shifting described above, the other five load management strategies can also be simulated on the basis of a proper stochastic load model.

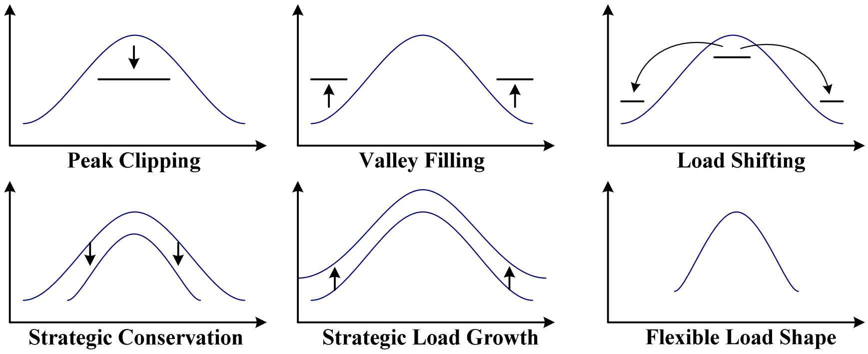

Fig. 2.21 Six types of load shape to be achieved by load management (Gellings, Smith 1989).

In the following subsections, a review of existing load models for generating load time series is first provided. Then, a statistical analysis is carried out to examine the measured load data. According to the statistical analysis, a suitable stochastic load model based on a seasonal ARMA model is developed and validated against measurements. Thereafter, the application of the developed stochastic load model for simulating the effect of load management is demonstrated. In the end, the section finishes with a conclusion.

2.2.2 Review of existing load models

In the literature, the load models developed to generate synthetic load time series fall into two categories: the deterministic model (Rahman, Rinaldy 1993, Sankarakrishnan, Billinton 1995, Wang, Billinton 1999) and the stochastic model (Suva et al. 2000, Chen, Bak-Jensen & Chen 2009). These models are mainly developed for sequential Monte Carlo simulation in reliability and planning analysis of power systems. The models proposed in (Sankarakrishnan, Billinton 1995, Wang, Billinton 1999) simulate load time series based on a typical daily load curve weighted by the peak load of a day, of a week and of a year. The model in (Rahman, Rinaldy 1993) is developed by fitting a polynomial curve to an inverted load duration curve. The load data simulated from the load duration curve do not possess any temporal correlation. The multilevel non-aggregate Markov load model proposed in (Suva et al. 2000) discretizes the load into N levels (e.g. five load levels), with a constant load transition rate for changing from one load level to another. However, these four load models cannot be used to perform arithmetic operations with Gaussian variables analytically. Therefore, they are not suitable for simulating the type of load management described in the previous section. The two models proposed in (Chen, Bak-Jensen & Chen 2009) are the joint-normal model and the AR(12) based model. The joint-normal model treats 24 hourly loads of a day as multivariate Gaussian stochastic variables. The joint-normal model is suitable for the above described application as it incorporates Gaussian stochastic variables explicitly. The only problem is that the joint-normal model has 600 parameters with 24 mean values and a 24×24 covariance matrix. Such a model requires a high number of training data in order to achieve accurate results. The AR(12) based model does not incorporate a Gaussian stochastic variable and is thus not applicable in this case.

2.2.3 Statistical analysis of load time series

The active power of a load time series measured at the Støvring distribution system in North Jutland is analyzed. The time series is hourly measurement from July 1, 2006 to January 31, 2007. The length of the time series is 5160. The load time series is shown in Fig. 2.22. Fig. 2.23 shows the periodogram of the load time series, which indicates that 24 h, 168 h (1 week) and 12 h are the three dominant periods of the time series. The one-week period is caused by the weekday/weekend load variation. In order to take into account the weekday/weekend variation as well as the seasonal load level, the data are grouped into summer weekdays, summer weekends, winter weekdays and winter weekends. Fig. 2.24 (a) shows the time series in summer weekdays. For the following analysis, only the data in summer weekdays will be considered. However, the same procedures can be used for the data in the other three groups.

As shown in (Chen, Bak-Jensen & Chen 2009), an hourly load can be represented by a Gaussian stochastic variable. As a Gaussian stochastic variable is only characterized by its mean and standard deviation, Fig. 2.24 (b) shows the diurnal mean and standard deviation of the summer-weekday time series. Fig. 2.24 (c) is the summer-weekday time series after the diurnal mean and standard deviation is removed. It is seen that the 24 h period is significantly weakened. In this way, the transformed time series shown in Fig. 2.24 (c) may be modeled by an ARMA process. In the end, a stochastic load model can be developed by combining the ARMA model and the diurnal mean and standard deviation. Although this type of model does not incorporate Gaussian variables directly, it can still be used to perform arithmetic operations with Gaussian variables. This is because a Gaussian variable is fully characterized by its mean and standard deviation.

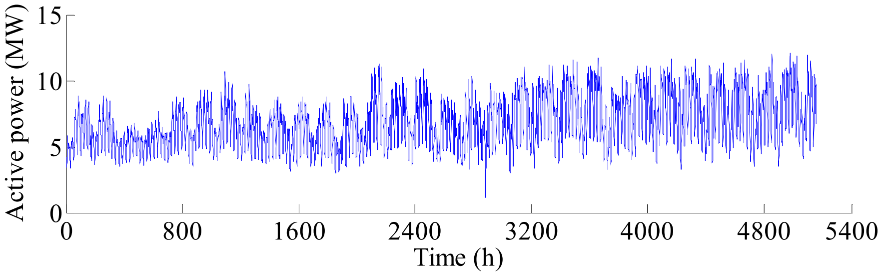

Fig. 2.22. Measured load time series from July 2006 to January 2007.

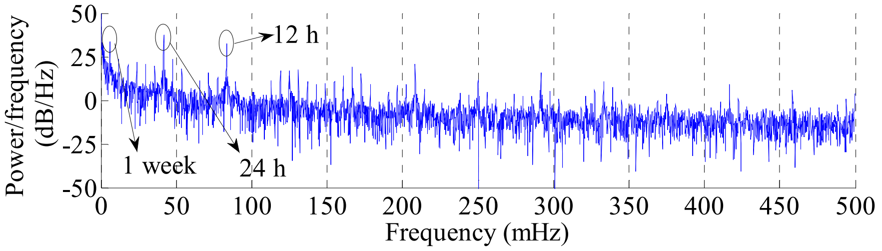

Fig. 2.23. Power spectral density of the load time series.

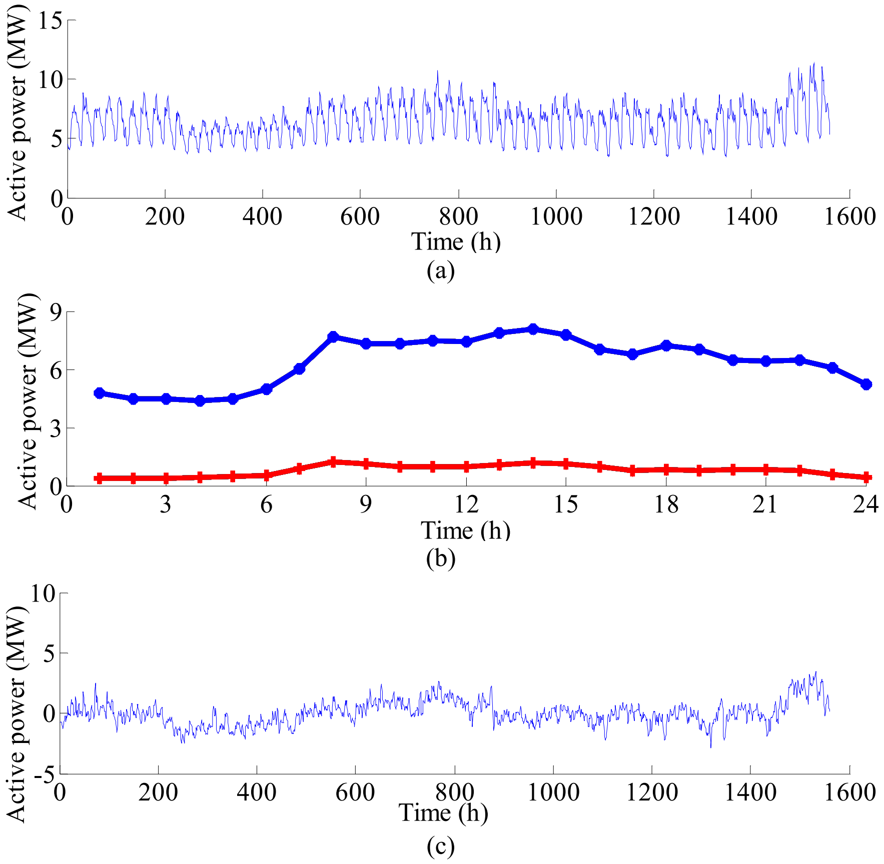

Fig. 2.24. Summer weekday: (a) Original time series, (b) Diurnal mean and standard deviation, (c) Time series after removal of diurnal mean and standard deviation

2.2.4 Seasonal ARMA model of load time series

a) Model identification

In order to identify the order of an ARMA model for the transformed load time series shown in Fig. 2.24 (c), the ACC and PACC of the time series are calculated and shown in Fig. 2.25. As the sample PACC has significant values at time lag 25 and 49 and the sample ACC has a rise at time lag 24 and 48, these indicate that the 24 h period is still present in the time series even after the diurnal mean and standard deviation are removed. However, a standard ARMA model is not able to take into account the 24 h period. Instead, a seasonal ARMA model may be employed.

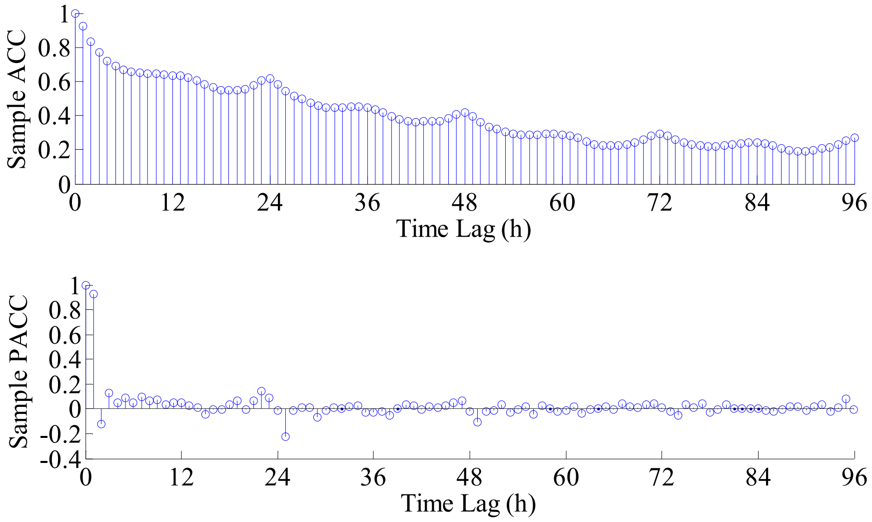

Fig. 2.25. Sample ACC (upper) and PACC (lower) of the transformed time series in Fig. 2.24 (c).

Generally, a multiplicative seasonal ARMA model is expressed as (Wei 1990):

$$\Phi_P\left(B^T\right)\phi_p\left(B\right)Z\left(t\right)=\theta_q\left(B\right)\Theta_Q\left(B^T\right)a\left(t\right), \tag{2.26}$$

where the seasonal coefficient *T* is the period of the time series, equal to 24 in this case. *Z*(*t*) is the transformed time series from simulation, and

$$\Phi_P\left(B^T\right)=1+\Phi_1 B^T+\Phi_2 B^{2T}+\cdots+\Phi_P B^{PT}, \tag{2.27}$$

$$\Theta_Q\left(B^T\right)=1+\Theta_1 B^T+\Theta_2 B^{2T}+\cdots+\Theta_Q B^{QT}, \tag{2.28}$$

$$\phi_P\left(B\right)=1+\phi_1 B^1+\phi_2 B^2+\cdots+\phi_p B^p, \tag{2.29}$$

$$\theta_q\left(B\right)=1+\theta_1 B^1+\theta_2 B^2+\cdots+\theta_q B^q. \tag{2.30}$$

$\{\Phi_i\}$ are the seasonal AR coefficients, $\{\Theta_i\}$ are the seasonal MA coefficients, $\{\phi_i\}$ are the regular AR coefficients, $\{\theta_i\}$ are the regular MA coefficients. In the case that $T = 1$, (2.27) has the same structure as (2.29), and (2.28) has the same structure as (2.30).

As shown in the lower panel of Fig. 2.25, the sample PACC at time-lag 1 to 3 has significant values. This implies an AR order of minimum 3. Between time-lag 4 and time-lag 12, the sample PACC is small but decays slowly. This may imply an MA order of minimum 1. The sample PACC at time-lag 25 also indicates a seasonal AR order of minimum 1. As a result, a seasonal ARMA(3,1)×$(1,0)_{24}$ model is identified tentatively for the transformed time series. The notation ARMA(3,1)×$(1,0)_{24}$ indicates that the model consists of a regular ARMA(3,1) model and a 24 h seasonal ARMA(1,0) model. By increasing the order of the seasonal ARMA model, it is found that a better fit can be achieved when the model orders are increased to the seasonal ARMA(9,1)×$(1,1)_{24}$ model. The sample ACC and PACC of the seasonal ARMA(9,1)×$(1,1)_{24}$ model are shown in Fig. 2.26. The sample ACC and PACC of the transformed time series are shown in Fig. 2.26 again for comparison.

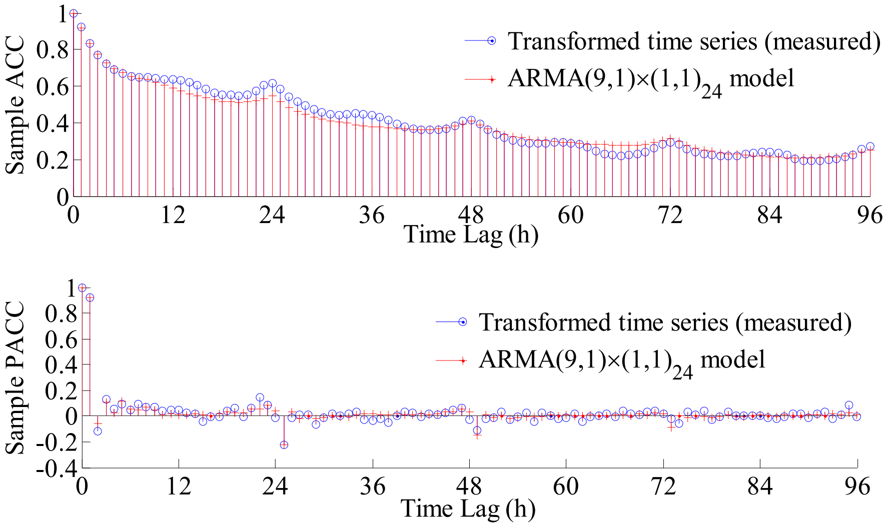

Fig. 2.26. Sample ACC (upper) and PACC (lower) of the seasonal ARMA(9,1)×(1,1)24 model.

It is seen from the figure that the seasonal ARMA(9,1)×$(1,1)_{24}$ model matches with the measured (transformed) time series adequately in terms of ACC and PACC. A further increase of the model order does not provide significant improvement in the fit of ACC and PACC. Therefore, according to the

Principle of Parsimony, the seasonal ARMA(9,1)×(1,1)$_{24}$ model is identified for the transformed time series. The mathematical expression of the seasonal ARMA(9,1)×(1,1)$_{24}$ model is:

$$\begin{aligned} Z(t) = -\Phi Z(t-24) - \sum_{i=1}^{9} \phi_i Z(t-i) - \Phi \sum_{i=1}^{9} \phi_i Z(t-24-i) \\ + a(t) + \theta a(t-1) + \Theta a(t-24) + \Theta\theta a(t-25) \end{aligned} \tag{2.31}$$

The model parameters are determined by minimizing the variance of the white noise $a(t)$. The parameter determination is implemented in MATLAB using the optimization toolbox (Mathworks 2009). The optimized parameters are $\Phi = -0.865$; $\Theta = -0.680$; $\theta = 0.097$; $\{\phi_i\} = \{-0.860, 0.071, -0.078, 0.060, -0.043, -0.033, 0.008, -0.023, -0.030\}$; $\sigma_a = 0.122$.

b) Model Validation

As a result, a stochastic load model can be established by combining the seasonal ARMA(9,1)×(1,1)$_{24}$ model with the diurnal mean and standard deviation shown in Fig. 2.24 (b). This is conducted by first simulating a time series using the seasonal ARMA(9,1)×(1,1)$_{24}$ model of sufficient length (integer multiple of 24). Then, the simulated time series is multiplied by the diurnal standard deviation and added with the diurnal mean. Mathematically, the final simulated load time series $Y(t)$ is expressed as:

$$Y(t)=Z(t)\times\sigma(\tau)+\mu(\tau) \tag{2.32}$$

where

$$\tau = \begin{cases} 24, & t=24, 48, 72, \ldots \\ t-24\times\text{floor}(t/24), & \text{otherwises} \end{cases}. \tag{2.33}$$

As a result, a simulated load time series is obtained as shown in Fig. 2.27. The length of the time series is 1560. As it is not straightforward to validate the stochastic load model analytically, the model will be validated numerically through Monte Carlo simulation, which generates a sufficiently long time series. Then, the simulated times series is validated against the measured load time series in Fig. 2.24 (a) in terms of probability distribution, sample ACC and sample PACC.

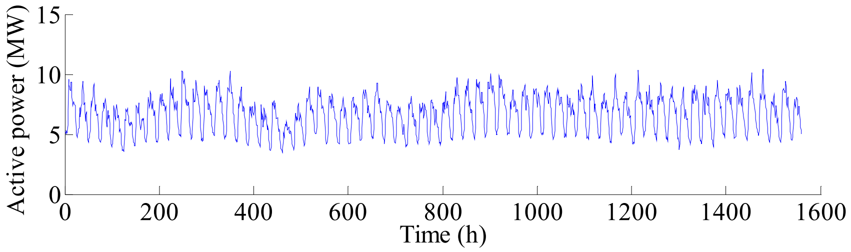

Fig. 2.27. Simulated load time series (summer weekday).

Fig. 2.28 shows the cumulative distribution function of the simulated and the measured load time series, which overlap each other. Fig. 2.29 shows the corresponding sample ACC and PACC. The simulated load time series fits very well with the measured load time series. Therefore, the developed stochastic load model, including (2.31) and (2.32), are validated against the measurements.

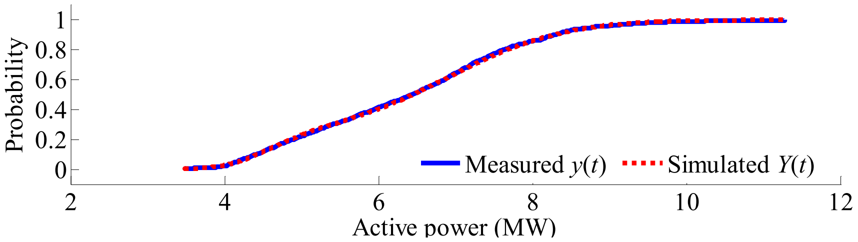

Fig. 2.28. Cumulative distribution function of a load time series: simulation versus measurement.

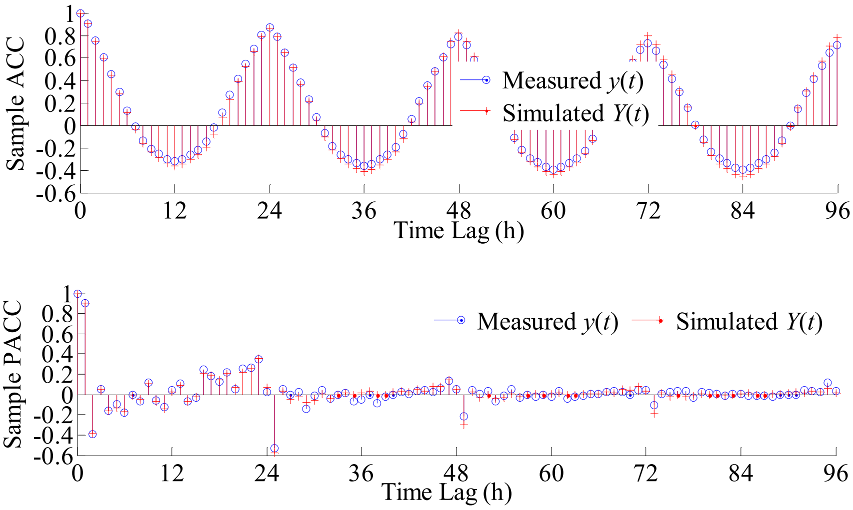

Fig. 2.29. Sample ACC (upper) and PACC (lower) of a load time series: simulation versus measurement.

Based on the same procedure of model identification and model validation, the seasonal ARMA model for summer weekends, winter weekdays and winter weekends are summarized as follows.

For summer weekends, the seasonal ARMA(4,0)×$(2,1)_{24}$ model is selected:

$$\begin{aligned} Z(t) = -\sum_{j=1}^{2}\Phi_j Z(t-24i) - \sum_{i=1}^{4}\phi_i Z(t-i) - \Phi_1\sum_{i=1}^{4}\phi_i Z(t-24-i) \\ -\Phi_2\sum_{i=1}^{4}\phi_i Z(t-48-i) + a(t) + \Theta a(t-24) \end{aligned} \tag{2.34}$$

with the parameters $\Phi = \{-0.993, 0.014, 0.086, -0.032\}$; $\Theta = -0.287$; $\{\phi_i\} = \{-0.993, 0.014, 0.086, -0.032\}$; $\sigma_a = 0.119$. The load on a summer weekend has a quite different model structure from the load on a summer weekday. This may be caused by different load patterns on a summer weekday and on a summer weekend. Detailed investigation can be conducted if one year or more years of load time series is available.

For winter weekdays, the seasonal ARMA(7,0)×$(7,1)_{24}$ model is selected:

$$\begin{aligned} Z(t) = -\sum_{j=1}^{7}\Phi_j Z(t-24j) - \sum_{i=1}^{7}\phi_i Z(t-i) - \sum_{j=1}^{7}\sum_{i=1}^{7}\Phi_j\phi_i Z(t-24j-i) \\ + a(t) + \Theta a(t-24) \end{aligned} \tag{2.35}$$

with the parameters $\Phi = \{-0.535, -0.051, 0.016, -0.035, -0.157, 0.084, 0.0042\}$; $\Theta = -0.455$; $\{\phi_i\} = \{-0.805, 0.011, -0.011, -0.007, -0.032, 0.006, -0.061\}$; $\sigma_a = 0.2004$.

For winter weekends, the seasonal ARMA(4,0)×$(2,2)_{24}$ model is selected:

$$\begin{aligned} Z(t) = -\sum_{j=1}^{2}\Phi_j Z(t-24i) - \sum_{i=1}^{4}\phi_i Z(t-i) - \Phi_1\sum_{i=1}^{4}\phi_i Z(t-24-i) \\ -\Phi_2\sum_{i=1}^{4}\phi_i Z(t-48-i) + a(t) + \Theta_1 a(t-24) + \Theta_2 a(t-48) \end{aligned} \tag{2.36}$$

with the parameters $\Phi = \{0.185, -0.468\}$; $\Theta = \{0.141, -0.312\}$; $\{\phi_i\} = \{-0.916, 0.243, -0.194, 0.006\}$; $\sigma_a = 0.224$.

2.2.5 Load management with the stochastic load model

As discussed in 2.2.1, the amount of load that is changed at an individual hour can be modeled by a Gaussian stochastic variable. The following example demonstrates how to use the developed stochastic load model to simulate a new load time series after a specific load management strategy is implemented. Assumed that 10% of the load, both mean value and variance, between 7 a.m. and 12 a.m. is planned to be shifted to the time between 1 a.m. and 4 a.m. This can be directly implemented through the change of the diurnal mean curve and the diurnal standard deviation curve as shown in Fig. 2.30. The solid curves represent the diurnal mean and standard deviation before the load shifting and the dotted curves represent the ones after the load shifting.

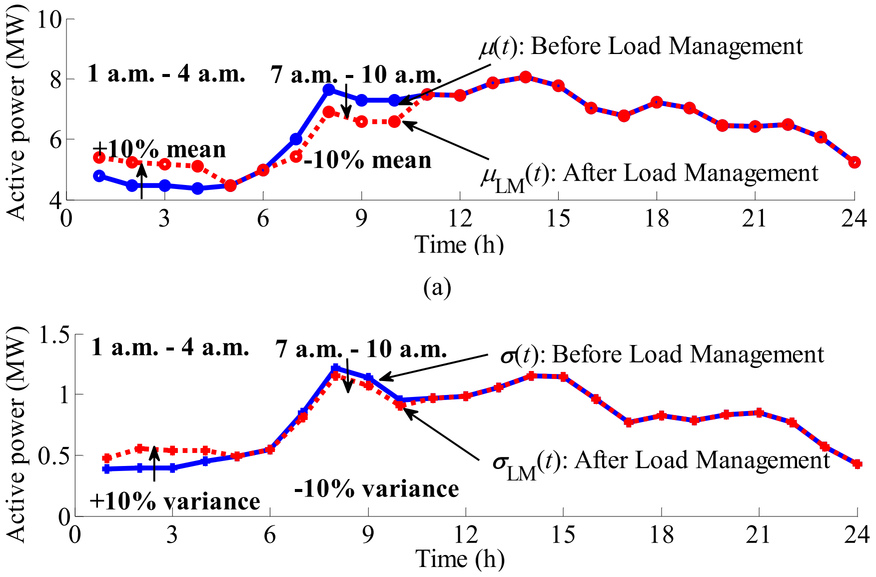

(a)

(b)

Fig. 2.30. 10% load shifted from 7 a.m.-12 a.m. to 1a.m.-4a.m.: (a) change of diurnal mean value, (b) change of diurnal standard deviation

Based on the new diurnal mean and standard deviation curves and the seasonal ARMA(9,1)×(1,1)$_{24}$ model in (2.31), a new load time series after the load shifting can be simulated through Monte Carlo simulation. The load shifting usually reduces the peak load and increases the base load so that the load variation becomes smaller. In order to demonstrate whether or not this is the case for the new load time series, a load duration curve can be used. A load duration curve is obtained by sorting out the time series data in the descending order. A load duration curve is equivalent to a cumulative distribution curve after certain transformations.

Fig. 2.31 shows the load duration curve before and after the implementation of the load shifting shown in Fig. 2.30. It is clearly shown in the figure that the peak load region is reduced and the base load region is increased after the load shifting. This example shows the effectiveness of the developed stochastic load model for simulating the consequence of load management in a load time series.

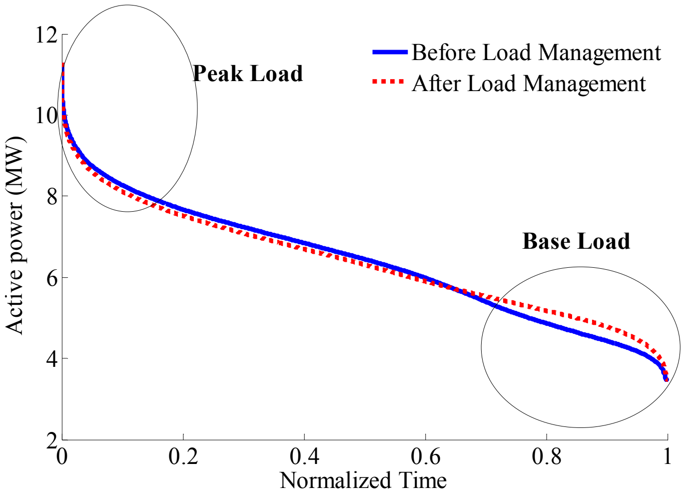

Fig. 2.31. Load duration curve of the simulated load time series before (solid) and after (dotted) the implementation of the load shifting in Fig. 2.30.

2.2.6 Conclusion of stochastic load model

In this section, a stochastic load model based on a seasonal ARMA process has been developed. The stochastic load model consists of a seasonal ARMA model, a diurnal mean curve and a diurnal standard deviation curve. The stochastic load model is validated against the measurements in terms of probability distribution, sample ACC and sample PACC. The model has 61 parameters and is much more parsimonious than a joint-normal model, which requires 600 parameters. The developed stochastic load model is useful for simulating a realistic load time series especially when the measurements are not available. The model can also be readily used to simulate the effect of load management by changing the load time series. This is demonstrated by a load-shifting example. As a result, the developed stochastic load model is a very effective tool for power system planning and reliability analysis incorporating demand side management.

2.3 Stochastic CHP model

2.3.1 Stochastic operation of CHP units

CHP units are one of the most common distributed generators in Denmark. This is because of their high energy efficiency and contribution to the reduction of CO_2 emission. As many other DGs, small CHP units benefit the operation of local distribution systems due to its close location to the electrical loads. These benefits include reduction of network power losses, deferral of network capacity expansion, improvement of supply reliability, etc. (Pecas Lopes 2002, Barker, De Mello 2000). These aspects are normally evaluated during the stage of system planning, which requires temporal simulation or sequential Monte Carlo simulation for a detailed study. To perform these simulation techniques, time series models of CHP generation are usually required.

Unlike WTs, the fuel of CHP units, such as biomass and natural gas, can be supplied on demand and is thus not a stochastic source. However, CHP units are turned on and off according to the regulating power, which reflects the heat load and electricity price during the day. In other words, the operation status of CHP units is largely determined by the stochastic variables of heat load and electricity price. Hence, the operation or generation status of CHP units at a specific time instant, e.g. an hour of a day, is a stochastic variable with a certain number of discrete states. Furthermore, for the operation of a CHP unit over a period of time, the status of the CHP unit at different time instants is not independent of each other. For instance, the status of the CHP unit at the current hour is most likely to be the same as the status at the previous hour. Consequently, the status of a CHP unit over a period of time is a discrete stochastic process.

For modeling a discrete stochastic process, standard ARIMA models can no longer be applied as they are for continuous stochastic processes (Box, Jenkins & Reinsel 1994). On the other hand, discrete Markov chains are suitable for modeling a discrete stochastic process and will therefore be investigated in the following section (Norris 1997).

2.3.2 Discrete Markov chain

Markov chains are the simplest mathematical models for stochastic phenomena evolving in time (Norris 1997). Random walk is a simple example of a discrete Markov chain, which describes random movement among a finite number of states. This section only considers a Markov chain on a finite number of states, i.e. $s_1, \ldots, s_n$. The probability that one moves to another state depends only on its current state, not on the previous states visited. Mathematically, it is expressed as

$$\begin{aligned}\mathbf{P}\left(Y_{t+1} = s_j \mid Y_0 = s_{i_0}, \ldots, Y_{t-1} = s_{i_{t-1}}, Y_t = s_i\right) \\ = \mathbf{P}\left(Y_{t+1} = s_j \mid Y_t = s_i\right) = p_{ij}\end{aligned}, \tag{2.37}$$

where the random process (Y_0, Y_1,…), with a n-state space $\mathbf{s} = \{s_1, \ldots, s_n\}$, is said to be a Markov chain with the transition matrix **P**. The transition matrix **P** consists of transition probabilities p_{ij}, which describe the probabilities of moving to state s_j when in state s_i. A Markov chain is (time) homogeneous if p_{ij} does not change with time t, otherwise inhomogeneous. An n-state transition matrix **P** is expressed as

$$\mathbf{P} = \begin{bmatrix} p_{11} & p_{12} & \cdots & p_{1n} \\ p_{21} & p_{22} & \cdots & p_{2n} \\ \cdots & \cdots & \cdots & \cdots \\ p_{n1} & p_{n2} & \cdots & p_{nn} \end{bmatrix}. \tag{2.38}$$

The first row in **P** provides the probabilities of moving to all states (state s_1 to s_n) from state s_1; the second row provides the transition probabilities of moving to all states from state s_2, and so on. The sum of the transition probabilities at each row is 1, i.e.

$$\sum_{j=1}^{n} p_{ij} = 1 \qquad \text{for all } i = 1, \ldots, n. \tag{2.39}$$

A Markov chain is said to be irreducible, if it is possible to go from any state to any other state in one or more steps; it is said to be periodic, if the return to a particular state only happens at regular intervals, otherwise aperiodic. A Markov chain has an invariant distribution if it is irreducible and aperiodic. A probability vector $\boldsymbol{\lambda} = (\lambda_1, \ldots, \lambda_n)$ with non-negative entries is said to be an invariant distribution of **P**, if it satisfies:

$$\boldsymbol{\lambda}\mathbf{P} = \boldsymbol{\lambda}, \tag{2.40}$$

where $\Sigma\,\lambda_i = 1$.The discrete Markov chain based on the model defined above is a 1st order Markov chain, namely, the probability of moving to another state depends only on its current state. The parameter number of a 1st order transition matrix is $\mathrm{n}\times(\mathrm{n}-1)$. The transition probability of a kth order Markov chain depends on the current state and its previous $(k-1)$ states. For example, the transition matrix of a 2nd order Markov chain can be written as

$$\mathbf{P}_{\mathrm{n}^2\times\mathrm{n}} = \begin{bmatrix} \mathbf{P}^{1}_{\mathrm{n}\times\mathrm{n}} \\ \cdots \\ \mathbf{P}^{\mathrm{n}}_{\mathrm{n}\times\mathrm{n}} \end{bmatrix}, \tag{2.41}$$

where $\mathbf{P}^{k}_{\mathrm{n}\times\mathrm{n}} = \left\{p_{kij}\right\}$ is a 1st order transition matrix with n Markov states. The parameter number for a kth order transition matrix is

$$M = \mathrm{n}^{k} \times \left(\mathrm{n}-1\right), \tag{2.42}$$

2.3.3 Analysis of measured CHP generation data

Before developing a Markov model for the CHP generation, it is valuable to identify the statistical behavior of the actual CHP generation. Fig. 2.32 (a) shows the hourly time series data between July 1, 2006 and January 31, 2007 recorded from a CHP plant connected to the Støvring substation. The CHP plant consists of three units, each with rated capacity of 3 MW. Thus, the CHP generation has four possible discrete states: 0, 3 MW, 6 MW and 9 MW. Furthermore, the generation status of the CHP units can change from any state to another as shown in Fig. 2.32 (b).

Fig. 2.33 shows the probability mass function of the CHP generation over the seven months. During the daily operation, all the CHP units are turned on for less than 10% of the time, while all of them are turned off for almost 50% of the time. This probability mass function of the generation states reflects the actual operation condition and should be modeled accurately.

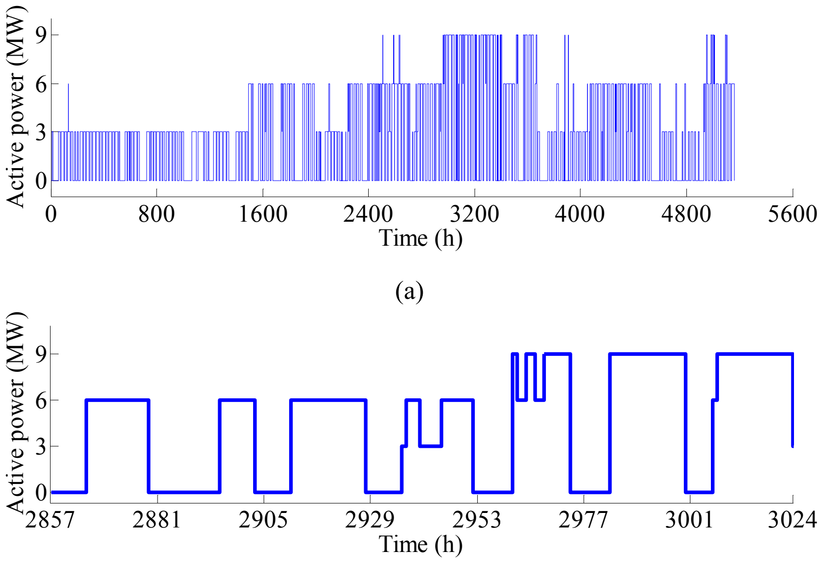

(a)

(b)

Fig. 2.32. Measured hourly CHP time series data (a) From July 1, 2006 to January 31, 2007, (b) one winter week.

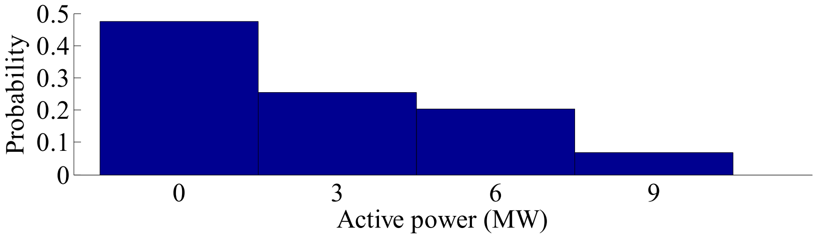

Fig. 2.33. Empirical probability mass of the measured CHP generation in Fig. 2.32 (a).

The temporal correlation of CHP generation is another important factor for the modeling of the CHP generation. The temporal correlation reflects how much the generation status of the CHP units at the next hour is influenced by their status at the current hour. Fig. 2.34 shows the sample ACC and PACC of the measured time series of the CHP generation.

As shown in the lower panel of the figure, the sample PACC has a peak value at time-lag one, which indicates a strong correlation of the CHP generation between two adjacent hours. This can be modeled by a 1st order discrete Markov chain. Those values of the sample PACC within the critical limits are considered to be zero. Furthermore, the sample ACC decays exponentially for the first 12 time lags and rises periodically every 24 time lags. This 24 h period also affects the values of the sample PACC around the time lag of 24. The difficulty of the modeling lies on the issue of how to account for the 24 h period. Further discussion will be provided in the next subsection.

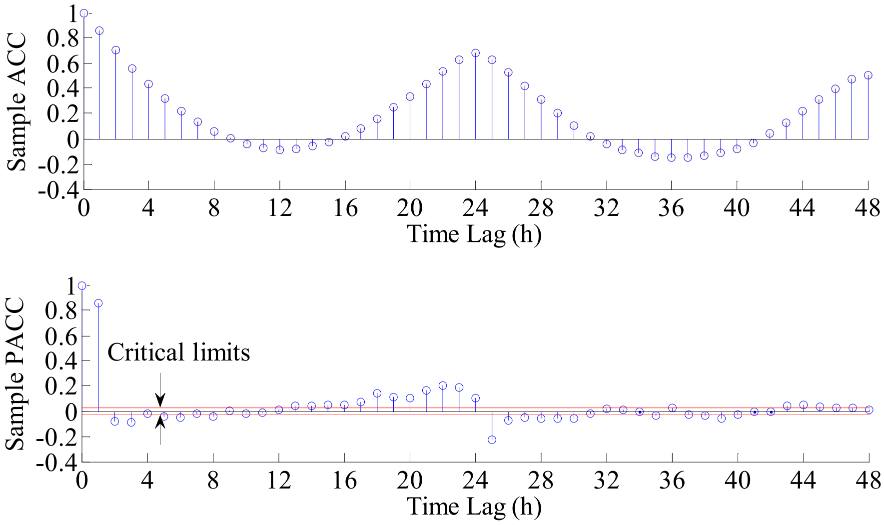

Fig. 2.34. Sample ACC (upper) and PACC (lower) of the measured CHP generation in Fig. 2.32 (a).

2.3.4 Discrete Markov model of CHP

a) 1st order discrete Markov model

Based on the statistical analysis carried out above, a 1st order discrete Markov model is tentatively chosen for modeling the CHP generation so that the strong correlation between two adjacent hours can be accounted for. A 1st order discrete Markov model can be developed by defining a transition matrix according to (2.37) and (2.38). The dimension of the transition matrix is n×n for an n-state Markov chain. According to the conditional probability, the transition probability p_{ij} can be obtained through

$$\begin{aligned} p_{ij} = \mathbf{P}\left(Y_{t+1} = \mathrm{s}_j \mid Y_t = \mathrm{s}_i\right) &= \frac{\mathbf{P}\left(Y_{t+1}=\mathrm{s}_j, Y_t=\mathrm{s}_i\right)}{\mathbf{P}\left(Y_t=\mathrm{s}_i\right)} \\ &= \frac{N_{ij}}{\sum_{j=1}^{\mathrm{n}} N_{ij}} = \frac{N_{ij}}{N_i} \end{aligned}, \tag{2.43}$$

where N_{ij} is the total number of counts when the state value moves from s_i to s_j in one step; N_i is the total number of counts when the state value is s_i. For the given measurements of the CHP generation shown in Fig. 2.32 (a), there are only four generation states with $\mathbf{s} = \{0, 3, 6, 9\}$. Based on (2.43), a 4×4 transition matrix can be calculated from the measured time series:

$$\hat{\mathbf{P}} = \begin{bmatrix} \mathbf{0.915} & 0.044 & 0.031 & 0.010 \\ 0.081 & \mathbf{0.897} & 0.019 & 0.003 \\ 0.074 & 0.023 & \mathbf{0.888} & 0.015 \\ 0.069 & 0.015 & 0.049 & \mathbf{0.867} \end{bmatrix} \tag{2.44}$$

It is observed from (2.44) that the diagonal elements of the transition matrix have much higher probability values than the off-diagonal elements. This implies a strong temporal correlation between two adjacent hours. For example, $p_{11} = 0.915$ means that given 0 power generation at the current hour, the probability of remaining 0 power generation at the next hour is 0.915; $p_{23} = 0.019$ means that given 3 MW power generation at the current hour, the probability of having 6 MW power generation at the next hour is 0.019. The rest of the transition probabilities can be interpreted in the same way. The large values of the diagonal elements are in accordance with the large value of the sample PACC at time-lag one, which is shown in the lower panel of Fig. 2.34. As a result, a 1st order discrete Markov model with the transition matrix of (2.44) is obtained. In the following, the model is verified against the measurements in terms of probability distribution, ACC and PACC.

For a 1st order discrete Markov model, the theoretical ACC at time-lag k can be directly obtained by (Chen et al. 2009):

$$\mathrm{ACC}(k) = \frac{\mathbf{m}^{\mathrm{T}}\mathbf{P}^{k}\mathbf{s} - \mu_Y^2}{\sigma_Y^2}, \tag{2.45}$$

where the superscript T indicates matrix transposition; μ_Y is the mean of the Markov chain and σ_Y is the standard deviation of the Markov chain, and

$$\mathbf{s} = [s_1, \ \cdots, \ s_\mathrm{n}]^{\mathrm{T}} \tag{2.46}$$

$$\mathbf{m} = \left[\pi(s_1)s_1, \quad \cdots, \quad \pi(s_n)s_n\right]^{\mathrm{T}} \tag{2.47}$$

where $\pi(s_i)$ is the state probability of the state value s_i. Alternatively, the ACC of the Markov model can be obtained from a Monte Carlo simulation of the model. The procedures of such a Monte Carlo simulation is summarized as follows:

1) Initialize the first value of the Markov chain $Y(1)$,
2) Calculate the cumulative transition matrix **F** from the transition matrix **P**:

$$\mathbf{F} = \left\{f_{ij}\right\} = \left\{\sum_{k=1}^{j} p_{ik}\right\} \tag{2.48}$$

3) Generate a random number r from a uniform distribution,
4) If $Y(t) = \mathrm{s}_i$, the time series value at $t = t+1$ is determined by

$$Y(t+1) = \begin{cases} s_1, & r \leq f_{i1} \\ s_j, & f_{i(j-1)} < r \leq f_{ij} \end{cases}, \tag{2.49}$$

5) Repeat 3) and 4) until t reaches the desired length L.

As a result, a Markov chain of length L is obtained from the Monte Carlo simulation. Therefore, the 1st order discrete Markov model can be validated by comparing the statistical properties of the simulated Markov chain and the measurements. These statistical properties include probability mass function and temporal correlation (ACC and PACC).

Fig. 2.35 shows the empirical probability mass function of the CHP generation obtained from the measurements and the simulated Markov chain. The match between the simulated and the measured CHP generation is very good. In fact, the probability mass of the CHP generation represents the state probability of each generation value. According to (2.40), the state probability vector **λ** is an invariant distribution of the transition matrix **P** (Norris 1997). This implies that the state probability of the simulated time series converges to that of the measurement as the simulation length increases. This is an advantage of using a discrete Markov model, which ensures an accurate modeling of the probability distribution.

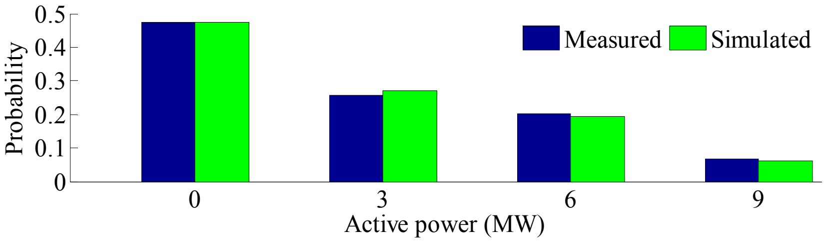

Fig. 2.35. Empirical probability mass of the measurements and simulated CHP generation by a 1st order Markov model.

Fig. 2.36 compares the temporal correlation of the simulated and the measured CHP generation in terms of sample ACC and PACC. The sample ACC of the simulated time series decays exponentially without rise at time-lag 24. This is expected as the 1st order Markov model does not include this 24 h period. This can also be seen on sample PACC around the time-lag 24, where the measured time series has non-zero values. However, it is observed from the sample PACC that the simulation matches well with the measurement at time-lag one. The following subsection discusses how to include the 24 h period into the Markov model.

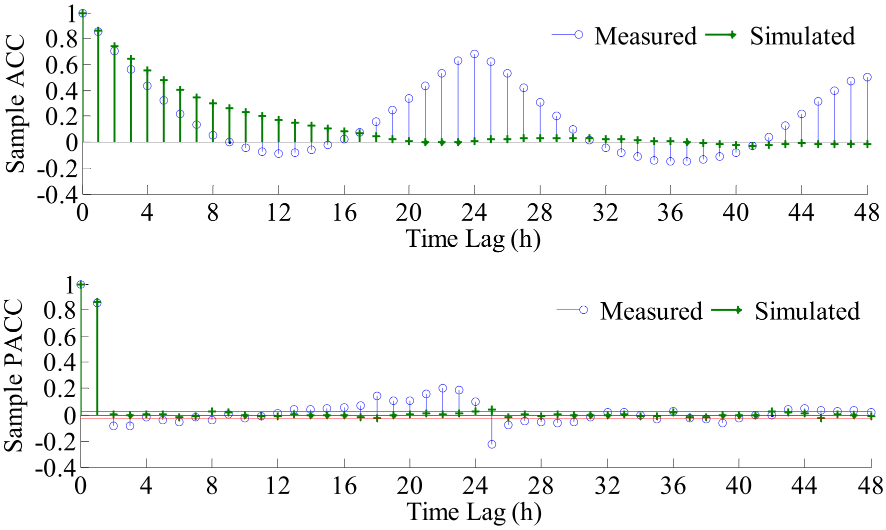

Fig. 2.36. Sample ACC (upper) and PACC (lower) of the measurements and simulated CHP generation by a 1st order Markov model.

b) Modeling of 24 h period by a 2nd order discrete Markov model

In order to model the 24 h period of the CHP generation, various potential approaches may be applied. One approach is to separate the hourly mean and standard deviation of a day from the rest of the time series. Then, the 1st order Markov model can be applied to the transformed time series. This is similar to the technique applied to the stochastic load model. However, the main problem with this approach is that the transformed time series will contain many more states than only four (0 MW, 3 MW, 6 MW and 9 MW). For example, if the state value 0 is subtracted by 24 different hourly mean values of a day, then 24 new state values may be obtained. As a consequence, a total state number of 96 may be obtained. This will result in a 96×96 transition matrix, which contains 9120 parameters. In this case, the model parameter number surpasses the measured data size, i.e. 5160. Thus, this approach is considered inappropriate. Another approach is to develop a higher-order Markov model. Consider that the CHP generation at hour t, $Y(t)$, is not only dependent on the state value at $t-1$, but also the one at $t-T$, where T is the period and equal to 24 in this case. This can be expressed in terms of conditional probability, which states the probability of $Y(t) = \mathrm{s}_j$ given that $Y(t-1) = \mathrm{s}_i$ and $Y(t-T) = \mathrm{s}_k$. Mathematically, a 2nd order transition matrix $\{p_{kij}\}$ can be formed with its transition probability expressed by:

$$\begin{aligned} p_{kij} = \mathbf{P}\left(Y_t = \mathrm{s}_j \mid \left(Y_{t-1}=\mathrm{s}_i, Y_{t-T}=\mathrm{s}_k\right)\right) &= \frac{\mathbf{P}\left(Y_t=\mathrm{s}_j, Y_{t-1}=\mathrm{s}_i, Y_{t-T}=\mathrm{s}_k\right)}{\mathbf{P}\left(Y_{t-1}=\mathrm{s}_i, Y_{t-T}=\mathrm{s}_k\right)} \\ &= \frac{N_{kij}}{\sum_{j=1}^{\mathrm{n}} N_{kij}} = \frac{N_{kij}}{N_{ki}} \end{aligned} \tag{2.50}$$

where $i, j, k = 1, \ldots, \mathrm{n}$; N_{kij} is the total number of counts when the state values at time t, $t-1$ and $t-T$ are s_j, s_i and s_k, respectively; N_{ki} is the total number of counts when the state value at time $t-1$ is s_i and at time $t-T$ is s_k. As a result, a 2nd order discrete Markov model is established with the transition probability defined in (2.50). In this case, the model parameter number is increased to 48. Fig. 2.37 shows the sample ACC and PACC of a time series simulated from the 2nd order discrete Markov model. The sample ACC has a periodic rise every 24 h., while the sample PACC also shows a similar trend as the measurements between time-lag 17 and 24. As compared to Fig. 2.36, the 2nd order discrete Markov model has a much better fit in temporal correlation than the 1st order discrete Markov model. Although this approach does not completely take into account the 24 h period, it improves the results of the sample ACC and PACC as compared to the 1st order Markov model.

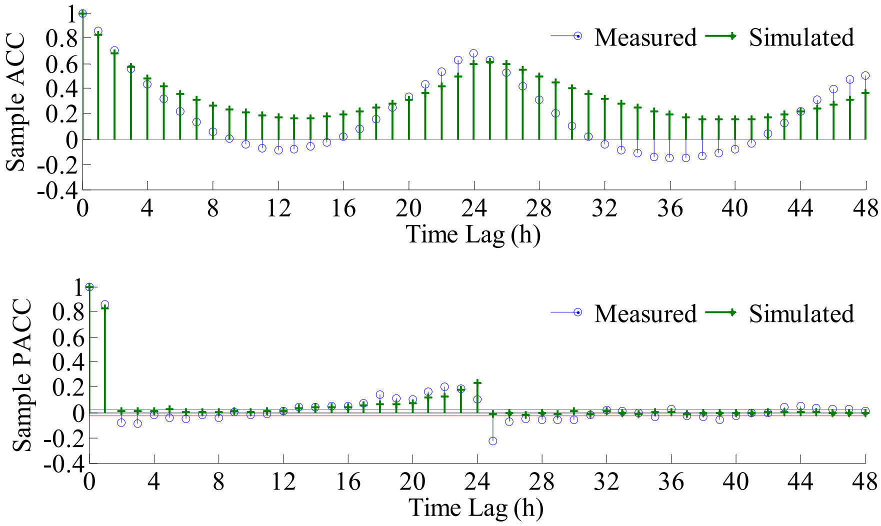

Fig. 2.37. Sample ACC (upper) and PACC (lower) of the simulated CHP generation by a 2nd order Markov model.

c) Model deficiency

As shown in Fig. 2.37, a 2nd order discrete Markov model provides a better modeling in the 24 h period of the CHP generation. Even though the fit in sample ACC around time-lag 12 is still quite poor, this can be improved by a 3rd order discrete Markov model taking into account the autocorrelation at time-lag 12. However, the improvement in the sample ACC and PACC does not guarantee that the hourly variation of the CHP generation during a day is properly modeled.

Fig. 2.38 (a) shows the hourly probability mass of the CHP generation from measurements. A strong diurnal variation is observed. For example, between 1 a.m. and 6 a.m., all the three units are off for more than 95% of the time, while between 9 a.m. and 20 a.m., one or more units are on for more than 70% of the time. These phenomena are mainly caused by the diurnal variation of heat load and electricity price. In contrast, as shown in Fig. 2.38 (b), the 2nd order discrete Markov model does not exhibit the same diurnal variation at all. The probability mass of each generation state is evened out over 24 hours. Therefore, even though the sample ACC and PACC of the 2nd order Markov model shows a 24 hour period, the diurnal variation of the probability mass is not captured by the model.

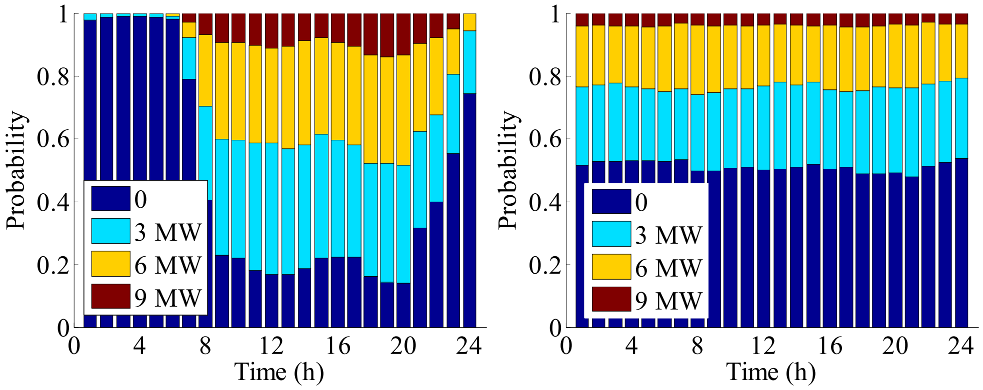

(a) (b)

Fig. 2.38. Diurnal probability mass of CHP generation: (a) measurements, (b) 2^{nd} order discrete Markov model.

d) Proposed Markov model

As shown in Fig. 2.38 (a), different hours have a quite different probability mass function. This indicates that it may not be appropriate to use the same transition matrix to simulate all the 24 hours. In other words, different hours of a day may be represented by a different transition matrix. For example, the probability mass functions between hour 1 and hour 6 are similar. The data at these hours can be represented by one transition matrix and the data at the rest of the hours can be represented by another transition matrix. This is demonstrated in Fig. 2.39, where two different transition matrices are obtained from the measured data at two different periods of a day (hour 1 – hour 6, hour 7 – hour 24).

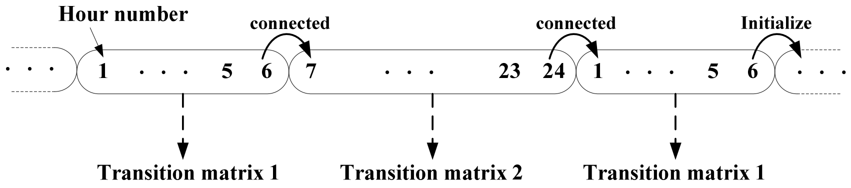

Fig. 2.39. Diagram of calculating two different transition matrices for different hours of a day.

After the two transition matrices are obtained, a Markov chain is simulated by performing a Monte Carlo simulation. The procedures of the Markov chain Monte Carlo simulation is summarized as follows:

1) Initialize the first value of the Markov chain $Y(1)$,
2) Simulate the first Markov chain for the first six hours, $Y(1)$, …, $Y(6)$, based on the transition matrix 1,

3) Use $Y(6)$ to generate $Y(7)$ based on the transition matrix 2,

4) Simulate the second Markov chain for the remaining hours of a day, $Y(7),\ldots, Y(24)$, based on the transition matrix 2,

5) Combine the two Markov chains to one Markov chain as $Y(1),\ldots, Y(24)$,

6) Store the combined Markov chain as a one-day simulation,

7) Use $Y(24)$ to generate a new $Y(1)$ based on the transition matrix 1,

8) Repeat 2) to 7) until the length of the Markov chain reaches the required value.

In this way, a Markov chain is obtained on the basis of the two transition matrices shown in Fig. 2.39. Step 3) and 7) connect the two Markov chains so that a smooth transition between the two chains can be achieved. This is demonstrated in Fig. 2.40, which shows the diurnal probability mass of the simulated Markov chain. Since hour 7, the transition matrix is switched from transition matrix 1 to transition matrix 2. A smooth shifting in the probability mass is observed at the hours after 7. This phenomenon is caused by the initialization (burn-in period) of the second Markov chain. A similar phenomenon is also observed from the measurements shown in Fig. 2.38 (a), between hour 7 and 9 and between hour 21 and 24; whereas the probability mass remains relatively stable between hour 1 and 6 and between hour 10 and 20. Nevertheless, the diurnal probability mass shown in Fig. 2.40 does not match that of the measurements shown in Fig. 2.38 (a). The implication that this model provides is that the probability mass function at each hour can be distinguished by using different transition matrices.

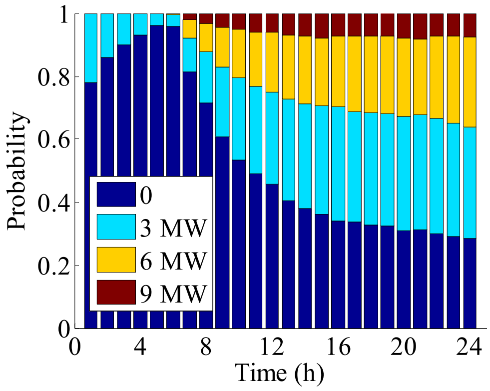

Fig. 2.40. Diurnal probability mass of CHP generation by using two transition matrices.

Based on the above analysis, an improvement may be achieved by categorizing the data into four groups represented by four different transition matrices. These four groups of data correspond to hour 1 – hour 6, hour 7 – hour 9, hour 10 – hour 20, hour 21 – hour 24. This concept is illustrated in Fig. 2.41. After the calculation of the four transition matrices, similar procedures as described above are followed to perform a Markov chain Monte Carlo simulation. It is noted that in this case, transition matrix 1 is only a 3×3 matrix. This is because the possible generation states between hour 1 and hour 6 are 0, 3 MW and 6 MW. However, in this case, there are four Markov chains in a day: Markov chain 1 ($Y(1), \ldots, Y(6)$), Markov chain 2 ($Y(7), \ldots, Y(9)$), Markov chain 3 ($Y(10), \ldots, Y(20)$), Markov chain 3 ($Y(21), \ldots, Y(24)$). As also indicated in Fig. 2.41, during the Monte Carlo simulation, Markov chain 1 is connected with Markov chain 2. Such a connection is made by generating $Y(7)$ conditional on $Y(6)$ according to transition matrix 2. A similar connection is also made between Markov chain 3 and Markov chain 4. However, Markov chain 2 is not connected with Markov chain 3. This leads to a relatively stable probability mass for Markov chain 3 between hour 10 and 20. The same explanation applies to the independence between Markov chain 4 and Markov chain 1.

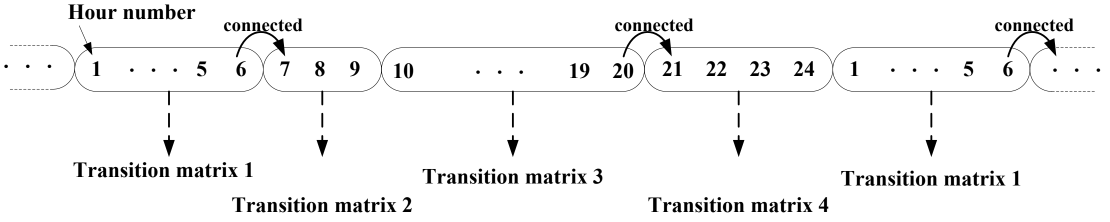

Fig. 2.41. Diagram of calculating four different transition matrices for different hours of a day.

Fig. 2.42 shows the diurnal probability mass of the simulated Markov chain based on the Markov model with four transition matrices. The diurnal probability mass from the measurements shown in Fig. 2.38 (a) is shown again in Fig. 2.42 (a) for comparison. In this case, a much better fit in diurnal probability mass is observed between the model and the measurements. Fig. 2.43 shows the sample ACC and the sample PACC of the proposed discrete Markov model. The sample ACC of the model is lower than that of the measurements. This may be caused by the independence between Markov chain 2 and Markov chain 3 and between Markov chain 4 and Markov chain 1. However, a strong 24 h period is still observed in the sample ACC of the model. The fit of the model can be further improved by using more transition matrices. In this case, with four transition matrices, the model parameter number is 42. This is even smaller than the 2nd order discrete Markov model, which has 48 parameters.

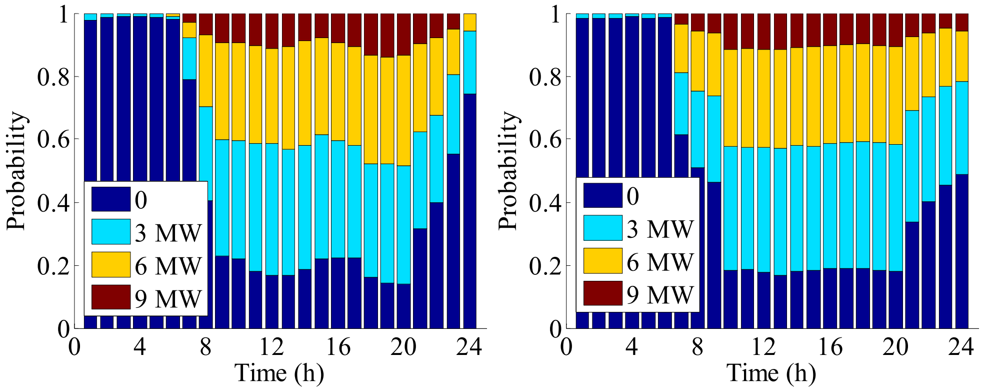

(a) (b)

Fig. 2.42. Diurnal probability mass of CHP generation: (a) measurements, (b) proposed Markov model with four transition matrices.

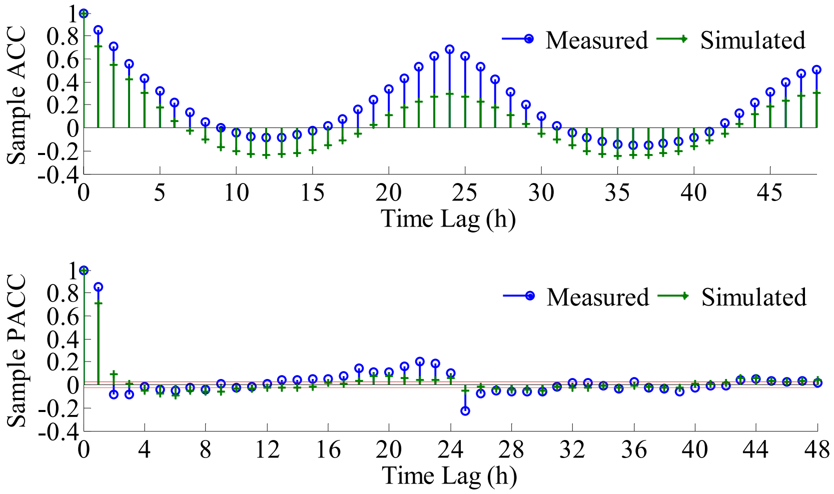

Fig. 2.43. Sample ACC (upper) and PACC (lower) of the simulated CHP generation by the proposed model.

In summary, the proposed discrete Markov model with four transition matrices has a better performance than the 2nd order discrete Markov model in terms of the diurnal probability mass and model parameter number. However, both models show a relatively poor fit in sample ACC and PACC as compared to the measurements.

e) Seasonal variation

The generation status of the CHP units reflects the variation of heat load and electricity price, which possess a strong seasonal, weekly and diurnal variation. Fig. 2.44 shows the empirical probability mass of the CHP generation at each state obtained from the measured data. According to the probability mass, it is evident that more units are turned on in a winter day than in a summer day, as well as in a weekday than in a weekend day. Normally, in summer, the maximum units turned on are two. In other words, there is always one spare unit, which may be used as a backup. Fig. 2.45 presents the empirical probability mass of the generation status of the CHP units at individual hours of a day, for four different types of days. The diurnal variation of the probability mass is different for the four types of days. This seasonal variation and weekday/weekend behavior can be accounted for by applying the proposed discrete Markov model with multiple transition matrices to each type of the day. The only difference is that each period has its own individual transition matrix.

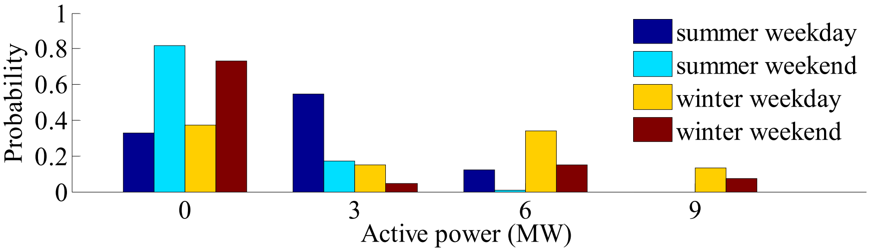

Fig. 2.44. Empirical probability mass of the measured CHP generation in Fig. 2.32 (a).

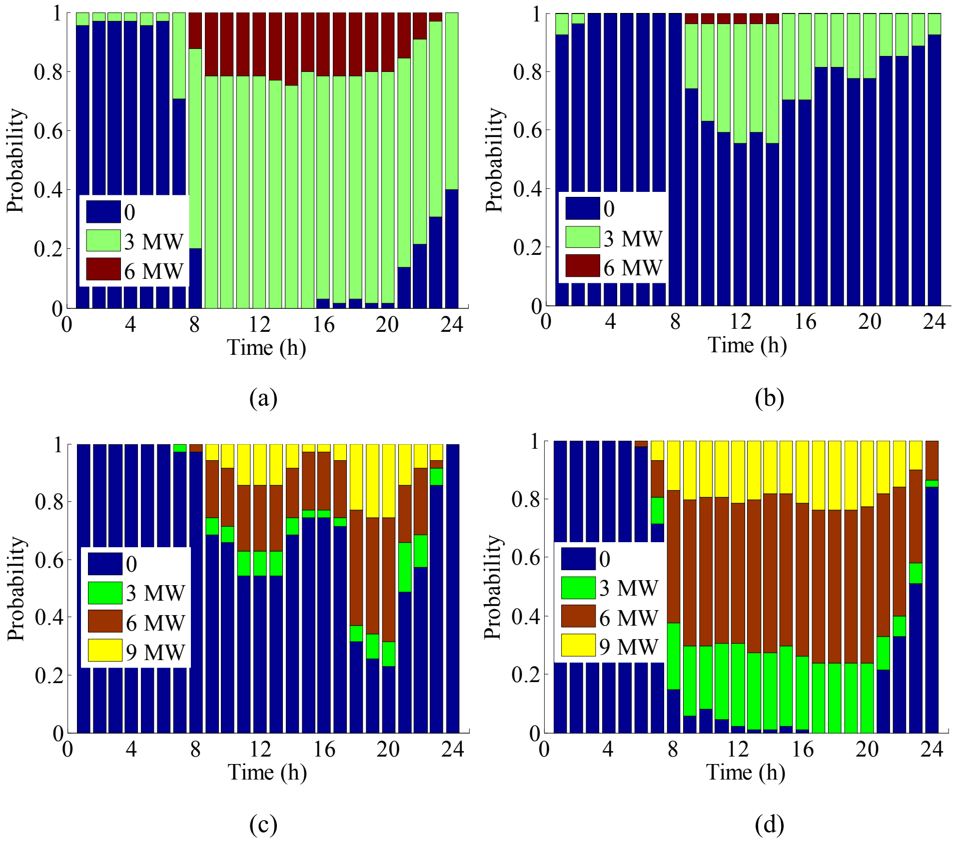

(a) (b)

(c) (d)

Fig. 2.45. Empirical probability mass of the measured CHP generation: (a) summer weekday, (b) summer weekend, (c) winter weekday, (d) winter weekend.

2.3.5 Conclusion of stochastic CHP model

In this section, a new discrete Markov model with multiple transition matrices has been developed for the CHP generation. A discrete Markov model is especially suitable for CHP generation as the generation status has a finite number of states. Furthermore, the state of the generation at the next hour is strongly dependent on the state at the current hour. However, the difficulty relies on the modeling of the 24 hour period of the CHP generation with an accurate diurnal probability mass function. This is accounted for by applying multiple transition matrices to different hours of a day. The simulation results show that the proposed discrete Markov model with multiple transition matrices outperforms a 2nd order discrete Markov Model in terms of diurnal probability mass function and model parameter number.

2.4 Summary

In this chapter, three stochastic models for WPG, load and CHP generation has been developed. A LARIMA model is selected for simulating WPG. A seasonal ARMA model is chosen for simulating load demand. A discrete Markov model with multiple transition matrices is applied for simulating CHP generation. These stochastic models have a certain degree of similarity to probability distribution models such as a cumulative distribution function, from which random samples can be drawn. However, these models are fundamentally different from probability distribution models as a sequence of random sampling from a probability distribution is independent of each other with no temporal correlation.

These stochastic models are developed for the correlated random sampling for sequential Monte Carlo simulations. Nevertheless, these models can be applied for a number of other situations. The applications of these stochastic models in the area of power systems include: 1) short-range power system planning, 2) reliability evaluation of power systems, 3) probabilistic load flow, 4) using the generated time series for testing forecasting algorithms of WPG, load and CHP generation, 5) simulating the effect of load management, and 6) sensitivity analysis to evaluate the impact in power systems due to the change of mean wind speed, peak load, etc.

Chapter 3

Probabilistic Load Flow Analysis

This chapter contains two parts. The first part focuses on numerical techniques for PLF calculations. First, a short review of PLF methods is provided. Then, the Monte Carlo based PLF method is discussed, followed by the convolution based and cumulants based PLF methods. The IEEE 14 bus system is used to demonstrate the three PLF methods. The second part of the chapter investigates the influence of temporal correlation in stochastic generation and load on the accuracy of Monte Carlo based PLF results. The investigation is demonstrated on the 20 kV Støvring distribution system with tap-changing transformers.

3.1 Probabilistic load flow

3.1.1 Introduction

Load flow calculation is a standard tool used to analyze the operation and planning of power systems. Normally, a load flow calculation solves system states and power flows for a given fixed value of power generations and load demands. This type of calculation is referred to as deterministic load flow (DLF). A DLF calculation does not consider uncertain phenomena in power systems, such as generator outages and load variations. Furthermore, modern power systems are commonly integrated with renewable energy based DG units. These renewable generations, such as wind power and photovoltaic generation, are intermittent and not fully controllable due to the stochastic nature of their prime sources. These uncertainties, including unit outages and stochastic generation and load, cannot be accounted for through a single DLF calculation. Therefore, in order to address these uncertainties, other methods, such as a probabilistic approach, fuzzy sets and interval analysis (Alvarado, Hu & Adapa 1992), can be adopted. This thesis focuses on the use of the probabilistic approach for modeling the power uncertainties in load flow calculations. Such an approach is also known as the PLF technique (Anders 1990).

PLF was first proposed in 1974 and has been developed and applied to power system normal operation, reliability evaluation, short-range/long-range planning, etc. (Borkowska 1974, Allan, Borkowska & Grigg 1974, Leite et al. 1990, Allan et al. 1981). PLF requires the probabilistic information of nodal power injections to obtain the probabilistic expressions of system states and power flows. The solution to a PLF calculation can be obtained in three ways: a numerical approach, an analytical approach and a combined approach (Jorgensen, Christensen & Tande 1998, Allan, Grigg & Al-Shakarchi 1976, Leite, Arienti 1990). The numerical approach resorts to a Monte Carlo simulation (Billinton, Li 1994), which substitutes a large number of values for the stochastic variables to obtain the PLF results numerically. In contrast, the analytical approach uses a convolution method (Allan et al. 1981), a cumulants method (Zhang, Lee 2004), etc. The convolution method is based on the probability distribution of stochastic variables, while the cumulants method is based on the moments and cumulants of stochastic variables. Both the numerical approach and the analytical approach have their own advantages and disadvantages. The main advantage of the numerical approach is that nonlinear load flow equations can be directly used in the PLF analysis, whereas the disadvantage is that a Monte Carlo simulation is usually very time-consuming. On the other hand, the numerical approach is much faster in computation speed. However, the main issue is that it involves complex mathematical computation which usually requires linearization of the load flow equations.

For the literature on PLF techniques published before 1988, (Anders 1990) and (Schilling et al. 1990) provide a very good summary and bibliography. The literature focuses on the linearization of LF equations, network outages and the interdependence among nodal power injections. For the literature published after 1988, the research work focuses on the efficiency of the PLF algorithms, the application in power system planning, the inclusion of voltage control devices and distributed generation, etc. (Leite et al. 1990, Su 2005, Hatziargyriou, Karakatsanis & Lorentzou 2005). These research results are summarized in (Chen, Chen & Bak-Jensen 2008) with an extensive bibliography attached in the end. The following sections explain in detail the PLF techniques using the Monte Carlo simulation, the convolution method and the cumulants method.

3.1.2 Monte Carlo simulation

The IEEE standard defines Monte Carlo simulation as a simulation in which random statistical sampling techniques are employed such that the result determines estimates for unknown values (IEEE Std. 610.3 1989). The definition indicates that the Monte Carlo simulation provides a numerical estimation of unknown parameters based on a random sample. The main elements of a Monte Carlo simulation include random number generation, random variate generation and variance reduction techniques.

Software such as Matlab provides pseudo-random number generators by using different algorithms, e.g. multiplicative congruential algorithms, Marsaglia’s subtract with borrow algorithm and the Mersenne

Twister algorithm (the Mathworks 2009). This chapter uses the Mersenne Twister algorithm. The algorithm generates uniformly distributed random numbers U within the interval [2^{-53}, $1 - 2^{-53}$].

A random number *u* can be used to determine a random sample *x* from a stochastic variable *X*. Such a random variate generation process can be conducted through several methods, such as inverse transform method and tabulating technique (Billinton, Li 1994). For example, the inverse transform method is to generate a random sample from the inverse cumulative distribution function of a random variable:

$$x = \mathrm{F}_X^{-1}\left(U\right) \tag{3.1}$$

where $\mathrm{F}_X(\ )$ is the cumulative distribution function of the random variable *X*. In the case that only observations or numerical data points are available, empirical distribution function of the observations can be derived and (3.1) can still be used to generate the random sample. Alternatively, the following method can be used

$$R = \mathrm{ceil}\left(U \times \mathrm{N}\right) \tag{3.2}$$

Where *R* is the position of the randomly selected observation; function ceil( ) is to round the elements to the nearest integers greater than or equal to the elements; N is the length of the observations.

Normally, a basic Monte Carlo simulation uses simple random sampling. The simple random sampling is a method of selecting n observations out of N such that each observation of a sample has an equal chance of being drawn (Cochran 1977). However, the simple random sampling requires a relatively large sample size in order to obtain stable Monte Carlo results. In order to improve the efficiency of a Monte Carlo simulation, variance reduction techniques can be utilized. The variance reduction techniques for random sampling include correlated sampling, control variates, dagger sampling, stratified sampling, importance sampling, etc. (Cochran 1977). A detailed discussion of these variance reduction techniques can be found in (Billinton, Li 1994, Cochran 1977). In this chapter, only the simple random sampling is used.

Furthermore, as discussed in the previous section, Monte Carlo simulation does not require linearization of the load flow equations. Therefore, the exact non-linear form of load flow equations as shown in (3.3)-(3.7) can be directly used to obtain the PLF results (Anders 1990).

$$P_i = V_i \sum_{k=1}^{n} V_k \left(G_{ik} \cos\theta_{ik} + B_{ik} \sin\theta_{ik} \right) \qquad (3.3)$$

$$Q_i = V_i \sum_{k=1}^{n} V_k \left(G_{ik} \sin\theta_{ik} - B_{ik} \cos\theta_{ik} \right) \qquad (3.4)$$

$$P_{ik} = -p_{ik} G_{ik} V_i^2 + V_i V_k \left(G_{ik} \cos\theta_{ik} + B_{ik} \sin\theta_{ik} \right) \qquad (3.5)$$

$$Q_{ik} = p_{ik} B_{ik} V_i^2 - B'_{ik} V_i^2 + V_i V_k \left(G_{ik} \sin\theta_{ik} - B_{ik} \cos\theta_{ik} \right) \qquad (3.6)$$

$$Q_i^{sh} = V_i^2 B_i^{sh} \qquad (3.7)$$

where P_i and Q_i are the net active and reactive power injection at bus i; P_{ik} and Q_{ik} are the active and reactive power flows in line ik at the bus i side; V_i and V_k are the voltage magnitude at bus i and k; θ_{ik} is the angle difference between the voltage at bus i and bus k ; G_{ik} and B_{ik} are the real and imaginary part of the corresponding admittance matrix; p_{ik} is the tap ratio of the tap-changing transformer connected between bus i and bus k, and is equal to 1 if it is a power line.

It is worth mentioning that the PLF results obtained from a Monte Carlo simulation are usually used as reference to validate results obtained by using analytical approaches (Allan, da Silva & Burchett 1981).

3.1.3 Convolution based PLF

The principle of the convolution based PLF method is to perform arithmetic calculations of the probability density functions. The probability density of system states and power flows can be obtained through convolution of the probability density of nodal power injections. The difficulties of applying such method are due to (Anders 1990, Allan, Al-Shakarchi 1976):

1) Non-linear load flow equations (3.3)-(3.7),
2) Correlated nodal power variables.

The difficulties can be overcome under the following approximations and assumptions:

1) Linearization of load flow equations,
2) The nodal power variables are independent or linearly correlated,
3) The distribution of nodal power variables is either a Gaussian distribution or a discrete distribution,

4) The network configuration and parameter remain unchanged.

Linearization of the load flow equations is conducted through a 1st-order Taylor expansion (Allan, da Silva & Burchett 1981). If the load flow equations (3.3) and (3.4) are represented by a more general form as:

$$\mathbf{Y} = \mathrm{g}(\mathbf{X}), \tag{3.8}$$

Then the 1st-order Taylor expansion around the mean value of the system states $\mathbf{X}_0$ is:

$$\mathbf{Y} \approx \mathbf{Y}_0 + \mathbf{J}(\mathbf{X} - \mathbf{X}_0) \tag{3.9}$$

where $\mathbf{Y}_0$ is the mean of the nodal power injections:

$$\mathbf{Y}_0 = \mathrm{g}(\mathbf{X}_0), \tag{3.10}$$

$$\mathbf{J} = \left.\frac{\partial \mathrm{g}}{\partial \mathbf{X}}\right|_{\mathbf{X}=\mathbf{X}_0}. \tag{3.11}$$

Consequently, the system states can be expressed as:

$$\mathbf{X} = \mathbf{J}^{-1}\mathbf{Y} + \left(\mathbf{X}_0 - \mathbf{J}^{-1}\mathbf{Y}_0\right). \tag{3.12}$$

Similarly, the power flow equations (3.5)-(3.7) are generalized as:

$$\mathbf{Z} = \mathrm{h}(\mathbf{X}). \tag{3.13}$$

The corresponding 1st-order Taylor expansion around $\mathbf{X}_0$ gives:

$$\mathbf{Z} \approx \mathbf{Z}_0 + \mathbf{K}(\mathbf{X} - \mathbf{X}_0) \tag{3.14}$$

where

$$\mathbf{K} = \left.\frac{\partial \mathrm{h}}{\partial \mathbf{X}}\right|_{\mathbf{X}=\mathbf{X}_0}, \tag{3.15}$$

$$\mathbf{Z}_0 = \mathrm{h}\left(\mathbf{X}_0\right). \tag{3.16}$$

Substitute (3.12) to (3.14) gives:

$$\mathbf{Z} = \mathbf{KJ}^{-1}\mathbf{Y} + \left(\mathbf{Z}_0 - \mathbf{KJ}^{-1}\mathbf{Y}_0\right), \tag{3.17}$$

According to (3.12) and (3.17), the system states and power flows are expressed as a linear combination of the nodal power variables **Y**. Assume that the nodal power variables are independent of each other. Then, the convolution technique can be applied to derive the probability density function of the system states **X** and power flows **Z** (Allan et al. 1981):

$$f\left(X_i\right) = f\left(\omega_1\left(Y_1 - Y_{1,0}\right)\right) \otimes \cdots \otimes f\left(\omega_{\mathrm{n}}\left(Y_{\mathrm{n}} - Y_{\mathrm{n},0}\right)\right) \tag{3.18}$$

$$f\left(Z_i\right) = f\left(\lambda_1\left(Y_1 - Y_{1,0}\right)\right) \otimes \cdots \otimes f\left(\lambda_{\mathrm{n}}\left(Y_{\mathrm{n}} - Y_{\mathrm{n},0}\right)\right) \tag{3.19}$$

where $\{\omega_i\}$ is the weight according to (3.12) and $\{\lambda_i\}$ is the weight according to (3.17); n is total bus number; ⊗ is the convolution symbol. Detailed convolution techniques of mixed continuous and discrete variables can be found in (Allan et al. 1981, Allan, Grigg & Al-Shakarchi 1976, Allan, da Silva & Burchett 1981).

3.1.4 Cumulants based PLF

As discrete states of nodal power variables increases, the number of convolution operation increases significantly. This increases the computation time of the PLF calculation. However, such a problem can be avoided if using cumulants based PLF method. The method performs arithmetic operation with cumulants of the stochastic variable instead of its probability density function (Zhang, Lee 2004). Take the stochastic variable $Z = X + Y$ for example. X and Y are two independent stochastic variables. The k^{th}-order cumulant of Z is equal to the sum of the k^{th}-order cumulant of X and Y. Then, the cumulants of Z can be converted to the central moments of Z (Stuart, Keith Ord 1994). Based on the central moments, the probability density function and the cumulative distribution function of Z can be approximated according to the Gram-Charlie series expansion or Cornish-Fisher series expansion (Stuart, Keith Ord 1994). The detailed implementation of using combined cumulants and Gram-Charlie series expansion for the PLF calculation can be found in (Zhang, Lee 2004).

3.1.5 Case study

The standard IEEE 14 bus test system is used to demonstrate the PLF methods. Fig. 3.1 shows the network configuration of the IEEE 14 bus system (Kodsi, Canizares 2003). The network data is summarized in (Kodsi, Canizares 2003). The probability distributions of the nodal power injections are listed in 0. In summary, the load at bus 14 is a discrete random variable with three discrete states. The distributions of the load and generation at other buses are all assumed to be Gaussian distributions. The PLF results are obtained by using three different methods: Monte Carlo simulation, convolution method and cumulants based Gram-Charlier series method. The sample size of the Monte Carlo simulation is 1000. A 6th-order Gram-Charlier series is used. Fig. 3.2 shows the probability density function of the voltage at bus 14. It is shown that the probability density function of the voltage obtained from the convolution method match the voltage from Monte Carlo simulation very well. The Gram-Charlier method is slightly worse than the convolution method, but the result also resembles the Monte Carlo results adequately.

Both the analytical methods require much shorter computation time than the Monte Carlo simulation. However, the accuracy of the results from the analytical methods is compromised. Although the difference is not significant as shown in Fig. 3.2, the error may become larger in the case of non-Gaussian and correlated nodal power variables. Furthermore, the analytical methods are not able to consider the effect of tap regulation by the tap-changing transformers. This may further increase the inaccuracy of the analytical methods. Therefore, the application of the analytical methods is limited. Moreover, for short-range and long-range power system planning, the computation time is not the main concern. Therefore, for the rest of the thesis, Monte Carlo simulation is used to obtain PLF results.

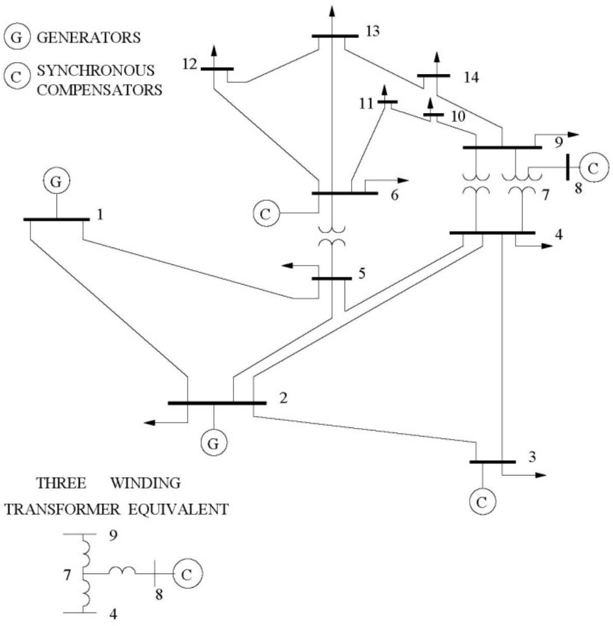

Fig. 3.1. IEEE 14 bus test system (Kodsi, Canizares 2003).

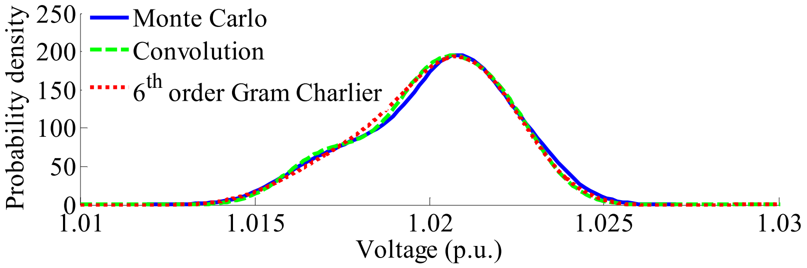

Fig. 3.2. Probability density functions of voltage at bus 14.

3.2 The effect of temporal correlation on PLF calculations

As discussed in Chapter 2, one of the important characteristics for the modeling of stochastic generation and load is the temporal correlation. The temporal correlation is accounted for in the time series simulation of the stochastic models. These time series of the stochastic generation and load are the inputs to the Monte Carlo based PLF algorithm, which also provides the time series outputs of bus voltage and network power flow. Nevertheless, the characteristic of interests of the voltage and power flow is their probability distribution, not the temporal correlation. This seems to indicate that although the temporal correlation is of importance for simulating stochastic generation and load, it may not be of importance for performing PLF calculations. In other words, as long as the probability distributions of stochastic generation and load are considered, accurate voltage and power flow results can be obtained. This may be the case for some certain power networks. However, this is not the case for a power system that contains time-dependent parameters, such as the tap position of tap-changing transformers and the capacitor status of switchable capacitor banks. The following subsections illustrate the importance of the temporal correlation in PLF calculations.

3.2.1 Time-dependent feature of tap adjustment

In a standard load flow calculation, a tap-changing transformer is represented by a π–model as shown in Fig. 3.3 (Saadat 2002). The π–model shows that as the tap ratio p is adjusted, both the series and the shunt impedance of the model will change. This change modifies both the diagonal and off-diagonal elements of the admittance matrix at the corresponding buses. In this way, the tap adjustment of the transformer affects the load flow results.

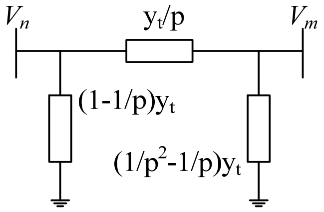

Fig. 3.3. π–model of a tap-changing transformer.

For the system operation of N consecutive hours, the system load flow at hour t can be expressed as:

$$\mathbf{Y}(t) = \mathrm{g}\left(\mathbf{X}(t), \mathbf{p}(t)\right), \tag{3.20}$$

where $t \in \mathbf{T}$; $\mathbf{T}=[1, 2, ..., \mathrm{N}]$; $\mathbf{Y}$ is the vector of nodal power injections and $\mathbf{X}$ is the vector of system states; $\mathbf{p}$ is the vector of tap ratio of the tap-changing transformers in the system.

The tap ratio (position) of a tap-changing transformer can be regulated through two modes: the voltage control mode and the line drop compensation mode (Willis 1997). In the following analysis, the voltage control mode is assumed. However, similar analysis can also be conducted for the line drop compensation mode.

For the k^{th} tap-changing transformer, the tap position at hour t remains the same as at hour $t-1$ if the controlled voltage is within the regulation range. However, the tap position is adjusted if the controlled voltage is outside the regulation range. This can be expressed as:

$$\mathrm{p}^k(t)=\begin{cases}\mathrm{p}^k(t-1)+\Delta\mathrm{p}^k, & V^k(t)<V_{\min}^k\\ \mathrm{p}^k(t-1), & V_{\min}^k\le V^k(t)\le V_{\max}^k\\ \mathrm{p}^k(t-1)-\Delta\mathrm{p}^k, & V^k(t)>V_{\max}^k\end{cases}, \tag{3.21}$$

where V is the controlled voltage and $[V_{\min}, V_{\max}]$ is the voltage regulation range of the tap-changing transformer. The time dependence of the tap ratio can be seen in (3.21).

In a Monte Carlo simulation of the stochastic generation and load, if the temporal correlation is not considered, an unbiased random sampling can be carried out to generate a sample of the stochastic generation and load from their empirical probability distributions. Alternatively, the random sample can be obtained directly from the measurements according to (3.2). In any case, the individuals in the sample are independent of each other. For the ease of illustration, a random sample of size n is generated according to (3.2). In other words, a random number vector $\mathbf{R} = [r_1, \ldots, r_{\mathrm{n}}]$ is generated to represent the n randomly selected hours from the total N hours.

Given such a random sample, a Monte Carlo based PLF can be performed. Similar to (3.21), the tap ratio at hour r_i of the k^{th} transformer in the Monte Carlo simulation is implemented as:

$$\mathrm{p}_{\mathrm{mc}}^k(r_i)=\begin{cases}\mathrm{p}_{\mathrm{mc}}^k(r_{i-1})+\Delta\mathrm{p}^k & V^k(r_i)<V_{\min}^k\\ \mathrm{p}_{\mathrm{mc}}^k(r_{i-1}), & V_{\min}^k\le V^k(r_i)\le V_{\max}^k\\ \mathrm{p}_{\mathrm{mc}}^k(r_{i-1})-\Delta\mathrm{p}^k & V^k(r_i)>V_{\max}^k\end{cases}, \tag{3.22}$$

where 'mc' indicates the Monte Carlo simulation and $r_i \in \mathbf{T}$.

Equation (3.22) is very similar to (3.21), but there is a major difference between the two equations. Assume that $r_i = t$, i.e. the randomly selected hour r_i is the t^{th} hour in the original measured time series. Then, the tap ratio $\mathrm{p}_{\mathrm{mc}}^k(r_i)$ will be the same as $\mathrm{p}^k(t)$ if $\mathrm{p}_{\mathrm{mc}}^k(r_{i-1})$ is equal to $\mathrm{p}^k(t-1)$. However, this is usually not the case as $r_{i-1} \neq t-1$ due to the random sampling of the Monte Carlo simulation. In other words, it may be the case that:

$$\mathrm{p}_{\mathrm{mc}}^{k}\left(r_{i-1}\right) \neq \mathrm{p}^{k}\left(t-1\right). \tag{3.23}$$

If (3.23) is true, the load flow results obtained from the Monte Carlo simulation will differ from the measurements. In other words, a Monte Carlo simulation with random sampling may provide inaccurate load flow results as the time sequence or the temporal correlation of the stochastic generation and load is not taken into account. This can be further demonstrated through the simulation results carried out on a distribution system described below.

3.2.2 Network and data set description

Fig. 3.4 shows a simplified network configuration based on the 20 kV Størvring distribution system. On the STKV feeder, there is one CHP plant with three generator units, each rated 3 MW. On the SØRP feeder, there are three fixed-speed WTs connected at the end of the feeder. The loads at SØRP are connected to bus 11, 13 and 14. Other feeders connected to the substation are represented by the aggregated load 'REST'.

Both the 150/60 kV and the 60/20 kV transformers are tap-changing transformers with the tap mounted at the low-voltage side. The set points of the two transformers are 60.2 kV (1.0033 p.u.) and 20.5 kV (1.025 p.u.), respectively. The 150/60 kV transformer has 13 tap steps, with maximum 4 steps above and 8 steps below its reference position. The 60/20 kV transformer has 21 tap steps, with maximum 11 steps above and 9 steps below its reference position. The tap steps are both 0.0166 p.u. According to the actual operation, the tap of the 60/20 kV transformer normally adjusts 1 or 2 times a day at most.

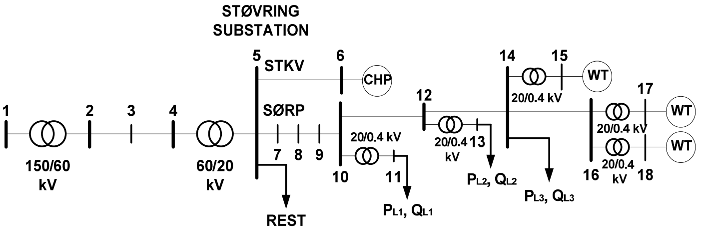

Fig. 3.4. Network configuration of Støvring Substation.

The hourly load measurements (both active and reactive power) from July 01, 2006 to January 31, 2007 are available. In addition, the hourly CHP measurements at the STKV feeder and the hourly wind power measurements at the SØRP feeder are also available. These hourly data are average data of each hour and the measurements are synchronized at the different locations.

Fig. 3.5 shows the empirical probability distributions of the measured data of: (a) CHP generation at STKV feeder, (b) total WPG at SØRP feeder, and (c) total load demand at SØRP feeder. The probability distributions are shown for both the summer and winter season. For the CHP generation and the load, the probability distribution of a weekday and of a weekend is also shown.

Furthermore, in the following analysis, the accuracy of the voltage magnitude is examined. This is because the tap regulation has a direct impact on the bus voltage magnitude. The measured bus voltage should be used as reference for verifying the Monte Carlo results. However, a direct voltage measurement is not available for the case network. Therefore, the reference voltage results are extrapolated by performing load flow calculations with all the power measurements input in chronological order. Consequently, the extrapolated voltage results are used as reference for examining the accuracy of the PLF results from Monte Carlo simulation.

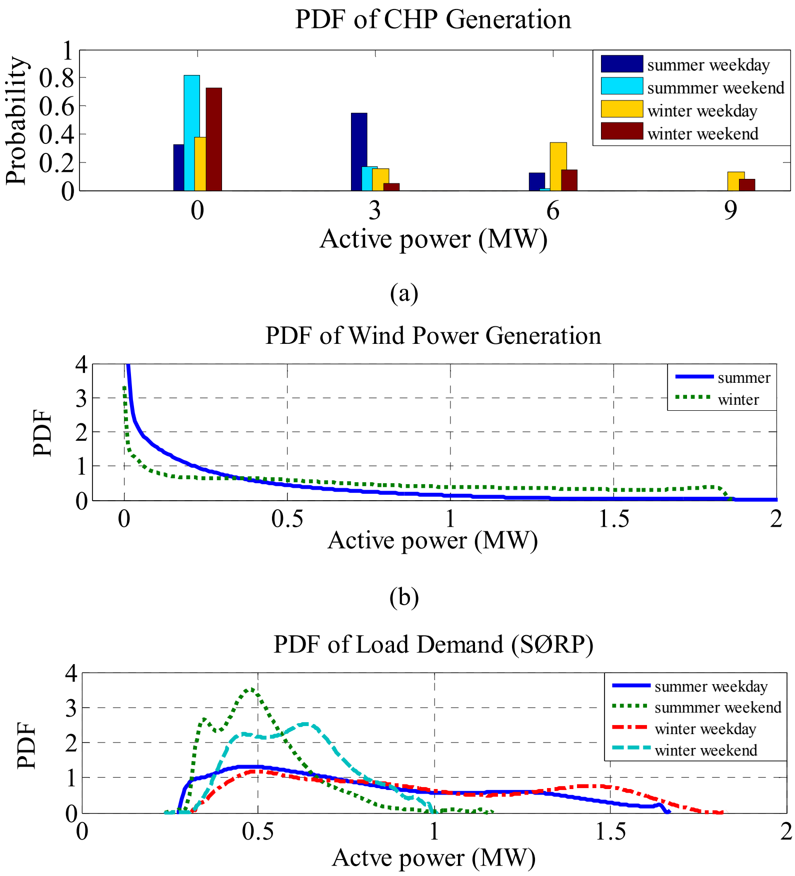

(a)

(b)

(c)

Fig. 3.5. Empirical probability density function of: (a) CHP generation, (b) wind power generation, and (c) SØRP load demand.

3.2.3 Monte Carlo based PLF using simple random sampling

a) Random sampling of nodal power injections

Fig. 3.6 shows the cumulative distribution function of the SØRP load in a summer weekday, both from the measurements and the random sampling. The size of the random sample is 600. As shown in the figure, the cumulative distribution function of the random sample matches that of the measurements very well.

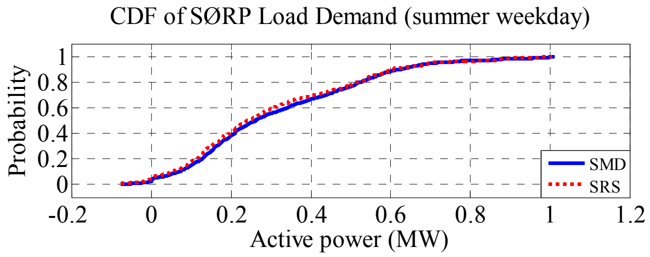

Fig. 3.6. cumulative distribution function of SØRP load demand in summer weekday: measurement data (solid curve) and random sampling (dotted curve).

In order to evaluate the accuracy of the random sampling with respect to the measurements, a 95% confidence interval is used to assess the mean and standard deviation of the random sample. For example, if the 95% confidence interval for the mean of the random sample contains the mean of the measurements, then the accuracy of the random sampling is considered sufficient. In this case, the mean of the measured SØRP load is 0.3180 MW and the standard deviation is 0.2265 MW. Furthermore, the 95% confidence interval can be calculated by drawing one hundred random samples, each of size 600. Such an approach of calculating 95% confidence interval is a typical bootstrap method (Chernick 2008). As a result, the 95% confidence interval for the mean of the random sample is [0.2968, 0.3377] MW and the interval for the standard deviation is [0.2169, 0.2365] MW. Both confidence intervals contain the corresponding measured values. This indicates that the random sampling is an accurate representation of the measurements.

In addition, it is better to use cumulative distribution function instead of probability density function to compare the random sample and the corresponding measurements. This is because the sample size and the measured data size are different. Furthermore, the empirical probability density function varies greatly as the number of bins changes, while the empirical cumulative distribution function is much less affected by the number of bins chosen.

b) Monte Carlo simulation with fixed-tap transformer

In this case, it is assumed that both tap-changing transformers in Fig. 3.4 have fixed taps. This assumption is to show the accuracy of a Monte Carlo based PLF when the system does not involve tap regulation. In the next subsection, the case with tap-changing transformers will be shown.

Fig. 3.7 shows the probability density function of the extrapolated voltage results at bus 5 in a summer weekday. The voltage results are obtained by performing load flow calculations with the nodal generation and load measurements in chronological order.

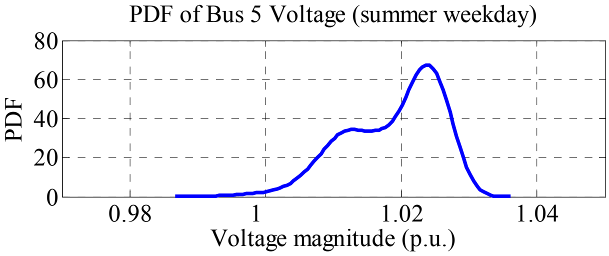

Fig. 3.7. probability density function of extrapolated voltage results at bus 5 in a summer weekday with fixed-tap transformers.

Fig. 3.8 shows the flow chart of the Monte Carlo based PLF. In this case, the tap adjustment is not implemented. The length of the Monte Carlo simulation is 600. As shown in Fig. 3.8, power data at the same hour is selected for different buses. This is to keep the cross-correlation among the generation and load at these buses.

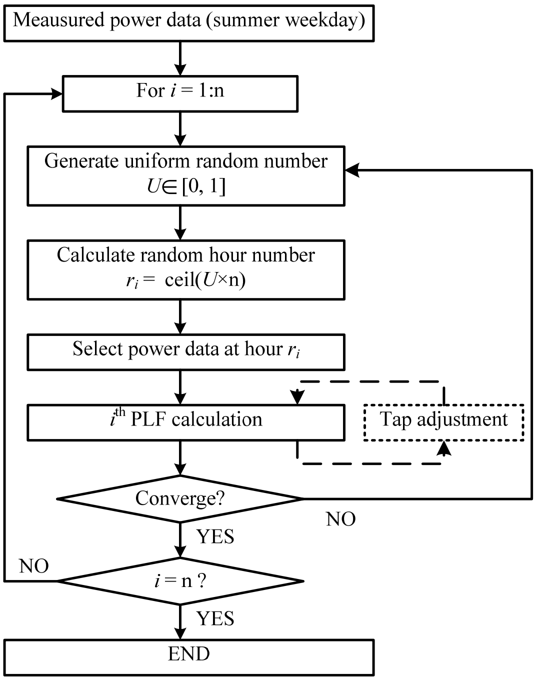

Fig. 3.8. Flow chart of Monte Carlo based PLF algorithm.

The Monte Carlo based PLF is carried out on the Støvring distribution system. Fig. 3.9 shows the cumulative distribution function of the voltage at bus 5 in a summer weekday obtained from the Monte Carlo simulation (dotted line denoted by SRS). For comparison, the cumulative distribution function of the extrapolated voltage measurements (solid line denoted by SMD) are also shown in the figure. The probability distribution from the Monte Carlo simulation matches very well with the measurements. This indicates that the Monte Carlo simulation with random sampling provide accurate PLF results.

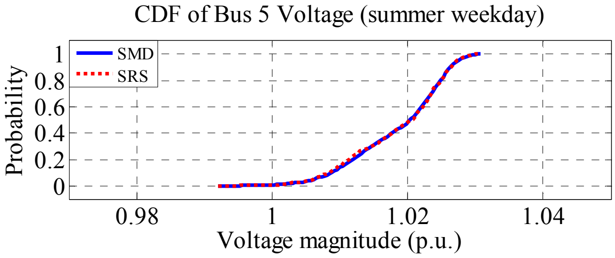

Fig. 3.9. cumulative distribution function of voltage at bus 5 in a summer weekday with fixed-tap transformers: extrapolated measurements (SMD) and Monte Carlo results with simple random sampling (SRS).

In order to obtain the 95% confidence interval of bus voltages, the Monte Carlo based PLF shown in Fig. 3.8 is performed for one hundred times. Table 3.1 summarizes the 95% confidence intervals of the mean and standard deviation of the voltage at bus 5 in a summer weekday. Both the 95% confidence intervals contain the corresponding measured value. This further verifies the accuracy of the Monte Carlo simulation. Similar results are observed for the summer weekend, winter weekday and winter weekend.

Table 3.1
95% confidence interval of mean and standard deviation of bus 5 voltage (in per unit) in summer weekday with fixed-tap transformer

	Measurement by extrapolation (fixed-tap)	PLF using SRS (fixed-tap)
μ	1.0188	[1.0182, 1.0193]
σ	0.0070	[0.0065, 0.0073]

Note: μ is mean value; σ is standard deviation

It is worth mentioning that the obtained extrapolated measured voltage is not validated against the actual measurements. However, this does not disprove the above analysis and results as the main purpose here is to show how a tap-changing transformer can affect the Monte Carlo based PLF results.

c) Monte Carlo simulation with tap-changing transformer

In this case, both the 150/60 kV and 60/20 kV transformers have the tap regulation as in the actual operation. The Monte Carlo based PLF is simulated according to Fig. 3.8, with the tap adjustment implemented as (3.22).

Fig. 3.10 shows the probability density function of the extrapolated voltage results at bus 5 in a summer weekday. The mean value of the voltage is around the reference value (1.025 p.u.) and the voltage is regulated within [1.084, 1.0416] p.u. The probability distribution of the voltage is fairly symmetrical with respect to the mean value. This is different from the case in Fig. 3.7 when the transformer has no automatic tap regulation. In summary, the voltage shown in Fig. 3.10 is used as reference to verify the Monte Carlo based PLF results in this case.

A Monte Carlo simulation is carried out according to Fig. 3.8 to obtain the PLF results. Fig. 3.11 shows the cumulative distribution function of the controlled voltage at bus 5 in a summer weekday obtained from the Monte Carlo simulation (dotted line denoted by SRS). For comparison, the cumulative distribution function of the extrapolated voltage measurements (solid line denoted by SMD) are also shown in the figure. Unlike the one shown in Fig. 3.9, there is an obvious shift (or bias) of the PLF results from the measurements. The main reason is that the tap position $p_{mc}(r_{i-1})$ from the Monte Carlo simulation at hour r_{i-1} is not always the same as the tap position $p(t-1)$ from the measurements at hour $t-1$. This difference between $p_{mc}(r_{i-1})$ and $p(t-1)$ leads to the discrepancy between $p_{mc}(r_i)$ and $p(t)$. Fig. 3.12 shows the probability of the discrepancy in tap position, which occurs for more than 40% of the time in total.

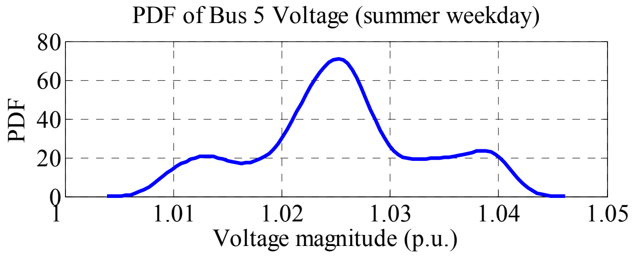

Fig. 3.10. Probability density function of extrapolated voltage results at bus 5 in a summer weekday with tap-changing transformers.

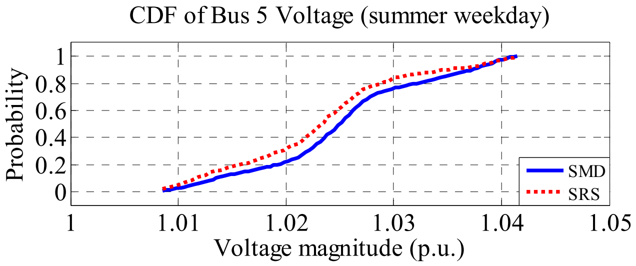

Fig. 3.11. cumulative distribution function of voltage at bus 5 in a summer weekday with tap-changing transformers: extrapolated measurements (SMD) and Monte Carlo results with simple random sampling (SRS).

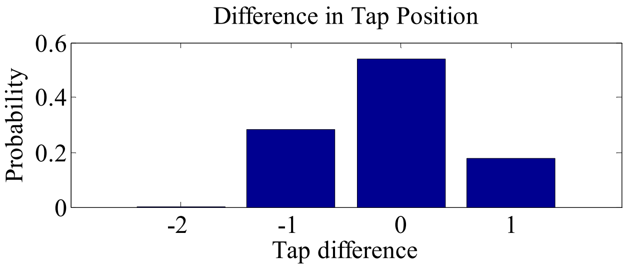

Fig. 3.12. The difference between the tap position in Monte Carlo simulation $p_{mc}(r_i)$ and the tap position from the extrapolated measurement $p(t)$.

Table 3.2 summarizes the 95% confidence intervals of the mean and standard deviation of the voltage at bus 5 in a summer weekday. The confidence interval of the mean does not contain the measured value. This corresponds to the shift in probability distribution observed in Fig. 3.12. In contrast, the 95% confidence interval of the standard deviation contains the measured value. This is mainly due to the fixed voltage regulation range of the tap-changing transformer. Therefore, it is demonstrated that, with automatic tap regulation, the Monte Carlo simulation with random sampling provides inaccurate PLF results.

Table 3.2
95% confidence interval of mean and standard deviation of bus 5 voltage (in per unit) in summer weekday with tap-changing transformer

	Measurement *(tap-changing)*	PLF using SRS (tap-changing)
μ	1.0253	[1.0223, 1.0247]
σ	0.0079	[0.0074, 0.0084]

In order to improve the PLF results, the time sequence or the temporal correlation of the stochastic generation and load needs to be considered. For this purpose, the stochastic models developed in Chapter 2 can be used in this case to account for the temporal correlation. This is a parametric approach, which is based on the models developed from the data. The following subsection proposes a simple nonparametric approach to include the temporal correlation in the random sample so that accurate PLF results can be obtained.

3.2.4 Monte Carlo based PLF using time-sequential sampling

As the inaccurate PLF results are caused by the incorrect tap positions, additional information of the tap regulation is needed. As shown in Fig. 2.8 (a), the tap position has a strong hourly variation in a day. This is mainly due to the diurnal variation of the load and CHP generation. Therefore, it is important to keep such a diurnal variation when we sample from the empirical probability distribution of the measurements. To address this issue, a different random sampling method is shown in Fig. 3.13, where ‘H’ stands for hour and ‘nx’ is the sample size of each hour. The method is referred to as time-sequential sampling. The time-sequential sampling first sorts the sample in hourly order. Then, a sample of size nx is generated for each hour. Finally, the sample in the hourly order is re-arranged into the time-sequential order. In this way, the diurnal variation of the stochastic generation and load are reflected in the final sample. A special case of the time-sequential sampling is to sample a random day at a time instead of a random hour.

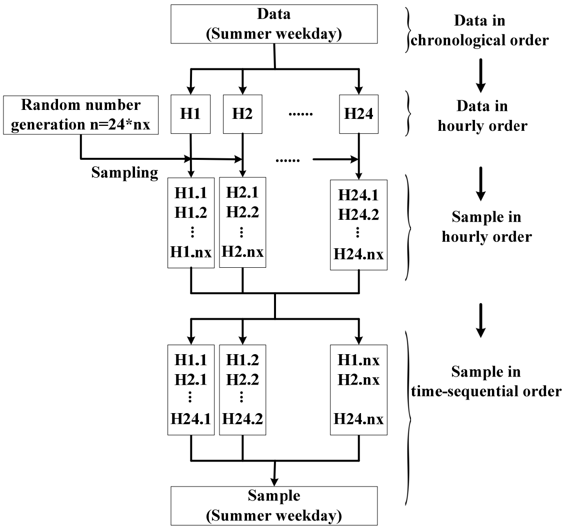

Fig. 3.13. Principle of time-sequential sampling.

According to Fig. 3.13, a sample of size 600 is obtained by sampling 25 random days. Given the sample, a Monte Carlo simulation is performed to obtain the PLF results. Fig. 3.15 shows the cumulative distribution function of the controlled voltage at bus 5 in a summer weekday obtained from the Monte Carlo simulation using time-sequential sampling (dotted line denoted by TSS). The shift in probability distribution observed in Fig. 3.12 is eliminated in Fig. 3.15. The improvement of the PLF results can be further explained by the difference of the tap position shown in Fig. 3.15. The figure indicates that for more than 90% of the cases, the tap position in the Monte Carlo simulation is the same as in the measurements.

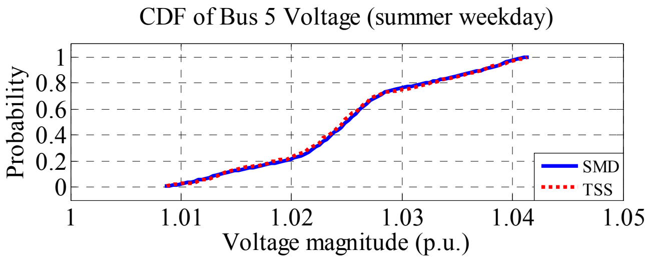

Fig. 3.14. cumulative distribution function of voltage at bus 5 in a summer weekday with tap-changing transformers: extrapolated measurement (SMD) and Monte Carlo simulation with time-sequential sampling (TSS).

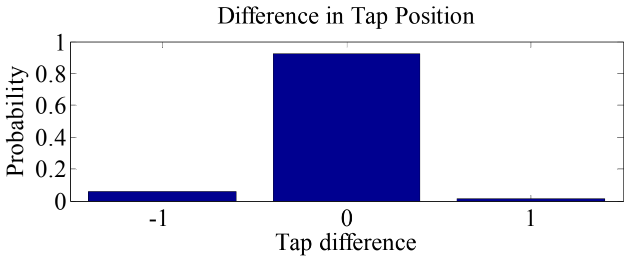

Fig. 3.15. The difference between the tap position in Monte Carlo simulation with time-sequential sampling $p_{mc}(r_i)$ and the tap position from the extrapolated measurement $p(t)$.

Fig. 3.16 shows the 95% confidence interval of the hourly mean value of the voltage at bus 5 in a summer weekday. Fig. 3.16 (a) is the result using the simple random sampling and Fig. 3.16 (b) is the result using time-sequential sampling. It is clearly shown that using the time-sequential sampling, the 95% confidence interval captures the hourly mean of the measurements very well, while it is not the case if using the simple random sampling. This further illustrates the importance of temporal correlation of stochastic generation and load in the Monte Carlo based PLF calculation.

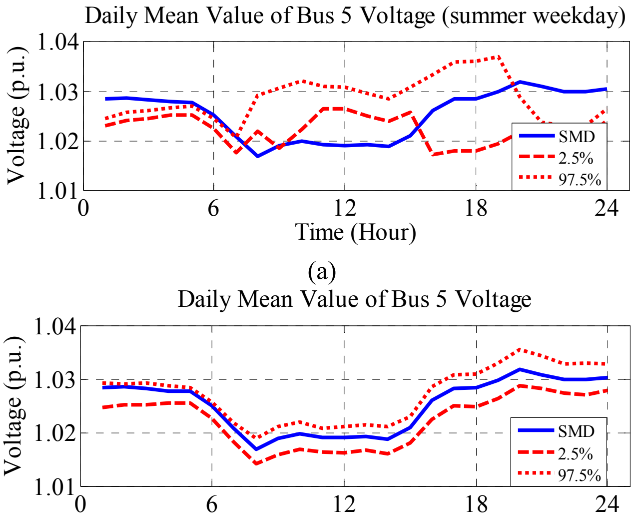

(a)

(b)

Fig. 3.16. 95% confidence interval of diurnal mean of voltage at bus 5 in a summer weekday with tap-changing transformer: (a) simple random sampling (b) time-sequential sampling.

3.3 Summary

This chapter is divided into two parts. The first part has discussed two main approaches for PLF analysis: the numerical approach and the analytical approach. The numerical approach is based on Monte Carlo simulation, while the analytical approach is based on the convolution method and the cumulants method. Both analytical methods are tested on the IEEE 14 bus system. The Monte Carlo simulation is used as reference to validate the simulation results from the analytical methods. The results show that both the convolution method and the cumulants method provide an accurate approximation to the Monte Carlo results in this case. However, in the case of non-Gaussian and correlated nodal power variables, the error of both analytical methods is expected to be larger. The second part of the chapter demonstrates the effect of temporal correlation in stochastic generation and load on a Monte Carlo based PLF calculation. It is observed that the tap position of the tap-changing transformer is time-dependent. The tap position may not be correct if the temporal correlation in stochastic generation and load is neglected. This also indicates that stochastic generation and load cannot be simply modeled by their probability distributions. Stochastic models that capture both the temporal correlation and the probability distribution are required in order to obtain accurate PLF results.

Chapter 4

Stochastic Optimization of Wind Turbine Power Factor

This chapter first presents the motivation of finding optimal WT power factors under the context of a short-range system planning, i.e. at the time scale of one year in this case. Then, it formulates the optimal WT power factor setting as a stochastic optimization problem. The procedures of the stochastic optimization are demonstrated using a modified 69-bus distribution network. In the end, the optimization results are provided and the corresponding economic benefits are evaluated regarding the optimal setting of the WT power factor.

4.1 Motivation

In order to fully utilize potential benefits and to minimize adverse impacts of WPG, many research efforts have been devoted to exploring the technical and economic contribution of wind power in power systems (Ackermann 2005). Due to their dispersed locations in distribution systems, WTs can be used to provide local reactive power consumption. This decreases the reactive power flow from the main grid and thus increases the active power transfer capacity of substation transformers. The reduced reactive power flow also brings down active and reactive power losses in distribution systems. The reduction of active power losses depletes the network operating costs without extra investment. Furthermore, the increase in transformer power transfer capacity may defer network expansion. All these benefits can be obtained by network operators if they have access to the power factor setting of the WTs. However, this is usually not the case if the network operators are not the owner of the WTs. On the other hand, the power factor setting of WTs are accessible to WT owners, although they may not be willing to change the setting unless there is an economic incentive to do so. In other words, WT owners may be motivated to change the power factor setting upon the request of network operators, if the network operators share the obtained economic benefits with WT owners. Thus, for the sake of mutual benefits, it is necessary to estimate the power losses in advance that may be reduced by the WT power factor setting and to quantify the corresponding economic benefits in the long run.

In order to evaluate such economic benefits, the capability of WTs to provide reactive power generation should be evaluated first. In other words, the power factors of WTs should be set at certain optimal values instead of at unity value in order to minimize power losses. Nevertheless, this optimal setting is strongly affected by the WPG and the load demand in the network. As both WPG and load demand vary stochastically, a stochastic optimization is required to find the optimal setting that adapts to the stochastic behavior of the system power flow for a certain period. Such a stochastic optimization entails the stochastic models of WPG and load demand developed in Chapter 2.

4.2 Optimization formulation

This section illustrates the stochastic optimization algorithm used to design the power factor setting of WTs by taking into account the stochastic behavior of WPG and load demand.

Normally, grid-connected WTs are controlled to have a unity power factor. For fixed-speed WTs without power-electronic controllers, unity power factor is achieved by switching on/off capacitor banks. For variable-speed WTs with power-electronic controllers, unity power factor can be controlled by the grid-side voltage source converter. There are several reasons to set WT power factor to unity. First, a unity power factor minimizes current flow and thus converter losses. Second, active power transfer capacity is maximized with no reactive power flow through the converter. However, from the network's perspective, WT power factor can be designed to minimize the power losses of the network. The reduced power losses lower the network operating cost for network operators.

However, system power losses vary due to the stochastic behavior, the seasonal variation, and the diurnal variation of WPG and load. Therefore, a stochastic optimization based on Monte Carlo simulation is adopted to minimize the overall system power losses. In order to account for the seasonal variation, the optimization process is divided into four main periods, which are a summer weekday, a summer-weekend day, a winter weekday and a winter-weekend day. To take into consideration the diurnal period, each period is further grouped into 24 hours. Therefore, for each of the four periods, the objective of the stochastic optimization is to minimize the expectation of the total active power losses of the network at hour *t*, P_L^t, with respect to the power factor angle $\boldsymbol{\varphi}^t$ of the WTs:

$$\min \ \mathrm{E}\left[P_L^t\left(\boldsymbol{\varphi}^t, \mathbf{P}_{WT}^t, \mathbf{P}_D^t\right)\right], \qquad \text{for } t = 1, 2, ..., 24, \tag{4.1}$$

where E[ ] is to take the expectation of; $\boldsymbol{\varphi} = [\varphi_1, \varphi_2, \ldots, \varphi_n]$ is the vector of WT power factor angle; n is the total number of WTs; $\mathbf{P}_{WT}^t$ is the vector of active WPG at hour *t*; $\mathbf{P}_D^t$ is the vector of active load demand at hour *t*. The load power factor is assumed constant.

$\boldsymbol{\varphi}^t$ consists of n deterministic variables, while $\mathbf{P}_{WT}^t$ contains n stochastic variables and $\mathbf{P}_D^t$ contains d stochastic variables. As P_L^t is a function of $\mathbf{P}_{WT}^t$ and $\mathbf{P}_D^t$, P_L^t is also a stochastic variable. However, due to the non-Gaussian distribution of $\mathbf{P}_{WT}^t$ and the nonlinear loss function $P_L^t(\,)$, it is not straightforward to evaluate the expectation of P_L^t analytically. Therefore, Monte Carlo simulations are adopted to evaluate the objective function (4.1). Such a Monte Carlo simulation calls for stochastic models that provide random samples of WPG and load demand.

The above objective function is subjected to the following four constraints:

$$\varphi_{\min} \le \varphi_i^t \le \varphi_{\max}, \qquad \text{for } i = 1, 2, ..., \text{n}, \tag{4.2}$$

$$\mathrm{P}\left(V_j^t > V_{\max}\right) \le 2.5\%, \qquad \text{for } j = 1, 2, ..., \text{J}, \tag{4.3}$$

$$\mathrm{P}\left(V_j^t < V_{\min}\right) \le 2.5\%, \qquad \text{for } j = 1, 2, ..., \text{J}, \tag{4.4}$$

$$\mathrm{P}\left(I_k^t > I_{k,\max}\right) \le 5\%, \qquad \text{for } k = 1, 2, ..., \text{K}. \tag{4.5}$$

where P( ) denotes the probability of; J is the total number of buses and K is the total number of branches. Equation (4.2) sets the lower ($\varphi_{\min}$) and upper ($\varphi_{\max}$) limits of WT power factor angle. Equation (4.3) specifies that the probability of overvoltage at bus j at hour t should be lower than 2.5%. Equation (4.4) specifies that the probability of undervoltage at bus j at hour t should be lower than 2.5%. Consequently, V_j^t is within the voltage limits at a probability of 95% or higher. Such probability constraints are in accordance with the requirements specified by the European Standard for Voltage Characteristics of Electricity Supplied by Public Distribution Systems (EN 50160 1999). Equation (4.5) states that the probability of overcurrent of branch k at hour t should be lower than 5%. In other words, I_k^t is lower than the current limit of that branch $I_{k,\max}$ at a probability of 95% or higher. The probability constraints of bus voltage and line current are further illustrated in Fig. 4.1.

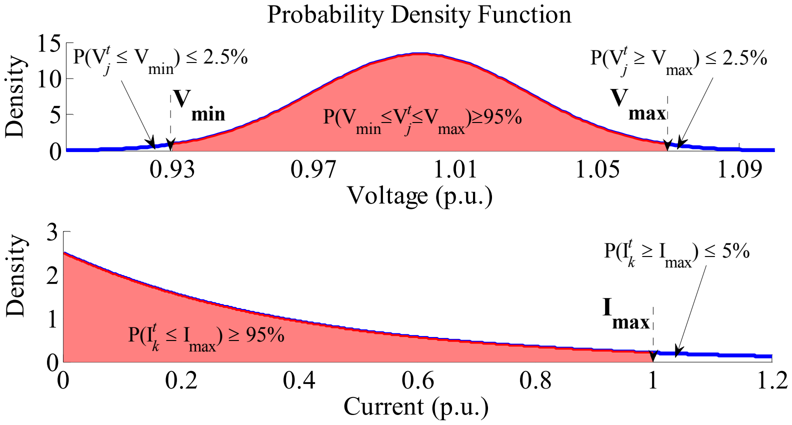

Fig. 4.1. Probability constraints of bus voltage and line current.

The foregoing formulation based on (4.1)-(4.5) is a nonlinear constrained stochastic optimization problem. Therefore, a sequential quadratic programming implemented in the optimization toolbox of MATLAB (Mathworks 2009) is combined with the Monte Carlo simulation to find the optimal solution. For the sequential quadratic programming, each optimization iteration consists of three steps. The first step is to calculate the Hessian of the Lagrange function. The Hessian is approximated by the gradient of the Lagrange function at two points. Then, the second step is to form a quadratic programming subproblem and solve it for the search direction and Lagrange multipliers. The third step is to obtain a proper step size by minimizing a descent function. Based on the search direction and the step size, the design variables can be updated. These three steps are repeated until stopping criteria are reached. A detail procedure of the sequential quadratic programming is provided in (Arora 2004).

Fig. 4.2 shows the flow chart of the stochastic optimization algorithm for each of the four periods. The algorithm mainly consists of three parts: time series simulation, load flow calculation using Monte Carlo simulation, and nonlinear constrained optimization by sequential quadratic programming. The stop criteria of the optimization include first-order optimality measure (e.g. the gradient of the objective function) and maximum number of iterations (Mathworks 2009).

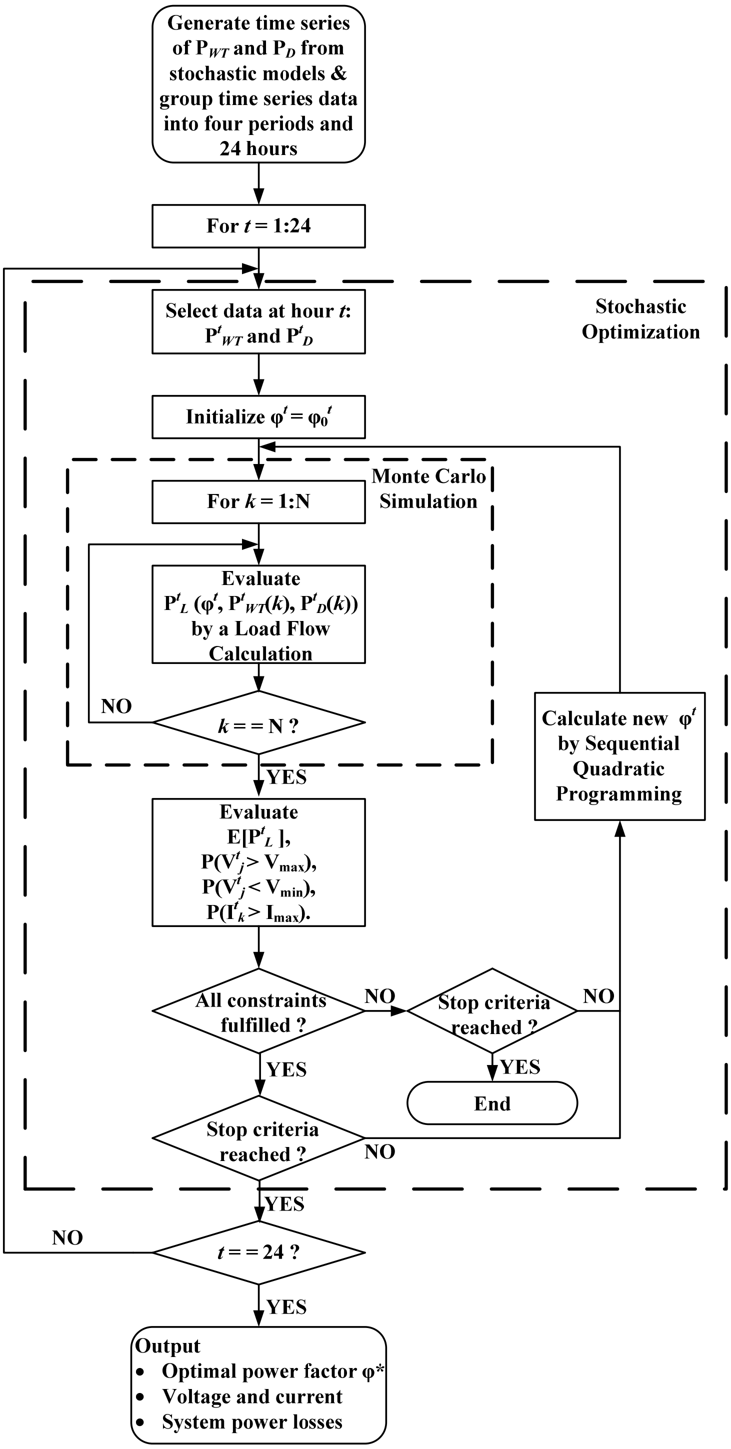

Fig. 4.2. Flow chart of the stochastic optimization algorithm for each of the four periods.

The optimization procedure is summarized as follows:

1) Simulate wind power and load time series using stochastic models and group the data into four periods with each period further grouped into 24 hours. For each period,
2) Initialize WT power factor $\boldsymbol{\varphi}^t$ at hour t,
3) For each group of the data and given $\boldsymbol{\varphi}^t$, perform Monte Carlo simulation of length N to obtain load flow results,
4) Evaluate the objective function and the probabilistic constraints based on the Monte Carlo simulation.
5) If the stop criteria are not reached, updates the WT power factor values $\boldsymbol{\varphi}^t$ by the sequential quadratic programming algorithm, and then go to step 3),
6) If any stop criterion is reached, terminate optimization at hour t. If t is less than 24, $t = t + 1$ and go to step 2). Otherwise, output optimization results.

When one stop criterion is reached but not all the constraints are fulfilled, the optimization algorithm fails to find a feasible solution. In this case, several means may be used to solve the problem. One is to modify the stop criteria by increasing the maximum number of iterations. Another one is to relax one of the constraints, such as widening the range of power factor angle specified in (4.2).

4.3 System description

This section describes the distribution system and data that are used to demonstrate the stochastic optimization problem formulated in section 4.2 for the optimal setting of WT power factors.

4.3.1 Case network

The case network is modified on the basis of a 69-bus radial distribution system (Das 2006). The modification consists of adding one 33/11 kV substation transformer and five WTs to the distribution system. The configuration of the case network is shown in Fig. 4.3, with the network data provided in (Das 2006). The case network has 70 buses in total. The capacity of the substation transformer is 12 MVA. The transformer is tap-regulated, with the voltage magnitude at the low-voltage side controlled within [1, 0.9833] p.u. There are in total 13 tap positions, with maximum six steps above and six steps below the tap reference position. One tap step adjusts voltage by 0.0167 p.u. The voltage limits of all buses are set to ±7% of the nominal value (11 kV), i.e. $V_{\max} = 1.07$ p.u. and $V_{\min} = 0.93$ p.u. The current limit of all lines is 157A.

The network is divided into two areas. Area A consists of feeder F1 and F2 and area B consists of feeder F3 and F4. The two areas are located close to each other. Therefore, the cross-correlation of WPG between area A and area B is very strong.

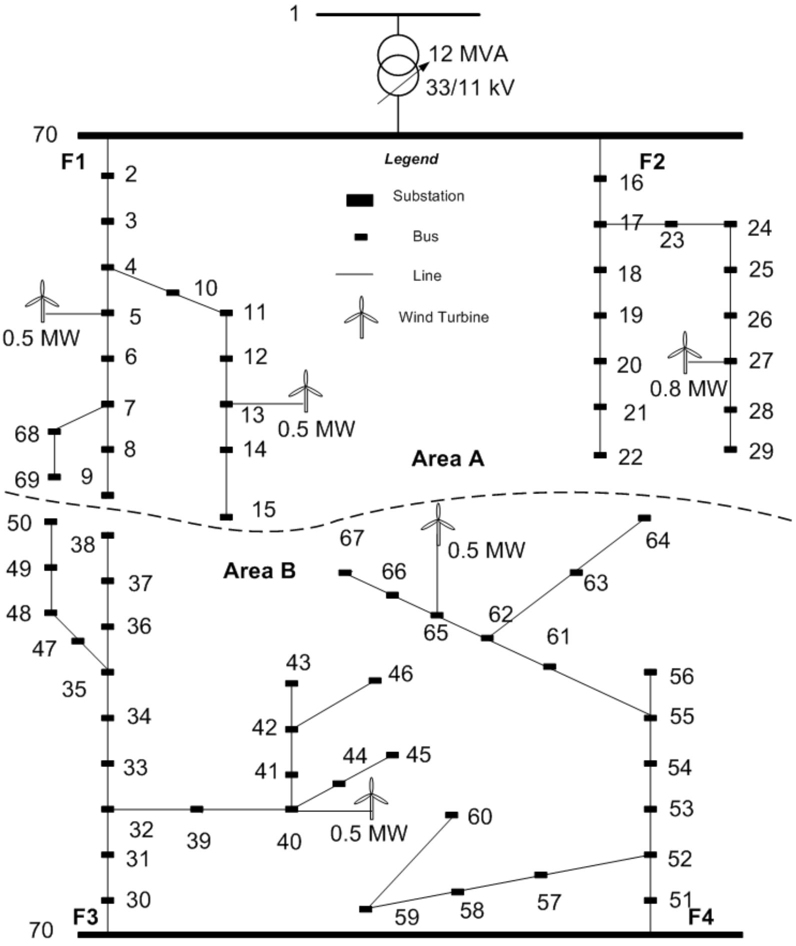

Fig. 4.3. The case network modified from the 69-bus distribution system (Das 2006).

4.3.2 Wind power data

As shown in Fig. 4.3, there are in total five WTs connected to the network, with three WTs in area A (bus 5, 13 and 27) and two WTs in area B (bus 40 and 65). The WT connected at bus 5, 13, 40 and 65 has a capacity of 0.5 MW, while the WT connected at bus 27 is rated 0.8 MW. The WPG from the three WTs in area A is assumed to be fully correlated with each other. The full correlation is also assumed to the

WPG from the two WTs in area B. Due to the close geography of area A and area B, WPG in area A is strongly correlated with WPG in area B. Such a strong cross-correlation is simulated using the bivariate-LARIMA model presented in section 2.1.6. In order to account for the seasonal variations, the bivariate-LARIMA model is developed for the summer and winter period individually. The corresponding model parameters for the summer and winter period are summarized in 0. On the basis of the model, bivariate wind power time series are simulated for a length of five years (43800 data points) for Monte Carlo simulations. Fig. 4.4 (a) shows the simulated bivariate wind power time series for a period of two weeks.

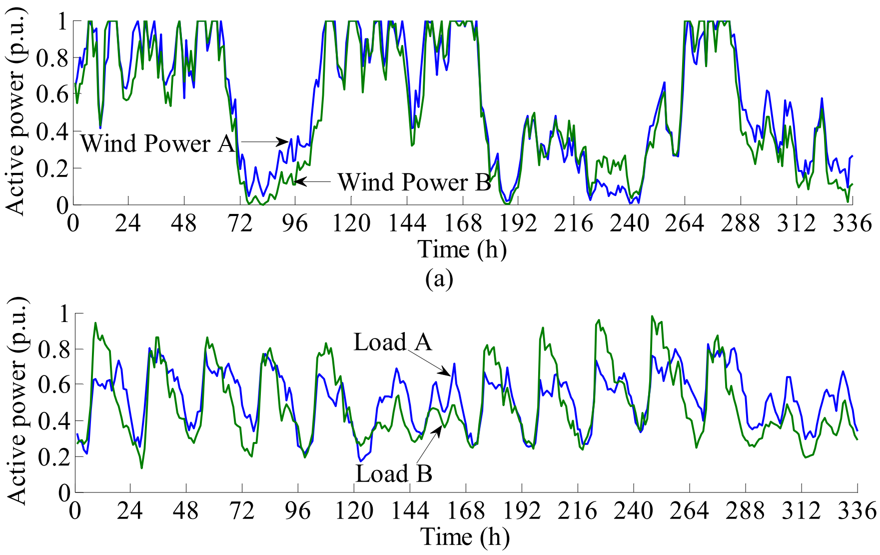

(a)

(b)

Fig. 4.4. Simulated time series of two weeks: (a) wind power generation, (b) load.

4.3.3 Load data

Load is connected to all the buses from bus 2 to bus 69. The peak load data at each bus are given in (Das 2006). The total peak load of the network is (2.90 + j1.99) MVA. Full correlation is assumed to the loads in area A and is also assumed to the loads in area B. However, the loads in area A are not fully cross-correlated with the loads in area B, although they are strongly cross-correlated. The strong cross-correlation of the load in area A and the load in area B are caused by the diurnal period of the load as well as the similar temperature in the two areas. The load model developed in section 2.2 is adopted for the simulation here. The model is based on an AR process and takes into account the seasonal variation, weekday/weekend and diurnal period of loads. Similarly, two load time series are simulated for a length of five years for Monte Carlo simulations. Fig. 4.4 (b) shows the two simulated load time series for a period of two weeks. The power factors of the loads are assumed time-invariant as provided in (Das 2006).

4.4 Simulation results and discussions

This section first presents the simulation results of the stochastic optimization of WT power factor. Then, the economic benefits of the optimal power factor setting are evaluated.

4.4.1 Optimal wind turbine power factor setting

Many countries, such as Denmark, Germany and the UK, specify power factor or reactive power generation requirement for grid-connected WTs (UNIFLEX PM 2007). The requirement varies from one country to another. For example, in the Danish grid code for grid-connected WTs, reactive power generation is confined to a control band with respect to active power generation. In practice, a grid-connected WT needs to fulfill the specific requirement depending on the regulation of the country. In this paper, the minimum power factor of WT is set to 0.8 both in leading and lagging directions. In other words, the maximum power-factor angle $\varphi_{\max}$ is 37^0 and the minimum power-factor angle $\varphi_{\min}$ is -37^0. Normally, power-electronic converters of WTs are usually over-rated at 130% of the rated power output. Consider that apparent power equals to $\sqrt{P^2+Q^2} = P^2\sqrt{1+\tan^2\varphi}$. Such a power factor requirement ensures that at the rated active power output, the maximum apparent power output ($1\sqrt{1+\tan^2\varphi_{\max}} = 125\%$) is within the converter rating.

Fig. 4.5 shows the optimal power factor angles of the WTs obtained from the stochastic optimization for a summer weekday, a summer weekend, a winter weekday and a winter weekend. All the power factor angles are positive, which indicates that the WTs generate reactive power. The power factor angles during a summer weekday are within [11, 32] degree, while the power factor angles during the other three periods are within [10, 24] degree. In addition, the power factor angles during a summer weekday fluctuate more frequently than during the other periods. This is caused by a relatively high wind power fluctuation in summer and a high load demand during weekdays. As shown in Fig. 4.5, it is also expected that the diurnal variation of load demand is reflected on the diurnal reactive power output of the WTs.

Fig. 4.6 shows the probability density function of the voltage at bus 27 over a year after the stochastic optimization. The mean value of the voltage is 0.99 p.u., and the standard deviation is around 2% of the mean value. In this case, the maximum allowed voltage (1.07 p.u.) is not exceeded. However, there is a bulge on the probability density function around 1 p.u. This is caused by the tap changer of the substation transformer, which regulates the voltage at bus 70 within [0.983, 1] p.u. As the WT is connected at bus 27, the voltage at 27 is on average slightly higher than the voltage at bus 70.

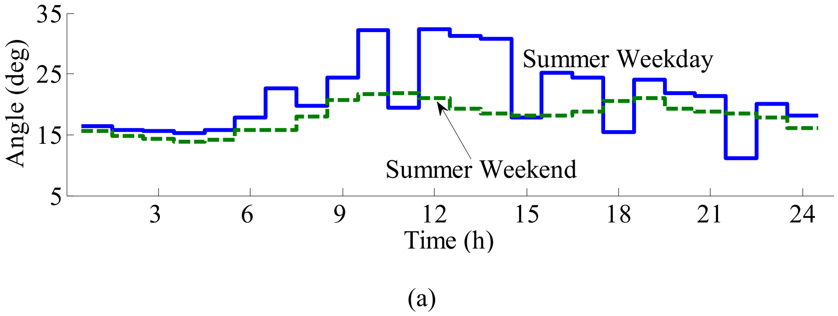

(a)

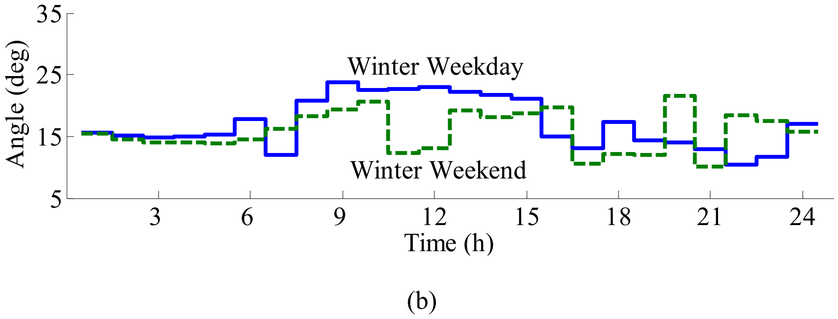

(b)

Fig. 4.5. Optimal daily power factor angles of WT at bus 27: (a) summer weekday and weekend, (b) winter weekday and weekend.

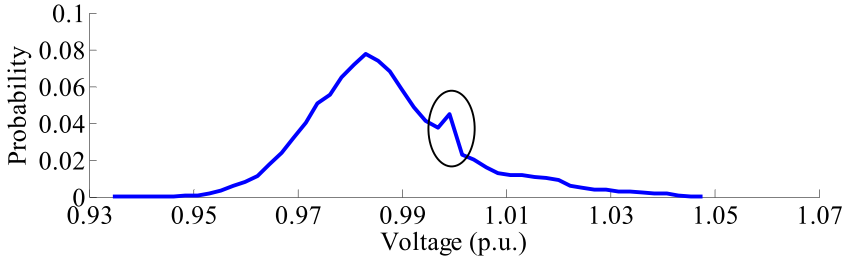

Fig. 4.6. Empirical probability density function of voltage at bus 27.

Fig. 4.7 shows the average daily power losses of the network during a summer weekday (SD), a summer weekend (SE), a winter weekday (WD) and a winter weekend (WE). The network power losses with

WTs using unity power factor setting is shown on the first bin, and with WTs using optimal power factor setting shown on the second bin. The network power losses are lowered when using the optimal WT power factor setting. As compared to the case with unity power factor setting, the network losses are reduced by 10.4% during a summer weekday, 7.4% during a summer weekend, 16.7% during a winter weekday and 10.9% during a winter weekend. As a result, the annual power losses are reduced approximately by 13% from 248 MWh with unity power factor of WTs to 215 MWh with optimal power factor setting of WTs. The significance of this amount of loss reduction will be evaluated in the following subsection.

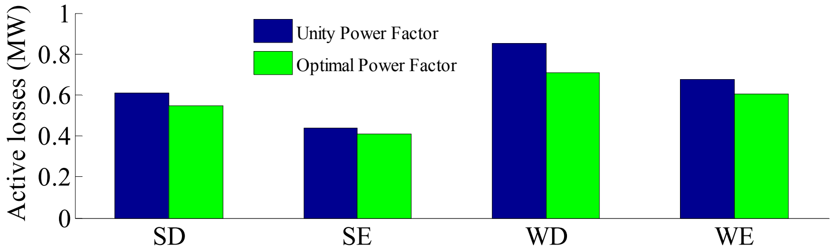

Fig. 4.7. Network average daily power losses during a summer weekday (SD), summer weekend (SE), winter weekday (WD) and winter weekend (WE)

4.4.2 Economic benefits of optimal power factor setting

The loss reduction due to the optimal power factor setting of WTs may provide economic benefits to both network operators and WT owners. In order to evaluate such economic benefits compared to the total cost of the system, a cost assessment is carried out over a period of twenty years of operation. For such a long-range system planning, the total assessed cost should include initial fixed costs, annual fixed costs and annual variable costs (Willis, Scott 2000). The initial fixed costs consist of a 33/11 kV 12 MVA tap-changing transformer, building cost, 33 kV and 11 kV switchgears, Petersen coil, assembling, and cable cost (20 km, XLPE three-core 150mm^2). Based on the price list provided by the local Danish DNO, these initial fixed costs are approximately 2.587 M€ in total. The annual fixed costs include the annual property tax, i.e. 3600 €, and annual maintenance and inspection cost, i.e. 6670 €. The above price values are provided by the Danish distribution network operator in Danish Krone (DKK) and are converted to € through the ratio of 7.50 DKK/€. The annual variable cost contains the electricity cost due to system power losses. Furthermore, system power losses may increase every year due to the annual load growth. According to the network operator, a typical annual load growth rate is 1.5% for a Danish distribution system in North Jutland. Fig. 4.8 shows annual system power losses over twenty years with the 1.5% annual load growth rate. A fixed electricity price 70 €/MWh is used here to calculate the cost of power losses.

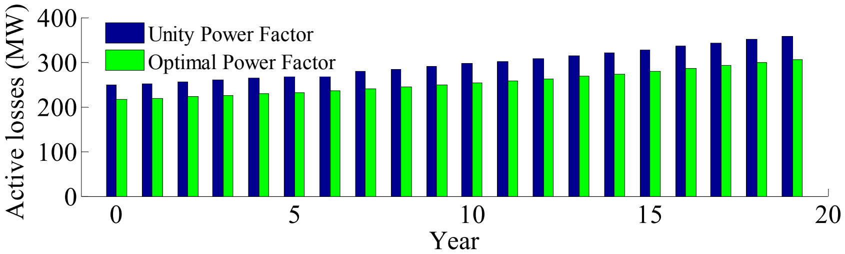

Fig. 4.8. Annual system power losses over 20 years with 1.5% annual load growth rate.

In order to evaluate the future money at the present value, present worth analysis is used. Present worth analysis is a method of measuring and comparing costs and savings that occur at different times on a consistent and equitable basis for decision-making (Willis, Scott 2000). The present worth analysis is based on the present worth factor PW, which represents the value of money one year from now in today's terms (Willis, Scott 2000). Thus, the present worth value of X euro T years from now is:

$$X_{\text{present worth}} = X \cdot PW^{T} \tag{4.6}$$

For example, if $PW = 0.9$, then 100 € a year from now worth 90 € at present, but 100 € five years from now worth only 59.05 € at present. Thus, present worth factor discounts the value of future costs and savings versus present costs and savings. Such a discount may be caused by interest rate, inflation, earnings target, investment risk, planning error, etc. Assume a 5% interest rate, a 2% inflation rate, a 2% earnings target, a 1% investment risk and a 1% planning error, the total discount rate becomes 11%. As a result, the present worth factor is around 0.9 (= 1 / (1+11%)). In the following analysis, this present worth factor of 0.9 is used.

Consequently, for the initial year, the total investment costs, including the initial fixed costs and the property tax of the initial year, are 2.590 M€ (= 2.587 M€ + 0.0036 M€); the maintenance and inspection costs are 6670 €. The annual power loss costs with unity and optimal power factor setting of WTs are listed in Table 4.1. The network total cost is evaluated over twenty years and summarized in Table 4.1.

As shown in Table 4.1, the network total cost is 2.848 M€ when the unity power factor setting of the WTs is used. However, the network total cost is reduced to 2.824 M€ when the optimal power factor setting of the WTs is used. A total amount of 24000 € will be saved in this case. This saved money can be shared between the network operator and the WT owners.

Table 4.1
Twenty-year evaluation of the network investment and operating cost (10^3 €)

Study Year	***Invest.***	***Maint. & Insp.***	***Loss Cost***		***Annual Cost***		***Present Worth Factor***	***Discount Cost***		***Wind Energy* (MWh*)***
			Unity	***Opt.***	***Unity***	***Opt.***		***Unity***	***Opt.***	
0	2590	6.67	17.4	15.1	2614	2612	1.000	2614	2612	8841
1	3.6	6.67	17.4	15.3	27.9	25.6	0.900	25.1	23.0	7957
2	3.6	6.67	17.9	15.5	28.2	25.8	0.810	22.8	20.9	7161
3	3.6	6.67	18.2	15.8	28.5	26.0	0.729	20.8	19.0	6445
…	…	…	…	…	…	…	…	…	…	…
19	3.6	6.67	25.1	21.4	35.4	31.6	0.315	4.8	4.3	2785
Total	2658.4	133.4	415	356	3207	3148		**2848**	**2824**	**77661**
Total wind energy transfer fee reduced is (2848-2824) × 10^3 € / 77661 MWh = 0.03 cents/kWh										

Assume that WT owners are rewarded with all the savings obtained (24000 €). This amount of money can be offered by network operators to WT owners in two forms. One is annual cash payment, which is 1200 € per year. Another one is to reduce the energy transfer fee that network operators charge WT owners. This requires the following calculation of the energy transfer fee for WT owners. During a year, the total wind energy generated is 8841 MWh (for the total WT capacity of 2.8 MW). According to (Willis, Scott 2000), the energy flow should also be discounted using the present worth factor. Therefore, as shown in Table 4.1, over a period of twenty years, the total wind energy generated is 77661 MWh. As a result, the energy transfer fee for WT owners is reduced by 0.03 cents/kWh (= 24000 € / 77661 MWh). Although this reduced energy transfer fee seems to be small, according to the local network operator, it actually can deplete the energy transfer fee by around 11% of what WT owners are paying at the moment (i.e. 0.28 cents/kWh). It is also worth mentioning that, for the above calculation, the optimal power factor setting is not updated every year even though the load grows annually. However, if the stochastic optimization is performed for every year considering annual load growth, a higher amount of annual system power losses can be achieved. Based on the above calculation, this will lead to a further reduction in total system costs and thus an even lower energy transfer fee for WT owners.

4.5 Summary

This chapter has proposed a stochastic optimization algorithm that provides optimal power factor settings of WTs for each hour of a day and for four types of days, i.e. a summer weekday, a summer-weekend day, a winter weekday and a winter-weekend day. As a result, a set of 96 power factor values is obtained for each of the WTs in the network. These power factor values considerably abate the system power losses under various combinations of WPG and load demand. In this case, an annual loss reduction of 13% is achieved. In light of the cost evaluation conducted, including the investment costs and operating costs of the network over a period of twenty years, the total costs are curtailed by 0.8%, which amounts to a saving of 24000 €. This amount of savings, if rewarded to the WT owners, may deplete the wind energy transfer fee by 11%. The developed stochastic optimization algorithm can be used as a basic tool by network operators to estimate power losses of their networks and to negotiate with WT owners to achieve a more economic operation of the system.

Chapter 5

Short-range distribution system planning

This chapter focuses on a short-range distribution system planning using measured time series data. First, the basic concept and process of a distribution system planning are introduced. Then, different scenarios for the distribution system planning are presented. Third, various simulation approaches for the system planning and evaluation methods for the simulation results are discussed. This is followed by a case study based on a distribution system at Støvring in North Jutland, Denmark.

5.1 Distribution system planning

Distribution system planning is a responsibility of distribution network operators to ensure that there is adequate substation capacity and feeder capacity to meet the load demand growth (Khator, Leung 1997). Distribution system planning can be divided into short-range planning and long-range planning, corresponding to the time scale of load forecasting (Gönen 1990). The main purpose of short-range planning is to make sure that the system can serve load while fulfilling all technical and environmental standards and criteria; whereas the aim of long-range planning is to make sure that the equipment and facilities purchased provide the lowest overall cost during their lifetime (Willis, Scott 2000). In other words, short-range planning aims at identifying problems and providing feasible solutions to the indentified problems in various lead times. The process of a short-range planning is shown in Fig. 5.1. The load forecast in the short-range planning refers to the forecast of annual peak load (Henault et al. 1970, Billinton, Huang 2008). In contrast, long-range planning assures that the decisions being made have the most lasting value.

Therefore, the time scale of a short-range planning normally varies from a few months to around five years, depending on the lead time required to implement the specific solution. For instance, it takes approximately one year to set up a DG rated between 1 and 10 MVA and five years to build a new primary distribution substation (Willis, Scott 2000). On the other hand, the time scale of a long-range planning may vary from 10 years to 30 years, depending on the life time of various equipment and facilities. For example, the life time of a WT is around 20 years. Furthermore, a long-range planning focuses on minimizing the overall cost accumulated along several short-range planning stages. Thus, it is usually formulated as multistage planning issues (Henault et al. 1970, Miranda, Ranito & Proenca 1994).

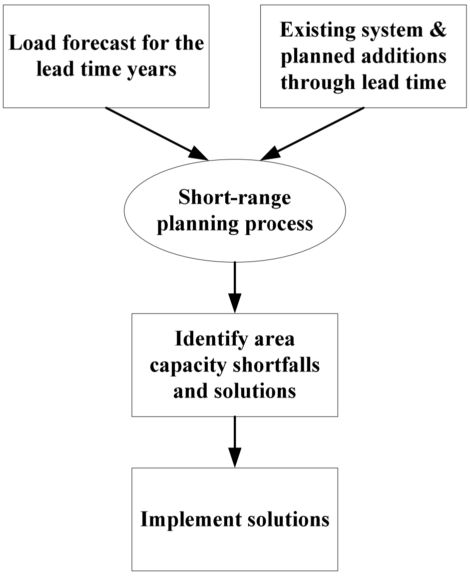

Fig. 5.1. Short-range planning process (Willis, Scott 2000).

This chapter studies the short-range planning issue of a distribution system. A distribution system at Størvring in North Jutland is used as a case network. The Størvring system consists of fixed-speed WTs, a CHP plant and a mixed type of loads. Due to the stochastic behavior of WPG, CHP regulation and load, a probabilistic method is adopted for analyzing the system planning process using available generation and load time series data from the measurements. Different scenarios and corresponding feasible options are demonstrated when investigating the system in a 5-year lead time.

5.2 Planning approach

5.2.1 Simulation approach for system planning

In order to study DG in system planning, a variety of simulation approaches can be used to evaluate the DG performance with different levels of detail. These approaches fall into three categories: screening approach, duration curve approach and temporal simulation approach (Willis, Scott 2000). The screening approach uses annual maximum, minimum or average values for simulation studies. For example, the annual average value of the energy production of DG can be used to evaluate the cost of the DG over its lifetime. The duration curve approach, such as a wind power duration curve and a load duration curve, provides more details than the screening approach. For instance, a load duration curve provides the information of load level and the percentage of time that load level occurs in a year (Harrison et al. 2007).

A duration curve can be transformed to a cumulative distribution function curve. In other words, the duration curve approach is similar to a standard probability approach. Nevertheless, the duration curve approach ignores the time dependence of the load and DG output. Therefore, the temporal simulation approach needs to be employed if more detailed information of the load and DG is to be included. Temporal simulation usually requires hourly or one-minute time series data of load and DG output over a typical peak day or the entire year.

5.2.2 Evaluation method for simulation results

If the temporal simulation approach is employed for load flow analysis, the load flow results, e.g. voltage at a busbar, will be a set of time series values. This is because the simulation approach requires inputs of time series data of load and DG. The obtained time series results can be evaluated through either a deterministic analysis or a probabilistic analysis. The deterministic analysis normally considers the maximum power flow through a transformer or the maximum or minimum voltage at a bus bar, etc. The rest of the time series results will be discarded. On the other hand, the probabilistic analysis evaluates the whole time series results through probability theory. In this case, power flow through a transformer or voltage at a bus bar is treated as a random variable. For random variables, standard probability measures that can be used are probability density function and cumulative distribution function. Alternatively, quantile values taken from a cumulative distribution function curve at regular intervals can also be used. Simulation based confidence interval can be used to provide an uncertainty estimation of a random variable. For instance, a 95% simulated confidence interval is the interval between the 2.5% and 97.5% quantiles of a random variable. An example of a 95% confidence interval of random variable X is shown in Fig. 5.2.

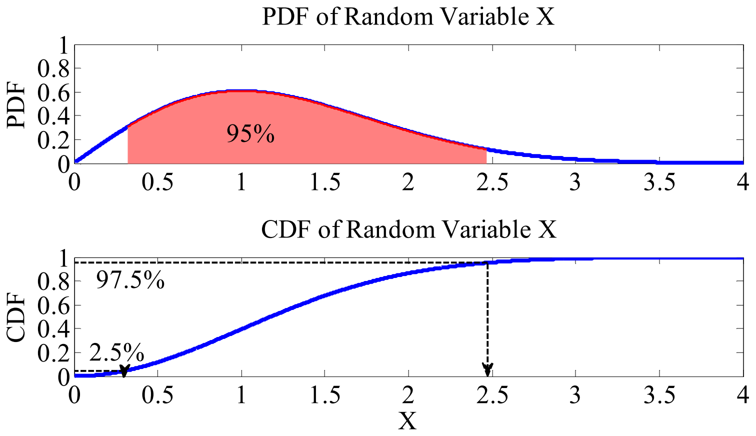

Fig. 5.2. 95% confidence interval of a random variable X.

5.3 Scenario analysis

A scenario analysis of a short-range planning is to propose feasible solutions based on identified capacity shortfalls and power quality standard violations. The following summarizes various system operating conditions and available options to solve the problems identified during the planning.

5.3.1 System operating conditions

The studied short-range planning process covers a five-year time span. According to the network operator, the annual demand growth rate at the Størvring area is around 1.5%. The considered cases during these five years are summarized as follows.

1) No component on outage
2) One substation transformer on outage
3) One cable or overhead line on outage
4) Substation circuit breaker open
5) Higher WT capacity

The above five system operating cases consist of the normal operating condition (1), the N−1 condition (2 and 3) and the lead-time modified system condition (4 and 5). Case 4 may also be an N−1 condition is the circuit breaker is opened unintentionally.

5.3.2 Options

If no problems are identified from the above operating conditions, the best option will be to do nothing. Otherwise, options to solve system capacity shortfalls, voltage limit and thermal limit violations should be conceived. For example, for the substation capacity shortfall, the transformer capacity may be upgraded. For the feeder capacity shortfall, according to the network operator, overhead line expansion is no longer considered an option as the local network operator finds it is too difficult to get permission from the government to install new overhead lines. Furthermore, the network operator is planning to replace existing overhead lines with underground cables so that line outage rate can be reduced in the case of storms. If the network is installed with power electronic based DG, both the active and reactive power output of the DG can be regulated to improve the system performance. Currently, in Denmark, the operational strategy of small CHP units is based on on/off control, which reflects the heat demand and electricity market price. It is suggested that a continuous control of CHP units may contribute to fulfilling the future demand growth. In summary, the potential options to solve the problems identified during the short-range planning are summarized as follows:

1) Substation transformer and/or cable expansion
2) Gas turbine based DG procurement
3) Demand side management
4) DG output control
5) Continuous operation of CHP units
6) Energy storage procurement, e.g. super capacitors
7) Reactive power compensation, e.g. capacitor or reactor
8) Network reconfiguration

5.4 Case study

This section first introduces the case network and the corresponding data set. Then, the system operating condition with one substation transformer on outage is chosen as a base case for planning studies. Two different solutions to system capacity shortfall are evaluated and compared both from a technical and an economic point of view. In the end, the impact of WPG on the frequency of transformer tap regulation is investigated.

5.4.1 Network and data set description

The case network is similar to the simplified 20 kV Støvring distribution system shown in Fig. 3.4, but with a more detailed network configuration as shown in Fig. 5.3. The network consists of ten primary feeders. The network data of the STKV and SØRP feeder are known. However, the network data of the other eight feeders are not available. The only data available are the aggregated load time series at each feeder. A detailed description of the data set is provided in section 3.2.2. In the following study, the network topology is assumed unchanged and the line outage rate is neglected.

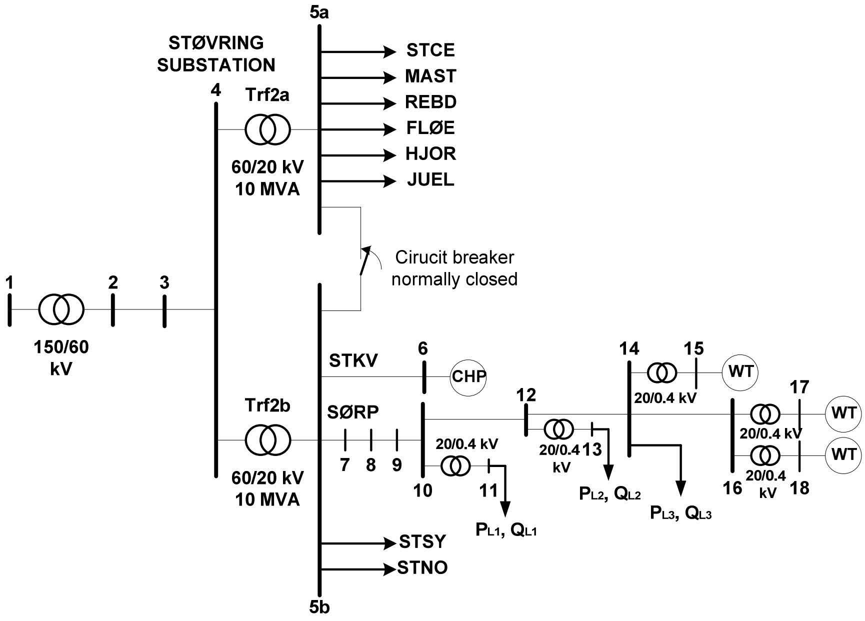

Fig. 5.3. Network configuration of Støvring distribution system.

5.4.2 Planning with one transformer on outage

Both the basic and temporal simulation approaches are used to identify the system capacity shortfall and to provide corresponding options under the condition that transformer Trf2b is on outage. The results obtained by the two approaches are summarized and compared.

a) Screening approach

The screening approach uses extreme values of generation and load data. There are three combinations of these extreme values, i.e. maximum load with no generation (screening 1), maximum load with maximum generation (screening 2) and minimum load with maximum generation (screening 3). This approach is simple but may overestimate the severity of the system capacity shortfall, which will require unnecessary investment with high cost. It is demonstrated later that the screening approach may ignore certain potential options and lead to a wrong decision-making.

Based on the screening approach, the loadings of the transformer Trf2a under three different extreme cases are summarized in Table 5.1. The maximum generation is 9 MW for CHP and 2 MW for WPG. The maximum load is (22.29 + j7.61) MVA and the minimum load is (0.62 + j0.10) MVA. As shown in Table 5.1, it is identified that transformer Trf2a will be overloaded in both power flow directions if no actions are taken. No line thermal violation or voltage violation is detected. One solution is to add a new transformer. According to the load flow analysis, an extra transformer capacity of at least 20 MVA is needed in order to keep its loading below 100%. Another potential solution is to use a gas turbine as DG. In this case, the total capacity of the gas turbine should reach at least 18 MW. However, under the condition of minimum load with maximum generation, the gas turbine cannot reduce the reverse power flow overloading of the substation transformer. In this case, the gas turbine based DG may be rejected by the decision maker.

Table 5.1
Loading of transformer Trf2a with transformer Trf2b on outage using screening approach

Transformer Loading		**Options**		
		Do nothing	***Transformer expansion (+20MVA)***	***Gas turbine based DG (+18 MW)***
Screening 1	max. load & no generation	273.1%	91.0%	96.7%
Screening 2	max. load & max. generation	163.1%	54.3%	98.0%
Screening 3	min. load & max. generation	−117.3%	−39.1%	−117.3%

Note: '−': indicates reverse power flow through transformer

b) Temporal simulation approach

When performing temporal simulation, however, a more detailed loading condition of the transformer Trf2a can be obtained.

Do nothing

If no actions are taken, the cumulative distribution function s of the loading of transformer Trf2a are shown in Fig. 5.4 (a). It is observed that the transformer overloading occurs only during weekdays, and that the maximum overloading is less than 140%. This is much lower than the results shown in Table 5.1, i.e. 273.1% under maximum load with no generation. It is also worth mentioning that no overloading occurs for the reverse power flow situation. More details can be observed from the daily loading curve. Fig. 5.4 (b) shows the daily mean value and 95% confidence interval (2.5% and 97.5% quantile) curves of the transformer loading in a summer weekday, while Fig. 5.4 (c) shows similar results in a winter weekday. From these daily loading curves, it is further discovered that the overloading occurs only at 8 a.m. in summer weekdays and between 7 a.m. and 12 a.m. in winter weekdays. This information is particularly important for the network operators in decision-making. However, it was not observed when using the screening approach with extreme values as discussed in the previous subsection.

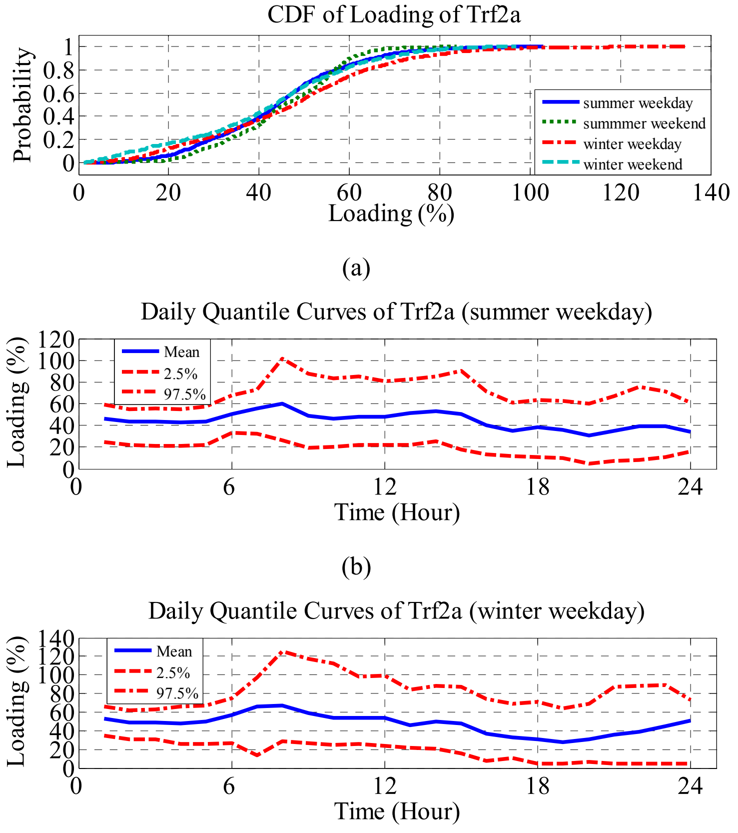

(a)

(b)

(c)

Fig. 5.4. Loading of transformer Trf2a: (a) cumulative distribution function curves, (b) daily mean value and 95% confidence interval in summer weekday, and (c) daily mean value and 95% confidence interval in winter weekday.

Transformer expansion

According to the temporal simulation of load flow calculation, an extra transformer capacity of only 6 MVA is needed in order to solve the transformer overloading problem. This is much lower than the required capacity of 20 MVA from the screening approach. Fig. 5.5 shows the corresponding daily mean value and 95% confidence interval curves in a summer and winter weekday after an extra 6 MVA transformer is included. As shown in Fig. 5.5, the loading at each hour of a day is reduced below 100%.

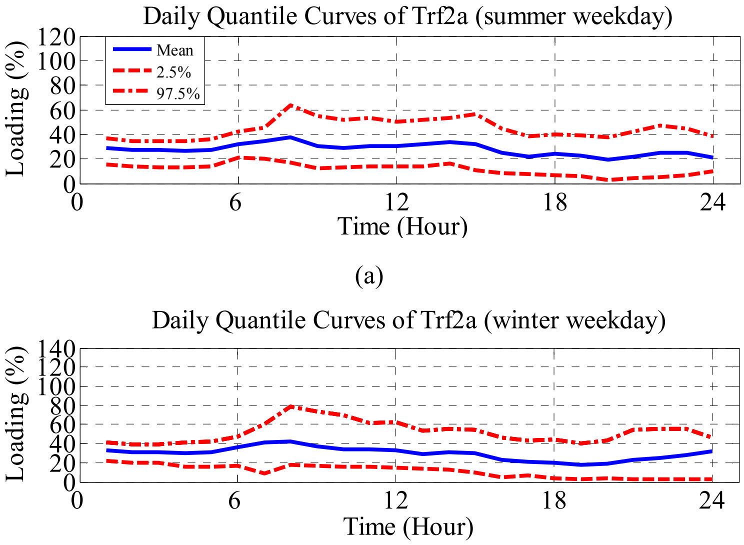

(b)

Fig. 5.5. Daily mean value and 95% confidence interval of the loading of transformer Trf2a with transformer expansion of 6 MVA: (a) summer weekday, and (b) winter weekday.

Gas turbine based DG

An alternative to transformer expansion is to procure a gas turbine as DG. The operation of the gas turbine can be flexible. The gas turbine can be turned on when the transformer overloading occurs and turned off when the system loading is low.

Based on the results of temporal simulation, a gas turbine with a capacity of 4 MW is sufficient to solve the transformer overloading problem; whereas a capacity of 18 MW is required according to the screening approach. In the simulation, it is assumed that the gas turbine operates at the unity power factor. Furthermore, the gas turbine is required to be turned on only between 7 a.m. and 12 a.m. in a summer and winter weekday and can be turned off for the rest of the time. This is adequate as transformer overloading occurs only at those hours as shown in Fig. 5.4.

The gas turbine should be connected to the location selected by the network operator based on a network with all the feeder configurations. In this case, the gas turbine is directly connected to the low voltage side of the substation bus bar to simulate its power contribution. Fig. 5.6 presents the corresponding daily mean value and 95% confidence interval curves of the transformer loading in a summer and winter weekday after the gas turbine is included. The transformer loading between 7 a.m. and 12 a.m. is reduced below 100% due to the operation of the gas turbine; whereas the loadings during the remaining hours remain unchanged. This is the main difference in operation between the option of substation transformer expansion and the procurement of a gas turbine. The flexibility of operation could provide an incentive for the network operator to consider the option of procuring gas turbine. A more detailed cost evaluation of the two options should be conducted to make the final decision.

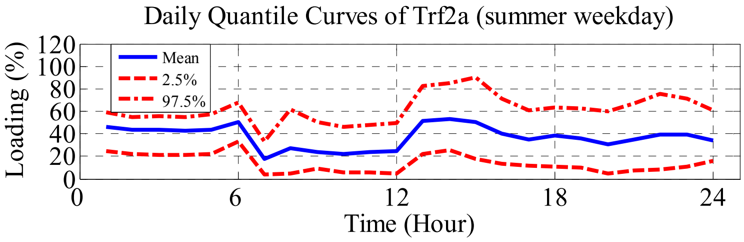

(a)

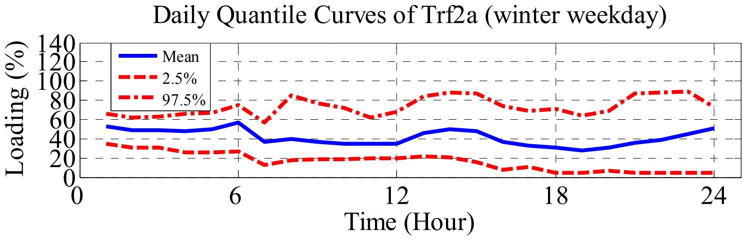

(b)

Fig. 5.6. Daily mean value and 95% confidence interval of the loading of transformer Trf2a with 4 MW gas turbine based DG turned on between 7 a.m. and 12 a.m.: (a) summer weekday, and (b) winter weekday.

5.4.3 Cost analysis of a gas turbine

In order to assess the cost effectiveness of purchasing a gas turbine, a cost evaluation of the gas turbine over its life time (20 years) is provided. The cost analysis should include the initial fixed cost C_{IF}, initial variable cost C_{IV}, annual fixed cost C_{AF} and annual variable cost C_{AV} (Willis, Scott 2000).

Based on the price lists provided in (Willis, Scott 2000), the cost of a gas turbine itself is $431.1/kW. Using the currency exchange ratio of 1.5$/€, the value is converted to €287.4/kW. As the 4 MW gas turbine is on for six hours between 7 a.m. and 12 a.m. during a weekday, this amounts to a total 1564 hours operation per year. Thus, the total energy production is 6256 MWh per year. The following summarizes the four cost components: C_{IF}, C_{IV}, C_{AF}, and C_{AV}. All the prices are based on the information provided in (Willis, Scott 2000).

1) The initial fixed cost C_{IF} consists of the cost of the gas turbine itself, site preparation, protection, backup tank, etc. For a 4 MW gas turbine, the cost of the turbine itself C_{GT} is €1,149,600. The rest of the initial fixed cost C_{RIF} amounts to €86,267. In total, the initial fixed cost is:

   $C_{\mathrm{IF}} = C_{\mathrm{GT}} + C_{\mathrm{RIF}} = €1,235,867$.
2) The initial variable cost is the fee for emissions permit for more than 1001 h/year operation, i.e. €2,133. Thus, the initial variable cost is :

   $C_{\mathrm{IV}} = €2,133$.
3) The annual fixed cost contains both the property tax C_{tax}, i.e. €2,316, and the annual mechanical & electrical inspection C_{insp}, i.e. €913. Thus, the annual fixed cost is: $C_{\mathrm{AF}} = C_{\mathrm{tax}} + C_{\mathrm{insp}} = €3,229$.
4) The annual variable cost is comprised of maintenance and fuel cost. The maintenance cost is 0.2 cents/kWh and the fuel cost is 2.44 cents/kWh. For 1564 hours per year operation at 4 MW output, the annual maintenance cost $C_{\mathrm{maint}} = €12,512$ and the annual fuel cost $C_{\mathrm{fuel}} = €152,646$. Thus, the annual variable cost is:

   $C_{\mathrm{AV}} = C_{\mathrm{maint}} + C_{\mathrm{fuel}} = €165,158$.

Table 5.2 summarizes the twenty-year cost evaluation of the gas turbine. For the initial year (year 0), the unit & site cost $C_{\mathrm{u\&s}} = C_{\mathrm{IF}} + C_{\mathrm{IV}} + C_{\mathrm{tax}} = €1,240,316$; the maintenance and inspection cost $C_{\mathrm{m\&i}} = C_{\mathrm{maint}} + C_{\mathrm{insp}} = €13,425$. A present worth (PW) factor of 0.9 is used to evaluate the future money at the present value (Willis, Scott 2000). The spot market price in west Denmark in 2007 is used here to calculate the revenue of selling electricity gained by the network operator (Energinet.dk 2009). As the gas turbine is only turned on between 7 a.m. and 12 a.m during a weekday, only the spot price during this period is used for the calculation.

As shown in Table 5.2, the total discounted cost over twenty years is around €2,717,145 and the total discounted energy production is around 54,964 MWh. Dividing the discounted cost by the discounted energy gives an evaluated cost of 4.944 euro cents/kWh for the gas turbine. The total discounted revenue gained by selling electricity is €2,341,047, which is lower than the total discounted cost €2,717,145. Thus, the net PW cost of using a gas turbine is €376,098. It is worth mentioning that the revenue considered here does not include the potential network loss reduction due to the use of the gas turbine. On the other hand, buying a 6 MW transformer itself will require an initial cost of around €400,000, not to mention other additional cost such as transportation and installation. Therefore, from the perspective of the long-term cost over twenty years, buying a gas turbine requires less cost than buying a transformer in order to solve the substation capacity shortfall problem.

Table 5.2
Twenty-year evaluation of a gas turbine for 1564 hours per year operation at full 4 MW output (in €).

Study Year	Unit & Site	Maint. & Insp.	Fuel Cost	Annual Cost	PW Factor	Disc. Cost	Disc. MWh Production	Disc. Sales
0	1,240,316	13,425	152,646	1,406,387	1.000	1,406,387	6,256	266,506
1	2,316	13,425	152,646	168,387	0.900	151,548	5,630	239,855
2	2,316	13,425	152,646	168,387	0.810	136,393	5,067	215,869
3	2,316	13,425	152,646	168,387	0.729	122,754	4,561	194,283
…	…	…	…	…	…	…	…	…
19	2,316	13,425	152,646	168,387	0.135	22,747	845	36,001
Total				4,605,740		**2,717,145**	**54,954**	**2,341,047**
Evaluated cost of a gas turbine= 2,717,145 / 54,954 = 4.944 cents/kWh Net PW cost of using gas turbine = €2,717,145 − €2,341,047 = €376,098								

5.4.4 Higher Wind Power Integration

The criterion from the local network operator for connecting WTs is that the maximum voltage increment at the connection point should not exceed 1% under no load condition. By obeying this criterion, based on the screening approach, the maximum WT capacity at SØRP feeder can be increased from 1.8 MW to 3.6 MW with the voltage increment of 0.9%. In addition, an extra 7.2 MW can be connected to the HJOR and FLØE feeder. In total, the WT capacity is increased to 10.8 MW, which is six times higher than the existing WT capacity. With the extra amount of wind power integration, no capacity shortfalls or thermal and voltage limits violation are detected.

The local network operator is concerned that the higher wind power integration, due to its fluctuating power, may increase the frequency of the transformer tap adjustment at the substation. This will aggravate the mechanical stress of the tap and increase the need of maintenance of the transformer. In order to evaluate the frequency of tap regulation, temporal simulation of load flow calculation is also carried out. Fig. 5.7 shows the daily tap position of transformer Trf2a in a winter weekday before and after the WT capacity is increased by six times. The legend 1, 2 and 3 indicates the tap steps above the reference position. It is observed that the tap position 2 and 3 between 6 a.m. and 12 p.m. is reduced due to higher wind power integration. Although not shown here, the results also indicate that the higher WT capacity does not increase the frequency of the tap regulation. This may be due to a positive correlation between the wind power generation and load demand.

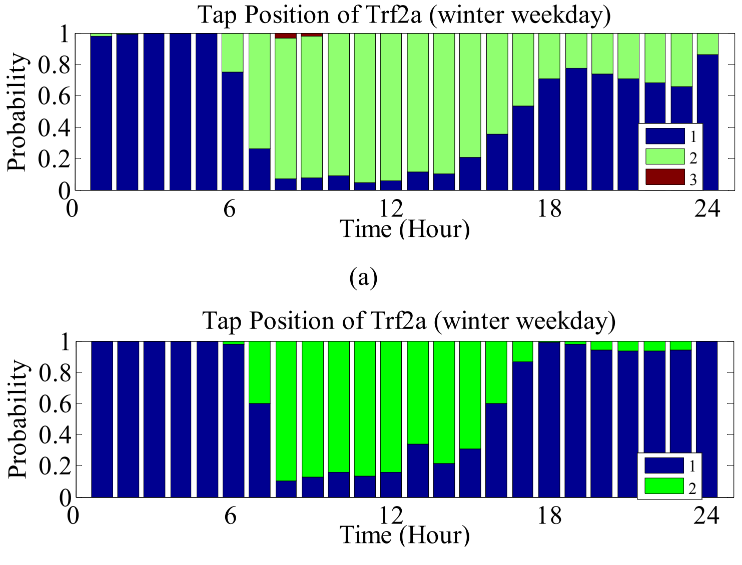

(a)

(b)

Fig. 5.7. Daily tap position of transformer Trf2a in a winter weekday: (a) before and (b) after WT capacity increased by six times

5.5 Summary

This chapter analyzes four scenarios for a five-year-ahead distribution system planning using measured time series data. It is demonstrated that the temporal simulation approach using time series data and the probabilistic analysis using probability density function, cumulative distribution function and 95% confidence interval provides much more accurate and insightful information than the screening approach with the deterministic analysis. An example of procuring a gas turbine as an alternative to the transformer expansion is presented. The flexible operation time of the gas turbine provides a good incentive for the distribution network operator to consider it as a feasible option before the decision-making. The cost analysis of a gas turbine provides further economic incentive for the distribution network operators to choose gas turbine as an alternative to transformer expansion. Finally, it is illustrated that higher wind power integration contributes to the reduction of the frequency of transformer tap adjustment.

Chapter 6

Optimal Cable Selection for Medium Voltage Wind Energy Network

This chapter presents the optimal cable design for a medium voltage wind energy network. First, the approximate formulas for voltage rise and power losses are studied. Then, economical loading range and load reach are introduced to determine the optimal cable conductor size. In the end, the Götene 20 kV wind energy network is used as an example to demonstrate the optimal cable sizing for the network.

6.1 Voltage rise and power losses

Fig. 2.1 shows a π-model of an AC cable that transmits wind power to the grid. In order to calculate voltage rise and power losses in the cable, the standard Newton-Raphson algorithm can be used.

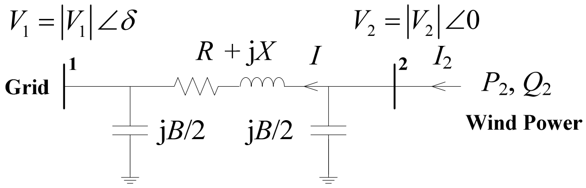

Fig. 6.1. π-model of an underground cable that transmits wind power to the grid.

However, the computation time may become a concern if thousands of such load flow calculations are performed. To address this, approximate but fast calculations can be used as long as the accuracy is within an acceptable range. The following derives the approximate equations for calculating the voltage rise and power losses of a cable and evaluates the corresponding error that occurs.

The voltage at the wind power side V_2 can be calculated by

$$V_2 = V_1 - \left(a + \mathrm{j}b\right), \tag{6.1}$$

where

$$a = \frac{1}{V_2}\left[RP_2 + X\left(Q_2 + |V_2|^2 B/2\right)\right], \tag{6.2}$$

$$b = \frac{1}{V_2}\left[XP_2 - R\left(Q_2 + |V_2|^2 B/2\right)\right]. \tag{6.3}$$

For per unit calculation, $|V_1| = 1$. Assuming $|V_2| \approx 1$ p.u. in (6.2) leads to

$$a \approx RP_2 + X\left(Q_2 + B/2\right). \tag{6.4}$$

As b in p.u. is normally close to zero, the voltage magnitude at the wind power side $|V_2|$ can be approximated by

$$|V_2| = \sqrt{|V_1|^2 - b^2} + a \approx |V_1| + a. \tag{6.5}$$

Thus, the voltage rise ΔV in p.u. is approximated by

$$\Delta V = |V_2| - |V_1| \approx a \approx RP_2 + X\left(Q_2 + B/2\right), \tag{6.6}$$

and the current magnitude $|I|$ is calculated by

$$|I| = \frac{\sqrt{P_2^2 + \left(Q_2 + |V_2|^2 B/2\right)^2}}{|V_2|}. \tag{6.7}$$

Accordingly, the active power losses can be calculated by

$$\Delta P = |I|^2 R = \frac{P_2^2 + \left(Q_2 + |V_2|^2 B/2\right)^2}{|V_2|^2} R, \tag{6.8}$$

and the reactive power losses are

$$\Delta Q = |I|^2 X - |V_2|^2 B = \frac{P_2^2 + \left(Q_2 + |V_2|^2 B/2\right)^2}{|V_2|^2} X - |V_2|^2 B\,. \tag{6.9}$$

The results obtained by using the approximated voltage formula (6.5) and the active power losses formula (6.8) are compared to the results obtained by the standard Newton-Raphson algorithm. The error is calculated by

$$\text{Error} = \frac{\text{Approximated value} - \text{Exact value}}{\text{Exact value}} \times 100\,, \tag{6.10}$$

where the exact value refers to the one obtained by the Newton-Raphson algorithm with a maximum tolerated error of 1e-6.

Fig. 6.2 shows the errors of the results obtained from the approximated formulas for different wind power injection P_2 and Q_2 (or the power factor angle). The active wind power ranges from 0 to 10 MW and the power factor ranges from 0.64 (for power factor angle of 50^0) to 1 in both lagging and leading directions. The test cable is a three-core XLPE cable with a conductor size of 120 mm^2. The impedance of the cable is $R = 3.2207\ \Omega$, X=1.0367 Ω, and the shunt susceptance B = 7.5398e-4 S.

As shown in Fig. 6.2, the errors are minimum when the WTs absorb reactive power. This is reasonable as it reduces reactive power flow in the cable and thus keeps the voltage at the wind power terminal $|V_2|$ close to 1 p.u. However, the voltage is overestimated as the power factor angle increases. This is mainly caused by neglecting b in (6.3) and the approximation of a in (6.4). According to (6.8), the overestimation of the voltage leads to an underestimation of the active power losses as shown in Fig. 6.2 (c) and (d). Furthermore, as shown in Fig. 6.2 (b) and (d), when the cable length increases to 10 km, the maximum error in voltage increases to around 1.1%. This occurs when the active power is 10 MW and the power factor angle is 50^0. This amount of error is not acceptable if the maximum error allowed in voltage is 0.5%. In this case, the standard Newton-Raphson algorithm should be used. The error in power losses is due to the error in voltage and the absolute error in power losses reaches maximum when the error in voltage reaches maximum.

Similar results are obtained for single-core XLPE cables in both flat and trefoil formation. In general, for a certain type of cable, as the conductor size increases, the corresponding error decreases. In summary, if the WT capacity is lower than 7 MW or if the WT power factor is around 1, the approximated formulas (6.5)-(6.9) can be used for a cable length up to 10 km.

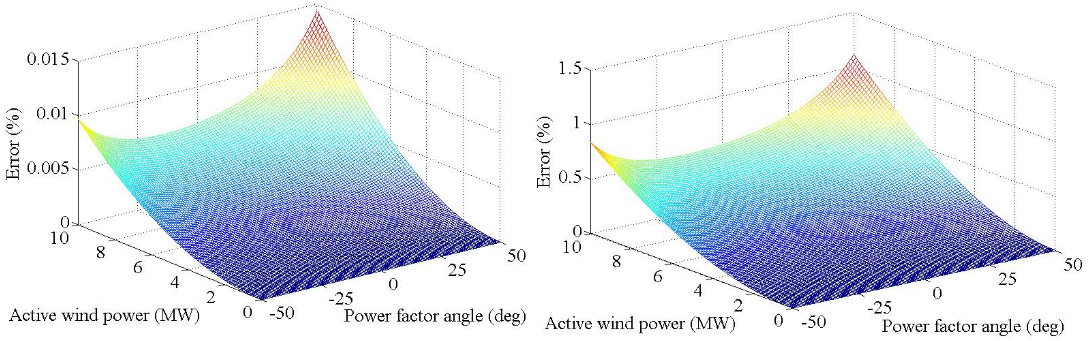

(a) L = 1 km (b) L = 10 km

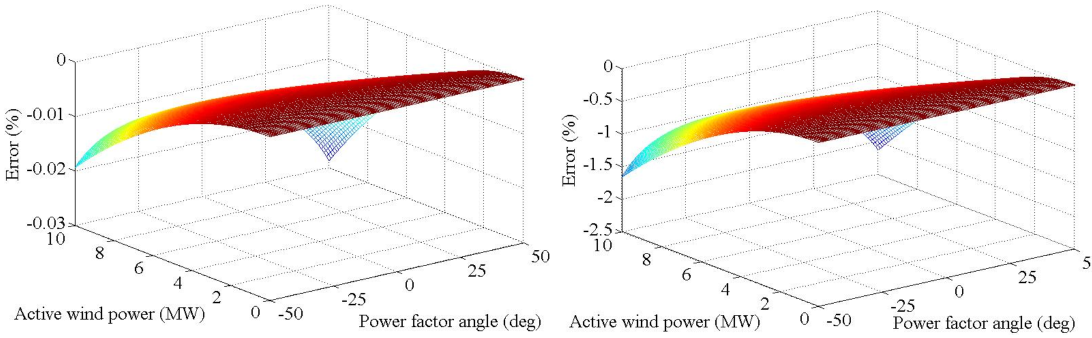

(c) L = 1 km (d) L = 10 km

Fig. 6.2. Error of approximated formulas when the cable length is 1 km and 10 km: (a) & (b) voltage at wind power terminal, and (c) & (d) cable active power loss.

The loss calculation in (6.8) includes only conductor losses of the cable. According to (IEC-60287-1-1 2001), the total losses of a cable include conductor losses, sheath losses, armour losses, and dielectric losses. The total losses are calculated by

$$P_{\text{loss}} = \Delta P\left(1+\gamma_1+\gamma_2\right)+W_d \tag{6.11}$$

where γ_1 is the ratio of sheath loss to resistive losses; γ_2 is the ratio of armour loss to resistive losses; the dielectric loss W_d is

$$W_d = B|V_1|^2 \tan\delta \tag{6.12}$$

where tanδ is the loss factor of the insulation. All these four loss elements in (6.11) should be accounted for when evaluating the total losses for a cable.

6.2 Cable sizing based on lowest total cost

Power losses of a cable are influenced by both the conductor size and the loading of the cable. A thicker cable induces less power losses and may cost less than a thinner cable over twenty years of operation, even though the thinner cable has a lower investment cost per km. The overall cost of a cable, however, also depends on the loading of the cable. In other words, for a certain loading range, cable A may be cheaper than cable B; for another loading range, it may be the other way around. The loading range in which a particular conductor offers lower cost than any other available conductors is called the economical loading range of the cable (Willis 1997).

The following example illustrates the economical loading ranges of two three-core cables with conductor sizes of 120 mm^2 and 150 mm^2, respectively. The impedance, current rating and cost of various types of XLPE cable can be found in 0 (ABB 2006). The total present worth cost of a cable is calculated by

$$C_{\text{cable}} = L \times C_{\text{inv}} + C_{\text{loss}} \tag{6.13}$$

where L is the length of the cable, C_{inv} is the investment cost of the cable per km, and

$$C_{\text{loss}} = P_{\text{loss}} \times \alpha \times \frac{1-PW^{\text{T}}}{1-PW} \tag{6.14}$$

where P_{loss} is the annual power losses of the cable calculated according to (6.11); α is the electricity price for the power losses; T is the number of evaluation years; PW is the present worth factor, which is used to evaluate the future money at the present value (Willis 1997). In this case, $L = 1$ km, $\alpha = 70$ €/MWh, $PW = 0.9$ and T = 20 years. As wind power is fluctuating throughout a year, the hourly wind power measurement from an 850 kW WT in Jung (Sweden) is used to calculate the power losses of the cable. Fig. 6.3 shows the measured wind power time series in 2007. The wind power generated from a WT is scaled up by the capacity of the WT. According to (Zhao 2006), the losses in a wind turbine system include gear box losses (if any), mechanical losses, generator losses, back-to-back converter losses (if any) and step-up transformer losses. In this case, a total loss of 5% of the generated wind power is assumed. Consequently, the actual wind power injected to the cable is de-rated to 95%

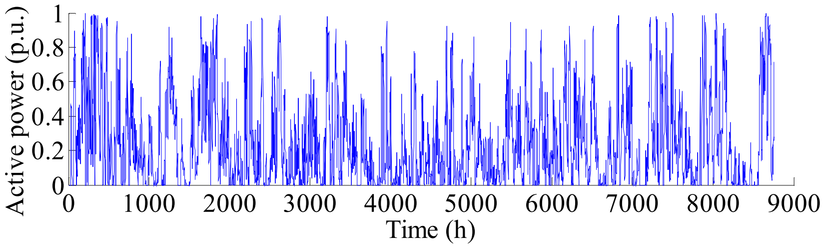

Fig. 6.3. Hourly measured wind power time series from an 850 kW wind turbine in 2007.

Fig. 6.4 shows the total present worth cost of a 120 mm^2 and a 150 mm^2 three-core cable with different WT capacities. The total present worth cost of the 120 mm^2 cable is lower when the WT capacity is below 4.9 MW; whereas the total present worth cost of the 150 mm^2 cable becomes lower when the WT capacity is higher than 4.9 MW. This is because of the lower cable losses on the thicker cable.

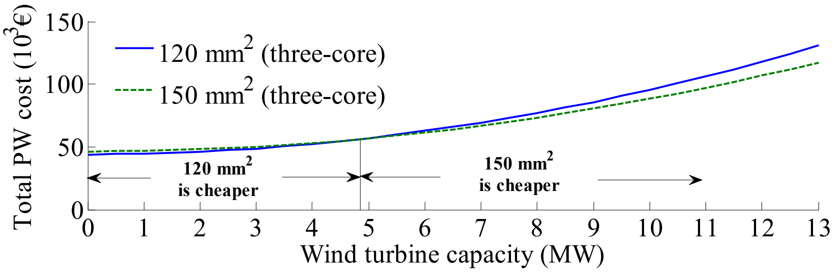

Fig. 6.4. Total present worth cost of a 120 mm^2 and a 150 mm^2 three-core cable with different WT capacities.

Fig. 6.5 shows the total present worth cost of three-core cables with the conductor sizes of 120 mm^2, 150 mm^2, 185 mm^2 and 240 mm^2. The figure further shows that the economical loading range of the 150 mm^2 cable is only between 4.9 MW and 5.6 MW. Instead, the 185 mm^2 cable becomes the cheapest choice when the WT capacity is between 5.6 MW and 7.3 MW, and the 240 mm^2 cable is the most economical one when the WT capacity is higher than 7.3 MW. As a result, each conductor size has its own loading range that gives the lowest cost.

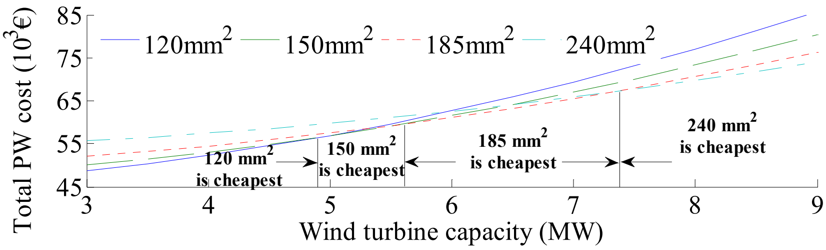

Fig. 6.5. Total present worth cost of three-core cables (120 mm^2, 150 mm^2, 185 mm^2 and 240 mm^2) with different WT capacities.

However, these loading ranges may be affected by the choice of cable length, evaluation period, *PW* factor and electricity price. In order to study and understand these effects, Fig. 6.6 presents the economical loading ranges of three-core cables for six different cases. The results are based on the calculations according to the approximate equations derived in section 6.1.

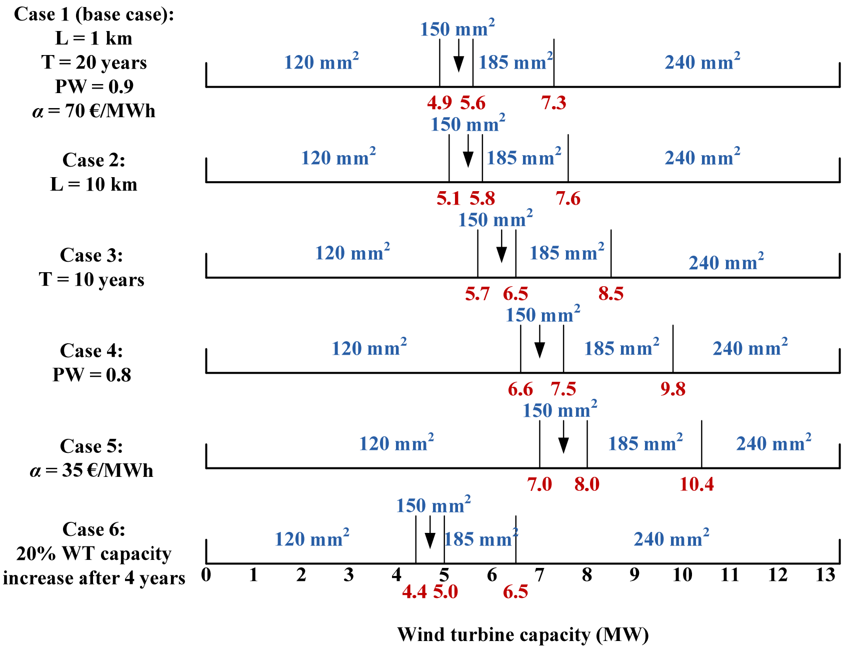

Fig. 6.6. Economical loading ranges of 20 kV three-core cables for six different cases.

Case 1 is the base case, corresponding to the result shown in Fig. 6.5. The 240 mm^2 cable has the thermal rating of 13.3 MW. Thus, the loading range is shown between 0 and 13.3 MW. Case 2 indicates that the economical loading ranges of the four conductor sizes remain relatively unchanged even though the cable length increases from 1 km to 10 km. According to (6.13), the total costs of the cables are shifted upward by around 10 times when the cable length is ten times longer. This keeps the economical loading range unchanged or slightly shifted to the right. This is an important observation as the economical loading range is relatively independent of the cable length. In Case 3, the evaluation period of the cable cost is reduced to 10 years. The breakpoints of the four economical loading ranges are moved slightly to the right. However, the change as compared to Case 1 is not as significant as one might expect. This is because according to (6.14), the present worth of the power losses drops by only 26% when the evaluation period is reduced from 20 years to 10 years. In other words, 74% of the present worth of the power losses occur during the first decade. Thus, a short evaluation period does not affect the total present worth cost of power losses to a large extent. In Case 4, the *PW* factor is reduced to 0.8. A reduced *PW* factor indicates a higher discount rate for further power losses. As a result, the present worth of the power losses over 20 years drops by around 44%. This explains why the breakpoints of the four economical loading ranges are moved further to the right. Thus, it is important to estimate the *PW* factor accurately for a specific case study. In case 5, the electricity price is reduced by half, i.e. 35 €/MWh. This results in a 50% reduction of the cost of power losses as compared to Case 1. Thus, the breakpoints move to the right even further. The influence of electricity price can be very significant. Case 6 investigates how the economical loading range changes if the WT capacity increases by 20% after four years of cable operation. The increase in WT capacity raises the amount of future losses. Consequently, as compared to Case 1, the break points of the economical loading ranges move to the left instead.

Table 6.1 summarizes the economical loading ranges of single-core cables with trefoil formation and flat formation. The trefoil formation has the same economical loading ranges as the flat formation except the one for the 1000 mm^2 conductor size. They are the same because of the identical resistance and price of the cable per km for the same conductor size. Although the inductance of the flat formation is around 1.6 times the value of the trefoil formation, this has very little impact on the active power losses according to (6.6)-(6.8). The difference for the 1000 mm^2 conductor size is because the flat formation has a higher current rating than the trefoil formation in general.

Table 6.1
Economical loading ranges (MW) of 20 kV single-core cables with trefoil and flat formation

Line conductor size (mm^2)	low	high
120	0	4.9
150	4.9	5.6
185	5.6	7.3
240	7.3	9.6
300	9.6	13.1
400	13.1	14.8
500	14.8	21.9
800	21.9	31.7
1000	31.7	40.5 (trefoil) 44.5 (flat)

6.3 Load reach

Economic loading range determines cable sizes on the basis of total cable costs, which depend on the power losses of each cable. However, in addition to power losses, voltage rise is another important factor for deciding whether or not a cable is suitable for transporting a certain amount of wind power to the grid over a long distance. The amount of voltage rise per km can be approximated by (6.6). Voltage rise of a cable at a given loading condition increases almost proportionally to the cable length. The cable reaches its maximum length when the voltage rises to the limits stipulated by technical standards (EN 50160 1999). This maximum length is referred to as the load reach of the cable. Formally, the load reach of a cable is defined as the maximum distance that the cable can transmit power before encountering engineering criteria, such as voltage limits (Willis 1997). For example, if the voltage limits are set to ±6%, and a cable has a 2% voltage drop per km at a given loading, then the load reach of the cable is 3 km. Mathematically, the load reach L^* is defined as (Willis 1997)

$$L^* = \frac{\Delta V_{\max}}{\Delta V(P)} \tag{6.15}$$

where $\Delta V_{\max}$ is the stipulated voltage limit; ΔV is the voltage drop per km expressed by (6.6), and is a function of the cable loading P. In this case, the unity power factor of WTs is assumed.

Furthermore, the load reach of a cable is called the economical load reach if the cable is loaded at the maximum value of its economical loading range indicated in Fig. 6.6. Table 6.2 summarizes the economical load reach of the four three-core XLPE cables at the 20 kV voltage level. The results are obtained on the basis of the economical loading ranges under the condition of Case 1. In practice, the ideal feeder length laid out is the economic load reach. For instance, as shown in Table 6.2, the economical load reach of the 240 mm^2 cable is 11.3 km. If the cable length is longer than 11.3 km, then the maximum loading of the cable must be reduced below its thermal limit (13.3 MW in this case) in order not to exceed the voltage limit. As a result, the cable capacity is not fully utilized. On the other hand, if the cable length is shorter than 11.3 km, the cable has a certain amount of 'unused' voltage rise even the cable is loaded at its thermal limit. Thus, the ideal cable length is the economical load reach of the cable.

Table 6.2
Economical load reach for 20 kV three-core XLPE cables based on the voltage limits of ±6%.

Conductor size (mm^2)	**Maximum loading (MW)**	**Maximum economical loading (MW)**	**Voltage rise per km (%)**	**Economical load reach (km)**
120	9.2	4.9	0.39	15.2
150	10.2	5.6	0.37	16.3
185	11.6	7.3	0.38	15.7
240	13.3	13.3	0.53	11.3

The economical load reach calculation in (6.15) is an approximate calculation based on the voltage rise per km. In general, the load reach of three-core cables at any loading can be obtained accurately through a standard optimal power flow algorithm. The objective function of the optimal power flow is to maximize the cable length at a given loading until the maximum voltage limit is reached. The load reach of the four three-core cables are shown in Fig. 6.7 (a) as a function of active power loading. Each curve has two parts corresponding to voltage limit and current limit. It is observed that the load reach (constrained by voltage limit) shortens exponentially as the loading increases. This is because of the inverse relation between load reach and active power as indicated in (6.15). The part constrained by current limit is not a vertical line but with a positive slope. This can be explained by the use of current rating instead of power rating, which increases slightly as the voltage increases. The exact economical load reach can be found in the curve at the corresponding maximum economical loading of the conductor. The results are very close to the values shown in Table 6.2, with approximately 5% difference.

Fig. 6.7 (b) shows the load reach of 240 mm^2 cables of three different types: three-core, single-core trefoil formation and single-core flat. The three cable types have very similar load reach when the loading is higher than 4 MW. However, the single-core cable with flat formation has the highest current limit, which is around 6% higher than the single-core cable with trefoil formation and 14% higher than the three-core cable. Fig. 6.7 is very useful for finding the load reach (and the economical load reach) of a cable at a given loading condition and for determining the maximum loading at a given load reach without violating the voltage limit and current limit requirements.

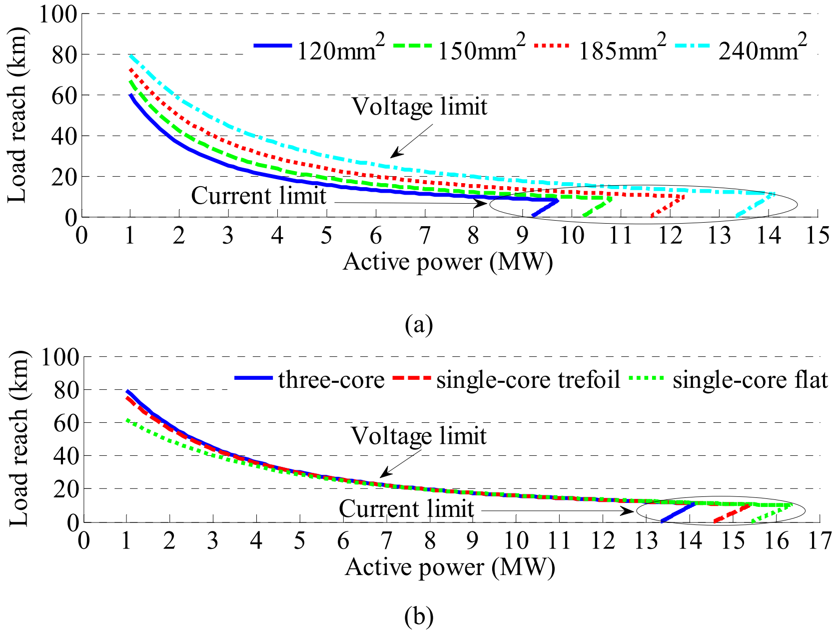

(a)

(b)

Fig. 6.7. Load reach of 20 kV XLPE cables at the voltage limit of 6%: (a) three-core, (b) 240 mm^2

The load reach and economical loading range of a cable seems to be independent of each other. However, the load reach affects the determination of the economical loading range of a cable. This can be illustrated through Fig. 6.8, which shows the voltage rise per km of the four 20 kV three-core cables as a function of loading. The economical loading ranges for the cables are marked by the thicker part of each line in the figure. Assume that a cable length of 17 km is required. For a 6% voltage limit, a maximum 0.35% voltage rise per km is allowed. If the WT has the capacity of 7 MW, according to the economical loading ranges shown in Fig. 6.8, the 185 mm^2 cable should be selected. However, in this case, the voltage rise per km is 0.37% and will lead to a voltage rise of 6.3% at the end of the cable. This is not allowed as it violates the voltage limit requirement. Consequently, the economical loading ranges should be updated to the one shown in Fig. 6.9. In this case, the 240 mm^2 cable should be selected instead. It is noted that only around 53% (= 7/13.3) of the thermal capacity of the 240 mm^2 cable is utilized. If considering that WPG is normally lower than 7 MW during a year, the planner may still choose the 185 mm^2 cable instead of the 240 mm^2 cable and limit the loading below 6.7 MW. This implies that a certain amount of wind energy needs to be curtailed during a year.

In summary, the following procedure is used to determine the optimal conductor size of cables:

1) Select all types and conductor sizes of cables that are available,
2) Determine the evaluation period, present worth factor and price per MWh power losses,
3) Calculate annual cable losses based on time series data of wind power,
4) Obtain economical loading ranges of all the cables based on the overall cost of each cable,
5) Derive load reach curves based on the voltage limits and current limits requirement,
6) Update the economical loading ranges based on the load reach curves,
7) Determine the optimal cable type and size according to the updated economical loading ranges and calculate corresponding overall costs.

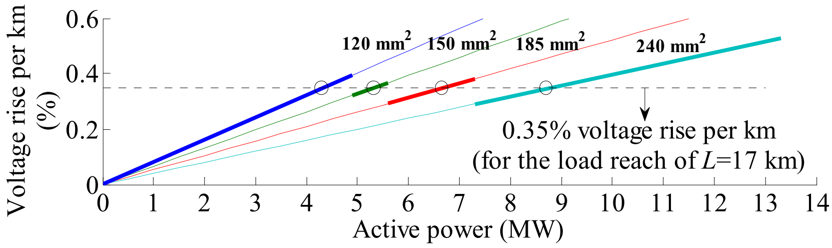

Fig. 6.8. Voltage rise per km of the four 20 kV three-core cables as a function of loading.

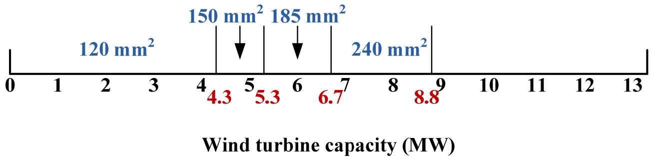

Fig. 6.9. Updated economical loading range of 20 kV three-core cables for the load reach of 17 km.

6.4 Götene 20 kV wind energy network

This section provides two examples of optimal cable sizing for a 20 kV wind energy network according to the procedure described above. The two examples have two different total WT capacities. The effect of WT capacity factor on the optimal cable sizing is investigated in the end.

6.4.1 Low wind turbine capacity

Fig. 6.10 shows the configuration of the 20 kV wind energy network connected to the Götene grid. There are in total 8 WTs, each rated 2 MW. The aim is to the select the conductor size of the cables to be used for the 20 kV network. The investigated cable conductor sizes are 120 mm^2, 150 mm^2, 185mm^2 and 240 mm^2. It is also assumed that the ground temperature is 20 ^{o}C, the laying depth is 1 m, and the ground thermal resistivity is 1 km/W. According to 0, the total cable current rating factor for the base case is 1. The cable conductor temperature is assumed to be 90 ^{o}C.

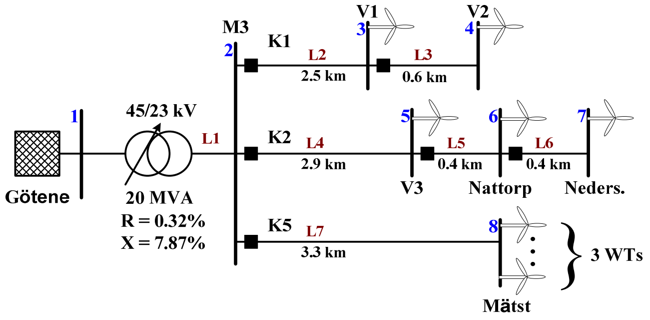

Fig. 6.10. 20 kV wind energy network connected to the Götene grid.

Assume that the *PW* factor is 0.9 and the evaluation period is 20 years. As demonstrated in Fig. 6.6, the electricity price used for evaluating the cost of power losses has a significant impact on the economical loading ranges of the cables. Therefore, the hourly time series of Elspot market price in 2007 from

Energinet.dk is used to calculate the cost (Energinet.dk 2009). The Elspot market price in 2007 is shown in Fig. 6.11. The maximum electricity price is 150.3 €/MWh and the minimum price is 4.09 €/MWh. On average, the electricity price is 30.3 €/MWh. The hourly wind power data shown in Fig. 6.3 is used to represent the WPG from WTs. A sheath loss factor (γ_1) of 5% is used. The armoring loss factor (γ_2) is neglected. The dielectric loss factor tanδ is 0.001.

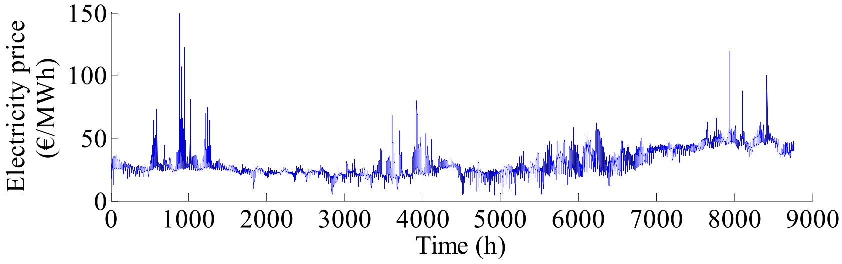

Fig. 6.11. Hourly Elspot market price in 2007 (Energinet.dk 2009).

Fig. 6.12 shows the economical loading ranges of the three-core cables obtained on the basis of the Elspot market price. The load reach curves of the cables are presented in Fig. 6.7 (a). In the network shown in Fig. 6.10, the maximum WT capacity at a feeder is 6 MW. According to Fig. 6.7 (a), the load reach of the three-core cables is at least 13 km at such a low loading. As the maximum length of a single cable in the network is only 3.3 km, there is no overvoltage problem in this case. Thus, the economical loading ranges presented in Fig. 6.12 can be directly used. The economical loading ranges clearly indicate that the cheapest solution is to use the 120 mm^2 cable when the WT capacity is below 7.5 MW. Thus, the 120 mm^2 cable is selected for all the six cables in the network.

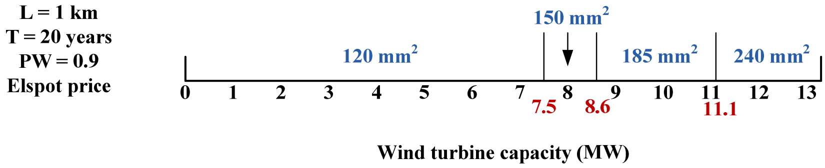

Fig. 6.12. Economical loading ranges of 20 kV three-core cable using Elspot market price.

The present worth costs of the total 10.1 km cables loaded with 16 MW WT are summarized in Table 6.3 for all the four conductor sizes. It is noted that using 120 mm^2 instead of 240 mm^2 saves 63,850 €, which is almost 13% of the total cost. This illustrates the importance of choosing the right cable size.

Table 6.3.
Present worth cost of the total 10.1 km three-core cables over 20 years.

Total WT Capacity (MW)	**Total Cable Costs (€)**				
	120 mm^2	**150 mm^2**	**185 mm^2**	**240 mm^2**	**Optimal cable size**
16 (Fig. 6.10)	506,200	518,640	536,120	570,050	506,200
30 (Fig. 6.13)	653,830	639,690	633,100	644,400	626,560

6.4.2 Higher wind turbine capacity

For a higher total wind turbine capacity in the network, the final choice of the cable conductor sizes may differ significantly. For example, if the WT capacity at each bus is increased to the values shown in Fig. 6.13 (with the total capacity of 30 MW), the corresponding optimal conductor size may change for each feeder or even each section of the feeder. Based on the economical loading ranges shown in Fig. 6.12, the optimal conductor sizes of the network are selected and shown in Fig. 6.13. These conductor sizes include 1 km of 120 mm^2 cable (L3 and L6), 2.9 km of 150 mm^2 cable (L2 and L5), 3.3 km 185 mm^2 cable (L7), and 2.9 km 240 mm^2 cable (L4). Table 6.3 also summarizes the present worth costs of the cables loaded with 30 MW WT using either only one of the four conductor sizes or the optimal combination of the conductor sizes. In this case, it turns out that using 120 mm^2 cable costs the most among the other four options. Using 185 mm^2 cable is cheaper than using any other conductor sizes alone. However, the cheapest solution is to implement the cables with the conductor sizes shown in Fig. 6.13. The minimum present worth cost of the cables is 626,560 €, which saves 27,270 € as compared to using 120 mm^2 cable alone.

In the case that the cable length of feeder K5 is 15 km instead of 3.3 km, the optimal conductor size for the feeder will be different. According to Fig. 6.7 (a), the load reach of a 185 mm^2 cable is only 12 km at the loading of 10 MW. Therefore, the 185 mm^2 cable can no longer be used. Instead, the 240 mm^2 cable is selected for the feeder K5. This leads to a final cost of 1,421,000 € for a total cable length of 21.8 km.

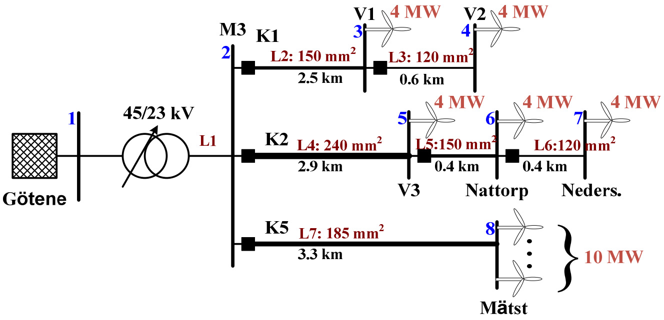

Fig. 6.13. 20 kV wind energy network with higher WT capacity.

6.4.3 The effect of WT capacity factor

WPG from a WT may vary greatly at a different location. In particular, the capacity factor of the WT changes as the wind condition changes. This may also happen at the same wind location in a different year. Although the WT capacity is not changed, the mean value or the capacity factor of a WT may increase if the wind level is relatively high during the year, and vice versa. This change in WPG affects the power losses on the cable, which may alter the economical loading range of the cables.

As the above analyses are all based on a one-year time series measured in 2007, which may not be representative of the WPG of the WT over 20 years. Therefore, it is useful to investigate the effect of WT capacity factor on the economical loading range and consequently the choice of cable conductor sizes. In order to perform such a sensitivity analysis, wind power time series measured at different years should be collected. However, these data are usually difficult to obtain, especially when the WT has only been operating for a short period. On the other hand, it is not possible to simply scale up or down the wind power time series as this will change the maximum wind power production. To address this issue, the stochastic wind power model developed in Chapter 2 can be particularly useful. The LARIMA(0,1,1) model can be used to generate synthetic wind power time series at any given capacity factor by tuning the parameter θ_0. Although the LARIMA(0,1,1) was developed for a different wind power time series at a different location, the conclusion drawn below is still valid.

Therefore, in order to investigate the effect of capacity factor of WTs, four synthetic wind power time series have been generated according to the LARIMA(0,1,1) model, with θ_0 equal to −0.1, −0.05, 0.03, 0.1, respectively. The capacity factors of the four time series are 0.18, 0.25, 0.38 and 0.48. Fig. 6.14 shows the corresponding economical loading ranges of the three-core cable for the four synthetic wind power time series. The economical loading ranges of the three-core cables are shifted to the left as the capacity factor of the WT increases. This is due to higher power losses on the cable when more WPG is transmitted. It is also observed that when the capacity factor is relatively low, the economical loading ranges are more sensitive to the change in the capacity factor. For example, for the case shown in Fig. 6.13, if the capacity factor of the WT is 0.18, then cable L2 should use 120 mm^2 conductor size instead of 150 mm^2. This sensitivity analysis also demonstrates that it is important to have a wind power time series of several years so that it covers various possible wind situations.

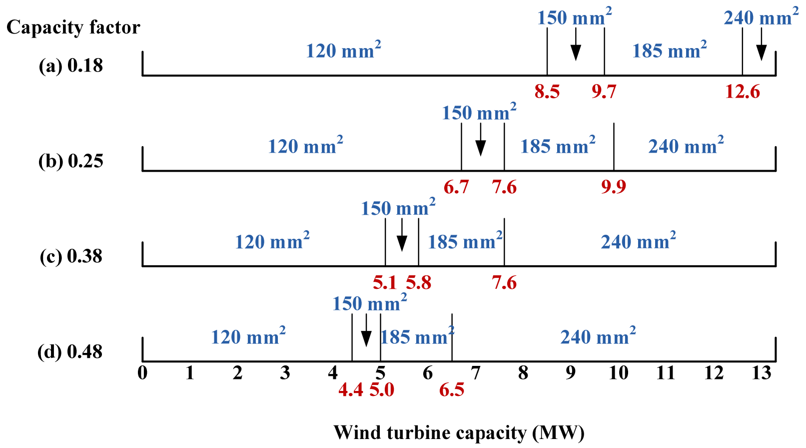

Fig. 6.14. The effect of wind turbine capacity factor on economical loading range.

6.5 Summary

This chapter has discussed the optimal cable sizing on the basis of economical loading range and load reach. The economical loading range provides the information about the cheapest cable type or conductor size at various loading conditions. In theory, the economical loading ranges are independent of the cable length if no voltage and current limits requirements are imposed. However, in reality, this is not the case. Therefore, the load reach information is introduced for each cable type and conductor size. The load reach transforms the voltage and current limits requirements into the information of maximum cable length under different loading conditions. In other words, load reach provides the information of how the voltage and current limits affect the choice of optimal cable design through the assessment of cable length. This significantly simplifies the evaluation of optimal cable sizing. Otherwise, the evaluation has to resort to a much more complex nonlinear constrained optimization problem that involves a significant number of discrete variables including cable type, conductor size and cable length and continuous variables such as the cable loading. In addition, the implication of the results from such an optimization problem is much more obscure than the ones obtained according to economical loading range and load reach. Finally, two cases with different network WT capacities are used to demonstrate the optimal sizing of the cables in the Götene 20 kV wind energy network. Both cases show savings that can be obtained by choosing the most economical conductor sizes for the network. A sensitivity analysis is followed to investigate the effect of WT capacity factor on the economical loading range and cable sizing. It is concluded that the economical loading ranges are shifted to the left when the capacity factor increases. In other words, it becomes more economical to use a thicker cable when the capacity factor of WTs is high.

Chapter 7

Stochastic Evaluation of Maximum Wind Turbine Capacity

This chapter aims to find the maximum WT capacity of a medium voltage distribution system. The evaluation considers the stochastic behavior of load demand and WPG. First, the evaluation is carried out on a single cable. Then, the evaluation is extended to a radial feeder. Third, an optimization algorithm that combines the constrained nonlinear optimization and the Monte Carlo based constrained load flow is proposed to assess the maximum WT capacity of a distribution system. Finally, a study case based on the 20 kV Støvring distribution system is used to demonstrate the proposed optimization algorithm.

7.1 Evaluation on a single cable

The capability of a cable to transmit power is constrained by the current and voltage limit requirements of the cable. Thus, a cable has a maximum intake of wind power. The evaluation of the maximum wind power is similar to the evaluation of the load reach of a cable shown in Fig. 6.7. The difference is that in this case it searches for the maximum wind power instead of the maximum cable length. Furthermore, the maximum wind power transmitted also depends on the power factor setting or the reactive power output of the WT. Such a maximization issue can be formulated as a standard nonlinear constrained optimization problem (Arora 2004). The objective function of the optimization problem is to maximize the WT capacity P_{r} with respect to the power factor ϕ of the WT:

$$\text{Max } P_{\mathrm{r}}(\phi), \tag{7.1}$$

subject to

$$|\phi| \le \phi_{\max}, \tag{7.2}$$

$$V_{\min} \le V_{\text{cable}} \le V_{\max}, \tag{7.3}$$

$$I_{\text{cable}} \le I_{\max}. \tag{7.4}$$

According to (7.1)-(7.4), simulations are carried out on a three-core 120 mm^2 cable with the same wind power time series as in Fig. 6.3. The cable length varies from 0.1 km to 60 km at a step of 0.1 km. Fig. 7.1 (a) shows the maximum WT capacity of the cable under three different power factor settings: 1) unity power factor ($\tan\phi = 0$), 2) power factor no less than 0.8 ($|\tan\phi| \le 0.75$), and 3) any power factor values ($|\tan\phi| \le \infty$). As expected, the solid curve ($\tan\phi = 0$) in Fig. 7.1 (a) is identical to the load reach curve (the solid one) shown in Fig. 6.7 (a). However, as the power factor range is widened, the maximum WT capacity is increased. For instance, for a 40 km cable, the maximum WT capacity of the cable is 1.8 MW when $\tan\phi = 0$, but increased to 2.4 MW when $|\tan\phi| \le 0.75$ and to 5.6 MW when $|\tan\phi| \le \infty$. This indicates that the power factor setting of the WT has a significant impact on the maximum wind power intake of a cable. Fig. 7.1 (b) shows the corresponding optimal power factor setting of the WT. In the case of $|\tan\phi| \le \infty$, the optimal power factor angle reaches -56^0 at the maximum WT capacity of 5.4 MW. Consequently, a large amount of reactive power is drawn by the WT to bring down the voltage rise. However, the large reactive power drawn causes high active power losses on the cable. This can be seen from Fig. 7.1 (c), which shows the active power injected to the grid as a percentage of the active power generated from the WT. In the case of -56^0 power factor angle, the injected power to the grid is less than 40% of the active power generated from the WT. In other words, more than 60% of the wind power is dissipated as losses. The high power losses are apparently not favored in the actual application. Furthermore, the rating of the WT converters is usually only overrated 125%. Thus, as also discussed in Chapter 4, it is reasonable to limit the WT power factor to a certain value such as 0.8.

Another way to increase the annual generated wind energy is to allow a certain amount of energy curtailment so that the installed WT capacity can be increased. The relation between the annual generated wind energy E and the installed WT capacity P_r can be calculated by:

$$E = C_f \cdot 8760 \cdot P_r \cdot (1 - C_E), \qquad (7.5)$$

where C_f is the capacity factor of the WPG; P_r is the installed capacity of the WT; C_E is the allowed energy curtailment in percentage. The capacity factor of the wind power time series in Fig. 6.3 is 0.25.

In the case when $C_E = 0$, which is no energy curtailment, the maximum WT capacity can be determined using Fig. 7.1 (a). In the case when $C_E > 0$, the maximum WT capacity depends on the probability distribution of the wind power. Fig. 7.2 shows the cumulative distribution function of the wind power time series in Fig. 6.3. If C_E = 5%, then the corresponding wind power is 0.812 p.u. Thus, the maximum WT capacity is increased to 123% (= 1/0.812). Consequently, according to (7.5), the annual generated wind energy E rises to 117% (= 123%×(1−5%)) of the value in the case when no energy curtailment is allowed. For this particular wind power time series, Fig. 7.3 shows the increased percentage of annual wind energy and installed WT capacity when the annual wind energy is curtailed from 0 to 20%. The figure shows that the annual wind energy has a slower increment than the installed WT capacity.

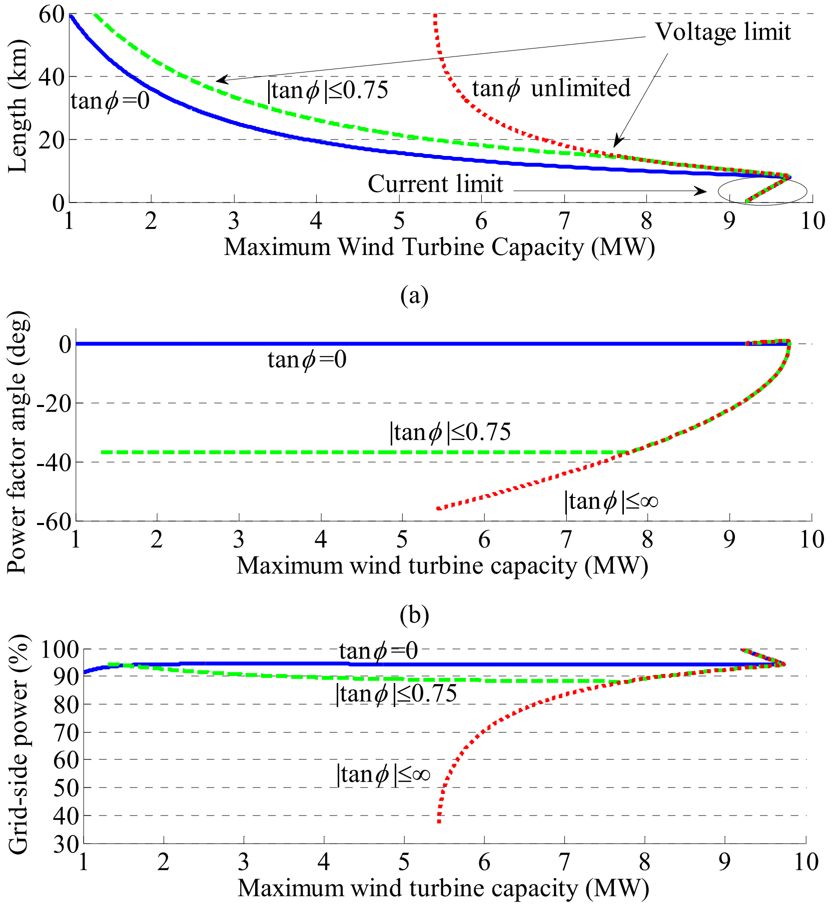

(a)

(b)

(c)

Fig. 7.1. Maximum wind turbine capacity of a 20 kV 120 mm^2 three-core cable under different power factor values: (a) for different cable length, (b) corresponding optimal power factor angle, and (c) grid-side active power in percentage of maximum wind turbine capacity.

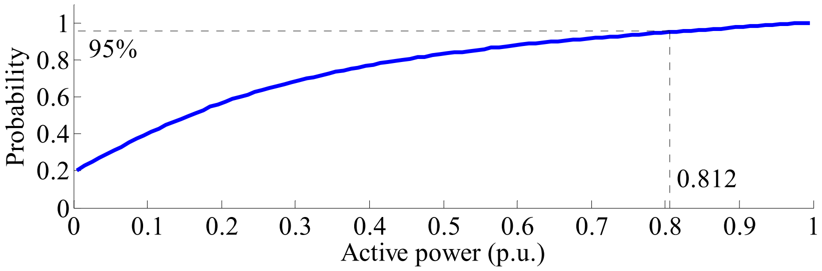

Fig. 7.2. Cumulative distribution function of the measured wind power time series shown in Fig. 6.3.

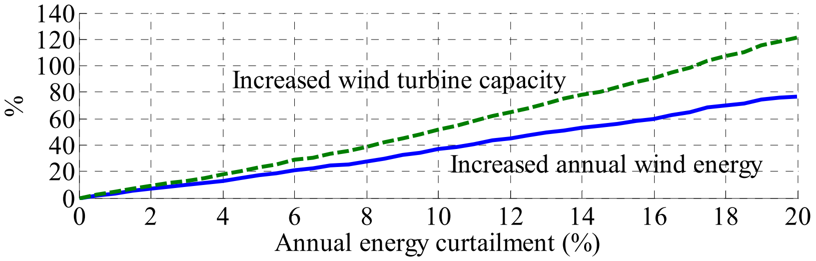

Fig. 7.3. Increased annual wind energy and wind turbine capacity due to annual energy curtailment.

7.2 Evaluation on a radial feeder

Normally, WTs are distributed along a radial feeder as shown in Fig. 7.4. According to Fig. 7.1 (a), when the voltage limit is the main constraint, the maximum WT capacity increases as the cable length decreases. Therefore, in order to maximize the total WT capacity on the feeder, all the WTs should be connected to as close as possible to the grid, e.g., bus 1. In this case, the method described in section 7.1 can be used to determine the maximum WT capacity. On the other hand, when the current limit becomes the main constraint, the maximum WT capacity increases as the cable length increases. This is because a longer cable induces higher voltage rise, which causes a lower current at a fixed power injection. This makes the optimal allocation of WTs less straightforward than the case with voltage limit constraint. The solution can also be based on the optimization similar to (7.1) but with two control variables. For instance, for the radial feeder shown in Fig. 7.4, assume that $n = 2$, $L_1 = L_2$, and the cable is three-core with conductor size of 120 mm^2. For such a two-section feeder, the maximum WT capacity at bus 1 (P_{r1}) and bus 2 (P_{r2}) are presented in Fig. 7.5. When the feeder length is longer than 16 km, the main constraint is the voltage limit (1.06 p.u.) at bus 2. Thus, all the wind power is injected to bus 1 (P_{r1} is maximum) and P_{r2} is zero. When the feeder length is shorter than 16 km, the current limit of section L_1 becomes the dominant constraint. Consequently, more and more wind power is injected into bus 2 so that the current through section L_1 is reduced as the voltages at bus 1 and bus 2 rises. When the feeder length decreases even further (≤ 10.7 km), the voltage at bus 2 drops rapidly, which leads to a slight cutback of P_{r2}.

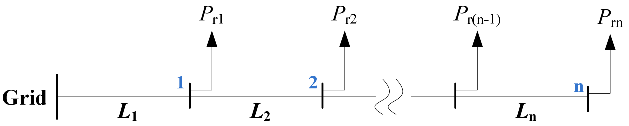

Fig. 7.4. WTs connected to a radial feeder of a cable.

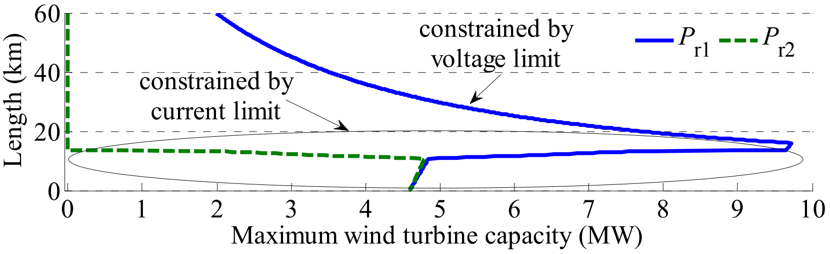

Fig. 7.5. Maximum wind turbine capacity at bus 1 and bus 2 of a two-section feeder.

It is also not complicated to evaluate the maximum WT capacity of the feeder if involving reactive power control of the WTs. Similar curves to the ones in Fig. 7.5 can be obtained. Furthermore, if energy curtailment is also considered, for the case when the dominant constraint is voltage limit, the solution is to curtail the wind energy from the WTs connected at the end of the feeder first. However, this is not the case when the dominant constraint is current limit. The optimal solution is not to cut for example 5% of wind energy at both WT locations as the maximum WT capacity of the feeder does not increase linearly with respect to the WT capacity at each location.

Moreover, in the case when the feeder is mixed with load demand and WPG as shown in Fig. 7.6, the optimal solution also becomes more complex. The reason is that the load demand at bus 1 causes a forward voltage drop, which varies as the load fluctuates. This voltage drop compensates the voltage rise caused by the wind power at bus 2. Consequently, the voltage at bus 2 is not necessarily the highest when the WT generates at its rated power as it also depends on the voltage drop at bus 1. In other words, if the strategy of energy curtailment is employed, it is not necessarily to curtail the top 5% wind energy as discussed in section 7.1. In this case, in order to evaluate maximum WT capacity, a more detailed analysis is required to include both the stochastic load variation and wind power variation. Such an analysis may require another optimization process for the energy curtailment.

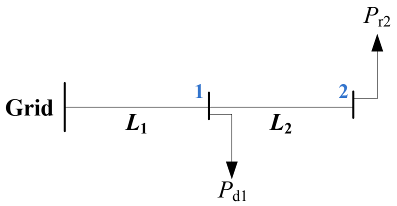

Fig. 7.6. A two-section feeder with load demand and wind power generation.

Fig. 7.7 (a) presents a potential solution to the above problem. It mainly consists of two optimization loops: the outer loop maximizes the total WT capacity and the inner loop minimizes the energy curtailment while fulfilling the technical constraints. In order to account for the stochastic variation of WPG and load when curtailing the wind energy, a Monte Carlo simulation is adopted to carry out the inner-loop optimization. This leads to a large number of optimization calculations, which increase the simulation time drastically.

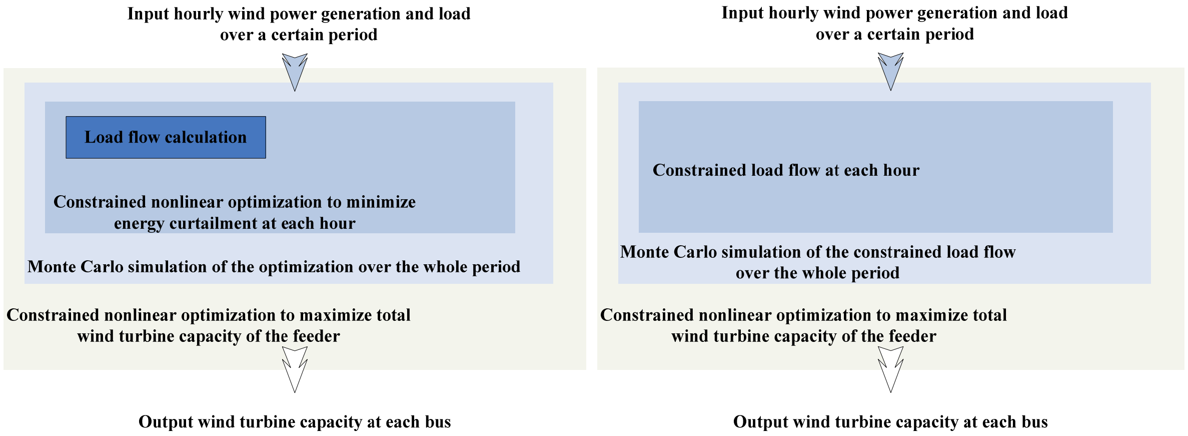

(a) (b)

Fig. 7.7. Potential solutions to finding the maximum wind turbine capacity of a feeder considering energy curtailment: (a) based on constrained nonlinear optimization, (b) based on constrained load flow.

In order to alleviate the computation burden, a constrained load flow algorithm (Karakatsanis, Hatziargyriou 1994) is employed to substitute for the load flow calculation and the inner-loop optimization. The new optimization process is shown in Fig. 7.7 (b). In this case, the inner-loop constrained nonlinear optimization is eliminated. In addition, the Monte Carlo simulation of the constrained nonlinear optimization is replaced by the Monte Carlo simulation of the constrained load flow. This contributes to the reduction of the computation time without compromising the accuracy of the optimization process. The following section introduces the constrained load flow algorithm based on sensitivity analysis (Karakatsanis, Hatziargyriou 1994, Hatziargyriou, Karakatsanis 1994, Hatziargyriou 2000).

7.3 Constrained load flow based on sensitivity analysis

This section presents the fundamental theory of constrained load flow based on sensitivity analysis. A detailed derivation of sensitivity factors is shown in 0.

7.3.1 Constrained load flow

The standard load flow equations can be formulated as (Karakatsanis, Hatziargyriou 1994):

$$\mathbf{Y} = \mathbf{g}(\mathbf{X}, \mathbf{U}), \tag{7.6}$$

$$\mathbf{Z} = \mathbf{h}(\mathbf{X}, \mathbf{U}), \tag{7.7}$$

where **Y** is the input vector of nodal power injections; **X** is a set of system states including voltage magnitude and phase angle; **Z** is a set of output vectors including active and reactive power flow; **U** is a set of control variables that constrain selected electrical quantities in a power system; **g** and **h** are standard load flow functions (Saadat 2002).

The common control variables **U** are as follows:

- Tap ratio *a* of tap-changing transformers,
- Amount of reactive power compensation, e.g. from switchable capacitor banks, static var compensators, static synchronous compensators, etc
- Voltage magnitude and active power generation at PV buses,
- Load to be shed.

Whereas the common constrained variables **W** are:

- Voltage magnitude at load buses or other critical buses,
- Reactive power generation/consumption at PV buses,

- Current magnitude, active power flow, reactive power flow or apparent power flow through power lines and transformers.

The control variables **U** are adjusted in order to fulfill the technical requirements of system operation. However, the control variables themselves are usually also constrained due to physical limitations. These limitations can be:

- Minimum and maximum values of tap ratio (maximum number of tap steps),
- Minimum and maximum values of reactive power generation/absorption, due to the limited capacity of an individual capacitor and number of capacitors, maximum equivalent inductance and capacitance of an static var compensator, current rating of power electronic valves and voltage of DC capacitor, etc.
- Minimum and maximum allowed voltage and active power setting of generators,
- Maximum amount of load that can be shed.

Normally, an unconstrained load flow calculation may result in a number of operating violations in the system states **X** and outputs **Z**. Thus, the main objective of a constrained load flow calculation is to confine the selected system states **X** and outputs **Z** within their allowed limits. This is achieved by adjusting the selected control variables **U**. The principle of the adjustment can be based on a sensitivity analysis, i.e. how sensitive the constrained variables are with respect to the changes of the control variables. The core of such a sensitivity analysis is to obtain the corresponding first-order sensitivity factor. This is discussed in detail in the following subsection.

7.3.2 Calculation of sensitivity factors

Assume that the constrained variables **W** are a function of system states **X** and control variables **U**:

$$\mathbf{W} = \mathbf{f}(\mathbf{X}, \mathbf{U})\,. \tag{7.8}$$

According to the common types of constrained variables described in the previous subsection, the function **f** contains a selected number of load flow equations in (7.6) and (7.7).

Linearizing (7.8) at the initial operating point ($\mathbf{X}_0$, $\mathbf{U}_0$) gives (Karakatsanis, Hatziargyriou 1994):

$$\mathbf{W} = \mathbf{W}_0 + \sum_{ct=1}^{\mathbf{M}} \frac{\mathrm{d}\mathbf{f}}{\mathrm{d}u_{ct}} \Delta u_{ct} \ , \tag{7.9}$$

where $\mathbf{W}_0 = \mathbf{f}(\mathbf{X}_0, \mathbf{U}_0)$; $\mathbf{M}$ is the vector of total control variables; $\frac{\mathrm{d}\mathbf{f}}{\mathrm{d}u_{\mathrm{ct}}}$ is the sensitivity factor. For a particular constrained variable w, the sensitivity factor can be further expressed as (Karakatsanis, Hatziargyriou 1994):

$$\frac{\mathrm{d}f(\mathbf{X},\mathbf{U})}{\mathrm{d}u_{ct}} = \frac{\partial f(\mathbf{X},\mathbf{U})}{\partial u_{ct}} + \left[\frac{\partial f(\mathbf{X},\mathbf{U})}{\partial \mathbf{X}}\right]^{\mathrm{T}} \frac{\partial \mathbf{X}}{\partial u_{ct}}, \tag{7.10}$$

where $\mathbf{X}=[x_1, \ldots, x_{2\mathrm{n-s-1}}]^{\mathrm{T}}$; $\mathbf{U}=[u_1, \ldots, u_{\mathrm{m}}]^{\mathrm{T}}$; n is the total bus number; s is the total PV bus number; m is the total number of control variables used to constrain w. The first-order partial derivative of (7.6) with respect to u_{ct} gives:

$$0 = \frac{\partial \mathbf{g}(\mathbf{X},\mathbf{U})}{\partial u_{ct}} + \frac{\partial \mathbf{g}(\mathbf{X},\mathbf{U})}{\partial \mathbf{X}} \frac{\partial \mathbf{X}}{\partial u_{ct}}. \tag{7.11}$$

Rearranging (7.11) gives:

$$\frac{\partial \mathbf{X}}{\partial u_{ct}} = -\left[\frac{\partial \mathbf{g}(\mathbf{X},\mathbf{U})}{\partial \mathbf{X}}\right]^{-1} \frac{\partial \mathbf{g}(\mathbf{X},\mathbf{U})}{\partial u_{ct}}. \tag{7.12}$$

Substituting (7.12) to (7.10) gives the expression of the sensitivity factor:

$$\frac{\mathrm{d}f(\mathbf{X},\mathbf{U})}{\mathrm{d}u_{ct}} = \frac{\partial f(\mathbf{X},\mathbf{U})}{\partial u_{ct}} - \mathbf{A}^{\mathrm{T}} \frac{\partial \mathbf{g}(\mathbf{X},\mathbf{U})}{\partial u_{ct}}, \tag{7.13}$$

where

$$\mathbf{A}^{\mathrm{T}} = \left[\frac{\partial f(\mathbf{X},\mathbf{U})}{\partial \mathbf{X}}\right]^{\mathrm{T}} \left[\frac{\partial \mathbf{g}(\mathbf{X},\mathbf{U})}{\partial \mathbf{X}}\right]^{-1} = \left[\frac{\partial f(\mathbf{X},\mathbf{U})}{\partial \mathbf{X}}\right]^{\mathrm{T}} \mathbf{J}^{-1}, \tag{7.14}$$

where **J** is the Jacobian matrix of the load flow equations. Matrix A has a dimension of $(2n - s - 1) \times 1$. In summary, (7.13) and (7.14) provide a generic calculation for the sensitivity factor of the constrained variable w with respect to the control variable u_{ct}. The following subsection provides an example to illustrate the sensitivity factor calculation concerning active and reactive power control of a WT.

7.3.3 Sensitivity analysis with wind turbines

A WT can control its reactive power output by switching capacitor banks or through power electronic controllers. A WT can also regulate its active power output through pitch control or crowbar. Normally, a WT does not control its terminal voltage and is thus treated as a PQ node in a load flow calculation.

During system operation when the power production is low and the load demand is high, undervoltage at the load buses may occur. In contrast, when the power production is high and the load demand is low, overvoltage at certain buses may occur. Undervoltage can be mitigated if the WTs generate reactive power to boost the bus voltage. Similarly, overvoltage can be mitigated if the WTs absorb reactive power from the network or reduce the active power injection to the network. Besides voltage regulation, the WTs can also reduce the line current by regulating the reactive power output and curtailing a certain amount of wind energy during contingency periods. This indicates that both active and reactive power outputs of WTs can be treated as control variables, while the bus voltage and line current can be treated as constrained variables. Therefore, the related sensitivity factors are $\mathrm{d}V/\mathrm{d}P$, $\mathrm{d}V/\mathrm{d}Q$, $\mathrm{d}I/\mathrm{d}P$ and $\mathrm{d}I/\mathrm{d}Q$. According to (7.13) and (7.14), in order to obtain these sensitivity factors, the following three terms need to be calculated:

$$\frac{\partial f(\mathbf{X},\mathbf{U})}{\partial u_{ct}}, \ \frac{\partial \mathbf{g}(\mathbf{X},\mathbf{U})}{\partial u_{ct}}, \text{ and } \frac{\partial f(\mathbf{X},\mathbf{U})}{\partial \mathbf{X}}.$$

In the following, only the calculation of sensitivity factors $\mathrm{d}V/\mathrm{d}P$ and $\mathrm{d}V/\mathrm{d}Q$, will be demonstrated. The derivation for other types of sensitivity factors can be found in 0.

The sensitivity factor calculation is demonstrated on the basis of the generic network shown in Fig. 7.8. In the network, a WT is connected at bus i, injecting active power P_i and reactive power Q_i to the network. Furthermore, the voltage magnitude at bus j and the current magnitude through line jk need to be constrained within the required limits.

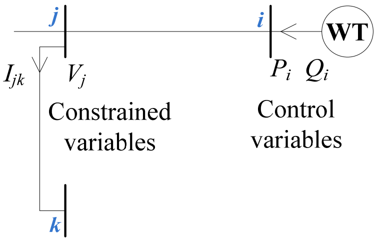

Fig. 7.8. A Generic network for sensitivity analysis with wind turbines.

In this case, the voltage magnitude V_j is constrained by controlling active power P_i and reactive power Q_i. Thus, the constrained variable is $W = f(\mathbf{X}, \mathbf{U}) = V_j$, and the control variables are $\mathbf{U} = [P_i,\ Q_i]$. Consequently, the sensitivity factors of interest are $\frac{\mathrm{d}V_j(\mathbf{X},\mathbf{U})}{\mathrm{d}P_i}$ and $\frac{\mathrm{d}V_j(\mathbf{X},\mathbf{U})}{\mathrm{d}Q_i}$. The following calculates the above three terms for these two sensitivity factors.

1) Calculation of $\frac{\partial f(\mathbf{X},\mathbf{U})}{\partial u_{ct}}$

As voltage magnitude is a system state, its partial derivatives with respect to system inputs are zero:

$$\frac{\partial V_j}{\partial P_i} = 0 \tag{7.15}$$

$$\frac{\partial V_j}{\partial Q_i} = 0 \tag{7.16}$$

2) Calculation of $\frac{\partial \mathbf{g}(\mathbf{X},\mathbf{U})}{\partial u_{ct}}$

According to (7.6), $\mathbf{g}(\mathbf{X}, \mathbf{U}) = \mathbf{Y}$, which is the nodal power injection. Thus, the nodal power injection at bus t does not depend on the nodal power injection at any other buses. This leads to:

$$\frac{\partial P_t}{\partial P_i} = \begin{cases} 1, & t = i \\ 0, & t \neq i \end{cases} \tag{7.17}$$

$$\frac{\partial Q_t}{\partial P_i} = 0 \tag{7.18}$$

$$\frac{\partial P_t}{\partial Q_i} = 0 \tag{7.19}$$

$$\frac{\partial Q_t}{\partial Q_i} = \begin{cases} 1, & t = i \\ 0, & t \neq i \end{cases} \tag{7.20}$$

3) Calculation of $\frac{\partial f(\mathbf{X}, \mathbf{U})}{\partial \mathbf{X}}$

System states X include voltage magnitude V_t and phase angle θ_t. Thus, it is straightforward that

$$\frac{\partial V_j}{\partial V_t} = \begin{cases} 1, & t = j \\ 0, & t \neq j \end{cases} \tag{7.21}$$

$$\frac{\partial V_j}{\partial \theta_t} = 0 \tag{7.22}$$

Consequently, according to (7.13) to (7.22), the sensitivity factor $\mathrm{d}V_j/\mathrm{d}P_i$ and $\mathrm{d}V_j/\mathrm{d}Q_i$ can be easily calculated.

7.3.4 Constrained load flow algorithm

Based on the above sensitivity calculations, Fig. 7.9 shows the flow chart of the constrained load flow algorithm. The constrained load flow algorithm implements three main subroutines into the standard Newton-Raphson based load flow algorithm. The main purpose of these subroutines is to constrain the bus voltages and the line currents by regulating the WT power output. The first subroutine checks if the lower limit of the voltage is violated. In the case of undervoltage, the reactive power control of the WT is activated. The second subroutine checks if the upper limit of the voltage is violated. In the case of overvoltage, the reactive power control is activated first. If the reactive power output reaches its limit, then the active power control takes over by curtailing wind power. The third subroutine checks if overcurrent through a line occurs. In this case, the strategy of wind power curtailment is applied.

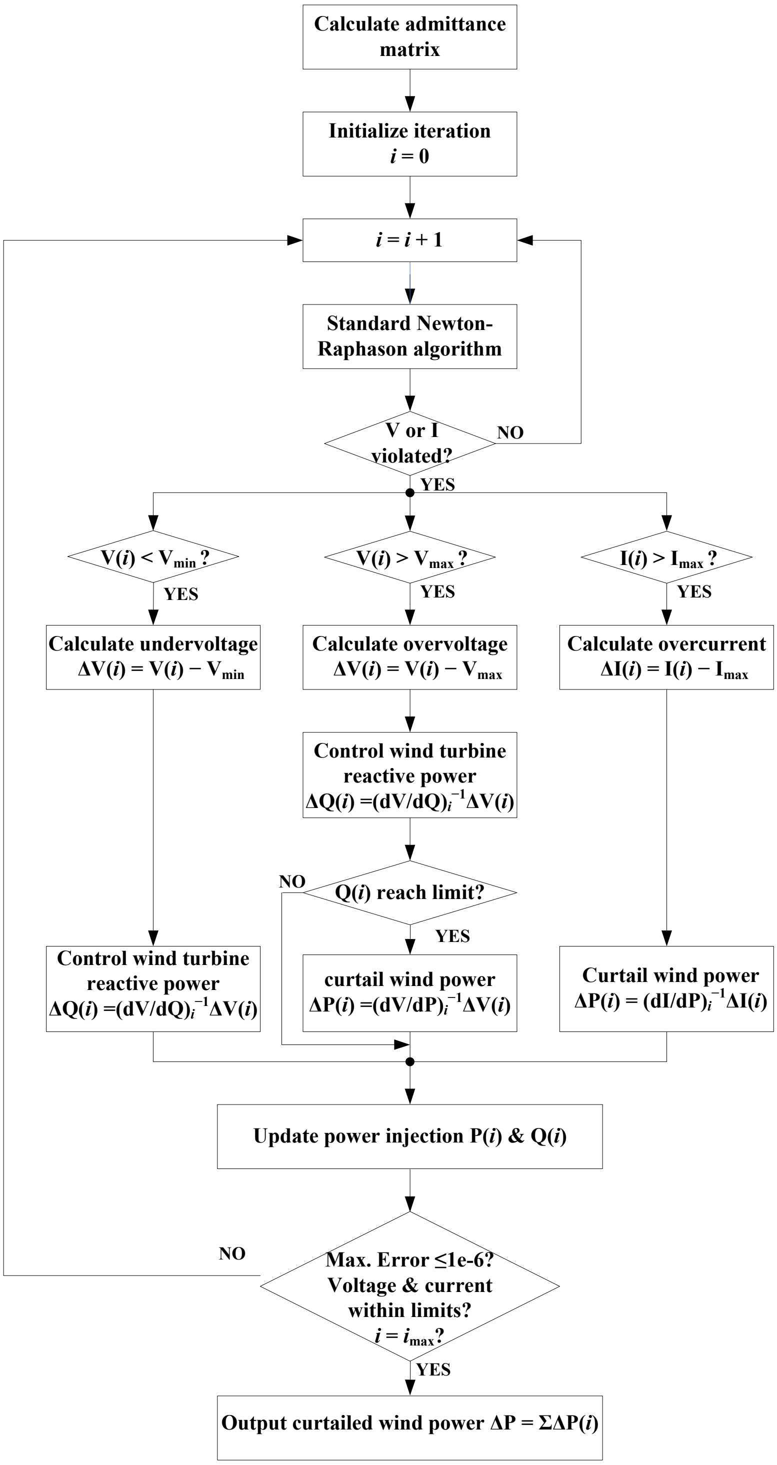

Fig. 7.9. Flow chart of constrained load flow algorithm with reactive power control and energy curtailment of WT.

7.3.5 Simulation results

In order to demonstrate the constrained load flow algorithm in Fig. 7.9, simulation studies are carried out on the two-section feeder shown in Fig. 7.6. The studies include the following three scenarios.

a) Constrain the voltage at bus 2 by controlling the WT reactive power output

In this scenario, the load power at bus 1 is (1 + j0.48) MVA, and the initial wind power at bus 2 is (5 + j0) MVA. The maximum reactive power of the WT is set to 75% of the rated capacity. The standard load flow results show that the voltage at bus 2 is 1.068 p.u. However, the maximum voltage allowed is 1.06 p.u. Thus, the voltage needs to be lowered by controlling the WT reactive power output.

Fig. 7.10 (a) shows the bus 2 voltage at each iteration of the constrained load flow. The voltage is settled to the maximum limit 1.06 p.u. in 12 iterations. Fig. 7.10 (b) shows the corresponding sensitivity factor dV_2/dQ_2, which evaluates the change in voltage at bus 2 with respect to the change in reactive power output of the WT at the same bus. The sensitivity factor is also updated at each iteration. The negative value indicates that the WT absorbs reactive power. According to the sensitivity factor, the voltage changes by around 5% for a unit change of reactive power.

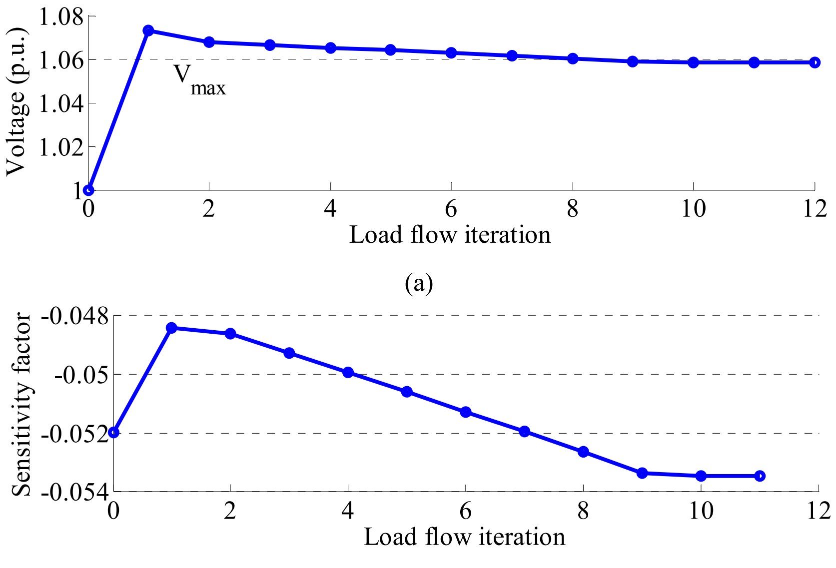

(a)

(b)

Fig. 7.10. Constrain bus voltage by controlling only reactive power output of a 5 MW wind turbine: (a) Voltage at bus 2, (b) sensitivity factor dV_2/dQ_2.

Fig. 7.11 (a) presents the step change of the WT reactive power at each iteration. Fig. 7.11 (b) shows the reactive power output at each iteration. In total, the WT absorbs 1.79 MVAr reactive power (power factor 0.94). For the first few iterations in a load flow calculation, the voltage deviation can be quite large, which may cause a large step change in reactive power. This may lead to an unnecessary reduction of the reactive power, which constrains the voltage to be well below the maximum limit. Thus, the step change in reactive power is limited to a certain maximum value. In this case, it is set to 0.25 MVAr. This can be seen in Fig. 7.11 (a) between iteration 1 and 7. When the voltage is slightly higher than the maximum value at 8th iteration, the reactive power output is adjusted by a small amount (−0.03 MVAr) so that the voltage at the next iteration reaches 1.06 p.u. This indicates that the first-order sensitivity factor can fine-tune the voltage when it is close to the reference value (1.06 p.u.).

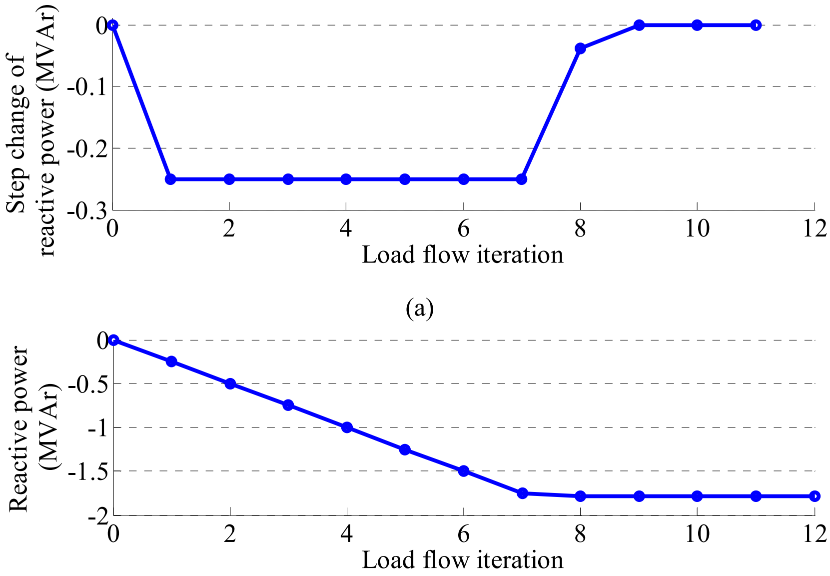

Fig. 7.11. Constrain bus voltage by controlling only the reactive power output of a 5 MW wind turbine: (a) step change of the wind turbine reactive power output, (b) the wind turbine reactive power output.

b) Constrain the voltage at bus 2 by controlling the WT reactive power and active power output

This scenario is similar to scenario a), but the initial wind power at bus 2 is increased to (8 + j0) MVA. If only using the reactive power control, the voltage at bus 2 converges to 1.076 p.u. as shown in Fig. 7.12. The voltage is not constrained to 1.06 p.u. This is because the reactive power absorbed by the WT reaches the maximum value. Thus, in order to keep the voltage within limits, the WT needs to reduce its active power generation. In other words, a certain amount of wind energy needs to be curtailed.

Consequently, with both the reactive and active power control of the WT, the voltage at bus 2 is reduced to its maximum value as shown in Fig. 7.13 (a). It takes around 34 iterations for the algorithm to converge. Fig. 7.13 (b) shows the sensitivity factor dV_2/dP_2, which evaluates the change in voltage at bus 2 with respect to the change in active power output of the WT. The negative value indicates that the WT needs to lower the active power output in order reduce the voltage. The sensitivity factor dV_2/dP_2 is around three times higher than the sensitivity factor dV_2/dQ_2 as shown in Fig. 7.10 (b). This is because for the three-core 120 mm^2 cable, the R/X ratio is around three.

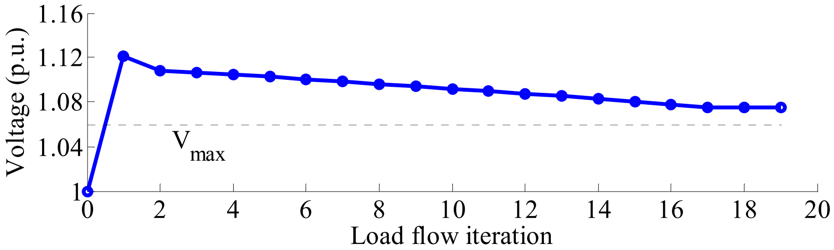

Fig. 7.12. Constrain bus voltage by controlling only the reactive power output of an 8 MW wind turbine with minimum power factor limit of 0.8.

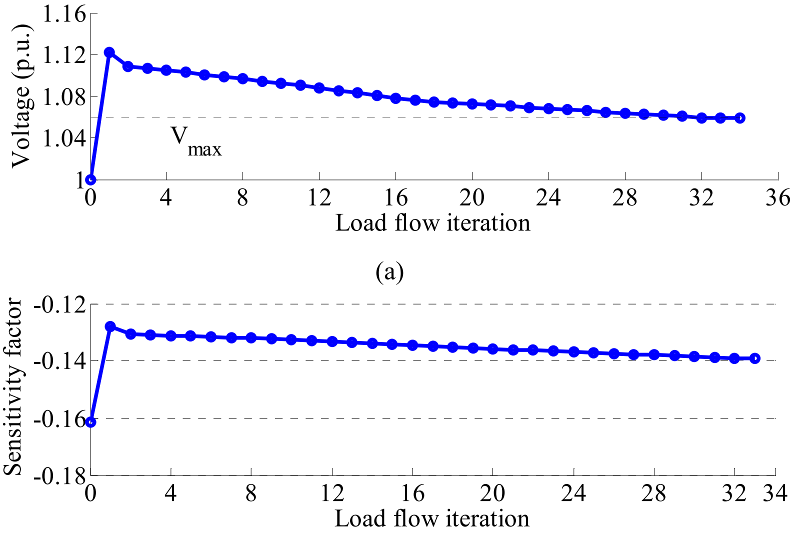

(a)

(b)

Fig. 7.13. Constrain bus voltage by controlling both the reactive and active power output of an 8 MW wind turbine: (a) Voltage at bus 2, (b) sensitivity factor dV_2/dP_2.

Fig. 7.14 (a) presents the step change of WT active power generation. Fig. 7.14 (b) shows the active power generation at each iteration. Before the 15th iteration, the active power control is not active. This is because in the case of overvoltage, as illustrated in Fig. 7.9, the reactive power control is executed before the active power control. In total, the active power generation of the WT is reduced by around 15% from 8 MW to 6.78 MW.

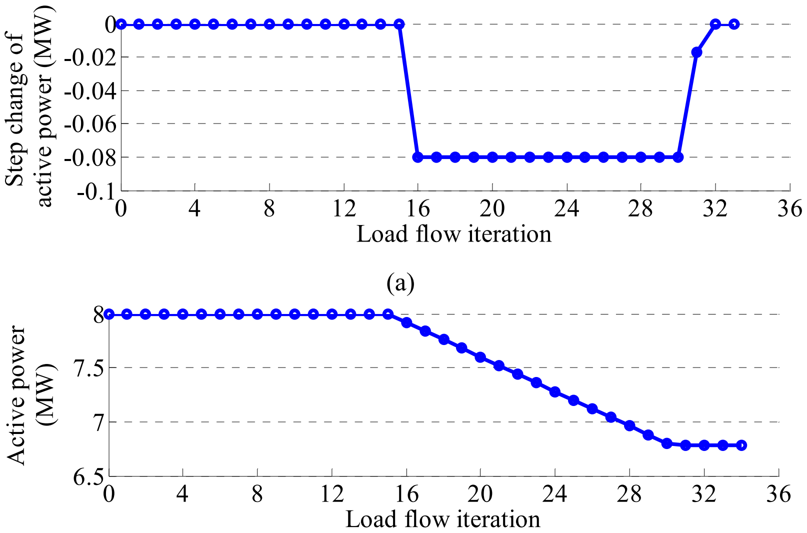

Fig. 7.14. Constrain bus voltage by controlling both the reactive and active power output of an 8 MW wind turbine: (a) step change of the wind turbine active power output, (b) the wind turbine active power output

c) Constrain the current at line L_2 by controlling the WT active power output

In this scenario, the initial wind power at bus 2 is further increased to (12 + j0) MVA and the feeder length is shortened to 5 km. This causes an overcurrent problem at the feeder section L_2. In the case of overcurrent, the reactive power of the WT is set to zero. Only the active power control of the WT is activated.

Fig. 7.15 (a) shows the current through section L_2. The current decreases gradually and converges to its rated value in 13 iterations. Fig. 7.15 (b) shows the sensitivity factor $\mathrm{d}I_2/\mathrm{d}P_2$, which evaluates the change in current at the feeder section L_2 with respect to the change in the active power output of the WT. The sensitivity factor $\mathrm{d}I_2/\mathrm{d}P_2$ is around 1. This is because the reactive power of the WT is zero and thus the active power is almost proportional to the current. Fig. 7.16 (a) presents the step change of WT active power output. The step change is limited to 0.24 MW. Fig. 7.16 (b) shows the WT active power output. In total, the active power generation of the WT is reduced by around 19% from 12 MW to 9.77 MW.

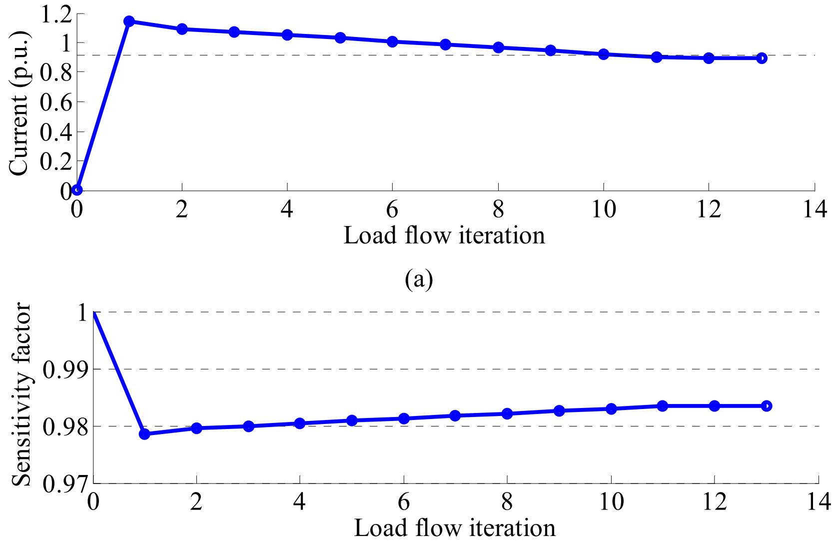

(a)

(b)

Fig. 7.15. Constrain line current by controlling the active power output of a 12 MW wind turbine: (a) Current at line L_2, (b) sensitivity factor dI_2/dP_2.

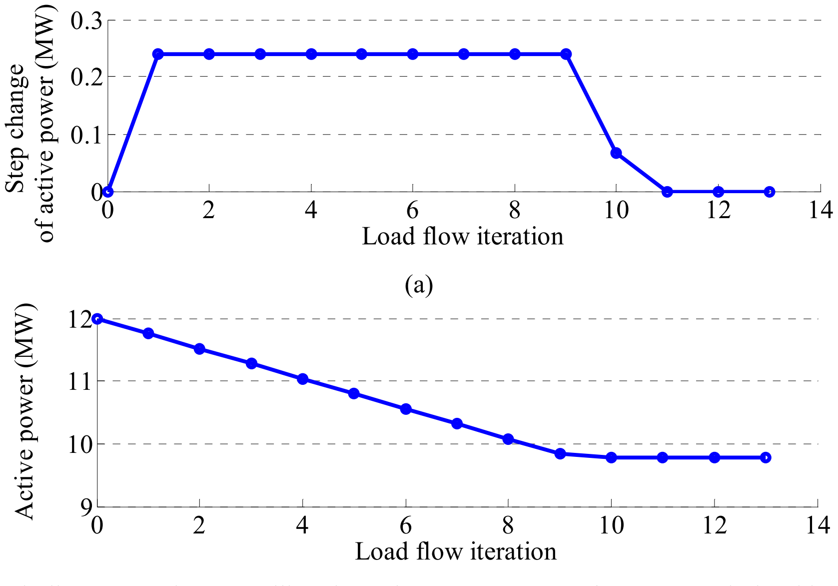

(a)

Fig. 7.16. Constrain line current by controlling the active power output of a 12 MW wind turbine: (a) step change of the wind turbine active power output, (b) the wind turbine active power output.

7.4 Optimal constrained load flow

The algorithm of the optimization procedures described in Fig. 7.7 (b) is presented in Fig. 7.17.

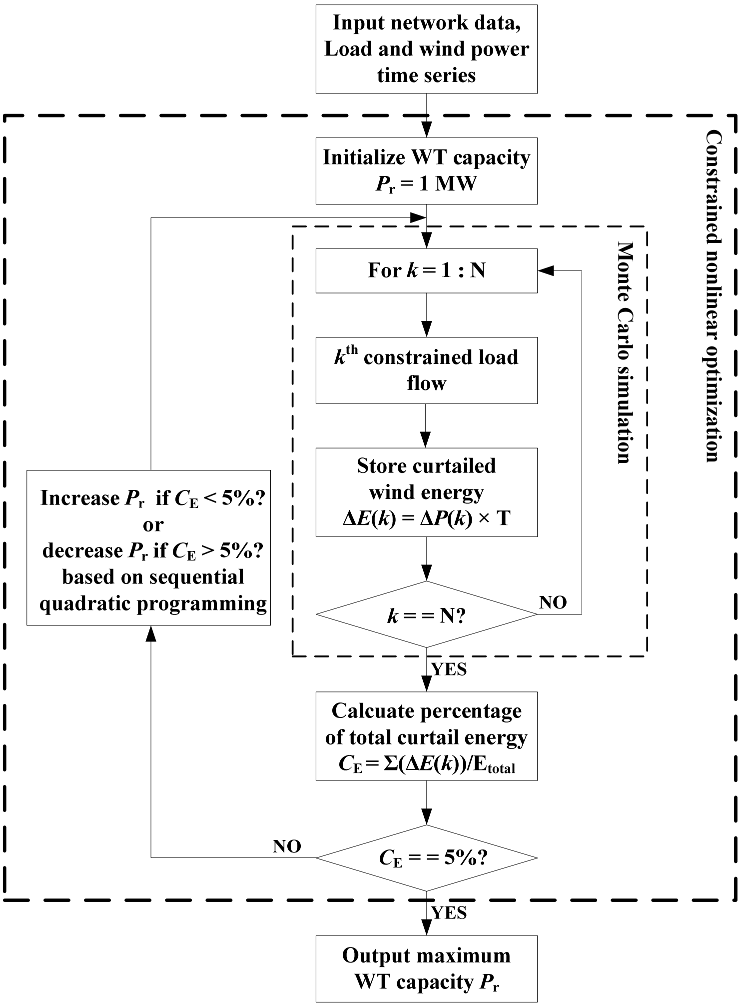

Fig. 7.17. Flow chart of the proposed algorithm for finding maximum wind turbine capacity of the network.

The algorithm combines constrained load flow and constrained nonlinear optimization. The algorithm requires inputs of wind power and load time series and provides outputs in the form of maximum WT capacity in a feeder or network. The algorithm mainly consists of two parts. The first part is the Monte Carlo simulation of the constrained load flow that is carried out for each time step of the time series data. The aim of the first part is to constrain the bus voltages and line currents within the required limits by regulating the reactive and active power output of the WTs. The second part is the constrained nonlinear optimization based on sequential quadratic programming (Mathworks 2009). The objective of this part is to find the maximum WT capacity in the network while allowing a given amount of annual energy curtailment. In the following section, the 20 kV Støvring distribution system is used to demonstrate the proposed algorithm.

7.5 Støvring 20 kV distribution system

7.5.1 Network description

Fig. 7.18 shows the modified configuration of the Støvring distribution system described in Fig. 3.4. There are two main modifications. The first one is that the substation is planning to supply a new load area, which is 5 km away. In the new load area, new WTs are also planned. The second one is that the old WTs connected to the end of the SØRP feeder are to be replaced by new WTs. The capacities of all the new WTs are to be decided. On the basis of such a network, the following two subsections demonstrate the Monte Carlo simulation with the constrained load flow and the optimal constrained load flow algorithm proposed in Fig. 7.17, respectively.

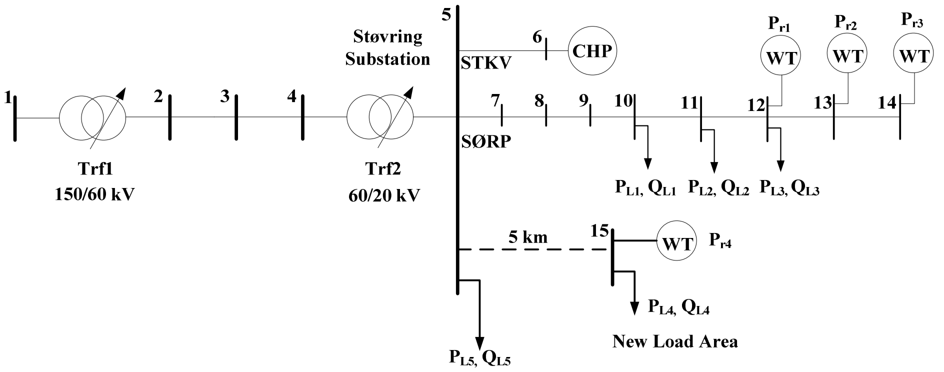

Fig. 7.18. Modified network configuration of the Støvring distribution system.

7.5.2 Monte Carlo simulation with constrained load flow

According to Fig. 7.17, the constrained nonlinear optimization provides inputs of the WT capacities to the Monte Carlo simulation of the constrained load flow. Assume that the WT capacity connected to the SØRP feeder is 3 MW each and the one connected to the new load area is 12 MW. The cable that supplies the new load area is a three-core cable with a conductor size of 120 mm^2. All the WTs can regulate the power factor within [0.95, 1] in both leading and lagging direction. The load, wind power and CHP data are shown in Fig. 3.5. The total length of the hourly time series available is 5160. The maximum allowed voltage is set to 1.06 p.u. The current rating of the 120 mm^2 cable is 265 A.

A Monte Carlo simulation of the constrained load flow is carried out on the network. Fig. 7.19 (a) shows the time series of the voltage at bus 14. The voltage is constrained under the maximum limit 1.06 p.u. Fig. 7.19 (b) shows the corresponding cumulative distribution function of the voltage, where around 15% of the time, the voltage is around 1.06 p.u. This indicates that overvoltage may occur if the reactive or active power control is not active.

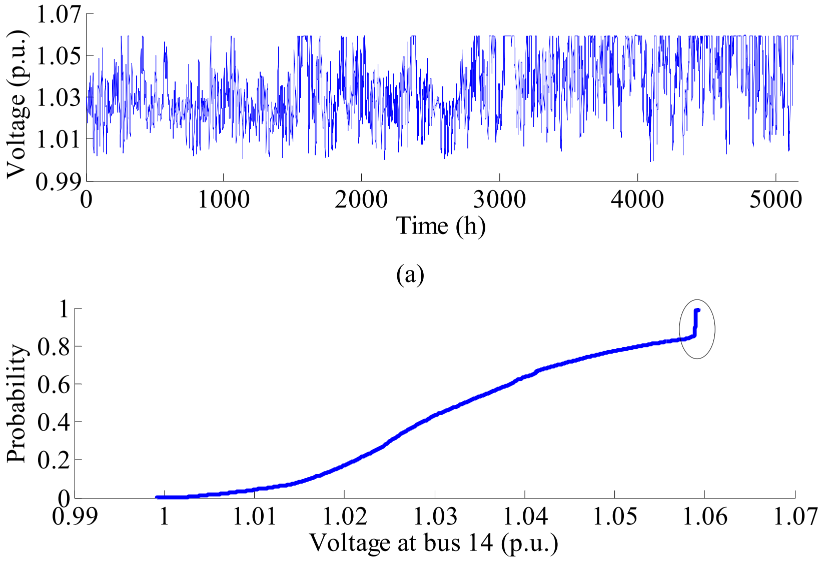

(a)

(b)

Fig. 7.19. Voltage magnitude at bus 14: a) time series, b) cumulative distribution function.

Fig. 7.20 shows the reactive power of the WT at bus 14. The reactive power is expressed in percentage of the WT capacity (3 MW). The negative value indicates that the WT absorbs reactive power to keep the bus voltage within limits. For around 15% of the time, the reactive power output of the WT is higher than 2% (0.06 MVAr). For the remaining 85% of the time, the reactive power output of the WT is close to but not exactly zero. This is because the reactive power control is already activated from the 2nd iteration of the constrained load flow algorithm. Even though the steady-state voltage may be lower than 1.06 p.u., the voltage at the early iterations may still be higher than 1.06 p.u. as the algorithm has not converged yet. However, this does not affect the effectiveness of the algorithm as a small amount of reactive power absorption only brings down the voltage slightly. Furthermore, as shown in Fig. 7.20 (b), for around 1% of the time, the reactive power absorption of the WT reaches its minimum value (0.99 MVAr). In this case, the active power control of the WT is activated. Fig. 7.21 shows the corresponding active power reduction when the reactive power control reaches its limit. A maximum reduction of 25% (0.75 MW) occurs during the whole period. However, the total energy curtailed during the whole period is only 0.6% (22.6 MWh).

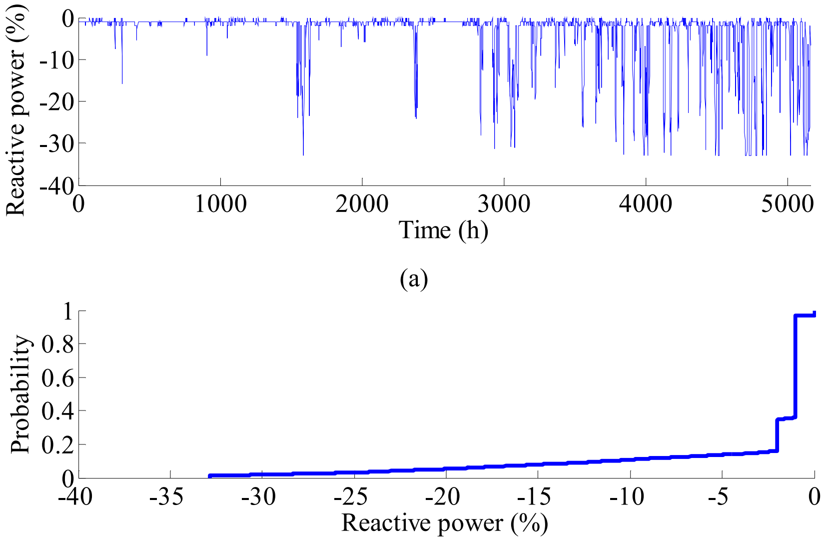

(a)

(b)

Fig. 7.20. Reactive power absorption of the WT at bus 14: a) time series, b) cumulative distribution function.

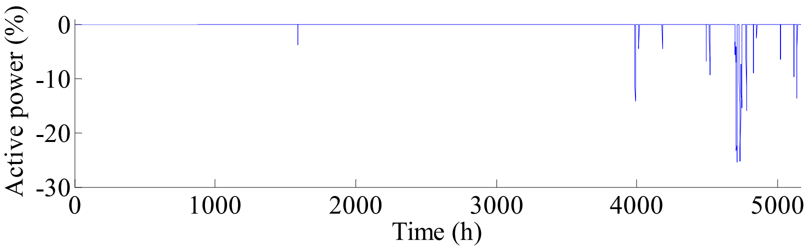

Fig. 7.21. Active power reduction of the WT at bus 14.

Fig. 7.22 (a) shows the current through the 5 km cable connecting the new load area. The current rating of the cable is 0.0918 p.u. (265 A). Overcurrent occurs for around 1% of the time. In the case of overcurrent, only the active power control is activated. Fig. 7.22 (a) shows the corresponding active power reduction of the WT at bus 15. A maximum reduction of 12% (1.44 MW) occurs during the whole period. However, the total energy curtailed during the whole period is only 0.3% (42.2 MWh).

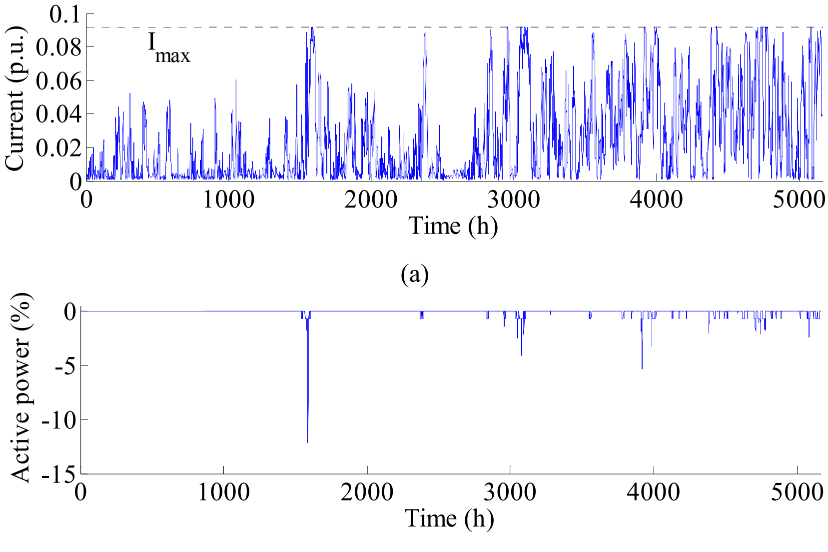

(a)

(b)

Fig. 7.22. New load area: a) current through the 120 mm^2 three-core cable, b) active power reduction of the WT at bus 15.

7.5.3 Optimal constrained load flow

According to Fig. 7.17, the maximum WT capacity of the distribution network can be evaluated by implementing a constrained nonlinear optimization on top of the Monte Carlo simulation. Such a combined optimization approach not only takes into account the stochastic behavior of load demand, WPG, and CHP generation, but also ensures that the energy curtailment strategy is executed under necessary conditions such as during high generation and low demand period.

It is assumed that the three WTs connected to the SØRP feeder have the same capacity and are controlled simultaneously. However, the WT in the new load area is controlled individually. It is also assumed that the substation transformer is large enough to transport the maximum reverse power flow.

Table 7.1 summarizes the maximum WT capacity of the network for five different cases. Case 1 is the base case, which does not implement the reactive and active power control strategies. In this case, the maximum capacity is 1.3 MW for each WT connected to the SØRP feeder, and 10.7 MW for the WT at bus 15. It is the voltage limit that stops the increment of the WT capacity at bus 12, 13 and 14. In contrast, it is the current limit that prevents the growth of the WT capacity at bus 15. In case 2, when 5% wind energy curtailment is allowed, the maximum WT capacity at bus 14 is increased by around 15%, while the maximum WT capacity at bus 15 is increased almost by 50%. Case 3 further allows the WT power factor to be between 0.95 and 1. This raises the maximum WT capacity at the SØRP feeder by almost three times. However, the power factor of the WT at bus 5 remains around 1 in order to minimize the current flow in the network. It can be seen from the first three cases that the energy curtailment strategy is more effective to increase the maximum WT capacity if the restricting factor is the current limit, whereas the reactive power control strategy is more effective if the restricting factor is the voltage limit. In case 5, the minimum power factor value is extended to 0.9. In this case, the maximum WT capacity at SØRP is increased by another 28%. The last case uses a 240 mm^2 cable instead of the 120 mm^2 cable for supplying the new load area. Compared to case 2, the maximum WT capacity at bus 15 is increased by 57%. This is expected as a thicker cable has a higher current rating. Thus, a thicker cable can be a good choice if more WTs are expected to be built in the future. For this particular network, the simulation time of each case is around 12 to 20 min.

Table 7.1
Maximum WT capacity based on the optimal constrained load flow algorithm.

Case	Cable size (mm^2)	Minimum power factor	Curtailed wind energy	Maximum WT capacity (MW)	
				$P_{r1} = P_{r2} = P_{r3}$	P_{r4}
1	120	1	0	**1.3**	**10.7**
2	120	1	5%	**1.5**	**15.9**
3	120	0.95	5%	**4.3**	**15.8**
4	120	0.90	5%	**5.5**	**15.7**
5	240	1	5%	**1.4**	**25.0**

7.6 Summary

This chapter has evaluated the maximum WT capacity of a single cable, a radial feeder and a distribution system in terms of network bus voltages and feeder cable capacity. Due to the stochastic behavior of load and wind power, the evaluation method requires a sophisticated optimization algorithm. The proposed algorithm in this chapter combines the sequential quadratic programming method and the Monte Carlo based constrained load flow algorithm, which incorporates the voltage and current limits into the load flow algorithm. Consequently, the proposed optimization approach can reduce the computation time significantly, for instance as compared to a two-loop optimization approach. Finally, it is concluded that both a reactive power control and an energy curtailment of WTs can effectively increase the maximum WT capacity in a network. In particular, the reactive power control is more helpful when the restricting factor is the voltage limit, while the energy curtailment strategy is more beneficial if the restricting factor is the current limit.

Chapter 8

Steady-State Frequency Deviation and Wind Power Forecasting Error

This chapter investigates the basic relation between the system steady-state frequency deviation and wind power forecasting error. First, an overview of different types of frequency control in power systems is provided. Then, in order to analyze the steady-state frequency deviation, primary frequency control of a synchronous generator is discussed. Third, a forecasting algorithm for predicting 15 min ahead wind power is illustrated. Finally, simulation results are carried out to demonstrate the wind power forecasting algorithm and the relation between the forecasting error and the system frequency deviation.

8.1 Overview of power system frequency control

According to the European Network of Transmission System Operators for Electricity (ENTSO-E), there are four types of frequency control in the European transmission system: primary control, secondary control, tertiary control and time control (ENTSO-E 2009).These four control schemes are implemented in a successive order at an increasing time scale.

Fig. 8.1 shows the relation between the four control schemes (ENTSO-E 2009). The primary control is activated automatically by the local generator to limit system frequency deviation. After a few minutes, upon the command of the transmission system operator (TSO), the secondary control may take over by responsible generators to restore the system frequency to the nominal value (e.g. 50 Hz). In some cases, the secondary control may be implemented automatically by a designated generator. Afterwards, the tertiary control may take over to restore the secondary control reserve of the responsible generators and/or to execute economic dispatch. The command is sent by the generation companies in the case of a monopoly market or by the TSO in the case of a pool market. The tertiary control is normally carried out every 15 min or every hour, depending on the local implementation. The time control is used to limit the discrepancy observed between synchronous time and universal coordinated time in the synchronous area.

Table 8.1 summarizes the characteristics of the four frequency control schemes in terms of their objective, time scale, main controller and action taker (ENTSO-E 2009, Rebours, Kirschen 2005). Although not included in the table, electricity customers who are willing to provide load-shedding service can also be action takers for secondary control.

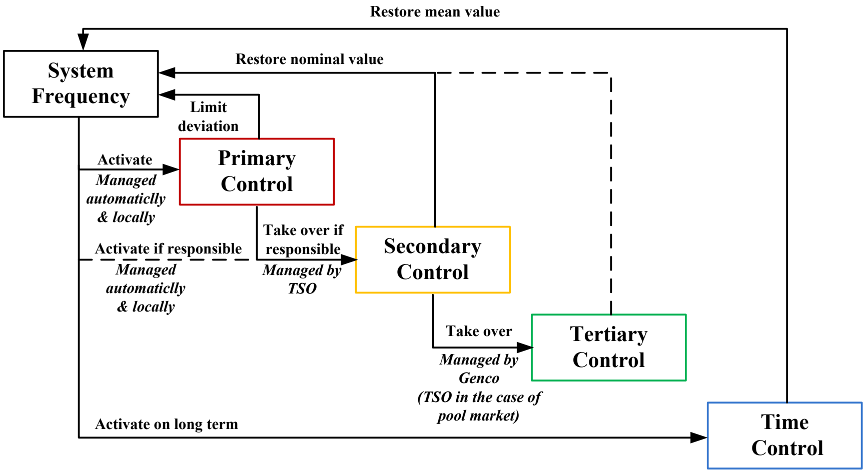

Fig. 8.1. Four frequency control schemes in the European transmission system (ENTSO-E 2009).

Table 8.1
Characteristics of four frequency control schemes.

	Objective	**Time Scale**	**Main Controller**	**Action Taker**
Primary Control	To limit and stabilize system frequency deviation	Seconds	Speed governor	Local automatic control
Secondary Control	To restore system frequency and tie line power to their target value	Seconds to 15 min	Automatic generation control	Normally TSO
Tertiary Control	To restore secondary control reserve, to manage congestions, to re-dispatch generation economically, etc.	15 min to 1 h	Economic Dispatch with security assessment	Generation company (TSO in pool market)
Time Control	To monitor and limit discrepancies observed between synchronous time and universal coordinated time in the synchronous area	One day	Reset set-point frequency for secondary control	Generation company & TSO

8.2 Primary frequency control of a synchronous generator

As discussed in section 8.1, the primary (frequency) control is implemented locally on a synchronous machine. Fig. 8.2 presents the scheme of the primary frequency control of a synchronous generator (Saadat 2002). The control loop mainly consists of a system frequency sensor, a droop control and a valve control mechanism. The valve control mechanism regulates the valve through a governor controller. Fig. 8.3 shows the corresponding control block diagram in Laplace domain (Saadat 2002). The control loop represents the system frequency deviation ($\Delta\Omega$) subject to a small perturbation of the load (ΔP_L).

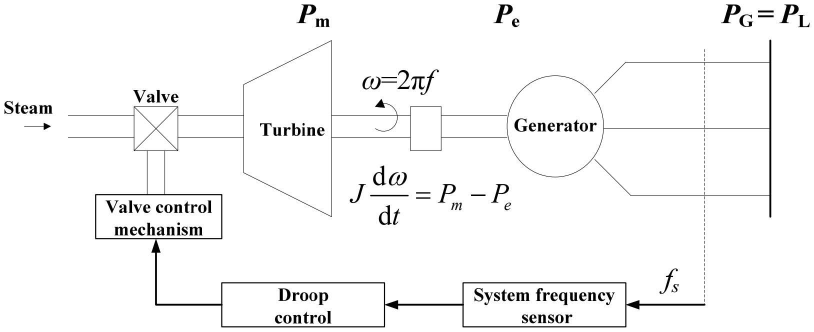

Fig. 8.2. Schematic diagram of primary frequency control of synchronous generator.

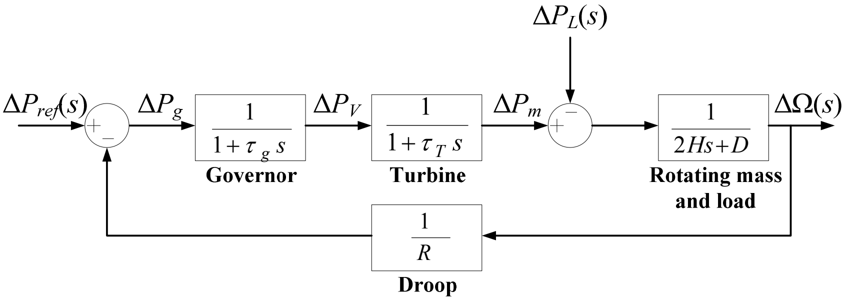

Fig. 8.3. Control block diagram of primary frequency control.

The close-loop transfer function of the control block diagram can be expressed as (Saadat 2002):

$$\frac{\Delta\Omega(s)}{-\Delta P_L(s)} = \frac{(1+\tau_g s)(1+\tau_T s)}{(2Hs+D)(1+\tau_g s)(1+\tau_T s)+1/R} \tag{8.1}$$

where ΔP_{ref} is the change of the power reference value given by the secondary and tertiary frequency control; τ_g is the time constant of the governor system; τ_T is the time constant of the turbine; H is the inertia constant of the rotating mass; D is the coefficient for the frequency-dependent load; R is the droop constant.

For a step change of system load, according to the final value theorem, the steady-state frequency deviation can be expressed as:

$$\Delta\omega_{ss} = \lim_{s\to 0} s\Delta\Omega(s) = (-\Delta P_L)\frac{1}{D+1/R}\,. \tag{8.2}$$

The steady-state frequency deviation depends on three parameters: the load disturbance ΔP_L, the coefficient for the frequency-dependent load D and the droop constant R. Fig. 8.4 shows the step response of the system frequency, where $\Delta P_L = 0.2$ p.u., $\tau_g = 0.2$ sec, $\tau_T = 0.5$ sec, $H = 5$ sec, $D = 0.8$, $R = 0.05$ p.u. (Saadat 2002). The frequency stabilizes at 49.52 Hz in around 35 sec after the load disturbance. This is in accordance with (8.2), which gives the steady-state frequency deviation of 0.48 Hz.

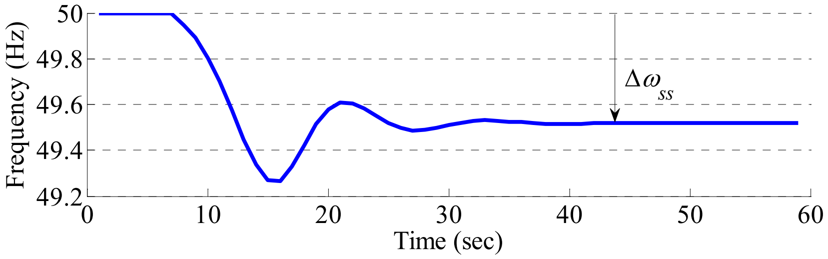

Fig. 8.4. Step response of primary frequency control.

8.3 15 min ahead wind power forecasting

The steady-state frequency deviation shown in Fig. 8.4 can be eliminated through the secondary frequency control performed by the TSO at the end of every 15 min interval. The secondary frequency control calls for the secondary control reserve (part of spinning reserve) in order to bring the system frequency back to the nominal value. However, if the knowledge of the load disturbance can be obtained before it actually occurs, then the steady-state frequency deviation can be reduced or even avoided. In other words, a smaller frequency deviation can be obtained in the case of a better load forecasting. Fig. 8.5 shows the actual load P_L, the forecasted load $\hat{P}_L$, and the forecasting error ΔP_L. In the case of wind power, which can be considered as a negative load of the system, an improved (15 min ahead) wind power forecasting can also reduce the system frequency deviation. Consequently, the system spinning reserve requirement can be cut down, which contributes to a reduction of the system operating cost for the TSO.

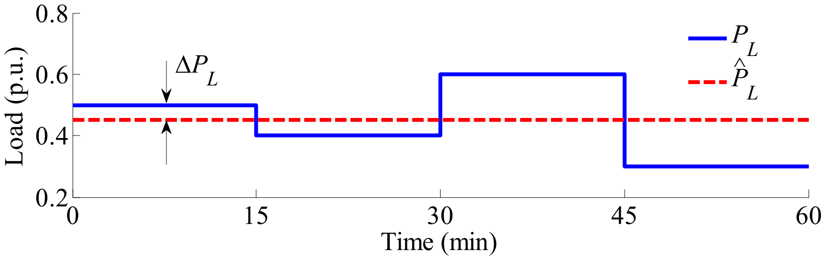

Fig. 8.5. Load disturbance ΔP_L between the actual load (solid) and the forecasted load (dashed) at a 15 min step.

Many research efforts have been devoted to wind power forecasting during the last two decades (Kariniotakis, Stavrakakis & Nogaret 1996, Madsen et al. 2005, Nielsen, Madsen & Nielsen 2006, Sideratos, Hatziargyriou 2007, Pinson et al. 2009). These forecasting algorithms fall into two categories: the physical approach and the statistical approach (Pinson 2006). In order to test the accuracy of these miscellaneous forecasting algorithms, it is necessary to possess a sufficiently long wind power time series measurement. In the case that wind power measurements are unavailable or the available time series is limited, stochastic models that can generate synthetic wind power time series is very useful. The following subsection demonstrates a simple algorithm for wind power forecasting of 15 min head using the synthetic wind power time series.

8.3.1 Forecasting based on LARIMA model

The standard reference model for wind power forecasting is the persistence model (Madsen et al. 2005). The persistence model states that the future wind power remains the same as the last measured value of wind power:

$$\hat{P}(t+k\,|\,t)=P(t)\,. \tag{8.3}$$

Normally, the persistence model provides the best forecast for a one-step ahead wind power forecasting. In contrast, advanced forecasting algorithms, such as artificial intelligence algorithms, have a better performance than the persistence model at large look-ahead steps. Nevertheless, the use of a more advanced forecasting model can be justified if it provides a better prediction than the persistence model. For example, a linear minimum mean square error (LMMSE) estimator may be sufficient if it can reduce the forecasting error as compared to the persistence model. A LMMSE estimator is to estimate the stochastic variable Y through a linear form (Simon 2002):

$$\begin{aligned}\hat{Y} &= h_0 + \sum_{m=1}^{M} h_m X(m) \\ &= h_0 + \mathbf{h} \cdot \mathbf{X}\end{aligned}, \tag{8.4}$$

where $\hat{Y}$ is the predicted value of Y; $X(1),\ldots, X(M)$ is a stochastic process whose realizations can be observed. The coefficients of the LMMSE estimator are given by:

$$\mathbf{h} = \left(\Sigma_{\mathbf{XX}}\right)^{-1} \Sigma_{\mathbf{X}Y}, \tag{8.5}$$

$$h_0 = \mu_Y - \left(\mathbf{h}\right)^{\mathrm{T}} \boldsymbol{\mu}_{\mathbf{X}}, \tag{8.6}$$

where $\Sigma_{\mathbf{XX}}$ is the covariance matrix of vector $\mathbf{X}$; $\Sigma_{\mathbf{X}Y}$ is the cross-covariance matrix between vector $\mathbf{X}$ and variable Y**;** $\mu_{\mathbf{X}}$ is the mean of vector $\mathbf{X}$ and μ_Y is the mean of variable Y. As shown in (8.5) and (8.6), it is necessary to obtain the covariance matrices $\Sigma_{\mathbf{XX}}$ and $\Sigma_{\mathbf{X}Y}$ in order to develop the LMMSE estimator. These two covariance matrices can be estimated from the available wind power time series. For example, a wind power time series can be obtained by simulating the LARIMA(0,1,1) model developed in section 2.1. However, the LARIMA(0,1,1) model is developed for hourly wind power measurements. 15 min wind power measurements may have a different model structure. According to the same procedure of model development described in section 2.1, a LARIMA(0,1,3) model is obtained for the 15 min WPG from the Nysted offshore wind farm. By simulating the LARIMA(0,1,3) model, two synthetic wind power time series are generated. The length of each time series is 5 years. One of the time series is used as the training data to estimate the covariance matrices $\Sigma_{\mathbf{XX}}$ and $\Sigma_{\mathbf{X}Y}$ for the LMMSE estimator. The other time series is used as testing data to evaluate the performance of the LMMSE estimator. The performance of the LMMSE estimator can be evaluated by mean square error (MSE) (Simon 2002):

$$\mathrm{E}\left[\Delta Y^2\right], \tag{8.7}$$

where E[ ] is to take the expectation, ΔY is the forecasting error defined by:

$$\Delta Y = Y - \widehat{Y}\,, \tag{8.8}$$

8.3.2 Simulation results

As shown in Fig. 2.10 (b), the LARIMA model has a square transformation. As the LMMSE estimator is a linear estimator, a better forecasting may be achieved by predicting the square-root of the wind power instead of the wind power directly. This is to reduce the nonlinearity of the original wind power time series. However, the nonlinearity because of the upper and lower limits is still present in the transformed wind power time series.

Based on the training data (with a square-root transformation) generated by the LARIMA(0,1,3) model, the covariance matrices $\Sigma_{\mathbf{XX}}$ and $\Sigma_{\mathbf{X}Y}$ are estimated. According to (8.5) and (8.6), the coefficients of the LMMSE estimator can be calculated. The order M of the LMMSE estimator is chosen to be 3. The coefficients of the estimator are: $h_0 = 0.0765$ and $\mathbf{h} = [1.21, -0.34, 0.12]^{\mathrm{T}}$. According to further simulation results, a higher model order does not improve the prediction results significantly.

The developed LMMSE estimator is then used to forecast the wind power of the testing data set at the look-ahead time of 15 min. Fig. 8.6 shows the testing wind power data and the forecasted wind power data using the persistence model and the LMMSE estimator over 150 min. It can be seen from the figure that for certain periods, e.g. between 15 min and 75 min, the LMMSE estimator provides a better wind power forecast than the persistence model. However, for some other periods, e.g. 90 min, the persistence model has a slightly better performance. Generally, the MSE of the persistence model is around 5.3% of the installed wind farm capacity (165.6 MW), while the MSE of the LMMSE estimator is reduced to 5.1%. The forecasting error by using the LMMSE estimator is around 4% lower than the persistence model. The forecasting error may be further reduced by using a better predictor such as a nonlinear estimator, which can take into account the nonlinearity of WPG. This, however, will not be investigated in this chapter as the purpose here is to show the possibility of using the stochastic wind power model for testing wind power forecasting algorithms and to study the relation between the frequency deviation and the forecasting error.

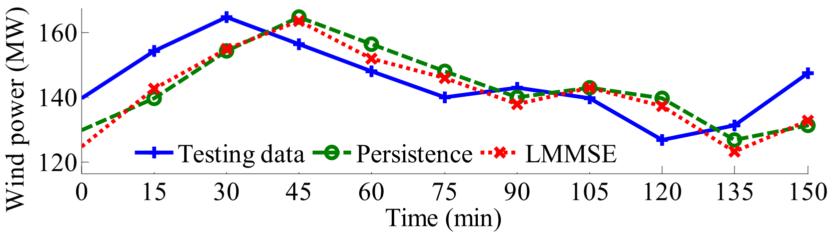

Fig. 8.6. 15 min ahead forecast of wind power time series: Testing data (solid), persistence model (dashed) and LMMSE estimator (dotted).

Fig. 8.7 shows the probability distribution (approximated by 50 bins) of the wind power forecasting error by using the LMMSE estimator over a period of 5 years. The forecasting error is expressed in percentage of the wind farm capacity. The figure indicates that the over-forecasting and the under-forecasting of wind power are symmetrical with respect to zero. The maximum forecasting error can reach around 50% of the installed capacity. According to (8.2), the steady-state frequency deviation is proportional to the forecasting error of wind power. Fig. 8.8 shows the steady-state frequency variation. The corresponding probability distribution is shown in Fig. 8.9. In this case, the maximum frequency reaches 52.71 Hz and the minimum value reaches 47.44 Hz. However, for 95% of the time, the system frequency is within [49.08, 50.85] Hz. This amount of frequency deviation requires spinning reserve in order to restore the system frequency to the nominal value.

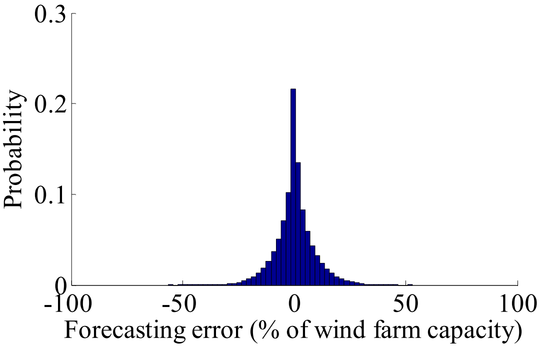

Fig. 8.7. Probability distribution of wind power forecasting error by LMMSE estimator.

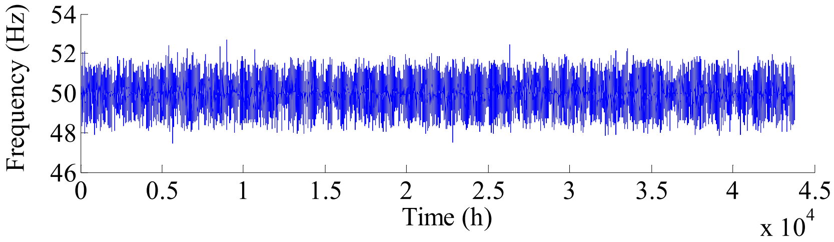

Fig. 8.8. Steady-state frequency variation caused by the 15 min wind farm forecasting error.

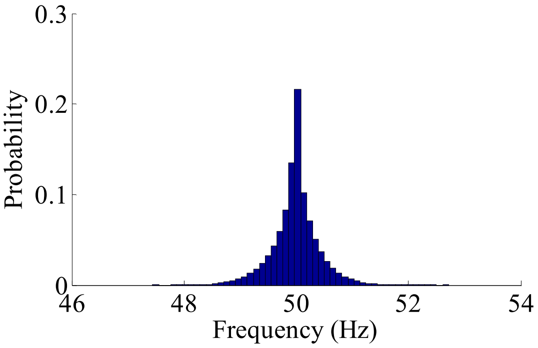

Fig. 8.9. Probability distribution of steady-state frequency variation.

The foregoing analysis is carried out on a simple system with one generator and one load. For a more complex system, however, similar approach can be adopted to analyze the impact of wind power and load forecasting on the frequency deviation of the system.

8.4 Summary

This chapter has provided a basic study on the relation between wind power forecasting error and system steady-state frequency deviation. For a single-generator-single-load system, the frequency deviation is proportional to the wind power forecasting error. However, the relation may become more complex in a system with multiple generators and loads. This can be investigated in the future work. This chapter has also tested the LMMSE estimator for forecasting 15 min ahead wind power. The test is carried out on the basis of the synthetic time series generated from the LARIMA model. The LMMSE estimator provides a better performance than the persistence model. However, a nonlinear estimator may be used to further reduce the forecasting error.

Chapter 9

Conclusions and Future Work

9.1 Summary

In this thesis, stochastic models of WPG, load demand and CHP generation have been developed. Several aspects of the operation and planning of a renewable energy based distribution system are investigated through a probabilistic approach. The contents of the thesis consist of seven topics:

1) Modeling of stochastic WPG, load demand and CHP generation,
2) PLF analysis for evaluating system steady-state performance,
3) Optimal power factor setting of WT for minimizing network power losses,
4) Short-range distribution system planning considering system capacity shortfalls,
5) Optimal cable selection for wind energy network through economic evaluation,
6) Maximum wind turbine capacity of a network considering energy curtailment,
7) Steady-state frequency deviation due to wind power forecasting error.

Topics 3)-6) are examined on the basis of PLF techniques presented in 2). The PLF analysis commonly relies on Monte Carlo simulation, which calls for stochastic models of renewable generation and load demand as developed in 1). The last topic evaluates the impact of wind power forecasting error on system steady-state frequency deviation. Furthermore, the stochastic wind power model is utilized to generate synthetic wind power time series, which are further used to test wind power forecasting algorithms. Based on the wind power forecasting error, the probability distribution of the steady-state frequency deviation is derived.

9.2 Conclusions

In this thesis, stochastic models are developed for simulating the stochastic process of WPG, CHP and load demand. For the stochastic wind power modeling, the important characteristics to be considered are probability distribution, temporal correlation, cross-correlation and seasonal variation. The diurnal period is regarded insignificant for the analyzed time series and thus ignored during the modeling. As a result, a LARIMA model and a multivariate-LARIMA model are developed for simulating a single and multiple wind power time series, respectively. Both models are validated against the field measurements from the Nysted offshore wind farm. For stochastic load modeling, in contrast to wind power, the diurnal period is an essential element to be considered. Consequently, a seasonal ARMA model is developed for simulating the stochastic process of the load demand. For stochastic CHP modeling, a discrete Markov chain model is selected to represent the generation states of a CHP plant, which is regulated on and off. These three stochastic models are particularly useful when time series measurements are not available. Furthermore, these stochastic models serve as the basis of Monte Carlo simulations for PLF analysis.

PLF analysis can be performed through Monte Carlo simulation, as well as through an analytical approach such as the convolution method and the cumulants method. Although the analytical approach is faster in computation time, it is not straightforward to account for non-Gaussian distributions and the temporal correlation and cross-correlation among stochastic processes. Furthermore, the analytical approach is not able to take into account the automatic tap regulation of tap-changing transformers. Therefore, Monte Carlo simulation is preferred for PLF analysis. Although the Monte Carlo simulation is computation-intensive, the simulation time is not a major concern for power system planning. It is also found that the automatic tap regulation of a transformer is time-dependent. Such a time-dependent feature requires a realistic simulation of the temporal correlation of stochastic generation and load. In other words, if the temporal correlation is ignored or inappropriately modeled, the tap position of the transformer may not be correctly simulated in a Monte Carlo simulation. As a result, the probability distribution of the bus voltage is shifted. This indicates that the modeling of temporal correlation is not only crucial for simulating stochastic generation and load, but also critical for obtaining accurate PLF results.

For the short-range planning of a distribution system, the substation capacity shortfall is normally dealt with by expanding the capacity of the substation transformer according to its maximum loading. However, based on the probabilistic analysis, the probability and the corresponding period when the capacity shortfall occurs during a day are identified. Accordingly, it is demonstrated that procuring a gas turbine as an alternative solution not only solves the capacity shortfall problem, but also provides economic benefits for the network operator in the long run.

Unity power factor setting of WTs is commonly used for WT owners. However, the optimal power factor setting of WTs can abate system power losses and thus the operating costs for the network operators. A stochastic optimization method is developed to find the optimal WT power factor setting while taking into account the stochastic behavior of WPG and load. The simulation results on the investigated network indicate that annual losses can be reduced by 13%. This corresponds to a saving of 0.8% of the total system costs. This amount of saving, if paid back to WT owners, may cut their wind energy transfer fee by 11% of the current cost. Therefore, such an optimization algorithm can be used as a basic tool by network operators to estimate power losses of their networks and to negotiate with WT owners to achieve a more economic operation of the system.

In order to integrate new WTs to the existing grid, network operators need to determine the cable type and optimal conductor size for connecting the WTs. The optimal cable sizing should consider both the technical constraints and economic benefits from a cable. Such an evaluation needs to account for the rated capacity of WTs and the stochastic behavior of WPG. The study demonstrates that by utilizing the economical loading range and load reach of the cable, the optimal conductor size of a cable can be determined. Such a method significantly simplifies the calculation, which can be easily adopted for practical applications.

In order to evaluate the maximum penetration level of wind power in the system, an optimal constrained load flow algorithm is proposed. The algorithm combines the sequential quadratic programming method and a Monte Carlo based constrained load flow algorithm. The system maximum WT capacity is obtained by performing reactive power control and energy curtailment of WTs. The simulation results show that the reactive power control is more effective when the restricting factor is the voltage limit, while the energy curtailment strategy is more beneficial when the restricting factor is the current limit.

The last part of the thesis investigates the relation between wind power forecasting error and system steady-state frequency deviation. For a single-generator-single-load system, the frequency deviation is proportional to the wind power forecasting error. However, this may not be the case in a system with multiple generators and loads. Furthermore, it is also demonstrated that the stochastic wind power model can be used as data source for testing various wind power forecasting algorithms.

9.3 Future Work

During the process of the research work, a number of interesting and promising research topics are identified. These research topics may deserve a further investigation in the future:

1) Implement diurnal period in the stochastic wind power model,
2) Model the cross-correlation between the WPG and load demand,
3) Derive analytical expressions for the probability density function of the LARIMA model,
4) Investigate year-to-year variation of WPG,
5) Study reliability issues of distribution systems using stochastic models of WPG and load,
6) Evaluate the effect of forecasting error on the system frequency deviation on a larger network,

7) Study the contribution of WTs to the primary frequency control of the system,
8) Optimal spinning reserve of power systems considering forecasting error of load and wind power generation under market environment.

References

ABB 2006, *XLPE Cable Systems: User's guide (Rev. 2)*, ABB, Västerås.

Ackermann, T. 2005, *Wind Power in Power Systems,* John Wiley & Sons, Chichester.

Allan, R.N. & Al-Shakarchi, M. 1976, "Probabilistic a.c. load flow", *Proceedings of the Institution of Electrical Engineers,* vol. 123, no. 6, pp. 531-536.

Allan, R.N., Borkowska, B. & Grigg, C.H. 1974, "Probabilistic analysis of power flows", *Proceedings of the Institution of Electrical Engineers,* vol. 121, no. 12, pp. 1551-1556.

Allan, R.N., da Silva, A.M.L. & Burchett, R.C. 1981, "Evaluation methods and accuracy in probabilistic load flow solutions", *IEEE transactions on power apparatus and systems,* vol. PAS-100, no. 5, pp. 2539-2546.

Allan, R.N., da Silva, A.M.L., Abu-Nasser, A.A. & Burchett, R.C. 1981, "Discrete Convolution in Power System Reliability", *Reliability, IEEE Transactions on,* vol. R-30, no. 5, pp. 452-456.

Allan, R.N., Grigg, C.H. & Al-Shakarchi, M.R.G. 1976, "Numerical techniques in probabilistic load flow problems", *International Journal for Numerical Methods in Engineering,* vol. 10, no. 4, pp. 853-860.

Alvarado, F., Hu, Y. & Adapa, R. 1992, "Uncertainty in power system modeling and computation", *IEEE International Conference on Systems, Man and Cybernetics*, pp. 754.

Anders, G.J. 1990, *Probability Concepts in Electric Power Systems,* Wiley, New York.

Arora, J. 2004, *Introduction to Optimum Design,* 2nd edn, Elsevier Academic Press, London.

Barker, P.P. & De Mello, R.W. 2000, "Determining the impact of distributed generation on power systems: Part 1 - Radial distribution systems", *Proceedings of the 2000 Power Engineering Society Summer Meeting, July 16, 2000 - July 20*Institute of Electrical and Electronics Engineers Inc, Seattle, WA, United states, pp. 1645.

Billinton, R., Fotuhi-Firuzabad, M. & Bertling, L. 2001, "Bibliography on the application of probability methods in powersystem reliability evaluation 1996-1999", *IEEE Transactions on Power Systems,* vol. 16, no. 4, pp. 595-602.

Billinton, R. & Allan, R.N. 1996, *Reliability Evaluation of Power Systems,* 2nd edn, Plenum, New York.

Billinton, R., Chen, H. & Ghajar, R. 1996, "Time-series models for reliability evaluation of power systems including wind energy", *Microelectronics Reliability,* vol. 36, no. 9, pp. 1253-1261.

Billinton, R. & Li, W. 1994, *Reliability Assessment of Electrical Power Systems Using Monte Carlo Methods* Plenum Press, New York.

Billinton, R. & Huang, D. 2008, "Effects of load forecast uncertainty on bulk electric system reliability evaluation", *IEEE Transactions on Power Systems,* vol. 23, no. 2, pp. 418-425.

Billinton, R. & Wangdee, W. 2007, "Reliability-based transmission reinforcement planning associated with large-scale wind farms", *IEEE Transactions on Power Systems,* vol. 22, no. 1, pp. 34-41.

Borkowska, B. 1974, "Probabilistic Load Flow", *Power Apparatus and Systems, IEEE Transactions on,* vol. PAS-93, no. 3, pp. 752-759.

Box, G.E.P., Jenkins, G.M. & Reinsel, G.C. 1994, *Time Series Analysis: Forecasting and Control,* 3rd edn, Prentice-Hall, Englewood Cliffs, NJ.

Brown, B.G., Katz, R.W. & Murphy, A.H. 1984, "Time series models to simulate and forecast wind speed and wind power", *Journal of climate and applied meteorology,* vol. 23, no. 8, pp. 1184-1195.

Castro Sayas, F. & Allan, R.N. 1996, "Generation availability assessment of wind farms", *Generation, Transmission and Distribution, IEE Proceedings-,* vol. 143, no. 5, pp. 507-518.

Celli, G., Ghiani, E., Mocci, S. & Pilo, F. 2005, "A multiobjective evolutionary algorithm for the sizing and siting of distributed generation", *IEEE Transactions on Power Systems,* vol. 20, no. 2, pp. 750-757.

Chen, P., Bak-Jensen, B. & Chen, Z. 2009, "Probabilistic load models for simulating the impact of load management", *IEEE PES General Meeting*Calgary.

Chen, P., Berthelsen, k.k., Bak-Jensen, B. & Chen, Z. 2009, "Markov model of wind power time series using Bayesian Inference of transition matrix", *35th Annual Conference of the IEEE Industrial Electronics Society (IECON)*IEEE, Porto.

Chen, P., Chen, Z. & Bak-Jensen, B. 2008, "Probabilistic load flow: A review", *3rd International Conference on Deregulation and Restructuring and Power Technologies, DRPT 2008, April 6, 2008 - April 9*Inst. of Elec. and Elec. Eng. Computer Society, Nanjing, China, pp. 1586.

Chernick, M.R. 2008, *Bootstrap Methods: A Guide for Practitioners and Researchers,* 2nd edn, John Wiley & Sons, New Jersey.

Cochran, W.G. 1977, *Sampling Techniques,* 2nd edn, Wiley, New York.

Danish Energy Agency 2009, , *Energy Statistics 2008* [Homepage of the Danish Energy Agency], [Online]. Available: http://www.ens.dk/en-US/Info/FactsAndFigures/Energy_statistics_and_indicators/Annual%20Statistics/Documents/Energy%20Statistics%202008.pdf [2010, Jan/09] .

Das, D. 2006, "A fuzzy multiobjective approach for network reconfiguration of distribution systems", *IEEE Transactions on Power Delivery,* vol. 21, no. 1, pp. 202-209.

El-Khattam, W., Bhattacharya, K., Hegazy, Y. & Salama, M.M.A. 2004, "Optimal investment planning for distributed generation in a competitive electricity market", *IEEE Transactions on Power Systems,* vol. 19, no. 3, pp. 1674-1684.

EN 50160 1999, *European Standard for Voltage Characteristics of Electricity Supplied by Public Distribution Systems*, European Committee for Electrotechnical Standardization (CENELEC), Brussels.

Energinet.dk 2009, Dec 09-last update*, Market data* [Homepage of Energinet.dk], [Online]. Available: http://www.energinet.dk/en/menu/Market/Download+of+Market+Data/Download+of+Market+Data.htm [2009, Dec 09] .

ENTSO-E 2009, *P1-Policy 1: Load-Frequency Control and Performance [C]*, European Network of Transmission System Operators for Electricity (ENTSO-E).

Gellings, C.W. & Smith, W.M. 1989, "Integrating demand-side management into utility planning", *Proceedings of the IEEE,* vol. 77, no. 6, pp. 908-918.

Gönen, T. 1990, *Electric Power Distribution System Engineering,* McGraw-Hill, New York.

Greatbanks, J.A., Popovic, D.H., Begovic, M., Pregelj, A. & Green, T.C. 2003, *On optimization for security and reliability of power systems with distributed generation*.

Harrison, G.P., Piccolo, A., Siano, P. & Wallace, A.R. 2008, "Hybrid GA and OPF evaluation of network capacity for distributed generation connections", *Electric Power Systems Research,* vol. 78, no. 3, pp. 392-398.

Harrison, G.P., Piccolo, A., Siano, P. & Wallace, A.R. 2007, "Exploring the tradeoffs between incentives for distributed generation developers and DNOs", *IEEE Transactions on Power Systems,* vol. 22, no. 2, pp. 821-828.

Hatziargyriou, N.D. 2000, "Probabilistic constrained load flow for optimizing generator reactive power resources", *IEEE Transactions on Power Systems,* vol. 15, no. 2, pp. 687-693.

Hatziargyriou, N.D. & Karakatsanis, T.S. 1994, "A probabilistic approach to control variable adjustment for power system planning applications", *Part 1 (of 2), March 21, 1994 - March 24*Publ by IEE, Coventry, UK, pp. 733.

Hatziargyriou, N.D., Karakatsanis, T.S. & Lorentzou, M.I. 2005, "Voltage control settings to increase wind power based on probabilistic load flow", *International Journal of Electrical Power and Energy Systems,* vol. 27, no. 9-10, pp. 656-661.

Hatziargyriou, N.D., Karakatsanis, T.S. & Papadopoulos, M. 1993, "Probabilistic load flow in distribution systems containing dispersed wind power generation", *IEEE Transactions on Power Systems,* vol. 8, no. 1, pp. 159-165.

Hatziargyriou, N.D. & Sakis Meliopoulos, A.P. 2002, "Distributed energy sources: Technical challenges", *2002 IEEE Power Engineering Society Winter Meeting, January 27, 2002 - January 31*Institute of Electrical and Electronics Engineers Inc, New York, NY, United states, pp. 1017.

Henault, P.H., Eastvedt, R.B., Peschon, J. & Hajdu, L.P. 1970, "Power system long-term planning in the presence of uncertainty", vol. PAS-89, no. 1, pp. 156-164.

IEC-60287-1-1 2001, *Electric cables-Calculation of the current rating*, International Electrotechnical Commission, Geneva.

IEEE Std. 610.3 1989, *IEEE Standard Glossary of Modeling and Simulation Terminology*.

Jorgensen, P., Christensen, J.S. & Tande, J.O. 1998, "Probabilistic load flow calculation using Monte Carlo techniques for distribution network with wind turbines", *8th International Conference on Harmonics and Quality of Power*, pp. 1146.

Karakatsanis, T.S. & Hatziargyriou, N.D. 1994, "Probabilistic constrained load flow based on sensitivity analysis", *IEEE Transactions on Power Systems,* vol. 9, no. 4, pp. 1853-1860.

Kariniotakis, G.N., Stavrakakis, G.S. & Nogaret, E.F. 1996, "Wind power forecasting using advanced neural networks models", *IEEE Transactions on Energy Conversion,* vol. 11, no. 4, pp. 762-767.

Keane, A. & O'Malley, M. 2007, "Optimal utilization of distribution networks for energy harvesting", *IEEE Transactions on Power Systems,* vol. 22, no. 1, pp. 467-475.

Keane, A. & O'Malley, M. 2005, "Optimal allocation of embedded generation on distribution networks", *IEEE Transactions on Power Systems,* vol. 20, no. 3, pp. 1640-1646.

Khator, S.K. & Leung, L.C. 1997, "Power distribution planning: A review of models and issues", *IEEE Transactions on Power Systems,* vol. 12, no. 3, pp. 1151-1159.

Kim, K., Lee, Y., Rhee, S., Lee, S. & You, S. 2002, "Dispersed generator placement using fuzzy-GA in distribution systems", *2002 IEEE Power Engineering Society Summer Meeting, July 21, 2002 - July 25*Institute of Electrical and Electronics Engineers Inc, Chicago, IL, United states, pp. 1148.

Kitagawa, T. & Nomura, T. 2003, "A wavelet-based method to generate artificial wind fluctuation data", *Journal of Wind Engineering and Industrial Aerodynamics,* vol. 91, no. 7, pp. 943-964.

Kodsi, S.K.M. & Canizares, C.A. 2003, *Modeling and Simulation of IEEE 14 Bus System with FACTS Controllers*, University of Waterloo, Waterloo.

Leite, d.S. & Arienti, V.L. 1990, "Probabilistic load flow by a multilinear simulation algorithm", *IEE Proceedings C: Generation Transmission and Distribution,* vol. 137, no. 4, pp. 276-282.

Leite, d.S., Arienti, V.L. & Allan, R.N. 1984, "Probabilistic load flow considering dependence between input nodal powers", *IEEE transactions on power apparatus and systems,* vol. PAS-103, no. 6, pp. 1524-1530.

Leite, d.S., Ribeiro, S.M.P., Arienti, V.L., Allan, R.N. & Do Coutto, M.B. 1990, "Probabilistic load flow techniques applied to power system expansion planning", *IEEE Transactions on Power Systems,* vol. 5, no. 4, pp. 1047-1053.

Leon-Garcia, A. 2009, *Probability, Statistics, and Random Process for Electrical Engineering,* 3rd edn, Pearson Prentice-Hall, Englewood Cliffs, NJ.

Linhart, H. & Zucchini, W. 1986, *Model Selection,* Wiley, New York.

Madsen, H., Pinson, P., Kariniotakis, G., Nielsen, H.A. & Nielsen, T.S. 2005, "Standardizing the performance evaluation of short-term wind power prediction models", *Wind Engineering,* vol. 29, no. 6, pp. 475-489.

Mathworks 2009, *MATLAB Optimization ToolboxTM 4, User's Guide*, Natick, MA.

Miranda, V., Ranito, J.V. & Proenca, L.M. 1994, "Genetic algorithms in optimal multistage distribution network planning", *IEEE Transactions on Power Systems,* vol. 9, no. 4, pp. 1927-1933.

Nara, K., Hayashi, Y., Ikeda, K. & Ashizawa, T. 2001, "Application of tabu search to optimal placement of distributed generators", *2001 IEEE Power Engineering Society Winter Meeting, January 28, 2001 - Febrary 1*Institute of Electrical and Electronics Engineers Inc, Columbus, OH, United states, pp. 918.

Negra, N.B., Holmstrm, O., Bak-Jensen, B. & Srensen, P. 2008, "Model of a synthetic wind speed time series generator", *Wind Energy,* vol. 11, no. 2, pp. 193-209.

Nielsen, H.A., Madsen, H. & Nielsen, T.S. 2006, "Using quantile regression to extend an existing wind power forecasting system With probabilistic forecasts", *Wind Energy,* vol. 9, no. 1-2, pp. 95-108.

Norris, J.R. 1997, *Markov Chains,* Cambridge University Press, Cambridge.

Ochoa, L.F., Padilha-Feltrin, A. & Harrison, G.P. 2008, "Time-series-based maximization of distributed wind power generation integration", *IEEE Transactions on Energy Conversion,* vol. 23, no. 3, pp. 968-974.

Papaefthymiou, G. & Klockl, B. 2008, "MCMC for wind power simulation", *IEEE Transactions on Energy Conversion,* vol. 23, no. 1, pp. 234-240.

Papaefthymiou, G. & Kurowicka, D. 2009, "Using copulas for modeling stochastic dependence in power system uncertainty analysis", *IEEE Transactions on Power Systems,* vol. 24, no. 1, pp. 40-49.

Papoulis, A. & Pillai, S.U. 2002, *Probability, Random Variables and Stochastic Processes,* 4th edn, McGraw-Hill, New York.

Pecas Lopes, J.A. 2002, "Integration of dispersed generation on distribution networks - Impact studies", *2002 IEEE Power Engineering Society Winter Meeting, January 27, 2002 - January 31*Institute of Electrical and Electronics Engineers Inc, New York, NY, United states, pp. 323.

Piccolo, A. & Siano, P. 2009, "Evaluating the impact of network investment deferral on distributed generation expansion", *IEEE Transactions on Power Systems,* vol. 24, no. 3, pp. 1559-1567.

Pinson, P. 2006, *Estimation of the Uncertainty in Wind Power Forecasting*, Mines ParisTech.

Pinson, P., Nielsen, H.A., Madsen, H. & Kariniotakis, G. 2009, "Skill forecasting from ensemble predictions of wind power", *Applied Energy,* vol. 86, no. 7-8, pp. 1326-1334.

Rahman, S. & Rinaldy 1993, "An efficient load model for analyzing demand side management impacts", *IEEE Transactions on Power Systems,* vol. 8, no. 3, pp. 1219-1226.

Rau, N.S. & Wan, Y.M. 1994, "Optimum location of resources in distributed planning", *IEEE Transactions on Power Systems,* vol. 9, no. 4, pp. 2014-2020.

Rebours, Y. & Kirschen, D. 2005, *A Survey of Definitions and Specifications of Reserve services*, The University of Manchester, Manchester.

Saadat, H. 2002, *Power System Analysis,* 2nd edn, McGraw-Hill, Singapore.

Sankarakrishnan, A. & Billinton, R. 1995, "Sequential Monte Carlo simulation for composite power system reliability analysis with time varying loads", *IEEE Transactions on Power Systems,* vol. 10, no. 3, pp. 1540-1545.

Schilling, M.T., da Silva, A.M.L., Billinton, R., El-Kady, M. & systems, P. 1990, "Bibliography on power system probabilistic analysis (1962-1988)", *IEEE Transactions on Power Systems,* vol. 5, no. 1, pp. 1-11.

Shamshad, A., Bawadi, M.A., Wan Hussin, W.M.A., Majid, T.A. & Sanusi, S.A.M. 2005, "First and second order Markov chain models for synthetic generation of wind speed time series", *Energy,* vol. 30, no. 5, pp. 693-708.

Sideratos, G. & Hatziargyriou, N.D. 2007, "An advanced statistical method for wind power forecasting", *IEEE Transactions on Power Systems,* vol. 22, no. 1, pp. 258-265.

Simon, H. 2002, *Adaptive Filter Theory,* 4th edn, Prentice Hall, Upper Saddle River, N.J.

Stuart, A. & Keith Ord, J. 1994, *Kendall's Advanced Theory of Statistics: Distribution Theory (Volume 1),* 6th edn, Edward Arnold, London.

Su, C. 2005, "Probabilistic load-flow computation using point estimate method", *IEEE Transactions on Power Systems,* vol. 20, no. 4, pp. 1843-1851.

Suva, L.D., Da, F.M., De, O.M. & Billinton, R. 2000, "Pseudo-chronological simulation for composite reliability analysis with time varying loads", *IEEE Transactions on Power Systems,* vol. 15, no. 1, pp. 73-80.

the Mathworks 2009, *Matlab Mathematics, User's Guide*, Natick, MA.

UNIFLEX PM 2007, *Converter applications in future European Electricity Network.*

Vovos, P.N., Harrison, G.P., Wallace, A.R. & Bialek, J.W. 2005, "Optimal power flow as a tool for fault level-constrained network capacity analysis", *IEEE Transactions on Power Systems,* vol. 20, no. 2, pp. 734-741.

Wang, P. & Billinton, R. 1999, "Time sequential distribution system reliability worth analysis considering time varying load and cost models", *IEEE Transactions on Power Delivery,* vol. 14, no. 3, pp. 1046-1051.

Wangdee, W. & Billinton, R. 2006, "Considering load-carrying capability and wind speed correlation of WECS in generation adequacy assessment", *IEEE Transactions on Energy Conversion,* vol. 21, no. 3, pp. 734-741.

Wei, W.W.S. 1990, *Time Series Analysis: Univariate and Multivariate Methods,* Addison-Wesley, Redwood City.

Willis, H.L. 1997, *Power Distribution Planning Reference Book,* Marcel Dekker, New York.

Willis, H.L. & Scott, W.G. 2000, *Distributed Power Generation: Planning and Evaluation,* CRC, Boca Raton.

Zhang, P. & Lee, S.T. 2004, "Probabilistic Load Flow Computation Using the Method of Combined Cumulants and Gram-Charlier Expansion", *IEEE Transactions on Power Systems,* vol. 19, no. 1, pp. 676-682.

Zhao, M. 2006, *Optimization of Electrical System for Offshore Wind Farms via a Genetic Algorithm Approach*, Department of Energy Technology, Aalborg University.

Zhu, J., Lubkeman, D.L. & Girgis, A.A. 1997, "Automated fault location and diagnosis on electric power distribution feeders", *IEEE Transactions on Power Delivery,* vol. 12, no. 2, pp. 801-809.

Appendix A

Parameter Estimation of Bivariate-LARIMA model

The estimated model parameters of the bivariate-LARIMA(0,1,1) model shown in Fig. 2.17 are summarized as follows.

$$\hat{\boldsymbol{\theta}}_1 = \begin{bmatrix} \hat{\theta}_{11} & \hat{\theta}_{12} \\ \hat{\theta}_{21} & \hat{\theta}_{22} \end{bmatrix} = \begin{bmatrix} -0.15 & -0.04 \\ -0.44 & 0.22 \end{bmatrix} \tag{A.1}$$

$$\hat{\boldsymbol{\Sigma}}_a = \begin{bmatrix} 0.62 & 0.56 \\ 0.56 & 0.61 \end{bmatrix} \quad , \tag{A.2}$$

$$\hat{\boldsymbol{\theta}}_0 = \begin{bmatrix} \hat{\theta}_{0,1} \\ \hat{\theta}_{0,2} \end{bmatrix} = \begin{bmatrix} 0.008 \\ 0.007 \end{bmatrix}. \tag{A.3}$$

The model parameters $\boldsymbol{\theta}_1$ and $\boldsymbol{\Sigma}_a$ are calculated from the covariance matrices of the two measured wind power time series through:

$$\begin{cases} \boldsymbol{\theta}_1^2 \boldsymbol{\Gamma}(1) + \boldsymbol{\theta}_1 \boldsymbol{\Gamma}(0) + \boldsymbol{\Gamma}^{\mathrm{T}}(1) = \mathbf{0} \\ \boldsymbol{\Gamma}(1) = -\boldsymbol{\Sigma}_a \boldsymbol{\theta}_1^{\mathrm{T}} \end{cases} , \tag{A.4}$$

where $\boldsymbol{\Gamma}(0)$ is the covariance matrix at time-lag zero and $\boldsymbol{\Gamma}(1)$ is the covariance matrix at time-lag one. $\boldsymbol{\Gamma}(0)$ and $\boldsymbol{\Gamma}(1)$ are estimated from the measured wind power time series. Equation (A.4) is also valid for multivariate-LARIMA(0,1,1) model.

The model parameter $\boldsymbol{\theta}_0$ is adjusted to match the mean values of the simulated time series ($Y_1(t)$ and $Y_2(t)$) with the measured values through a Monte Carlo simulation.

When the bivariate-LARIMA model is applied to the summer and winter season individually, the corresponding model parameters are summarized as follows. For summer season,

$$\hat{\boldsymbol{\theta}}_{\mathbf{1},\mathrm{sm}} = \begin{bmatrix} -0.18 & 0.01 \\ -0.46 & 0.25 \end{bmatrix}, \tag{A.5}$$

$$\hat{\boldsymbol{\Sigma}}_{a,\mathrm{sm}} = \begin{bmatrix} 0.68 & 0.61 \\ 0.61 & 0.65 \end{bmatrix}, \tag{A.6}$$

$$\hat{\boldsymbol{\theta}}_{0,\mathrm{sm}} = \begin{bmatrix} -0.03 \\ -0.04 \end{bmatrix}. \tag{A.7}$$

For winter season,

$$\hat{\boldsymbol{\theta}}_{\mathbf{1},\mathrm{wt}} = \begin{bmatrix} -0.11 & -0.10 \\ -0.42 & 0.18 \end{bmatrix}, \tag{A.8}$$

$$\hat{\boldsymbol{\Sigma}}_{a,\mathrm{wt}} = \begin{bmatrix} 0.56 & 0.51 \\ 0.51 & 0.56 \end{bmatrix}, \tag{A.9}$$

$$\hat{\boldsymbol{\theta}}_{0,\mathrm{sm}} = \begin{bmatrix} 0.04 \\ 0.05 \end{bmatrix}. \tag{A.10}$$

Appendix B

Probability Distribution Data for the IEEE 14 Bus System

The probability distribution of the generation at bus 2 in the IEEE 14 bus system shown in Fig. 3.1 is assumed to be a Gaussian distribution with mean value of 18.3 MW and the standard deviation of 12.7% of the mean value.

The rest of the loads are assumed to have a Gaussian distribution. Table B.1 summarizes the probability data of these loads. The standard deviation is expressed in percentage of the mean value. The probability distribution of the active power of the load connected at bus 14 is a discrete distribution. The corresponding probability is summarized in Table B.2.

Table B.1
Discrete probability distribution of the active power of the load connected at bus 14.

Bus no.	Active power		Reactive power	
	μ (MW)	σ (%)	μ (MVAr)	σ (%)
3	94.2	10.0	0	0
4	47.8	11.0	−3.9	9.7
5	7.6	5.0	1.6	5.0
6	11.2	1.0	0	0
9	29.5	1.0	0	0
10	9.0	10.0	16.6	5.0
11	3.5	9.5	1.8	9.5
12	6.1	1.0	1.6	8.6
13	13.5	1.0	5.8	9.5
14	0	0	5.0	8.6

Table B.2

Discrete probability distribution of the active power of the load connected at bus 14.

Bus no.	Active power	
	Value (MW)	Probability
14	13	0.35
	15	0.45
	18	0.20

Appendix C

Technical Data of XLPE Underground Cable

The technical data of the XLPE underground cable is summarized from the ABB cable catalog. The Data are for cables in the ground with aluminum conductor.

C.1 Cable Impedance

This subsection summarizes resistance, capacitance and inductance of standard ABB 20 kV three-core cables as shown in Table C.1, and 20 kV single-core XLPE cables as shown in Table C.2.

Table C.1
Resistance, capacitance and inductance of ABB XLPE cable: three-core, 20 kV.

Conductor cross section	**Screen cross section**	**R (20^oC)**	**C**	**L**
mm^2	**mm^2**	**Ω/km**	**µF/km**	**mH/km**
25	10	1.20	0.15	0.43
35	16	0.868	0.17	0.40
50	16	0.641	0.18	0.39
70	16	0.443	0.20	0.37
95	25	0.320	0.22	0.35
120	25	0.253	0.24	0.33
150	35	0.206	0.26	0.32
185	35	0.164	0.28	0.32
240	35	0.125	0.31	0.30

The resistance values are given at the conductor temperature of 20 ^oC. The resistance values at another temperature can be obtained through

$$R_1 = R_0\left[1+\alpha\left(T_1 - T_0\right)\right] \tag{C.1}$$

where R_0 and R_1 are the resistance at temperature T_0 and T_1, respectively; α is the coefficient. $\alpha = 0.0039$ for aluminum and $\alpha = 0.00382$ for copper.

The inductance of single-core cable is related to the distance between conductors. The inductances shown in the tables are given by standard ABB XLPE cables. However, inductance can also be calculated by

$$\mathrm{L} = 0.05 + 0.2\ln\left(\frac{\mathrm{K}\cdot s}{r}\right) \tag{C.2}$$

where L is in mH/km; K = 1 and 1.26 for trefoil formation and flat formation, respectively; *s* is the distance between conductor axes (mm); *r* is the conductor radius (mm).

Table C.2
Resistance, capacitance and inductance of ABB XLPE cable: single-core, 20 kV.

Conductor cross section	**Screen cross section**	**R (20^{o}C)**	**C**	**L (Trefoil)**	**L (Flat)**
mm^2	**mm^2**	**Ω/km**	**μF/km**	**mH/km**	**mH/km**
50	16	0.641	0.18	0.45	0.74
70	16	0.443	0.20	0.42	0.70
95	25	0.320	0.22	0.40	0.68
120	25	0.253	0.24	0.39	0.65
150	35	0.206	0.26	0.37	0.63
185	35	0.164	0.28	0.36	0.62
240	35	0.125	0.31	0.35	0.60
300	35	0.100	0.34	0.33	0.57
400	35	0.0778	0.38	0.32	0.56
500	35	0.0605	0.42	0.31	0.54
630	35	0.0469	0.47	0.30	0.52
800	35	0.0367	0.52	0.30	0.50
1000	35	0.0291	0.57	0.29	0.48
1200	35	0.0247	0.67	0.28	0.46
1400	35	--------	0.74	0.28	0.45
1600	35	0.0186	0.77	0.27	0.45
2000	35	0.0149	0.83	0.27	0.44

C.2 Cable current rating

XLPE cables can be loaded continuously to a conductor temperature of 90 °C. The continuous current ratings for three-core cables are given in Table C.3, and for single-core cables in Table C.4.

Table C.3
Current rating (in A) for three-core cables: rated voltage up to 220 kV.

Cross Section mm^2		**16**	**25**	**35**	**50**	**70**	**95**	**120**	**150**
Conductor Temperature	**65°C**	74	95	115	135	165	195	220	245
	90°C	89	115	135	160	195	230	265	295
Cross Section mm^2		**185**	**240**	**300**	**400**	**500**	**630**	**800**	**1000**
Conductor Temperature	**65°C**	280	320	365	410	465	525	585	645
	90°C	335	385	435	490	560	635	715	785

Table C.4
Current rating (in A) for single-core cables: rated voltage 10-70 kV, 25 or 35 mm^2 screen

Cross Section mm^2	**Flat formation**				**Trefoil formation**			
	Cross bonded		**Both ends**		**Cross bonded**		**Both ends**	
	65°C	**90°C**	**65°C**	**90°C**	**65°C**	**90°C**	**65°C**	**90°C**
95	220	265	215	260	210	250	210	250
120	250	300	245	295	235	285	240	285
150	280	335	270	325	265	320	265	320
185	320	380	300	365	300	360	300	360
240	370	445	345	420	350	420	350	420
300	420	500	385	465	395	475	390	470
400	480	575	430	520	455	545	445	540
500	550	660	480	585	520	620	505	610
630	630	755	530	650	590	710	570	690
800	710	855	580	710	665	805	640	775
1000	795	960	625	775	740	895	700	855
1200	860	1040	660	815	795	965	750	915
1400	920	1115	685	855	845	1030	790	965
1600	970	1175	710	885	890	1080	820	1005
2000	1060	1285	745	930	960	1170	875	1075

The initial current ratings shown in Table C.3 and Table C.4 are calculated based on the following conditions, where D_e is the diameter of a cable.

- Ground temperature: 20 °C
- Laying depth L: 1.0 m
- Distance '*s*' between cable axes laid in flat formation: 70 mm+D_e
- Ground thermal resistivity: 1.0 Km/W

However, there are several rating factors to calculate the final current rating of a cable. These are:

1) Cross section area of metal (copper) screen (f_1)
2) Laying depth (f_2)
3) Ground temperature (f_3)
4) Ground thermal resistivity (f_4)
5) Phase spacing (flat formation) (f_5)
6) Groups of cables (f_6)
7) Cables in pipes (f_7)

The final current rating of a cable should be obtained by

$$\mathrm{I} = \mathrm{I}_0 \cdot \left(f_1 \cdot f_2 \cdot f_3 \cdot f_4 \cdot f_5 \cdot f_6 \cdot f_7 \right). \tag{C.3}$$

C.3 Cable cost

The prices for the 20 kV single-core cable used in the thesis is summarized in Table C.5. The prices for the 20 kV three-core cable are assumed to be the same as corresponding single-core cables.

Table C.5
20 kV single-core cable price.

Conductor size (mm^2)	Price (DKK/km)
120	330,000
150	347,500
185	367,900
240	400,000

Appendix D

Sensitivity Factor Calculation for Constrained Load Flow

D.1 Calculation of sensitivity factors

a) Function of constrained variable w

In order to numerically calculate the sensitivity factor, the functions **f** of different constrained variables **W** need to be first identified. For the constrained variables described in section 7.3.1, the functions **f** are as follows.

- If $w = V_\mathrm{i}$, where V_i is the voltage magnitude at bus i, then

$$f = V_i \tag{D.1}$$

- If $w = Q_{Gi}$, which is the reactive power generation/consumption at the PV bus i, then

$$f - Q_{Li} = \begin{cases} -V_i^2\left(B_{ii}^0 + B_{ik}/a_{ik}^2\right) + V_i \sum\limits_{\substack{k=1\\ \neq i}}^{n-m-1} V_k/a_{ik}\left(G_{ik}\sin\theta_{ik} - B_{ik}\cos\theta_{ik}\right), & \begin{array}{l} \mathit{ik\ is\ transformer} \\ \mathit{\&\, i\ is\ tap\ side} \end{array} \\ V_i \sum\limits_{k=1}^{n-m-1} V_k/a_{ik}\left(G_{ik}\sin\theta_{ik} - B_{ik}\cos\theta_{ik}\right), & \mathit{for\ the\ rest} \end{cases} \tag{D.2}$$

where Q_{Li} is the total reactive load connected to bus i; a_{ik} is 1 if line ik is a power line, or the tap ratio if line ik is a tap-changing transformer; a_{ii} is defined as 1; $B_{ii}{}^0$ is the tap-ratio independent part of the total diagonal susceptance of bus i.

- If $w = P_{ij}$, which is the active power flow through line ij at bus i side, then

$$f = \frac{1}{a_{ij}}\left[G_{ij}V_i^2 - G_i^{'}V_i^2 - V_iV_j\left(G_{ij}\cos\theta_{ij} + B_{ij}\sin\theta_{ij}\right)\right] \tag{D.3}$$

where G_{ij} and B_{ij} is the real and imaginary part of the series admittance of line ij;

$$G_i^{'} = \begin{cases} 0, & \text{if line } ij \text{ is a power line} \\ \left(a_{ij} - 1\right) G_{ij}, & \text{if line } ij \text{ is a transformer\&bus } i \text{ is the tap side} \\ \left(1/a_{ij} - 1\right) G_{ij}, & \text{if line } ij \text{ is a transformer\&bus } i \text{ is the nontap side} \end{cases} . \quad \text{(D.4)}$$

- If $w = Q_{ij}$, which is the reactive power flow through line *ij* at bus *i* side, then

$$f = \frac{1}{a_{ij}} \left[-B_{ij} V_i^2 + B_i^{'} V_i^2 - V_i V_j \left(G_{ij} \sin\theta_{ij} - B_{ij} \cos\theta_{ij} \right) \right] \quad \text{(D.5)}$$

where

$$B_i^{'} = \begin{cases} B_{ij}^{s} / 2, & \text{if line } ij \text{ is a power line} \\ \left(a_{ij} - 1\right) B_{ij}, & \text{if line } ij \text{ is a transformer\&bus } i \text{ is the tap side} \\ \left(1/a_{ij} - 1\right) B_{ij}, & \text{if line } ij \text{ is a transformer\&bus } i \text{ is the nontap side} \end{cases} , \quad \text{(D.6)}$$

and B_{ij}^{s} is the total susceptance of the power line.

- If $w = S_{ij}^2$, which is the square of the apparent power flow through line *ij* at bus *i* side, then

$$f = P_{ij}^2 + Q_{ij}^2 \quad \text{(D.7)}$$

- If $w = I_{ij}^2$, which is the square of the current flow through line *ij* at bus *i* side, then

$$f = \frac{P_{ij}^2 + Q_{ij}^2}{V_i^2} \quad \text{(D.8)}$$

- If $w = Q_i^{sh}$, which is the shunt reactive power compensation at bus *i*, then

$$f = V_i^2 B_i^{sh} \tag{D.9}$$

where B_i^{sh} is the equivalent shunt susceptance.

b) Expression of $\left[\dfrac{\partial f(\mathbf{X},\mathbf{U})}{\partial u_{ct}}\right]^{\mathrm{T}}$

Once the function f is indentified, the partial derivation of the function f with respect to the control variable u_{ct} is easy to derive. As discussed in section 7.3.1, there are mainly five types of control variables, i.e. tap ratio a, amount of reactive power compensation, voltage magnitude of a PV bus, active power of a PV bus and the load power to be shed. The term $\left[\dfrac{\partial f(\mathbf{X},\mathbf{U})}{\partial u_{ct}}\right]^{\mathrm{T}}$ indicates the change of the constrained variable w due to the change of the control variable u_{ct}, under the assumption that all the other system states (excluding w) remain unchanged (i.e. $\dfrac{\partial \mathbf{X}}{\partial u_{ct}} = 0$).

- If $w = V_{\mathrm{i}}$, for all the types of u_{ct},

$$\frac{\partial V_i}{\partial u_{ct}} = 0\,. \tag{D.10}$$

- If $w = Q_{Gi}$,
  if u_{ct} is the tap ratio a_{ik} and bus i is the tap side, then

$$\frac{\partial Q_{Gi}}{\partial a_{ik}} = 2V_i^2 \frac{B_{ik}}{a_{ik}^3} - \frac{V_i V_k \left(G_{ik}\sin\theta_{ik} - B_{ik}\cos\theta_{ik}\right)}{a_{ik}^2}\,. \tag{D.11}$$

if u_{ct} is the tap ratio a_{ik} and bus i is the non-tap side, then

$$\frac{\partial Q_{Gi}}{\partial a_{ik}} = -\frac{V_i V_k \left(G_{ik}\sin\theta_{ik} - B_{ik}\cos\theta_{ik}\right)}{a_{ik}^2}\,. \tag{D.12}$$

if u_{ct} is the voltage V_i of the PV bus i, then

$$\frac{\partial Q_{Gi}}{\partial V_i} = -2B_{ii}V_i + \sum_{\substack{k=1\\ \neq i}}^{n-m-1} V_k / a_{ik} \left(G_{ik} \sin\theta_{ik} - B_{ik} \cos\theta_{ik} \right). \tag{D.13}$$

for other types of u_{ct},

$$\frac{\partial Q_{Gi}}{\partial u_{ct}} = 0\,. \tag{D.14}$$

- If $w = P_{ij}$,

  if u_{ct} is the tap ratio a_{ij}, then

$$\frac{\partial P_{ij}}{\partial a_{ij}} = \frac{1}{a_{ij}^2}\left[-2G_{ij}V_i^2 + V_iV_j\left(G_{ij}\cos\theta_{ij} + B_{ij}\sin\theta_{ij}\right)\right], \text{ if the tap side is bus } i; \tag{D.15}$$

or

$$\left.\begin{aligned} \frac{\partial P_{ij}}{\partial a_{ij}} &= \frac{1}{a_{ij}^2}\left[-G_{ij}V_i^2 + \left(2/a_{ij} - 1\right)G_{ij}V_i^2\right] \\ &\quad + \frac{1}{a_{ij}^2}\left(G_{ij}\cos\theta_{ij} + B_{ij}\sin\theta_{ij}\right)V_iV_j \end{aligned}\right., \text{ if the tap side is bus } j. \tag{D.16}$$

if u_{ct} is the voltage V_i of the PV bus i, then

$$\frac{\partial P_{ij}}{\partial V_i} = \frac{1}{a_{ij}}\left[2V_i\left(G_{ij} - G_i^{'}\right) - V_j\left(G_{ij}\cos\theta_{ij} + B_{ij}\sin\theta_{ij}\right)\right]. \tag{D.17}$$

if u_{ct} is the voltage V_j of the PV bus j, then

$$\frac{\partial P_{ij}}{\partial V_j} = \frac{1}{a_{ij}}\left[-V_i\left(G_{ij}\cos\theta_{ij} + B_{ij}\sin\theta_{ij}\right)\right]. \tag{D.18}$$

for other types of u_{ct},

$$\frac{\partial P_{ij}}{\partial u_{ct}} = 0. \tag{D.19}$$

- If $w = Q_{ij}$,

  if u_{ct} is the tap ratio a_{ij}, then

$$\frac{\partial Q_{ij}}{\partial a_{ij}} = \frac{1}{a_{ij}^2}\left[2B_{ij}V_i^2 + V_iV_j\left(G_{ij}\sin\theta_{ij} - B_{ij}\cos\theta_{ij}\right)\right], \text{ if the tap side is bus } i; \tag{D.20}$$

or

$$\begin{aligned}\frac{\partial Q_{ij}}{\partial a_{ij}} = {} & \frac{1}{a_{ij}^2}\left[B_{ij}V_i^2 - \left(2/a_{ij} - 1\right)B_{ij}V_i^2\right] \\ & + \frac{1}{a_{ij}^2}\left(G_{ij}\sin\theta_{ij} - B_{ij}\cos\theta_{ij}\right)V_iV_j\end{aligned}, \text{ if the tap side is bus } j. \tag{D.21}$$

if u_{ct} is the voltage V_i of the PV bus i, then

$$\frac{\partial Q_{ij}}{\partial V_i} = \frac{1}{a_{ij}}\left[-2V_i\left(B_{ij} - B_i^{'}\right) - V_j\left(G_{ij}\sin\theta_{ij} - B_{ij}\cos\theta_{ij}\right)\right]. \tag{D.22}$$

if u_{ct} is the voltage V_j of the PV bus j, then

$$\frac{\partial Q_{ij}}{\partial V_j} = \frac{1}{a_{ij}} \left[-V_i \left(G_{ij} \sin\theta_{ij} - B_{ij} \cos\theta_{ij} \right) \right]. \qquad (D.23)$$

for other types of u_{ct},

$$\frac{\partial Q_{ij}}{\partial u_{ct}} = 0\,. \qquad (D.24)$$

- If $w = S_{ij}^2$,

  if u_{ct} *is the tap ratio* a_{ij} *or the voltage* V_i (V_j)*of the PV bus i (j), then*

$$\frac{\partial S_{ij}^2}{\partial u_{ct}} = 2\left(P_{ij} \frac{\partial P_{ij}}{\partial u_{ct}} + Q_{ij} \frac{\partial Q_{ij}}{\partial u_{ct}} \right) \qquad (D.25)$$

where the expressions for P_{ij} and Q_{ij} are (12) and (13), respectively; the expressions for the two partial derivative terms are found from the previous two bullets.

for other types of u_{ct},

$$\frac{\partial S_{ij}^2}{\partial u_{ct}} = 0 \qquad (D.26)$$

- If $w = I_{ij}^2$,

  if u_{ct} *is the tap ratio* a_{ij}, *then*

$$\frac{\partial I_{ij}^2}{\partial a_{ij}} = \frac{2}{V_i^2}\left(P_{ij} \frac{\partial P_{ij}}{\partial u_{ct}} + Q_{ij} \frac{\partial Q_{ij}}{\partial u_{ct}} \right). \qquad (D.27)$$

if u_{ct} is the voltage V_i of the PV bus i, then

$$\frac{\partial I_{ij}^2}{\partial V_i} = -\frac{2}{V_i^3}\left[S_{ij}^2 - V_i\left(P_{ij}\frac{\partial P_{ij}}{\partial V_i} + Q_{ij}\frac{\partial Q_{ij}}{\partial V_i}\right)\right]. \tag{D.28}$$

if u_{ct} is the voltage V_j of the PV bus j, then

$$\frac{\partial I_{ij}^2}{\partial V_j} = \frac{2}{V_i^2}\left(P_{ij}\frac{\partial P_{ij}}{\partial u_{ct}} + Q_{ij}\frac{\partial Q_{ij}}{\partial u_{ct}}\right). \tag{D.29}$$

for other types of u_{ct},

$$\frac{\partial I_{ij}^2}{\partial u_{ct}} = 0. \tag{D.30}$$

- If $w = Q_i^{sh}$,

  if u_{ct} is the voltage V_i of the PV bus i, then

$$\frac{\partial Q_i^{sh}}{\partial V_i} = 2V_iB_i^{sh}. \tag{D.31}$$

if u_{ct} is the susceptance B_i^{sh} of the shunt compensator at bus i,

$$\frac{\partial Q_i^{sh}}{\partial B_i^{sh}} = V_i^2. \tag{D.32}$$

c) Expression of $\dfrac{\partial \mathbf{g}(\mathbf{X}, \mathbf{U})}{\partial u_{ct}}$

The expression of the partial derivative of load flow equations with respect to the control variables is independent of the chosen constrained variables. The term $\mathbf{J}^{-1}\dfrac{\partial \mathbf{g}(\mathbf{X},\mathbf{U})}{\partial u_{ct}}$ indicates the change of all the system states **X** (voltage magnitude and phase angle) due to the change of the control variable u_{ct}. The load flow equation (1) can be expressed as:

$$P_i = \begin{cases} -V_i^2\left(G_{ii}^0 + G_{ik}/a_{ik}^2\right) + V_i \sum\limits_{\substack{k=1\\ \neq i}}^{n-m-1} V_k/a_{ik}\left(G_{ik}\cos\theta_{ik} + B_{ik}\sin\theta_{ik}\right), & \begin{matrix} \textit{ik is transformer} \\ \textit{\& i is tap side}\end{matrix} \\ V_i \sum\limits_{k=1}^{n-m-1} V_k/a_{ik}\left(G_{ik}\cos\theta_{ik} + B_{ik}\sin\theta_{ik}\right), & \textit{for the rest} \end{cases} \tag{D.33}$$

$$Q_i = \begin{cases} -V_i^2\left(B_{ii}^0 + B_{ik}/a_{ik}^2\right) + V_i \sum\limits_{\substack{k=1\\ \neq i}}^{n-m-1} V_k/a_{ik}\left(G_{ik}\sin\theta_{ik} - B_{ik}\cos\theta_{ik}\right), & \begin{matrix} \textit{ik is transformer} \\ \textit{\& i is tap side}\end{matrix} \\ V_i \sum\limits_{k=1}^{n-m-1} V_k/a_{ik}\left(G_{ik}\sin\theta_{ik} - B_{ik}\cos\theta_{ik}\right), & \textit{for the rest} \end{cases} \tag{D.34}$$

where G_{ii}^{0} is the tap-ratio independent part of the total diagonal conductance of bus i; P_i and Q_i is the equivalent active and reactive power injections to bus i:

$$\begin{cases} P_i = P_{Gi} - P_{Li} \\ Q_i = Q_{Gi} - Q_{Li} + Q_i^{sh} \end{cases} \tag{D.35}$$

where P_{Gi} (P_{Li}) and Q_{Gi} (Q_{Li}) are the active and reactive generation (load) injected to bus i.

- If u_{ct} is the tap ratio a_{ik},

$$\frac{\partial P_i}{\partial a_{ik}} = \begin{cases} 2V_i^2 \dfrac{G_{ik}}{a_{ik}^3} - \dfrac{V_i V_k \left(G_{ik} \cos\theta_{ik} + B_{ik} \sin\theta_{ik} \right)}{a_{ik}^2} & i \textit{ is tap side} \\ -\dfrac{V_i V_k \left(G_{ik} \cos\theta_{ik} + B_{ik} \sin\theta_{ik} \right)}{a_{ik}^2} & i \textit{ is nontap side} \\ 0 & ik \textit{ is power line} \end{cases} \tag{D.36}$$

$$\frac{\partial Q_i}{\partial a_{ik}} = \begin{cases} 2V_i^2 \dfrac{B_{ik}}{a_{ik}^3} - \dfrac{V_i V_k \left(G_{ik} \sin\theta_{ik} - B_{ik} \cos\theta_{ik} \right)}{a_{ik}^2} & i \textit{ is tap side} \\ -\dfrac{V_i V_k \left(G_{ik} \sin\theta_{ik} - B_{ik} \cos\theta_{ik} \right)}{a_{ik}^2} & i \textit{ is nontap side} \\ 0 & ik \textit{ is power line} \end{cases} \tag{D.37}$$

- If u_{ct} is the voltage V_i at the PV bus i,

$$\frac{\partial P_j}{\partial V_i} = \begin{cases} 0 & j \textit{ is PV bus or } j = i \\ V_j / a_{ji} \left(G_{ji} \cos\theta_{ji} + B_{ji} \sin\theta_{ji} \right) & j \neq i \end{cases} \tag{D.38}$$

$$\frac{\partial Q_j}{\partial V_i} = \begin{cases} -2B_{ii}V_i + \sum\limits_{\substack{k=1 \\ \neq i}}^{n-m-1} V_k / a_{ik} \left(G_{ik} \sin\theta_{ik} - B_{ik} \cos\theta_{ik} \right), & j = i \\ -V_j / a_{ji} \left(G_{ji} \sin\theta_{ji} - B_{ji} \cos\theta_{ji} \right), & j \neq i \end{cases} \tag{D.39}$$

- If u_{ct} is the active power generation P_{Gi} at the PV bus i,

$$\frac{\partial P_j}{\partial P_{Gi}} = \begin{cases} 1 & j = i \\ 0 & j \neq i \end{cases}, \tag{D.40}$$

$$\frac{\partial Q_j}{\partial P_{Gi}} = 0 . \tag{D.41}$$

- If u_{ct} is the equivalent susceptance of the shunt compensator B_i^{sh},

$$\frac{\partial P_j}{\partial B_i^{sh}} = 0 , \tag{D.42}$$

$$\frac{\partial Q_j}{\partial B_i^{sh}} = \begin{cases} V_i^2 & j = i \\ 0 & j \neq i \end{cases} . \tag{D.43}$$

- If u_{ct} is the load to be shed P_{Li}+jQ_{Li}, then

$$\frac{\partial P_j}{\partial P_{Li}} = \begin{cases} -1, & j = i \\ 0, & j \neq i \end{cases} , \tag{D.44}$$

$$\frac{\partial Q_j}{\partial Q_{Li}} = \begin{cases} -1, & j = i \\ 0, & j \neq i \end{cases} . \tag{D.45}$$

d) Expression of $\frac{\partial f\left(\mathbf{X}, \mathbf{U}\right)}{\partial \mathbf{X}}$

The term $\frac{\partial f\left(\mathbf{X}, \mathbf{U}\right)}{\partial \mathbf{X}}$ indicates the change of the constrained variable w due to the change of all the system states **X**.

- If $w = V_\mathrm{i}$,

$$\frac{\partial V_i}{\partial V_t} = \begin{cases} 1, & t = i \\ 0, & t \neq i \end{cases} , \tag{D.46}$$

$$\frac{\partial V_i}{\partial \theta_t} = 0. \tag{D.47}$$

- If $w = Q_{Gi}$,

$$\frac{\partial Q_{Gi}}{\partial V_t} = \begin{cases} -2V_i B_{ii} + \sum\limits_{\substack{k=1 \\ \neq i}}^{n-m-1} V_k \left(G_{ik} \sin \theta_{ik} - B_{ik} \cos \theta_{ik} \right) \big/ a_{ik}, & t = i \\ V_i \left(G_{it} \sin \theta_{it} - B_{it} \cos \theta_{it} \right) \big/ a_{it}, & t \neq i \end{cases}, \tag{D.48}$$

$$\frac{\partial Q_{Gi}}{\partial \theta_t} = \begin{cases} 0, & t = i \\ -V_i V_t \left(G_{it} \cos \theta_{it} + B_{it} \sin \theta_{it} \right) \big/ a_{it}, & t \neq i \end{cases}. \tag{D.49}$$

- If $w = P_{ij}$, (indicate that $i \neq j$)

$$\frac{\partial P_{ij}}{\partial V_t} = \begin{cases} \left[2V_i \left(G_{ij} - G_i^{'} \right) - V_j \left(G_{ij} \cos \theta_{ij} + B_{ij} \sin \theta_{ij} \right) \right] \big/ a_{ij}, & t = i \\ -V_i \left(G_{ij} \cos \theta_{ij} + B_{ij} \sin \theta_{ij} \right) \big/ a_{ij} & t = j \\ 0, & t \neq i, j \end{cases}, \tag{D.50}$$

$$\frac{\partial P_{ij}}{\partial \theta_t} = \begin{cases} -V_i V_j \left(-G_{ij} \sin \theta_{ij} + B_{ij} \cos \theta_{ij} \right) \big/ a_{ij}, & t = i \\ -V_i V_j \left(G_{ij} \sin \theta_{ij} - B_{ij} \cos \theta_{ij} \right) \big/ a_{ij} & t = j \\ 0, & t \neq i, j \end{cases}. \tag{D.51}$$

- If $w = Q_{ij}$, (indicate that $i \neq j$)

$$\frac{\partial Q_{ij}}{\partial V_t} = \begin{cases} \left[2V_i \left(B_{ij} - B_i^{'} \right) - V_j \left(G_{ij} \sin\theta_{ij} - B_{ij} \cos\theta_{ij} \right) \right] \Big/ a_{ij}, & t = i \\ -V_i \left(G_{ij} \sin\theta_{ij} - B_{ij} \cos\theta_{ij} \right) \Big/ a_{ij} & t = j \\ 0, & t \neq i, j \end{cases}, \tag{D.52}$$

$$\frac{\partial Q_{ij}}{\partial \theta_t} = \begin{cases} -V_i V_j \left(G_{ij} \cos\theta_{ij} + B_{ij} \sin\theta_{ij} \right) \Big/ a_{ij}, & t = i \\ V_i V_j \left(G_{ij} \cos\theta_{ij} + B_{ij} \sin\theta_{ij} \right) \Big/ a_{ij} & t = j \\ 0, & t \neq i, j \end{cases}. \tag{D.53}$$

- If $w = S_{ij}^2$, (indicate that $i \neq j$)

$$\frac{\partial S_{ij}^2}{\partial V_t} = 2P_{ij} \frac{\partial P_{ij}}{\partial V_t} + 2Q_{ij} \frac{\partial Q_{ij}}{\partial V_t}, \tag{D.54}$$

$$\frac{\partial S_{ij}^2}{\partial \theta_t} = 2P_{ij} \frac{\partial P_{ij}}{\partial \theta_t} + 2Q_{ij} \frac{\partial Q_{ij}}{\partial \theta_t}. \tag{D.55}$$

- If $w = I_{ij}^2$, (indicate that $i \neq j$)

$$\frac{\partial I_{ij}^2}{\partial V_t} = \begin{cases} -\frac{2}{V_i^3} \left(P_{ij}^2 + Q_{ij}^2 \right) + \frac{1}{V_i^2} \frac{\partial S_{ij}^2}{\partial V_i}, & t = i \\ \frac{1}{V_i^2} \frac{\partial S_{ij}^2}{\partial V_t}, & t \neq i \end{cases} \tag{D.56}$$

$$\frac{\partial I_{ij}^2}{\partial \theta_t} = \frac{1}{V_i^2} \frac{\partial S_{ij}^2}{\partial \theta_t} \tag{D.57}$$

- If $w = Q_i^{sh}$,

$$\frac{\partial Q_i^{sh}}{\partial V_t} = \begin{cases} 2V_i B_i^{sh}, & t = i \\ 0, & t \neq i \end{cases}, \tag{D.58}$$

$$\frac{\partial Q_i^{sh}}{\partial \theta_t} = 0\,. \tag{D.59}$$